Importance of Heat Transfer During Carbon Monoxide Oxidation

by

Robert T. Henderson

A dissertation submitted to the Graduate Faculty of
Auburn University
in partial fulfillment of the
requirements for the Degree of
Doctor of Philosophy

Auburn, Alabama
August 1, 2015

Keywords: Microfibrous entrapped catalyst, CO, Carbon Monoxide, Oxidation
Effective Thermal Conductivity, Kinetic Model

Approved by

Bruce J. Tatarchuk, Chair, Professor of Chemical Engineering
Mario R. Eden, Professor of Chemical Engineering
Steve R. Duke, Associate Professor of Chemical Engineering
Bart C. Prorok, Professor of Mechanical Engineering

Abstract

Interest in Carbon Monoxide Oxidation dates back to 1922 by Irving Langmuir himself. Since, a wide body of work has surfaced. Commercially available catalysts work in low humidity and high CO concentrations, such as Moleculite and Carulite at temperatures above 25 °C. Aurolite, a more recent gold based catalyst, is active all the way down to -40 °C. Above room temperature and 50% relative humidity, RH, there are few options. A Pt-CeO_2 on SiO_2 catalyst has been developed to fill the gap above 50% RH. Experimental results are obtained and modeled for a wide variety of working conditions with special attention paid to heat effects.

Oxidation of CO is widely known to display negative order kinetics with respect to CO. It is also highly exothermic with an activation energy of 283 kJ/mol. This combination of factors amplifies sensitivity to temperature and concentration changes. It also muddies kinetic data with high CO concentrations or conversions. Literature typically operates around 1% CO which corresponds to a 100 °C adiabatic heat rise in a packed bed. Experiments were performed at low CO concentrations, below 2500 ppm, and will be presented and modeled using the Pt-CeO_2 on SiO_2 catalyst in excess oxygen. The large humidity range, from 0% to 90%, demands water adsorption on the SiO_2 based packed bed also be accounted for. This has strong heat effects of its own; which are typically the domain of water/silica based adsorption chillers. The demands of the system necessitated a heterogeneous surface coverage based model which accurately models the oxidation of CO in a wide range of face velocities, CO concentrations, temperatures and humidity levels.

The effect of axial conductivity, k_{eff}, on the reaction system is also shown to significantly alter reactor performance. k_{eff} is modified by using four different carrier gases: He, N_2, Ar and Kr. This changed k_{eff} from .51 W/(m*K) to .091 W/(m*K). The results show an increase in the temperature at the front of the packed bed, and thus better CO conversion. The model is employed to offer insights into the reactor's behavior. Finally, a comparison is made using Microfibrous media, MFM. The MFM holds the catalyst in a copper sinter locked mesh which allows for excellent heat conduction. The MFM entrapped catalyst has a k_{eff} of .54 W/(m*K) in flowing N_2 and exhibits an increase in catalytic performance and longevity relative to a packed bed.

Acknowledgments

I would like to thank Dr. Bruce J. Tatarchuk for all the guidance and encouragement. I would also like to thank all the committee members Dr. Eden, Dr. Duke and Dr. Prorok. My time at Auburn would not have been as safe or fun without the help of Dwight Cahela. Dr. Donald R. Cahela also deserves thanks for answering many many questions. This work would not be possible without the good workers at Intermicron, namely: Dr. Paul S. Dimick and Dr. Hongyun Yang. Many thanks to all the great member of the Center for Microfibrous Materials Manufacturing.

I also need to thank my wonderful family and friends, especially my girlfriend, Jillian E. Birch.

Table of Contents

List of Tables

List of Figures

List of Abbreviations

Symbol	Name	Units
$\%D$	Crystallite Dispersion	
A	Pre-exponential Factor	$1/s, m^3/s, m^6/s$
a_P	Surface Area Catalyst per volume Bed	m^2/m^3
Bo	Bodenstein number	
C	Concentration	mol/m^3 or mol/cm^2
C_P	Heat Capacity	$J/(m^3 \cdot K)$
d	Diameter	m
D	Diffusivity	m^2/s
e	Charge of an Electron	C
E_A	Activation Energy	$J/(mol \cdot K)$
F	Collision Rate	$mol/(m^3 \cdot s)$
F	Faraday Constant	A/mol
h	heat transfer Coefficient	$W/(m^2 \cdot K)$
k	Reaction constant	$1/s, m^3/s, m^6/s$
k	Boltzmann Constant	J/K
K	Equilibrium Constant	1/Pa
k_E	Effective Thermal Conductivity	$W/(m \cdot K)$

L	Reactor total Length	m
M_{W}	Molecular Weight	g/mol
P	Pressure	Pa
R	Gas Constant	J/(mol·K)
r	Reaction rate	mol/(m^3·s)
RE	Reynolds Number	
S	Sticking Coefficient	
Sc	Schmidt Number	
Sh	Sherwood Number	
T	Temperature	K, °C
u	Superficial Gas Velocity	m/s
v	Velocity	m/s
V	Volume	m^3
X	Conversion	
ΔH_{Rx}	Heat of reaction	kJ/mol

Greek Symbols

β	Radial Dispersion Factor	
γ	Shape Factor	
δ	Film thickness	m
ε	Adsorption Potential	J/ mol
$\boldsymbol{\varepsilon_{AB}}$	Characteristic Lenord-Jones Energy	J

ζ	Dimensionless Temperature	
θ	Fraction Monolayer	
μ	Viscosity	Pa·s
ρ	Density	Kg/m^3
σ	Surface Charge	C/m^2
σ^2_{AB}	Mean Characteristic Length	m
τ	Tourtuosity	
τ	Time constant	1/s
χ	Heterogeneous Contacting Efficiency	
ψ	Surface Potential	V
ψ	Dimensionless Gas Concentration	
Ω_d	Diffusion Collision Integral	
ϕ	Void fraction	

Superscripts

·	Molar bases

Subscripts

∞	Infinity, limiting value
at	Atomic
ax	Axial
B	Bulk

C	Critical point	
c	External mass transfer rate	m/s
Cat	Catalyst	
CO	Carbon Monoxide	
D	Desorption	
eff	Effective Thermal Conductivity	W/(m·K)
ext	External mass transfer Coefficient	1/s
f	Fluid Phase	
G	Gas Phase	
Inert	Inert	
m	Molecular	
O	Oxygen	
p	Particle	
r	Radial Direction	
re	Reactor	
rx	Reaction	
S	Surface	
Sat	Saturation	
vs	Volume Surface Mean	
z	Axial Direction	

Chapter 1 : Introduction

1.1 Motivation

Carbon monoxide is odorless and colorless in air. In humans, the CO inhaled takes the place of oxygen on the iron in red blood cells. The red blood cells contain Fe^{2+} which is oxidized by the lungs and used to carry oxygen to all parts of the body. CO has a 200 to 250

Table 1-1: Symptoms for different time and CO concentration levels.

Concentration of CO / ppm	Time		Symptoms
35	8	h	Maximum exposure allowed by OSHA in the workplace over an eight hour period.
200	2-3	h	Mild headache, fatigue, nausea and dizziness.
400	1-2	h	Serious headache-other symptoms intensify. Life threatening after 3 hours.
800	45	min	Dizziness, nausea and convulsions. Unconscious within 2 hours. Death within 2-3 hours.
1,600	20	min	Headache, dizziness and nausea. Death within 1 hour.
3,200	5-10	min	Headache, dizziness and nausea. Death within 1 hour.
6,400	1-2	min	Headache, dizziness and nausea. Death within 25-30 minutes.
12,800	1-3	min	Death

times higher affinity for Fe^{2+} than oxygen [1]. Thus, CO replaces oxygen in the blood leading to cellular hypoxia[2].

The CO infected hemoglobin forms Carboxyhemoglobin, COhb. The levels of which are determined by the concentration and duration of CO exposure. Table 1-1 provides a breakdown of symptoms for different exposure levels.

The effects are also damaging to a proton exchange membrane fuel cell (PEM). PEM fuel cells need an oxygen supply for the cathode. This supply ideally will be from the atmosphere. The cathode side of the fuel cell is brought to 96% efficiency from as little as 20ppm CO in the oxygen supply [3]. A filter which can work in a wide variety of conditions, including high humidity and low CO concentrations, is needed.

The potential for Carbon Monoxide generation is ubiquitous in the industrial workplace and transportation, both public and private. The sources are common and unavoidable. Universal devices such as vehicles (including forklifts) which pollute the roadway and plant floor, portable generators, gasoline powered tools, space heaters, compressors, furnaces and boilers contribute to the rise of CO above safe levels [4].

Applications include: cathode fuel cell CO filtering, in car passenger CO filter, a filter for Navy aircraft carrier launched jets or a filter for CO levels found during a fire. The cathode performance in a fuel cell is heavily degraded by the presence of CO. In the car, jet cabin and fire escape mask applications, CO removal seeks to reduce CO levels for the safety of a human occupant.

The CO oxidation reaction is highly temperature dependent and displays a negative reaction order. These two factors point to the importance of the temperature profile in the packed bed and the dependence on the thermal conductivity of the bed on reactor performance.

The best catalyst thus far for room temperature CO oxidation in high RH is a, developed in house, Pt- CeO_2 based catalyst. Pt, being an expensive ingredient, also needs to take a cost effective route if the catalyst ever hopes to see application.

1.2 Objectives

The objective of this work is twofold: to demonstrate the effective catalytic oxidation of CO at room temperature, humid conditions, while maintaining low pressure drop, and to capture the unstable, sometimes odd reaction kinetics that can result from a negative order reaction which is both exothermic and temperature sensitive. There are a number of strategies to achieve this.

The previous work by Punde et al. has provided a good start to the catalyst formulation. The base catalyst recipe was tweaked through a few parameters such as catalytic precursor and impregnating solution pH. Drying steps, to eliminate the need for vacuum drying, were also changed. The primary aim of the recipe tweaks is to help with scale up issues that could be encountered down the road to potential commercialization.

The packing mechanism was investigated. Specifically, the comparison of a packed bed with microfibrous entrapped media. Particularly, the effect of thermal conductivity was explored. The high heat of reaction, small activation energy of CO oxidation and negative order reaction kinetics led to strong thermal effects. In the real world, particle size is limited in a packed bed. Microfibrous media was exploited to provide a medium in which small particles can be used in rough real world environments.

The effect of thermal conductivity was found to be very important. In order to gain experimental proof, different carrier gases were used to enhance thermal conductivity. He, Ar, N_2 and Kr were all used to alter the effective thermal conductivity in a packed bed. This allows the reaction kinetics to be studied in a familiar packed bed setting.

To aid in the optimization and understanding of the system, a reaction model was developed and employed. The model needed to capture the heat effects stemming from the exothermic nature of the reaction, and the thermal conductivity of the reactor. As well as, accurately predict the effects of CO concentration and humidity on conversion. This model lays the foundation of understanding the reaction beyond simply a qualitative sense.

Chapter 2 : Literature Review

2.1 History and Introduction of Catalytic CO oxidation

The current state of catalytic CO oxidation research provides a plethora of different catalysts which deactivate or ignite based on challenge gas conditions. The commercial catalysts consist of a simple mixture of two metal oxides such as Hopcalite or a more complex noble metal on metal oxide support such as Aurolite. The academic literature abounds with different recipes, configurations and testing procedures.

The reaction itself is very simple. In it, CO is oxidized to form CO_2 by the following the equation:

Equation 2-1: $CO + \frac{1}{2}O_2 \rightarrow CO_2$

This is a highly exothermic reaction which also displays self poisoning. From a cursory look at CO oxidation it appears simple. However, the high heat of reaction and self poisoning give rise to a very complex reaction which has been studied for over 90 years.

In the beginning it was Langmuir himself who first dove into investigating CO oxidation on Pt. His first paper on the subject was published in 1922. In it, he presented the negative dependence of reaction rate on CO concentration and proposed an Eley-Rideal type reaction mechanism; in which, the CO must strike atomically adsorbed O on the Pt surface [5].

Around this same time Hopcalite was being developed. Copper and manganese had shown reactivity for CO oxidation[6]. The mixture of the two proved even better, and it allowed the reaction to proceed even around room temperature. Although the catalyst has proven effective for dry conditions, humidity quickly deactivates the catalyst [7]. This shortcoming greatly reduces the real world application space.

In 1989 a new class of catalyst was demonstrated effective for the job. Finely dispersed noble metal catalysts proved effective for low temperature CO oxidation. The discovery of the highly active nano-sized gold on TiO_2 by Haruta et al. set off a large body of research[8]. Since, the research space has grown to include Platinum, Palladium, Iridium and Co_2O_3 on Oxide supports such as ZrO_2, TiO_2, Fe_2O_3, CeO_2, Al_2O_3, SiO_2, SnO_2 and others[9][10][11][12][13][14][15].

These formulations have been tested for CO removal in high concentrations (≈1%) with only a few getting to much lower CO concentrations[14]. The adiabatic heat rise of the CO oxidation reaction is almost a degree per 100 ppm CO converted[16]. This leads to a 97 °C adiabatic heat rise for a complete conversion of a 1% CO mixture. Limiting the reaction to a lower concentration (≤1000 ppm) will do much to simplify the heat effects while testing.

Moisture also greatly affects catalytic performance and is crucial in many applications. The literature provides several examples of CO oxidation thriving or deactivating depending on moisture content [11][17][18][19][20]. The gold on Titania catalyst shows a beneficial effect for low moisture content passing through a maximum or simply showing only a positive effect at 0°C[21][22]. Filtration in moist environments ranging from 25% relative humidity, RH, to 100% at room temperature is needed for real world applications, such as a CO filtration during a fire or in car cabin air filter[2]. This is explored in detail in section 2.3.2: Mechanisms for supported Pt on Metal Oxide and the Role of Water

Literature typically classifies the myriad of noble metal-metal oxide catalyst in groups by metal, ex. Group VIII includes Ni, Pd and Pt. Although some conclusions can be drawn, a more useful classification is by which environment the catalyst thrives or deactivates in. The dominate factors are humidity, temperature and CO concentration. Although, the dependence on CO concentration is inextricably intertwined with temperature.

2.2 Comparison of Different Catalyst Recipes

Literature has made a few trends clear. However, testing is lacking. To draw conclusion from different catalyst formulations, one needs similar testing environments. Ideally low CO concentrations would be tested along with higher concentrations. However, the dominant testing procedure found in literature occurs at 1% CO inlet concentration. This can further be broken up along two more axes: dry vs. humid and H_2 rich vs. O_2 rich. The oxygen rich environments are considered more closely here; although, H_2 rich environments will be mentioned.

To compare the wide range of catalyst formulations on somewhat consistent bases, the turnover frequency or TOF is charted along with temperature. The TOF is defined as the number of molecules reacting per active site per second. In practice, active site is defined as surface noble metal atoms. Although some works attempt to discriminate which surface metal atoms can actually be considered active sites through a probe molecule such as methanol, the vast majority use the simple definition of active site[23]. To calculate TOF from literature, which rarely gives TOF's explicitly, one can use catalyst loading and wt% metal, $M_{wt\%}$ along with dispersion, $\%D$, or crystallite size to determine the surface Pt atoms and thus the TOF. Given the reaction rate, r in terms of weight catalyst along with $M_{wt\%}$ and $\%D$:

Equation 2-2:

$$TOF = \frac{r}{M_{wt\%} \cdot \%D}$$

To get the *%D* through crystallite size, which itself can be calculated through transmission electron microscopy, TEM, small angle X-ray scattering, SAXS and XRD or some other technique, a universal relationship is helpful to make as few assumptions as possible about crystallite shape. Crystallite sizes are typically calculated by, d_{vs} or volume-surface mean diameter, via the following relation[24]:

Equation 2-3:

$$d_{vs} = \frac{\sum_i n_i d_i^3}{\sum_i n_i d_i^2}$$

where n_i is the number of particles with diameter d_i. It can be shown that for a number of different assumed shapes, the *%D* and ratio of d_{vs}, to atomic diameter,d_{at}, fall on the same line given by the following relation:

Equation 2-4:

$$\frac{d_{vs}}{d_{at}} = \frac{k_c}{\%D^{\left[\frac{1}{(3-Dc)}\right]}}$$

Table 2-1: Parameters and their correlation coefficient needed for determination of *%D* or d_{vs} in Equation 2-3

Range of %D	D_c	k_c	Correlation Coeff
0.01 - 0.2	2.00	5.01 ± 0.01	0.9993
0.2 - 0.92	2.19 ±0.01	3.32 ±0.06	0.991

Equation 2-3 along with Table 2-1 allow for an easy transition from *%D* to d_{vs} for a wide variety of crystallite shapes[25]. This method was used to process the data given in articles to determine the *%D* and thus the *TOF*.

2.2.2 TOF at different Temperatures for Different Catalyst Formulations

Table 2-2 shows a list of Catalyst surveyed which show activity at temperatures 0 °C and below. The list is wholly made of Au based catalyst aside from some based on Co. The favorite paired metal oxide is TiO_2, but SiO_2, Al_2O_3, and Fe_2O_3 also show some activity. When temperatures reach -70 °C Au on TiO_2 and Fe_2O_3 are the only catalyst which show any activity. Au on TiO_2 is now the bases for the commercially available Aurolite.

Table 2-2: TOF for different catalyst compositions at or below 0 °C. The inlet feed is 1% CO and experiments are conducted in an excess of O_2

Catalyst Formulation	TOF·100 / s for low Temperatures in °C		
	-70	-20	0
5% Co on TiO2[26]			0.000
14.7% Au on SiO2[27]	0.000	0.000	0.000
4.2% Au on Al2O3[27]	0.000	0.138	0.359
0.94% Au on Al2O3[27]	0.000	0.454	1.817
6% Au on α-Fe2O3[28]	1.204	1.926	2.007
5% Co on Al2O3[26]			2.380
4.7% Au on TiO2[27]	0.132	2.215	2.636
2.0% Au on TiO2[27]	0.161	3.003	3.229
5% Co on SiO2[26]			3.234
1% Au on TiO2[29]		5.039	8.540
1% Au on TiO2 [30]	0.427	5.039	8.540

Room temperature begins to open up the possibilities for different catalytic compositions. Table 2-3 shows the wide range of formulations tried. Here Au, Pt, Pd and Co all show activity for CO oxidation when paired with the right support. Non noble metal catalyst, like CeO_2 -13% Co_3O_5, does not show activity at room temperature. However, if that catalyst is paired with the group VIII metal Pd, the catalyst becomes active. That is not to say non-noble catalysts are the only ones that work. There are many Co based catalyst which perform well under these dry conditions with a high CO concentration in the feed. Once again, Au on TiO_2 is the most active catalyst. Although some Pd paired with Ce_2O_3 are very close.

Table 2-3: *TOF* for different metal-metal oxide compositions at 20°C to 30 °C. The inlet feed is 1% CO and the experiments are conducted in an excess of O_2. The temperature is 25 °C for * 30 °C for **; otherwise, it is 20 °C.

Catalyst Formulation	TOF·100 / s for low Temperatures in °C
CeO2- 30%Co3O5[31]	0.00
0.5% Pd on CeO2[31]	0.00
10% Au on Co3O4*[32]	0.00
2.34% Pt on ZnO **[11]	0.00
2.54 % Pt on NiO **[11]	0.41
2% Pt on SiO2[33]	0.50
10% Au on CeO2*[32]	0.55
0.5% Pd on 30% Co3O5 CeO2[31]	1.07
5% Co on TiO2[26]	1.10
2.94 % Au on SnO2[34]	1.44
0.29% Pd on Al2O3*[35]	2.38
0.18% Pd on 5.5% ZrO2 on Al2O3*[35]	2.76
5% Co on Al2O3[26]	3.42
5% Co on SiO2[26]	4.09
1.2% Pt on Fe2O3**[11]	5.21
1% Au on TiO2[29]	8.54
1% Au on TiO2 (calc at 473)[30]	8.54
1% Pd on CeO2-TiO2[36]	11.05
0.2% Pd on 4.45% Ce on Al2O3*[35]	13.05
.15% Au on TiO2**[9]	13.21

Table 2-4 lists the catalysts tested between 50°C and 200 °C. Many formulations work in this very hot space. While at 50°C some formulations show no activity, such as 10% Au on Co_3O_4 or 2.34% Pt on ZnO, everything else does. Pd, Au, Pt and Co (believed to be in oxide form) all work on a myriad of supports. This reaction space is less interesting than the catalysts that work at room temperature and below. It is hard to discriminate between working catalyst. One would just pick the cheapest formulation and in the right case that could just be 90 year old hopcolite.

Table 2-4: ***TOF*** **for different metal-metal oxide compositions at 50°C to 200 °C. The inlet feed is 1% CO and the experiments are conducted in an excess of O_2**

Catalyst Formulation	TOF·100 / s for low Temperatures in °C				
	50	80	100	150	200
10% Au on Co_3O_4[32]	0.00	0.41	1.48	6.58	
2.34% Pt on ZnO [11]	0.00	0.27	0.45	8.90	
CeO_2- 13%Co_3O_5[31]	0.01	0.07	0.15	0.22	
0.5% Pd on CeO_2[31]	0.25	0.84	1.52	8.45	
0.5% Pd on CeO_2[31]	0.25	0.84	1.52	8.45	
1% Pt on y-Al_2O_3[37]	0.29	0.29	0.29	0.29	17.58
2.54 % Pt on NiO [11]	0.41	0.98	6.56	8.20	
10% Au on CeO_2[32]	0.82	2.06	5.15	6.86	
2% Pt on SiO_2[33]	1.10	1.40	1.70	2.50	
1% Pt on CeO_2[38]	1.44	21.61	27.37	28.23	28.23
5% Co on TiO_2[26]	1.59	1.10	0.73	5.74	1.65
1% Pt on TiO_2[37]	3.15	5.78	7.35	20.49	52.55
0.18% Pd on 5.5% ZrO_2 on Al_2O_3[35]	3.67	7.35	12.86	37.67	91.87
0.29% Pd on Al_2O_3[35]	3.96	15.84	12.67	52.27	79.19
2.94 % Au on SnO_2[34]	4.36	4.40	4.55		
5% Co on Al_2O_3[26]	4.39	4.76	5.13	0.67	6.10
5% Co on SiO_2[26]	5.00	3.97	2.50	5.92	6.10
3.6% Au on 4.9% Fe on zeolite-Y check [19]	8.60				
1.2% Pt on Fe_2O_3[11]	10.76	17.36	17.36	17.36	
0.2% Pd on 4.45% Ce on Al_2O_3[35]	17.39	40.59	62.33	115.96	142.06
.15% Au on TiO_2[9]	28.30				
81% Co and 19%Fe composite Oxide[39]		0.00	0.01	0.06	0.16
1% Pt on Nb_2O_5[40]		0.00	1.26	7.96	41.91
1.6% Pt on Al_2O_3[41]		0.86	1.29	2.58	25.79
.26% Au on Fe_2O_3[9]			10.48		

2.2.3 Effect of Humidity at Catalytic Performance in Literature

Humid conditions impose a strong dampening effect on conversion for many catalysts while some react in the opposite way. Figure 2-1 illustrates a positive or negative effect of moisture at various temperatures for various catalysts. Around room temperature, Au Pt and Pd show an enhancement from water vapor when paired with the right support.

Au gets a positive effect from $SrCO_3$, $BaCO_3$ and even Al_2O_3[42]. On the other hand TiO_2 seems to have a negative effect for anything other than very a very small vol% H_2O[9]. When the temperature is increased, Au on CeO_2 supported on Al_2O_3 goes from having a small positive effect to a negative after 100 °C when exposed to 1.9 vol% H_2O[18]. Data from Marteines et al. shows a positive effect for moisture at these hot temperatures with 3.3 vol% H_2O for Au on CeO_2. He also shows Au supported on Al_2O_3 shows a negative effect indicating the base support plays a role and maybe Al_2O_3 does not work well as a support when water is in the feed stream

Pt has a wide variety of supports which show a positive influence of water. Pt on ZnO, CeO_2-TiO_2 and Fe_2O_3 all show positive effects at about 50% RH around room temperature. Only very few supports like CeO_2-ZrO_3 and NiO show a detrimental effect of moisture on conversion, and CeO_2-ZrO_2 begins an enhancing effect after 50 °C[11][43].

At 25 °C 100% RH is 3.1% vol% water. When the temperature is raised the effect of much higher water contents can be tested. It can be shown that Pt on Fe_3O_4 exhibits no change in reactivity all the way up to 15% and 16% water in the feed at 125°C and 150 °C[44][45]. Pt on SnO_2 also shows a positive effect in 10 vol% water [46]. At 80 °C it can be shown the choice of promoter on a Pt can determine if a support will remain active in water. Cu has a positive impact on reactivity in 10 vol% water while Co does not[47]. The only other poorly working Pt based catalyst is Pt on commercial a-type zeolite which deactivates at in 10 vol% water anywhere from 100 °C to 200 °C[48].

Pd shows mixed results. With a positive effect when paired with CeO_2 – TiO_2 to a negative effect when paired with FeOx[49][50].

Figure 2-1: Here we can see the effect of water on various catalyst recipes cataloged by temperature and vol% water in the feed. The black line represents the vol% water at 50% RH. Green implies No effect, Red a Negative Effect and blue a positive effect.

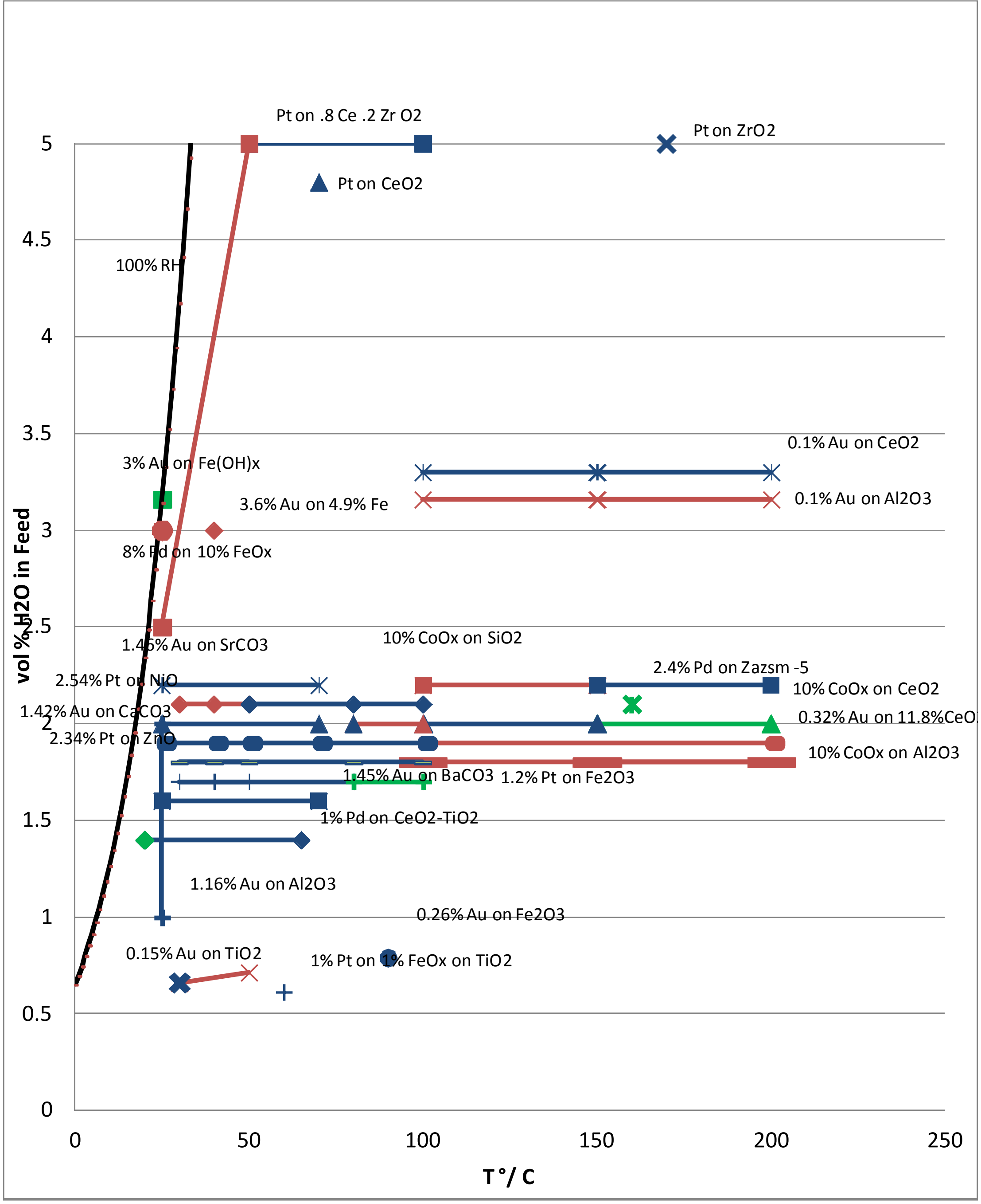

2.2.4 Catalyst activity data at low concentration and under consistent conditions

Literature tests these catalysts at different moisture levels and concentrations. The absence of a consistent testing basis makes it very difficult to draw anything but the crudest conclusion. To fight the inconsistent testing conditions in literature, Punde et al. catalogued many different mixtures and tested them under a single set of conditions. Each was tested at 0% and 50% RH at 25 °C and under a low CO concentration to negate heat effects[51].

Table 2-5 catalogues many different catalyst formulations. It shows a few definite

Table 2-5: Different Catalyst recipes were tested at low co concentration and 50% humidity.TestConditions:CO: 250ppm; Face Velocity: 30cm/sec; Temperature: 25°C; Humidity: 50% RH; Particle Size: 200µm; Bed Ht: 3.0mm[51]

Catalyst	Conv. (25°C; 50% RH)	Conv. (0% RH)
10%CuOx/SiO_2	NA	NA(T≤200°C)
15%CeOx/SiO_2	NA	NA (T≤200°C)
10%MnOx/SiO_2	NA	NA (T≤200°C)
5% CuOx – 15%CeOx/SiO_2	NA	NA (T≤200°C)
5%AgOx – 15% CeOx/SiO_2	NA	NA (T≤200°C)
15%CoOx/SiO2	NA	10% (T = 100°C)
5%CuOx – 15% CoOx/SiO_2	NA	15% (T = 75°C)
5%CeOx – 15% CoOx/SiO_2	NA	25% (T = 75°C)
5%CoOx – 15% CeOx/SiO_2	NA	10% (T = 125°C)
5% Pt – 15%SnOx/? -Al_2O_3	55 %	ND
5% Pd – 15%SnOx/SiO_2	15 %	ND
5% Pt – 20%ZrO2/SiO_2–DP	38 %	ND
2.5% Pd –2.5% Pt – 16% CeO_2/SiO_2 –IN	86 %	ND
5%Pt/SiO_2	40 %	ND
5%Pt/γ -Al2O_3	23 %	ND
5%Pd/SiO_2	7 %	ND
5%Pd/ γ -Al_2O_3	<5.0 %	ND
5%Pt –5% CoOx/SiO_2	26 %	ND
5%Pt –5% CoOx/ γ -Al_2O_3	31 %	ND
5%Pt –5%MnOx/SiO_2	28 %	ND
5%Pt –5%MnOx/ γ -Al_2O_3	25 %	ND
5% Pt – 15%SnOx/SiO_2	70 %	ND
5%Pd – 16%CeO_2/SiO_2 –Pd	22 %	ND
5% Pt – 20%ZrO_2/SiO_2–GR	42 %	ND
5%Pd – 16%CeO_2/SiO_2 –DA	36 %	ND
2.5% Pt – 16% CeO_2/SiO_2 –IN	99 %	ND

trends. The catalysts not promoted with Pt or Pd simply could not perform at low temperatures. The single metal oxide catalyst such CuOx, MnOx and CeOx when dispersed on SiO_2 showed no activity wet or dry all the way up to 200 °C. CoOx was the exception to this showing giving a small conversion at 100 °C in dry air. CoOx on SiO_2 has been reported to show 80% conversion in dry air at room temperature at 1% CO [26]. The difference in activity can be attributed to the high heat rise in the bed. 1% CO can lead to a 97 °C rise in the bed. Whereas, a 250 ppm CO challenge gas only leads to a 2.5 °C increase.

The second set of catalysts consists of a metal oxide deposited on CeOx and CoOx. Here none of the catalysts display any activity at room temperature and 50% RH. In a dry environment 5% CuOx – 15%CeOx/SiO_2 and 5%AgOx – 15% CeOx/SiO_2 fail to show any conversion up to 200 °C; while, 5%CuOx – 15% CoOx/SiO_2, 5%CeOx – 15% CoOx/SiO_2 and 5%CoOx – 15% CeOx/SiO_2 do show some starting at 75 °C. At 1% CO inlet concentration Luo et al. test their CeO_2- 13%Co_3O_5 catalyst and show 5% conversion at 50 °C and 12% at 75 °C. At low conversions the catalyst does not get the benefit of a large temperature rise due to the high heat of reaction and does not allow the bed to ignite.

To reach all the way down to room temperature in humid conditions one must add a noble metal promoter such as Pt or Pd. Interestingly, none of the metal promoted catalyst shows any activity at 0% RH. This is a strong indicator in a change of reaction mechanism. The catalyst with Pt or Pd promoter must form some intermediate with water to complete the reaction pathway.

In every instance Pd is used on the same support as Pt, the Pt based catalyst out performs the Pd catalyst: Pt and Pd on SiO_2 gives 40% and 7% conversion respectively; on Al_2O_3 one sees 23% and <5%. On CeO_2 it is 99% vs. 36%. The trend shows Pt as the superior choice for CO oxidation in humid conditions and low temperatures. This is even true for the mixed Pt-Pd catalyst which produces 86% conversion. This sounds high until one looks at the same catalyst without the Pd performing at 99% conversion.

The Pt on CeO_2 is paid so much attention here because it is the catalyst which will be tweaked later. It is prudent to show this catalyst also outperforms commercial catalyst available on the market. Table 2-6 shows 4 commercially available catalyst along with 4% Pt - 16 % CeO_2 on SiO_2. The Pt – CeO_2 on SiO_2 catalyst greatly outperforms the commercial offerings. The catalyst was designed with these specific conditions in mind, so the results are not too surprising. The Aurolite, for instance, should easily outperform the Pt based catalyst in dry conditions[52].

Table 2-6: Commercial catalyst are compared to 4% Pt – 16% CeO_2 on SiO_2. Test conditions:CO: 250ppm; Face Velocity: 30cm/sec; Temperature: 25°C; Humidity: 50% RH; Particle Size: 200µm, 3m NanAucat was tested as obtained 1- 2mm; Space velocity: 100 s^{-1}[52]

Catalyst	CO Conv. %	Rate
Carulite	<5%	0.09
Moleculite	<5%	0.05
Aurolite(1% Au on TiO_2)	25%	0.44
3M NanAucat (Au based)	30%	0.52
4% Pt - 16 % CeO_2 on SiO_2	99%	1.75

2.3 Mechanistic Studies for CO oxidation

It was mentioned earlier that Langmuir himself first proposed an Elley-Ridel type reaction mechanism for CO oxidation over platinum at high and low (500K) temperatures.

Equation 2-5: $CO_{(g)} + Pt_{(S)} \rightarrow CO\text{-}Pt_{(S)}$

Equation 2-6: $O_2 + 2Pt_{(S)} \leftrightarrow 2O\text{-}Pt_{(S)}$

Equation 2-7: $CO_{(g)} + O\text{-}Pt \rightarrow CO_2 + Pt_{(S)}$

In the low temperature region (500K) CO in gas form, $CO_{(g)}$, adsorbs onto the Pt surface, $Pt_{(S)}$, nearly covering it via Equation 2-5. Only a small amount of Oxygen is able to atomically adsorb. The small amount of oxygen that does adsorb via Equation 2-6 reacts with $CO_{(g)}$ via Equation 2-7:. At high temperatures, 750K to 1150K, the surface is covered by atomic oxygen and the reaction proceeds again by Equation 2-7. The rate limiting step in this case is the rate of bombardment of CO on the surface. The last conceivable reaction, $O_{2(g)}$ reacting with adsorbed CO proceeds too slowly to be useful[5].

It was not until 1979 when the generally agreed up Langmuir-Henshelwood reaction mechanism was put forth:

Equation 2-8: $$CO\text{-}Pt_{(S)} + O\text{-}Pt_{(S)} \rightarrow CO_{2(g)} + 2Pt_{(S)}$$

Equation 2-8 outlines the surface reaction between atomically adsorbed oxygen and carbon monoxide[53]. Equation 2-8 together with Equation 2-5 and Equation 2-6 make up the simplest complete mechanism for low temperature CO oxidation.

If this were all that was going on then this would be a simple reaction. The CO oxidation reaction suffers from many complicating effects on the Pt surface. Self Poisoning and the role of water are two important effects for this paper. Subsurface oxygen utilization, oxide formation and face restructuring are also important but not germane to this paper[54][55]. These effects lead to oscillations and other phenomenon which, although interesting, do not help here[56].

Another complicating factor is the use of an oxygen rich supports for Pt. The main pathway that keeps the reaction going, despite CO's ability to cover the Pt surface that Langmuir ran into, is an exchange of oxygen from the support to the Pt itself. The mechanism of this exchange is complicated further by the presence of water in the feed. This is discussed further in section 2.3.2: Mechanisms for supported Pt on Metal Oxide and the Role of Water.

2.3.1 Self Poisoning

Self poisoning of CO on the Pt surface arises from the high heat of adsorption of CO on Pt. The values differ based on the surface plane. Pt(111), P(100) and Pt(110) are reported to have 138 kJ/mol, 134 kJ/mol and 109 kJ/mol respectively at low coverage. They also change with surface coverage and bonding type. At 0 coverage a Heat of adsorption of 206 kJ/mol was measured on Pt vs. 115 kJ/mol at a monolayer[57].

A useful way to characterize the high adsorption of CO on Pt is through the sticking probability of CO when it strikes the Pt surface. Figure 2-2 shows the decrease in sticking probability of CO as coverage increases at 300 °K. Every time CO strikes a clean surface it has an astounding 8 in 10 chance to stick. This is very high and does not decrease linearly with CO coverage[58]. This is a typical value for initial sticking probability over Pt{111}. Table 2-7 includes other observed values and their crystallographic plane.

Table 2-7: Initial sticking coefficients, *So*, and max monolayer of coverage for CO on Pt for different crystallographic planes.

Surface	So	θ_{max}
Pt{100}[59]	0.6	0.75
Pt{100}[60]	0.24	
Pt{110}[61]	1	1
Pt{110}[62]	1	1
Pt{111}[60]	0.34	
Pt{111}[63]	1	
Pt{111}[64]	1	
Pt{111}[65]	0.85	0.5
Pt{211}[60]	0.27	

The shape of the sticking probability curve exhibits cursor mediated behavior. The CO strikes the surface and forms and intermediate which can diffuse across the surface and finally adsorb when it finds an open spot. This behavior along with a high heat of adsorption gives rise to the strong poisoning ability of CO on Pt surfaces. All the sources agree on this fact[66]. Its adsorption of CO is especially aggressive when compared to oxygen [67].

Oxygen has a near constant and low sticking coefficient. Yeo et al. also tabulated the sticking coefficient of oxygen at .064 at 0 coverage and .02 above 0.6 monolayer[58]. The sticking coefficient of CO is 12.5 times higher than that of O_2 at zero surface coverage. This does a lot to explain the high rate of CO poisoning. Other sources indicate sticking probabilities of 0.2 and 0.08 for Pt{111} with a max coverage of 0.45 [67][68].

Figure 2-2: Sticking probability and heat of adsorption for CO on a Pt{111} surface at 300 °C. The ■ denote Heat of adsorption while ♦ is sticking probability[58].

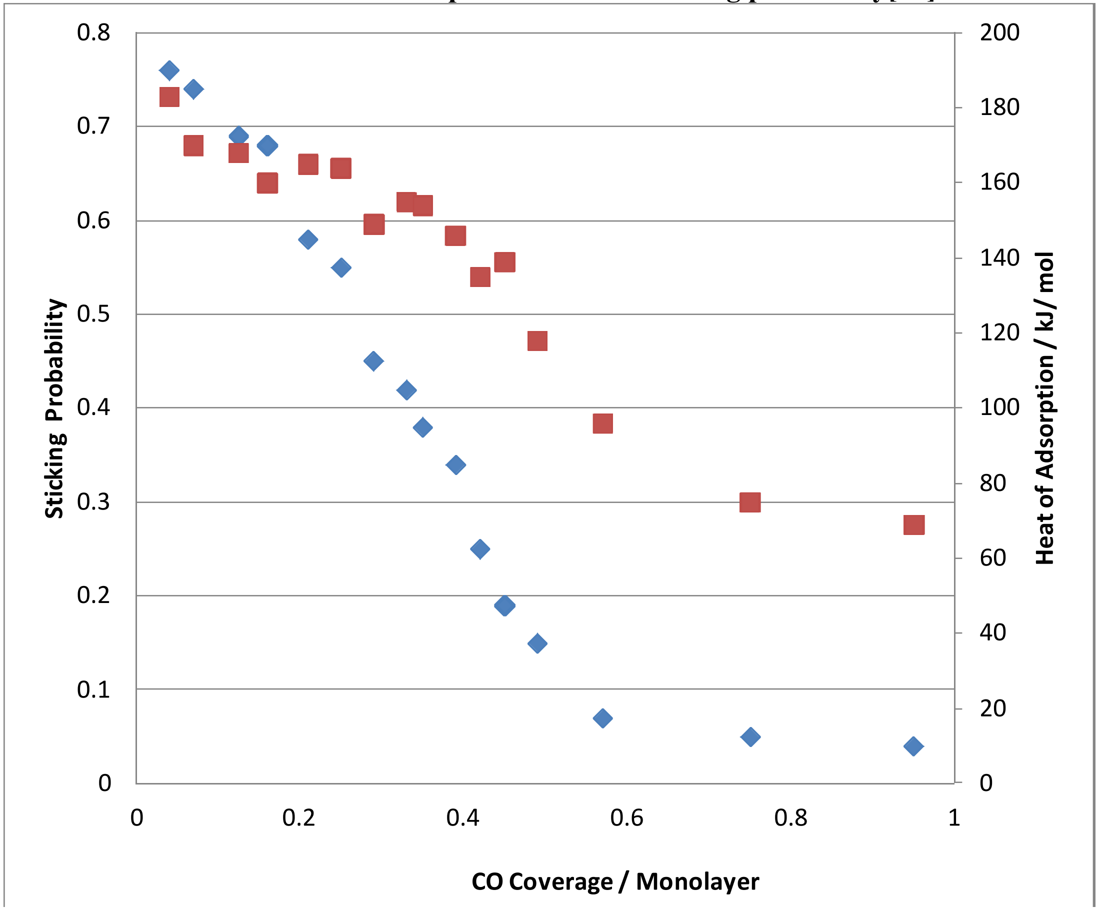

While CO desorption is regularly discounted at room temperature on Pt. O_2 desorption does occur at an appreciable rate. The weakly adsorbing oxygen relative to CO adsorption gives rise to asymmetric inhibition. In this state the CO can displace O adsorbed on the surface. O, however cannot displace adsorbed CO. This is partially due to the dissociative adsorption of O_2 on Pt. It needs two Pt sites right next to each other to adsorb[69]. Desorption follows Equation 2-9. Here r_D is the desorption rate A_D is the pre-exponential factor and θ is the surface coverage. Because this is O_2 desorption, the order is 2[66].

Equation 2-9:

$$r_D = A_D e^{-Ea/RT} \theta^2$$

Table 2-8: Desorption pre-exponential factors and activation energy for Oxygen desorption from Pt

Surface	A_D in cm^2/s	Ea in kJ/mol
Pt(ribbon)[70]	$1.95 \cdot 10^{-2}$	195
Pt{110}[71]	$6.5 \cdot 10^{-7}$	125.5
Pt{111}[72]	$2.4 \cdot 10^{-2}$	213

2.3.2: Mechanisms for supported Pt on Metal Oxide and the Role of Water

The bare metal surface is too prone to poisoning to be of much use as a commercial catalyst at room temperature. One way to alleviate the dual role of the noble metal as both an O_2 and CO adsorber is to pair the metal with an oxide support to provide oxygen to the CO covered metal. CeO_2 has long been the choice for automotive three way catalyst [73] and also has shown remarkable catalytic activities when paired with Pt as can be seen in Table 2-5 earlier. Although literature is full of different oxide supports.

Jain et al. discussed the two site mechanism between a noble metal and oxide support. In the work many oxide supports are compared with non-modified Pt on Al_2O_3. There was a significant increase in catalytic activity between the plain Pt catalyst and those decorated with metal oxides. The order was found to follow Co ≈ Fe > Mn > Sn ≈Cu ≈Ni >Cr. Interestingly Mn activity increased markedly when water was introduced in the feed. This indicates a water based intermediate is needed for oxygen transfer between the Pt and Mn. It could also mean a change in solely the Mn[74].

In 2009 Xu et al. prepared an inverse catalyst of FeO{111} on Pt{111}. They adsorbed CO on the Pt portion then OD on the FeO. Using thermal desorption spectroscopy (TDS) both a D_2O peak is seen as well as a CO_2 peak at 400 K. This peak did not exist when just CO was adsorbed onto the Pt surface. This indicates O_2 is exchanged through an OH containing intermediate on the perimeter between Pt and FeO[75].

In 2004 Uner et al. tested the apparent reaction orders of Pt on CeO_2 and compared it to Pt on γ-Al_2O_3. They found the reaction order of CO for just the Pt on γ-Al_2O_3 is -2 and O_2 is 0.9. This is contrasted with Pt on CeO_2 which showed a reaction order of -1 for CO and 0.1 for O_2[76]. The change in O_2 dependence indicates the reaction is no longer dependent on gas phase oxygen when the CeO_2 is present. This leads to an exchange of O between CeO_2 and Pt.

Equation 2-10: $$\text{O-Ce}_{(S)} + \text{Pt}_{(S)} \rightarrow \text{O-Pt}_{(S)} + \text{Ce}_{(S)}$$

Equation 2-10 along with Equation 2-5 and Equation 2-8 make up the reaction mechanism which is expressed:

Equation 2-11: $$r = \frac{k}{1 + KP_{CO}}$$

A reaction order of -2 for CO on the Pt-γAl_2O_3 arises when the dissociative adsorption of oxygen is the rate limiting step[77]. When oxygen is fed from the periphery, this order changes to -1.

Equation 2-12 was derived in 1973 to describe a range of behavior in CO oxidation. If equilibrium K is large, then the equation displays negative order reaction mechanics. That is CO inhibition. If *K* is small the order is positive 1 for CO concentration.

Equation 2-12: $$r = \frac{kP_{CO}P_{O2}}{(1 + KP_{CO})^2}$$

The importance of water for the Pt-CeO_2 catalyst is apparent. In Table 2-5 water is essential to get any activity at all. Kim et al. concluded moisture increased the reactivity on Pt-Mg/Al_2O_3 catalyst by preventing the adsorption of CO on Pt[78]. Bergald et al. conducted TPR experiments with Pt on and varying O CO and pre-adsorbed water states. Water was found to lower the CO_2 production temperature which leads to the following reaction mechanism taking place on the Pt[79]:

Equation 2-13: $$H_2O\text{-}Pt_{(S)} + O\text{-}Pt_{(S)} \rightarrow 2OH\text{-}Pt_{(S)}$$

Equation 2-14: $$CO\text{-}Pt_{(S)} + OH\text{-}Pt_{(S)} \rightarrow 2OH\text{-}Pt_{(S)}$$

Equation 2-15 $$O\text{-}Pt_{(S)} + H\text{-}Pt_{(S)} \rightarrow OH\text{-}Pt_{(S)} + Pt_{(S)}$$

Equation 2-16: $H\text{-}Pt_{(S)} + OH\text{-}Pt_{(S)} \rightarrow H_2O\text{-}Pt_{(S)} + Pt_{(S)}$

DFT calculations were carried out to verify this hypothesis and found it unlikely. Gong and Hu determined a carboxyl intermediate was the most likely case as seen in Equation 2-17[80].

Equation 2-17: $COOH\text{-}Pt_{(S)} + H_2O\text{-}Pt_{(S)} \rightarrow CO_2\text{-}Pt_{(S)} + 2H_2OPt_{(S)}$

Mhadeshwar and Vlachos produced a microkinetic model to explore the different contributions from different proposed reaction pathways. They found the addition of the carboxyl group pathway produced results with were much closer to experiment[81].

A more popular role of water is the formation of a carbonate species which enhances the oxygen transfer from support to noble metal. Date et al. suggested as much on supported Au catalyst[82]. This also came up during PROX reactions which suggested a $HCOO^-$ intermediate on $Fe_2O_x/Pt/TiO_2$ catalyst[83].

2.3.3 Effect of Temperature

The temperature affects the catalyst behavior in more than just the obvious. The oxidation reaction of CO is highly exothermic. Using heat of formation data, the heat of reaction, ΔH, is 283 kJ/mol[16]. The high heat of reaction along with the negative reaction order leads to a very unstable zone between ignition and extinction of catalyst. This is one of the ways in which CO oxidation stays complicated and challenges the isothermal reaction assumption whenever it is present.

The Arrhenius equation below, where *A* is the pre exponential factor *Ea* is the activation energy and *R* is the gas constant, is the widely accepted dependence of reaction rate *k* with temperature.

Equation 2-18:

$$k = Ae^{-Ea/RT}$$

Values for the activation energy are typically apparent activation energies from measuring the slope of the ln(r) vs 1/T. Table 2-9 shows *Ea* from literature for Pt noble metal catalyst with different supports.

Table 2-9 : Activation energy, *Ea*, for different Pt based catalyst during CO oxidation.

Catalyst	Ea kJ/mol
2% Pt on SiO_2[33]	54.8
Pt/CeO2/ γ-Al2O3[76]	50
Pt-Co-Ce/Al2O3[84]	24.79
1% Pt on Mordenite[84]	40.1
1% Pt on Al2O3[85]	62.7
Pt-CoOx on SiO2 [86]	41.84
5.5% Pt on 17% CeO2 on SiO2	29.4

The last entry, Pt-CeO_2 on SiO_2 will be referenced later in this work. It is the working catalyst prepared by Punde et al.[51]. To put these values into perspective an *Ea* of 30 kJ/mol increases the reaction rate by 1.5 times for a temperature change from 300 K to 310 K. An *Ea* of 60 kJ/mol increases the reaction rate 2.2 times over the same range. This may not seem like too much but when coupled with negative order reaction kinetics the affect is amplified.

Figure 2-3 shows the different between first order and negative order reaction kinetics. The shape of the curves is very telling. The first order kinetics of Figure 2-3a are a smooth sigmoid s shape.

The dashed line indicates less of temperature dependence than the solid due to a change of *Ea* form 50 kJ/mol to 100 kJ/mol respectively. The same increase in slope is seen in Figure 2-3b with the same change in *Ea*.

The interesting difference between the two is the sharp increase in slope of the negative kinetic order case when compared to the first order case. In the first order case, the increase in temperature speeds up the reaction while the decrease in reactants slows it down. This leads to the softer slopes of first order reactions. The negative order case, on the other hand, increases very rapidly above 50% conversion. In this case, the temperature increase increases reaction rate along with the decrease in reactants. The two reinforce each other to lead to such a high increase in conversion over a short temperature range.

Another consequence of a negative order reaction is the increase in reaction rate due to mass transfer limitation followed by an abrupt decrease. The three zones are high

Figure 2-3: Light off plots. (a) First order reaction; (b) Negative first order reaction. Solid line E = 100 kJ/mol; dashed line E = 50 kJ/mol[87].

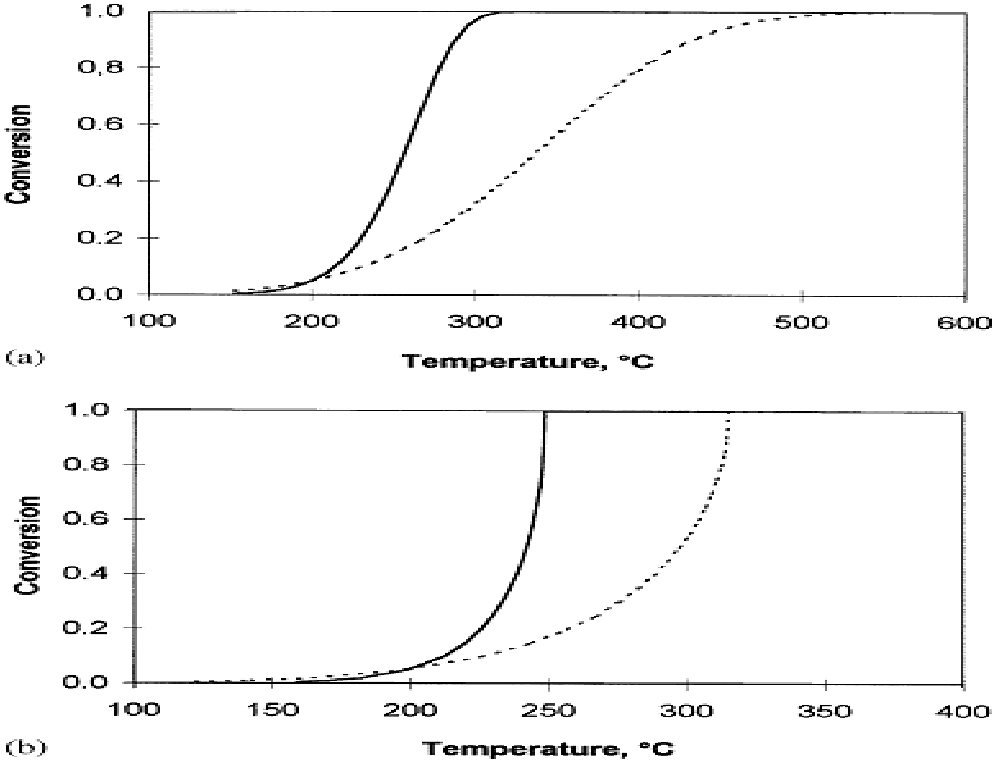

concentration, where the mass transfer rate's influence on the reaction is low. This leads to an intermediate region, where the decrease in concentration at the catalyst surface actually increases concentration. Then finally, at low concentration the mass transfer rate dominates and decreases conversion due to lack of reactants [87].

Along the length of the reactor the CO concentration can change quite drastically with conversion. This is derived from the ΔH which has an adiabatic temperature rise of about 1 °C per 100 ppm CO converted to CO_2. Because of the large heat rise and affect of reaction rate, an understanding of heat transfer in packed beds is needed.

Packed beds have generally poor heat transfer. While gas is flowing the mixing of gas and the conduction of through the solid particles gets put together into an effected thermal conductivity, k_E. k_E can be radial or axial. k_E is thought to be made up of two contributions, a stagnate contribution k_0 and that due to macroscopic flow effects k_k[88].

Equation 2-19:

$$k_E = k_0 + k_K$$

Equation 2-20 derives the k_K from the ratio of the Pe to a particle size fitting parameter K[89].

Equation 2-20:

$$\frac{k_K}{k_g} = \frac{Pe}{K}$$

Pe is the Peclet number and k_g is the thermal conductivity of the gas in the system. For the axial case K is 2[90]. The radial case is a function of the particle diameter, d, and the reactor diameter, d_{re} [91]:

Equation 2-21:

$$K_r = 8\left[2 - \left(1 - 2\frac{d}{D_{re}}\right)^2\right]$$

The stagnate portion of Equation 2-19, k_0, is determined by five main effects: conduction through the gas and solid phase, radiative heat exchange between void areas and solid layers and pressure dependent conductivity. The typical value for a packed bed is about 0.2 W/(m·K) or less. A packed bed of alumina is reported to be 0.2 W/(m·K); Silica is .14 W/(m·K) and a 25% mixture of silica in alumina 0.175 W/(m·K)[92].

The largest resistance to thermal conduction in a packed bed is the point contact between two spheres. This is exceedingly small surface bottlenecks the heat transfer in the solid phase. Thus the majority of heat transfer occurs through the fluid in the interstitial space. This was tested by Schumann and Voss. They submerged their reactor in a hot fluid and measured the heat rise of the center plane. Their results, in Figure 2-4, demonstrated a large change in k_{eff} as the pressure increased. At low pressure there is a steep drop off with k_{eff}

Figure 2-4: Change in k_{eff} with pressure for 1.2 µm steel spheres in air. The steep drop off of k_{eff} at low pressure indicates almost all heat is transferred through the fluid phase[93].

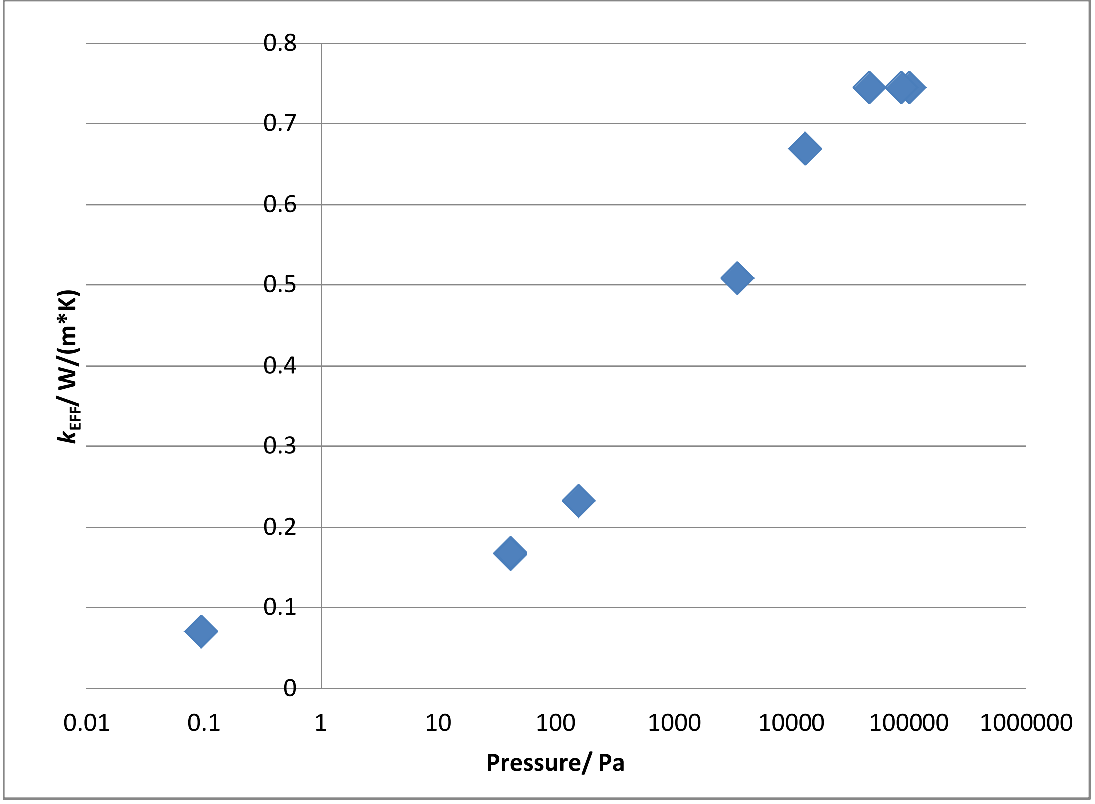

going as low as .07 W/(m·K) at 0.9 Pa. This is contrasted with a maximum k_{eff} of 0.75 W/(m·K) at 101,325 Pa[93].

The effect of thermal conductivity on systems other than CO has received some attention. Yakhnim et al. documented traveling hotspots during the catalytic oxidation of H_2. In this case a monolith was used which, despite poor thermal conductivity, was able to have hotspots travel upstream, downstream or even keep stationary depending on the fluid velocity[94].

Temperature waves during CO oxidation have been studied and observed flowing both up and down stream. The extinction-ignition behavior of CO oxidation leads to a hysteresis and traveling temperature waves. Sun et al. showed the speed of the traveling extinction wave to be positively correlated with CO concentration [95].

Puszynski et al. showed on a $Pt\text{-}Al_sO_3$ catalyst that traveling temperatures wave also depends on axial position in the reactor. They also showed the direction of the traveling wave depends on initial conditions of the reactor as well as the inlet CO concentration.

Figure 2-5: Axial Temperature profile over time following the change in inlet CO concentration from 3.90% to 3.15%. $Pt\text{-}Al_2O_3$ catalyst displays a temperature wave which migrates upstream a 60 cm reactor [96].

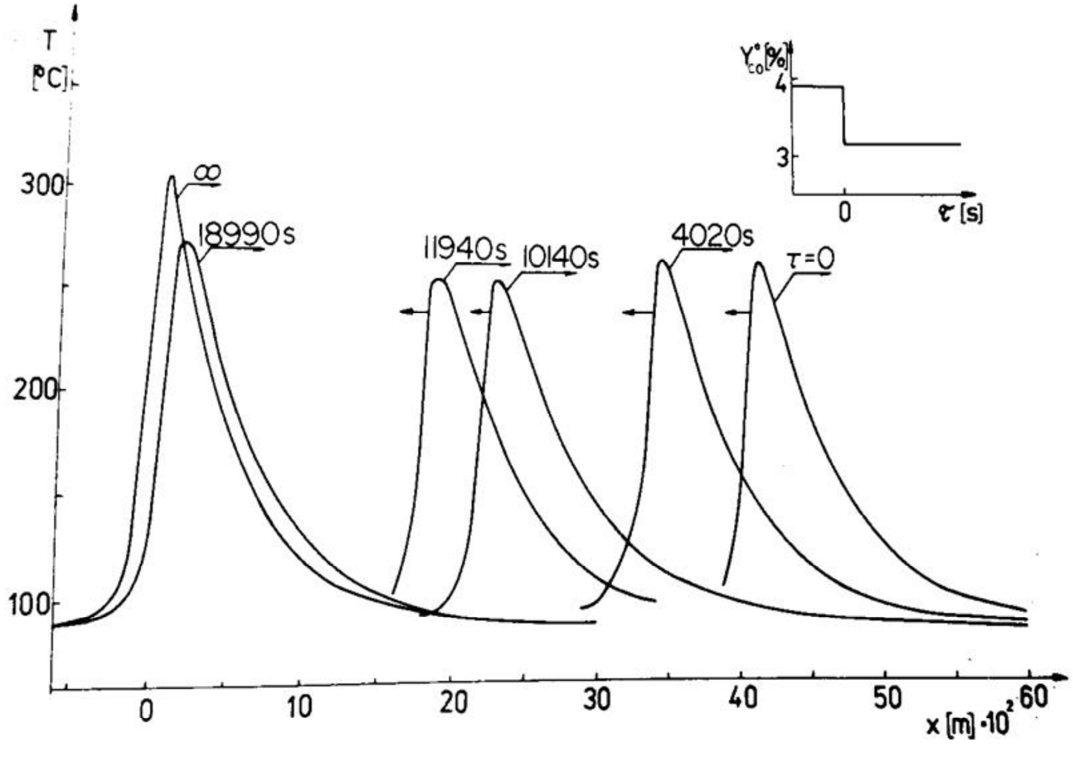

Above a certain concentration the temperature wave travels downstream as the bed deactivates. Below a certain value the wave travels up stream. Pusyzynski et al. did this with 3.15% and 5.4% CO in the feed. In Figure 2-5 a wave is seen with a 210 °C maximum. Over the course of 5.5 h the temperature wave moves from 43 cm into the bed to the front. The high CO concentration used leads to an extremely high temperature rise which makes it easy to see the wave propagate. They also viewed periodic behavior within the reactor [96].

Pusyzynski et al. went on to theoretically categorize these effects. When testing axial and radial dispersion effects, it was proposed that two stable steady states may exist in a long nonadiabatic reactor. The reaction kinetics are also of paramount importance. The Langmuir-Henshelwood reaction increases the sensitive zone over that of a second order reaction[97]. Parametric sensitively was used by Bious et al. to describe small changes in reaction parameters, including temperature and inlet concentration leading to large changes in reactor conditions. They used an early analog computer to solve the flow and reaction equations in 1956[98].

The effect of thermal conductivity on CO reactivity is not well studied. Yakum, Pusyzynski and others tested changes in face velocity, reactant concentration and temperature, but not thermal conductivity. Punde et al. suggested an increase in thermal conductivity increases the long-term stability of the bed by keeping the front of the bed hot[51]. This is much like Pusyzynski, however, Punde et al. had access to higher conductivity materials. Still, no axial temperature profiles were taken to look into the packed bed and match with a suitable model. The poor thermal conductivity of packed beds is contrasted with that of microfibrous materials.

2.4 Microfibrous Media

Microfibrous media consist of a sinter locked mesh of metal fibers which can be used to entrap the sorbent or catalyst needed. The media was first developed in 1987 by the Department of Chemical engineering and the Space Power institute at Auburn University.

Figure 2-6: Rolled microfibrous entrapped material.

The metal mesh is produced via a wet-laid paper process which has proven to be scalable. Figure 2-6 shows metal fiber sheets mass produced and rolled.

Traditionally microfibrous media is assembled in the wet-laid process with catalyst particles mixed in from the beginning. The fibers, cellulose and particles needed are mixed in an aqueous solution and dropped on a metal screen. The resulting sheet is a combination of particles trapped in a cellulose and metal fiber paper sheet. The sheet is pre-oxidized at 450 °C to remove the cellulose then heated to the metal's sintering temperature to produce the sinter locked mesh[99]. Polymer and ceramic fibers have also been used.

Catalyst particles can range anywhere from 50µm – 300µm in diameter and the fibers themselves range from a very fine 2 µm to a large 20 µm fiber. Different mixtures are used based on requirements[100]. Figure 2-7 shows a typical nickel fiber mesh with entrapped silica. Particle sizes are optimally trapped between 100µm and 200µm. The void fraction of these meshes can be as high as 0.98. Although, typical values are 0.8 to 0.9[101]. Trapping particles in a mesh, as seen Figure 2-7, allows for smaller particles to be used. Small

Figure 2-7: SEM image of a typical nickel fiber mesh with entrapped silica support particles. The fibers are 8μm and 4μm. The silica particles in the mesh are 150μm – 250μm.

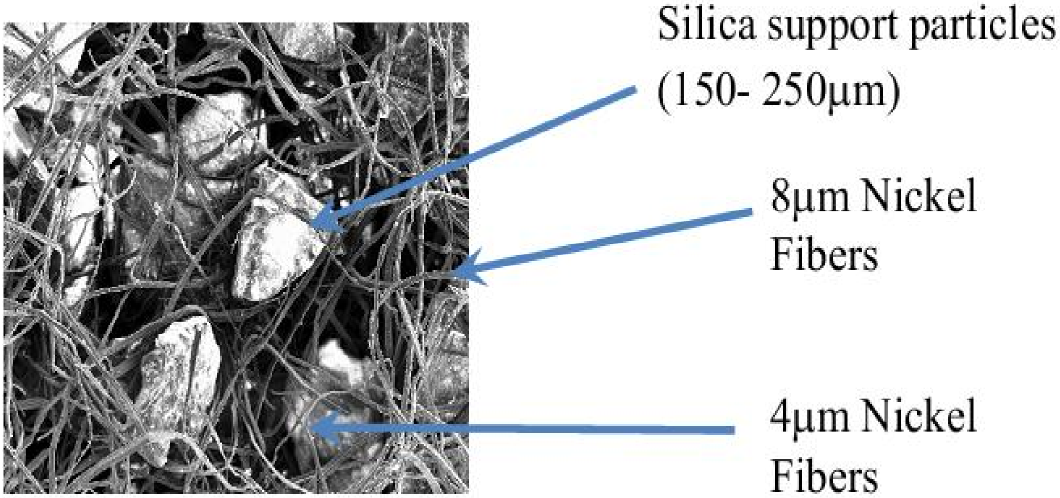

particles (< 1mm) in a packed bed system are difficult to take into real world applications. The thermal conductivity of the bed is increased relative that of packed beds.

Microfibrous entrapped sorbents/catalyst have been demonstrated multiple times to be useful over a packed bed. The cathode of a PEM fuel cell is sensitive to VOC's. Microfibrous material was used in a filter to successfully remove VOC's[102]. Ozone is a difficult and harmful contaminant to remove. Microfibrous media was demonstrated to be more efficient than a simple packed bed packing scheme[103].

CO oxidation has also been tackled with the use of microfibrous media. In 2005 the fire escape mask was targeted. A Pt on Al_2O_3 catalyst was entrapped in nickel microfibrous mesh. The end results were a ten times lower amount of catalyst needed, four times less pressure drop and one tenth the weight of competing commercial products[104]. In 2005 microfibrous entrapped Pt-Co on Al_2O_3 catalyst was used to clear CO from practical reformate streams used by a PEM fuel cell. An increase in performance was recorded due to increase in contacting efficiency of the small particles used in the microfibrous mesh. The entrapped particle's activity was maintained at higher gas hourly space velocity than that of a packed bed[105]. In 2012 microfibrous materials were used in conjunction with a Pt-CeO_2 on SiO_2 catalyst to improve reactivity [52].

Pressure drop is also an important factor which microfibrous media improves upon. The lower pressure drop is largely due to the increased void fraction of microfibrous media over a packed bed. The effect of void fraction not only decreases pressure drop, it also decreases volumetric reaction rate. This was illustrated by by Gu et al. and Kalluri et al. during catalytic ozone decomposition [106][107].

Figure 2-8 shows the decrease in mass transfer between a packed bed and MFEC. They are both higher than a monolith which is not limited by void fraction, but by particle size. Ozone decomposition, as measured in Figure 2-8, is mass transfer limited. This allows the result to be generalized to any mass transfer limited reaction. As will be seen in 6.2.3 Results and Discussion CO oxidation is also mass transfer limited at CO concentrations less than 200 ppm with 210 μm to 150 μm particles at a face velocity of 15 cm/s.

The decrease in heterogeneous mass transfer, in microfibrous media, is exceeded by the lack of pressure drop. To account for the two, heterogeneous contacting efficiency, HCE, is used. HCE is logs conversion divided by unit pressure drop. This allows the packaging system to be judge by how much work has to be put into it to remove contaminates. The origin of HCE is a more specialized version derived by Kolodzief and Lojewska which they termed Performance evaluation criteria. PEC follows the symmetry of heat and mass transfer. In that, small heat exchangers can be judged more fairly when better contacting at the expense of flow resistance is taken into account. This is also true for structured catalytic reactors[108].

The first part needed is logs removed of contaminates. This is defined by the mass efficiency χ_M. In the case of ozone decomposition or any first order reaction:

Figure 2-8: The mass transfer coefficient vs. face velocity for a packed bed, MFEC and monolith. During catalytic ozone decomposition, a first order process. Packed bed: 150-250 µm Al_2O_3 .6 void fraction; Monolith: 12.5 µm washcoat, and MFEC with 0.75 void of 150-250 µm Al_2O_3 and 8 µm nickel fibers.

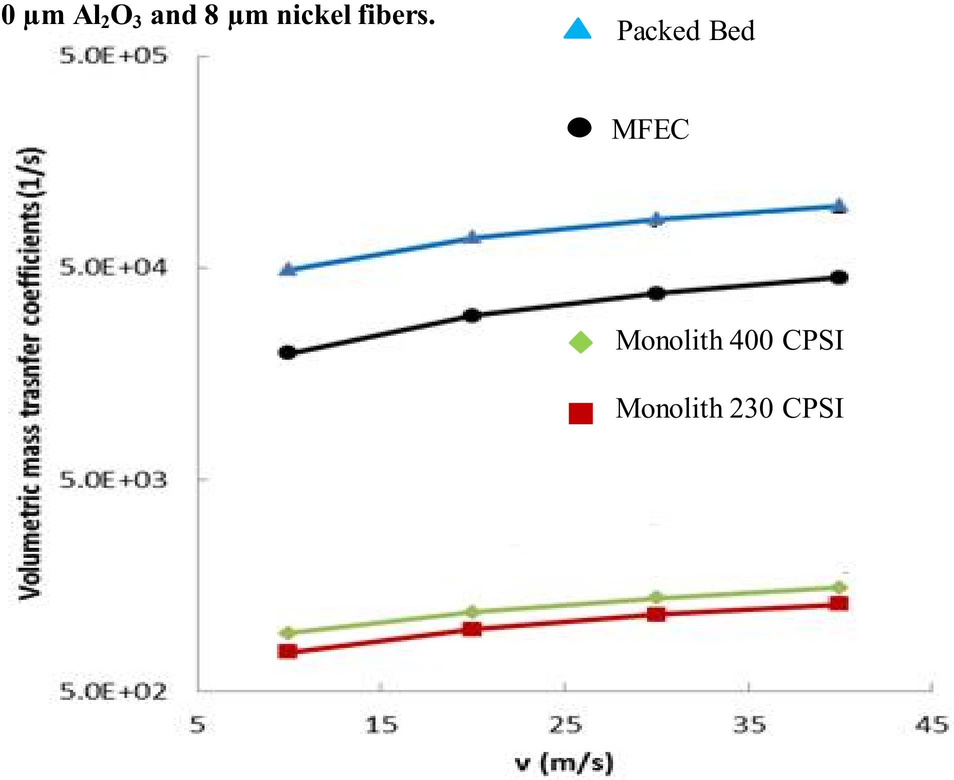

Equation 2-22:

$$\chi_M = \ln\left(\frac{C_{A,in}}{C_{A,out}}\right)$$

where $C_{A,in}$ and $C_{A,out}$ are the inlet and outlet reactant concentrations respectively. The second part is the double Euler number or flow efficiency, χ_F. χ_F takes into account the pressure drop across the reactor, ΔP, the fluid density, ρ, and the velocity, v. It is given by:

Equation 2-23:

$$\chi_F = \frac{\Delta P}{\rho v^2 / 2}$$

The ratio of the two is the HCE, χ.

Equation 2-24:

$$\chi = \frac{\chi_M}{\chi_F} = \frac{\ln(\left(\frac{C_{A,in}}{C_A}\right)}{\frac{\Delta P}{\rho v^2}}$$

Gu and Kalluri both have shown increased χ with respect to MFEC. Figure 2-9 displays the effect on χ for various reactor types and at velocities between 10 and 40 m/s. Here it is shown that even though the MFEC had a lower mass transfer coefficient as compared to a packed bed in Figure 2-8, χ is higher. The packed bed's volumetric mass transfer coefficient actually drops below the monolith. The lower pressure drop of the monolith is why it is used instead of a packed bed in many applications. While the pressure drop will not be measured in this work, the low pressure drop of the MFEC is one reason it is explored for use in CO oxidation. In section 1.1 a number of possible applications are outlined. All of these applications benefit from lower pressure drop. This is true especially for human power devices like a gas mask.

Figure 2-9: Changes in HCE, χ, with face velocity.

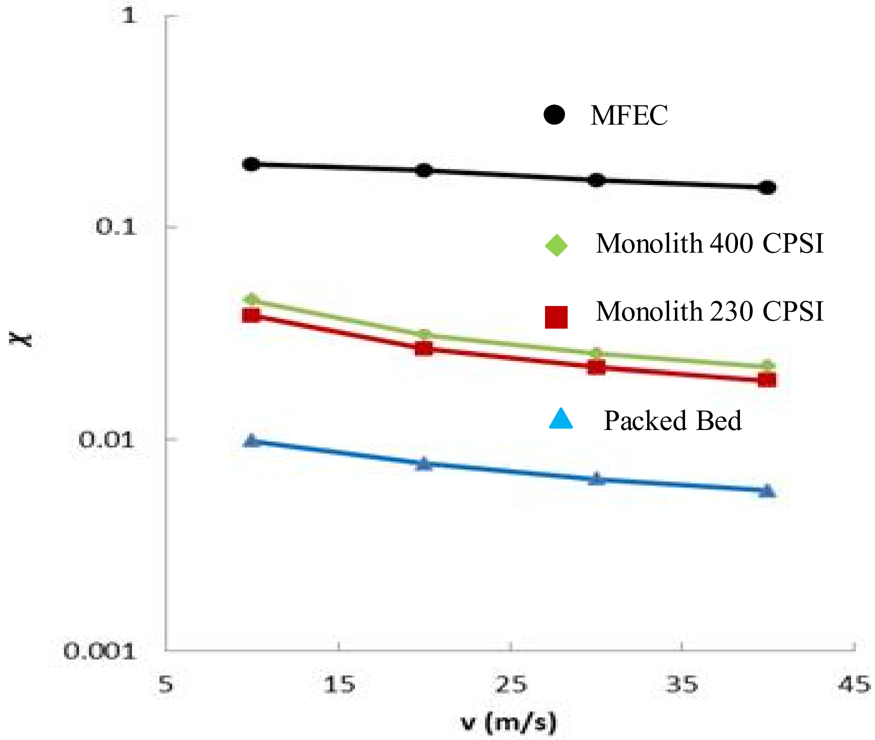

Another advantage of microfibrous media is the ability to pleat. The pleat factor is the area of the microfibrous filter divided by the cross sectional area of the reactor. The pleat factor allows the microfibrous media to adapt to the restrictions of its surrounding. Residence time can be increased without increasing pressure drop. This is in stark contrast to a packed bed or monolith. Once again χ is used to determine the effectiveness of the reactor design in Figure 2-10. Here the affect of pleating the microfibrous entrapped catalyst. A pleat factor of 4 is found to give the highest performance. The pleat factors can be thought of as straight across the reactor for PF = 1, a V shape for PF = 2 and a W shape for PF = 4. Increasing the cpsi of a monolith does increase χ. However, once velocity picks up the pressure drop increases which decreases the flow efficiency and lowers χ. The most one can do with a packed bed in a fixed reactor space is increase the bed depth. This is found to only lower χ the deeper the bed gets.

Figure 2-10: HCE, χ, for different Pleat factors compared to multiple packed beds and monoliths during ozone decomposition. The challenge gas consisted of 1.5 ppm ozone at 422 K.

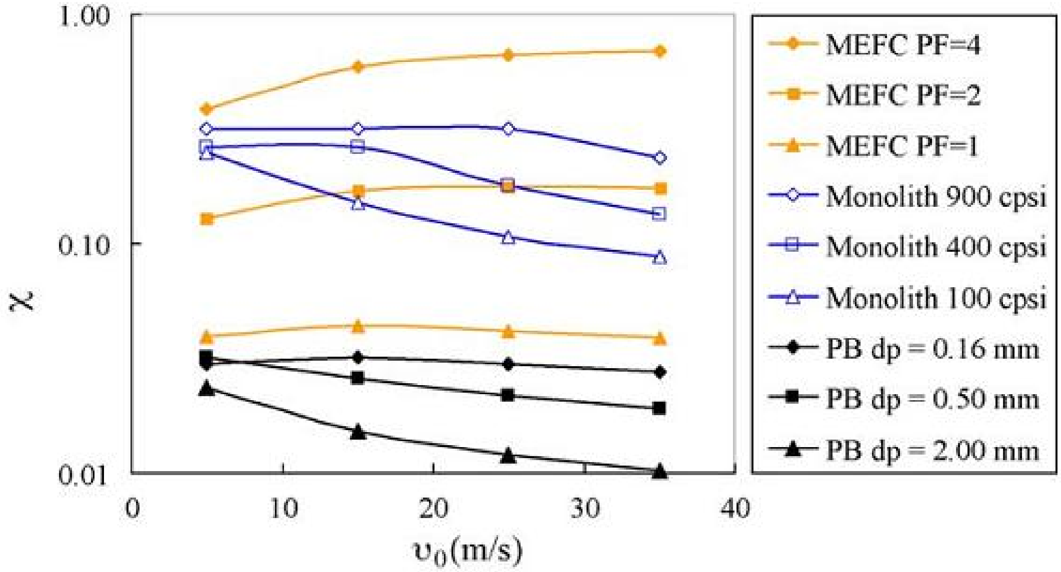

A drawback of using microfibrous media with impregnated materials is the particles must be entrapped in the mesh and then impregnated with active catalytic surfaces. The bare support particles are heated to the sintering temperature of the metal which can cause loss of surface area and thus activity. After the support particles go through the sintering phase, a clumsy procedure of adding the nitrate components to the support are done while the particles are in the metal [109].

To get around this draw back a new metal entrapped mesh is used. The microfibrous material is made without any particles trapped inside. The sheets are made extremely "fluffy" but still produced through a wet laid process. The extremely high void fraction allows catalyst particles to fall into the metal mesh were it becomes trapped in the tangled, sintered fibers. Pressure is applied to the top of the fibers and the compression locks the catalyst particles into place. This method is dry and requires no extra processing for the catalyst particles [110]. The preforms, as they are called, are available from Intramicron Inc. The precise procedure is explored in more detail in section: 3.2.9 Entrapment in Microfibrous Media.

2.5 Summary

Carbon monoxide is harmful to humans as well as the cathode of PEM fuel cells. The extremely high affinity of CO for hemoglobin and Pt are the root cause. Even small amounts, on the order of 20 ppm are needed to see adverse effects. Not to mention, higher concentrations of CO lead to unconsciousness and death in humans. It is clear a filter is needed to clean the air. This filter will encounter many environments, hot and cold, humid and dry in the real world.

There is an incredibly large body of research into different types of CO catalyst. After Au on TiO_2 was discovered to be active at low temperatures in the 80's, almost the entire periodic table was explored for active catalyst that could work in different environments. Dry and cold, all the way down to -40 °C, environments are dominated by Au on TiO_2. As temperature increases, the options for catalyst choice explode. Section 2.2 details the different recipes and compares them based on TOF. If the conditions are dry enough the copper and manganese mixture Hopcalite is usable. For humid conditions, however, there is still a need. A Pt-CeO_2 on SiO_2 catalyst proved very effective. The Pt-CeO_2 on SiO_2 catalyst is what this work is based on. The catalyst deactivates in dry environments, the opposite of most other formulations.

The kinetics of the CO reaction is what attracted Lagmuir in the first place. A negative order reaction is rare and allows for lots of interesting behavior. In general, a negative order reaction is prone to hysteresis and incredibly sharp increases in reactivity as the reactant concentration decreases. Just as CO adsorbs strongly on hemoglobin, it also adsorbs on the noble metal of the catalysts. CO has essentially zero desorption rate at room temperature and a sticking coefficient close to 1. It is easy to see how CO, a reactant, is also a poison.

The Pt-CeO_2 on SiO_2 catalyst deactivates in dry conditions. This is a great strength of this catalyst, but it also complicates kinetic testing. The adsorption and desorption of water on SiO_2 has its own heat effects and the concentration of water on the catalyst generally lags the equilibrium concentration in the surrounding air. This must be taken into account during the modeling phase.

The noble metal-transition metal oxide catalyst, which has proven so effective, alleviates the situation by pairing the CO susceptible noble metal with an oxygen rich oxide. Allowing a constant oxygen source to the noble metal helps in two ways: The first is providing O to react with the CO itself. The second, and more important, is the vacant site which is left behind after CO is oxidized and leaves the surface. This constant removal of CO from the surface prevents the complete poisoning of the catalyst, and the reaction can proceed even in high CO concentration environments.

CO oxidation reaction is highly exothermic. It produces about 283 kJ/mol of heat. The heat then fuels the reaction further. When the high heat of reaction is combined with negative order kinetics, it is easy to see how the reaction is so sensitive. Generally, a small reaction zone occurs in a plug flow reactor in which most of the reaction takes place. Even with the poor thermal conductivity of a packed bed, traveling hotspots have been observed. These hotspots can be made to go up stream or down depending on the challenge gas' concentration and temperature. The hotspot moving down stream in the reactor signals a deactivating bed. Here the reaction is on the low side of the hysteresis. The reaction traveling up steam is the bed activating, as it switches from the low to high reaction rate side of the hysteresis.

The intense changes in reaction rate over short distances allow for small changes to have large effects on outlet concentration. Changing the thermal conductivity of the reactor has already been shown to stabilize the reaction. Microfibrous media has been used to overcome the low thermal conductivity of a packed bed. Increasing the thermal conductivity from 0.02 W/(m·K) to 0.5 W/(m·K) could be the reason.

Microfibrous media has other advantages as well. A higher void fraction than packed bed allows for much lower pressure drop through the reactor. The decrease in pressure drop is only half of the story however. An increase in void fraction does increase the boundary layer between the catalyst particle and the bulk fluid. In a mass transfer limited reactions, which CO oxidation is at low concentrations, this actually decreases the reaction rate. The decrease in pressure drop more than offsets the lower reaction rate, so χ increases. That is to say, more reactant is removed per unit pressure drop. There are also practical considerations. Microfibrous media acts a frozen fluidized bed. Smaller particle can be used, not only to avoid excessive pressure drop, but also to freeze the particles in place and prevent shifting that would be seen in a packed bed. Microfibrous media can also be pleated. Pleating allows the filter to be fit to increase catalyst loading without increasing pressure drop.

Catalytic CO oxidation is a rich system with many years of research behind it. It still draws in new studies and applications all the time. The introduction of Au on TiO_2 led to a large increase in interest yet again. The negative reaction order and high heat of reaction are responsible for a very complex system. In this system small changes in reaction variables, such as thermal conductivity, can mean the difference between a dependable useful filter, or a short acting, bulky one. It is the intention of this work to better understand CO oxidation through development of a model which helps explain what takes place in the reactor during humid conditions at room temperature.

Chapter 3 : Experimental

3.1 Materials

Catalysts are prepared using nitrate precursors for CeO_2 and Pt deposition. The supports used are high surface area silica which is sometimes sieved to attain the needed particle size distributions.

The starting materials used for Pt deposition are Diammineplatinum(II) nitrite in solution with ammonium hydroxide. It is 5 wt% as Pt from Strem chemicals with cas#14286-02-3. The chemical formula is $(NH_3)Pt(NO_2)_2$. And Tetraammineplatinum(II) nitrate cas# 20634-12-2 from Strem. The chemical formula is $[Pt(NH_3)_4](NO_3)_2$ and takes the form of a solid white to off white powder. Ceria Oxide precursor is Cerium nitrate hexahydrate from Aldrich cas# 10294-41-4. It has chemical formula $Ce(NO_3)_3 \cdot 6(H_2O)$ and takes the form of lumpy crystals. The support silica is davisil silica gel grade 645 and 644. Silica gel 645 is sieved between 60-100 mesh and 644 100-200 mesh, cas# is 112926-00-8. The silica gels have an average pore size of 60 Å, BET surface area of 300 m^2/g and pore volume of 1.15 cc/g.

For the CO source 5% CO in N_2 from Airgas is used. This is mixed with air provided by the compressed house air stream. The air is filtered to remove hydrocarbon contaminants. Nitrogen used in BET surface area and pore volume measures is UHP grade 99.99% pure from Airgas. The CO used for CO chemisorptions is UHP grade 99.99% from Airgas. The Argon and 5% H_2 in argon used for TPR measurements is 99.99% pure UHP grade from Airgas.

Microfibrous materials used are obtain from Intramicron Inc. The materials are nickel and copper fibers of 8 μm and 12 μm. They are prepared as performs to allow dry entrapment of catalyst particles. A thorough explanation of the process can be found in section 3.2.9 Entrapment in Microfibrous Media

3.2 Methods

3.2.1 Activity measurement Apparatus

Catalyst activity measurements were needed in a wide concentration and humidity range. The apparatus was designed for stable temperatures within 0.2°C. This is difficult when close to room temperature. The system was designed with stability in mind.

Figure 3-1: A diagram for the CO oxidation apparatus.

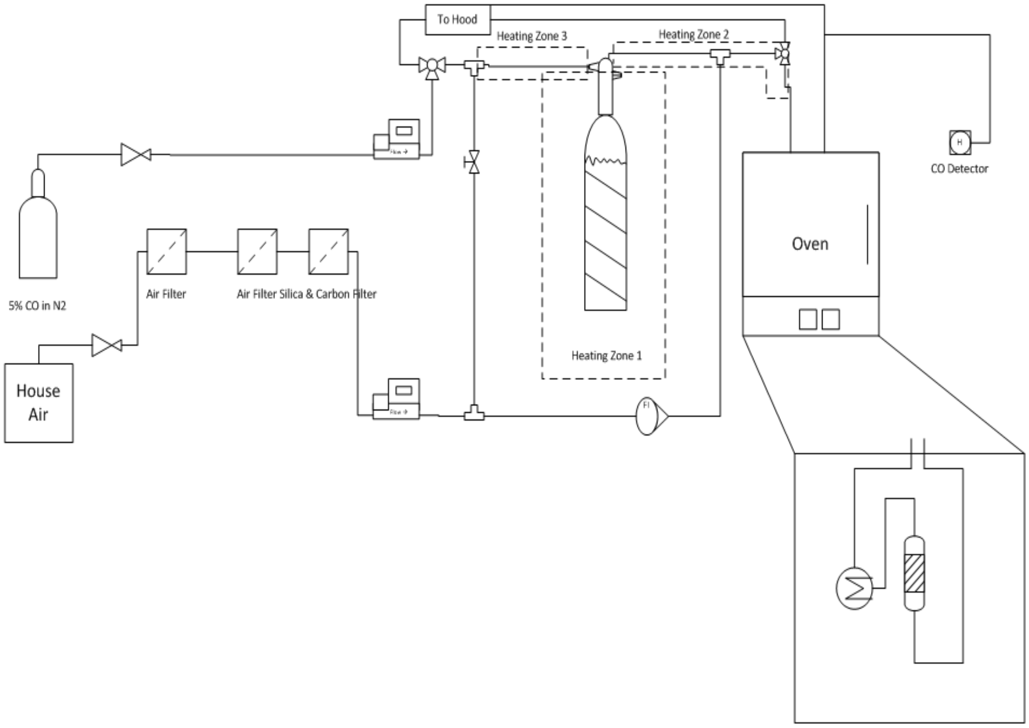

Figure 3-1 shows a diagram of the apparatus. From the beginning, house air is filter by three consecutive filters to remove containments. The first is a Watts Fluidair standard regulator; the second is a Motorguard M30, and the third is a packed tube filled with silica and activated carbon. Alternatively, tank air is used, breathing quality from Airgas. With the tank air all filters are skipped, and the air is fed directly into the mass flow controller. This air stream is then split with one branch flowing to a bubbler for water saturation and a second branch to an Omega FL-3804st rotometer. The RH is controlled by varying the fraction of flow through diverted through the rotometer. To get a good starting point to tune the RH, a mass balance is performed around the bubbler to get the final RH at the reactor. To do this the vapor pressure of the exit stream of water is calculated. It is assumed to be completely saturated. Equation 3-1 gives the molar flow rate of water exiting the reactor. $\dot{V}_{WET}$ is the volumetric flow rate of the gas diverted through the bubbler, T_{Bubbler} is the temperature of the bubbler R is the gas constant and A,B and C are the Antoine equation coefficients.

Equation 3-1:

$$\dot{C}_{H_2O} = \frac{\dot{V}_{WET} \cdot 10^{A - \frac{B}{C + T_{Bubbler}}}}{RT_{Bubbler}}$$

Equation 3-2 then gives the saturation molar flow rate of water in the combined dry and wet streams, where the temperature is replaced with that of the reactor and $\dot{V}_{Total}$ is the volumetric flow rate of the combined streams.

Equation 3-2:

$$\dot{n}_{H_2O,Sat} = \frac{\dot{V}_{Total} \cdot 10^{A - \frac{B}{C + T_{Rr}}}}{RT_{\mathrm{Re}}}$$

Equation 3-1 and Equation 3-2 are then combined to give the Relative humidity of the stream defined by:

Equation 3-3:

$$RH = \frac{\dot{C}_{H@O}}{\dot{C}_{H@O,Sat}}$$

It is important to not simply take the ratio of the wet and total $\dot{V}$. Generally, the bubbler is kept at a higher temperature than the reactor to decrease the flow through it and thus the pressure drop across it. In the reactor, the RH is measured by VWR hygrometer model 4085 certified through NIST standards. The 10 mm probe sits just behind the reactor and reads the RH ±1.5% accuracy between 10% RH and 90% RH. The 5% CO in N_2 mixture flows through a mass flow controller (Alicat Scientific 0-200 ml/min) into the dry stream. It is recombined with the wet stream after the bubbler. The flow of the air and CO mixture is adjusted to give the desired concentration and face velocity.

The CO air mixture flows into temperature controlled oven where it traverses 30 ft of ¼" copper tubing. The tubing damps any temperature disturbances that might be incurred up stream. The mixtures flows through the 5/8" ID reactor tube which is packed catalyst particles. Inlet and outlet CO concentrations were measured using a QRea electrochemical sensor which has a 1.0 ppm CO threshold with data logged every 30 s. After the detector the gas is exhausted through the fume hood.

3.2.2 BET

N_2 adsorption-desorption isotherms were collected for surface area analysis. The common Brunauer-Emmett-Teller, BET, procedure was used. About 0.3 g of material was outgasssed at 200 °C to clean the surface. The measurements were taken with a Quantachrome AS1 analyzer performing a 5 point BET analysis. The subsequent data was extrapolated using the AS1 Win software.

3.2.3 Chemisorption

CO chemisorption was carried out using the same Quantachrome AS1. The material is outgassed under vacuum at 200 °C for 30 min, reduced in hydrogen at 250 °C for an hour and outgassed again before chemisorption analysis took place at 250 °C. Isotherms were collected at 30 °C and extrapolated using a stoiciometry of CO/Pt = 1. Hemispherical particles were assumed for average particle size quantification. H_2 chemisorption was also used with the same procedure as above only H_2 was adsorbed onto the surface at 30 °C instead of CO. The analysis was carried out using the Quantachrome ASI win software.

3.2.4 TPR

TPR spectra was collected with 5% H_2 in Ar reducing gas. The flow rate was set to 15 ml/min and was held steady with a 0-100ml/min alicat mass flow controller. Typically 0.2 g catalyst was used for each run and the temperature was ramped from 40 °C to 760 °C at 10°C/min. The water from exiting the reactor was caught in a water trap held at -78 °C with an isoproponal slurry. The samples were first dried in flowing air at 115 °C for 30 min. The reactor is then flushed with Ar for 30 min and finally the 5% H_2 Ar gas mixture is introduced. The spectra are collected by a TCD detector attached to a SRI-310 gc.

To calibrate the TCD and TPR apparatus a small amount of CuO was reduced. The resulting peak was integrated to give an area. This area was compared to the amount of CuO reduced in the reactor to convert the signal in mV to mmolH_2/s consumed.

3.2.5 XRD

Powder X-ray diffraction (XRD) analysis was performed on a Rigaku Miniflex with Cu source at 30 KV/15mA. The scanning speed was set to 2 °/min (2θ) in the range of 5° to

85°. Species verification as well as crystallite size analysis was performed. Crystallite size was found using the Scherrer equation as implemented in JADE 6.5. The instrumental line broadening was determined by an in house CeO_2 on SiO_2 sample annealed to remove crystallite defects and increase crystallite size.

3.2.6 pH Measurement

pH was measured with a IQ150 with glass pH probe. The literature claims accuracy of pH = ±.01. Measurements were taken by calibrating the probe in two buffer solutions at pH 4 and 10. The probe was immersed in the fluid until a steady pH value could be read.

3.2.7 Axial Temperature Profile Measurement Apparatus and Heater

The temperature is an incredibly important aspect of CO oxidation as discussed earlier. To measure the profile down the length of the reactor a special reactor custom made at the Auburn Glass Shop. The purpose of this reactor is twofold: First, to measure the temperature profile down the packed bed or microfibrous bed in the axial direction. The second is to allow placement of a heater which can be controlled to input heat at the front or back of the reaction zone at prescribed powers.

Figure 2-3 gives a schematic of the reactor made. The eight thermocouples are spaced 2.8 mm apart. Each Thermocouple is inserted in a 1mm hole drilled into the glass. This allows for a smooth surface and no channeling. The tube is 0.625" ID and 0.74" OD to fit in the existing apparatus. The heater at the bottom is generally packed in silica gel to avoid contact with the walls and to hold it in place. Quartz wool is placed on the bottom of the heater for a tight fit and to allow the leads to the power supply to exit the bottom. The power supply leads exit through two holes which are sealed by septums to keep an airtight fit. The power supply is capable of delivering 30 W total with a 1 amp max. The heater itself consists of two concentric quartz rings with Nichrom wire wrapped around. The heat is delivered as an even plane by topping the heater with a small microfibrous copper sheet.

Figure 3-2: Schematic of reactor with 8 temperature ports and two ports for a positive and negative contact to the heater section. The heater is movable and capable of heating the gas 200 K if needed.

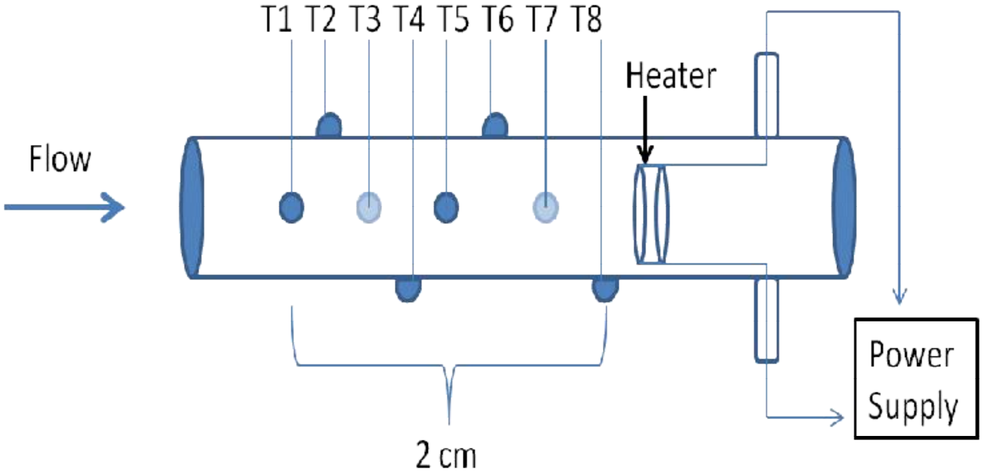

3.2.8 Catalyst Recipe

The catalyst recipe was initially optimized by Punde et al.[51]. The original Pt-CeO_2 recipe will be briefly described here. Following that, a more detailed recipe using the Tetraammineplatinum(II) nitrate Pt precursor, TAPN, will be explained.

The recipe starts with the drying of Davisil Silica gel 645 at 125 °C for an hour. While this is drying a Cerium(III) Nitrate Hexahydrate aqueous solution is mixed to give anywhere from 16wt%-22wt% CeO_2 on the final catalyst after calcinations and nitrate decomposition. The aqueous solution of cerium nitrate is mixed to incipient wetness of the silica support. The mixture is then vacuum dried for 4 hours or a dictated by weight change, and finally, calcined at 300 °C for 2h. The Pt solution Diammineplatinum(II) nitrite is mixed with the CeO_2-SiO_2 support. This is dried at 125 °C for 3 hours then calcined at 500 °C for 2 hours[51].

The revised procedure uses TAPN precursor instead of DADNP and changes the drying procedure of cerium nitrate away from vacuum drying. The recipe is given in great detail to aid in reproducibility which has proven a problem in the past. Table 3-1 describes the expected and measured density after each step. Densities were typically above the predicted by about 5%. This is acceptable for reproducible catalyst.

- Recipe for Pt - CeO_2 on SIO_2 CO oxidation Catalyst.
    - CeO_2 on SiO_2 preparation
        - CeO_2 solution
            - Mix Cerium(III) Nitrate Hexahydrate [$Ce(NO_3)_3 \cdot 6H_2O$, cas#10294-41-4] with DI water such that the final catalyst will have 22% CeO_2 by weight. The ratio of Mass of CeO_2 Precursor(M_{CeNH}) to volume of solution(V_{soln}) is given below. The pore volume of SiO_2(PV_{SiO2}) multiplied by the SIO$_2$ weight gives the minimum amount of solution needed

$$\frac{M_{CeNH}}{V_{soln}} = \frac{Mw_{CeNH}}{PV_{SIO_2} Mw_{CeO_2}} \left(\frac{wt\%_{CeO_2}}{1 - wt\%_{CeO_2}} \right) \left(\frac{1 + wt\%_{Pt}}{1 - wt\%_{Pt}} \right) \bullet \left[1 - \left(\frac{wt\%_{CeO_2}}{1 - wt\%_{CeO_2}} \right) \left(\frac{wt\%_{Pt}}{1 - wt\%_{Pt}} \right) \right]^{-1}$$

                - Typically to impregnate 30 g of SIO_2, a solution of 1.36g CeNH/cc is prepared by mixing 27.40g CeNH with 28.12g H_2O. This should prepare 40 ml of solution
            - After mixing let the solution stir for at least 30 minutes
        - Impregnating the Silica

Figure 3-3: Water content in $Ce(NO_3)_3 \cdot 6H_2O$ solution on SiO_2 while drying. Drying performed at 50 °C in flowing N_2 with 25g SiO_2 impregnated with 27 mL of CeO_2 precursor in 2” ID quartz tube.

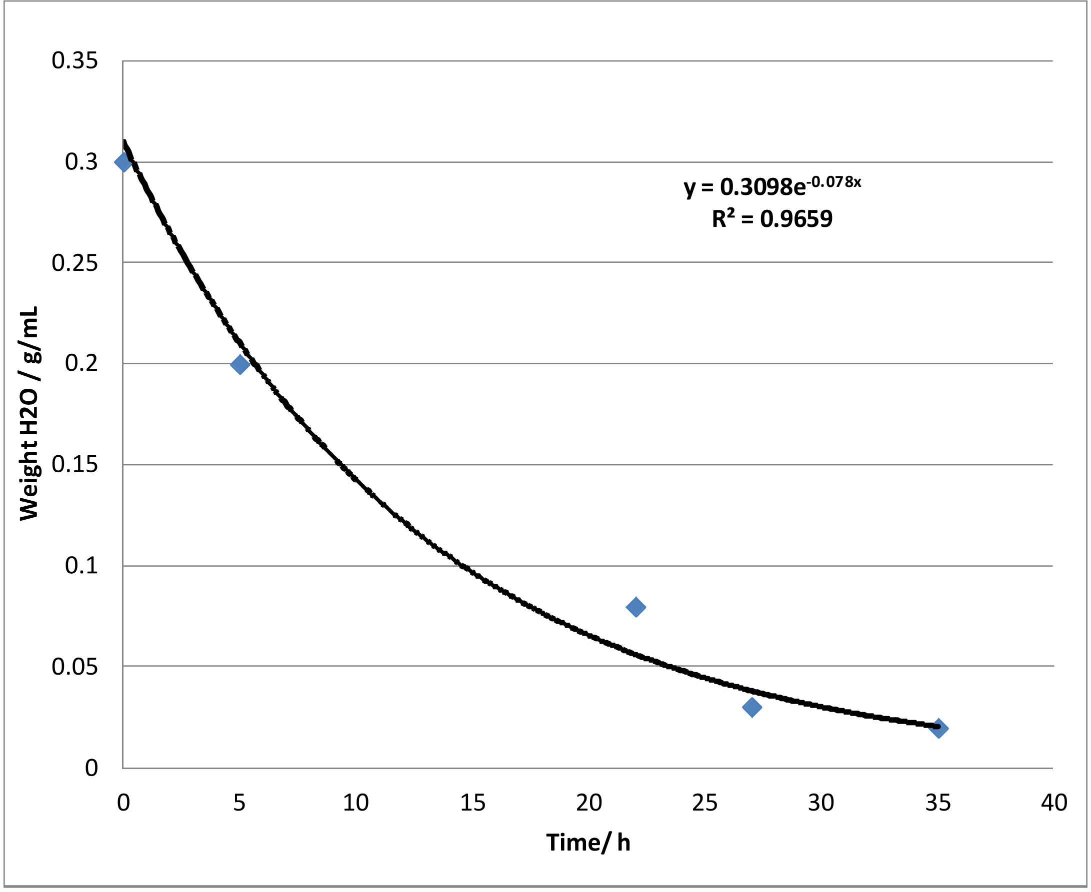

- Use Davisil 645 Silica Gel and assume a PV of 1.1 cc/g
    - Typically 30 g batches are done requiring 33ml of CeNH solution
- Impregnate the SIO_2 with the CeNH solution stirring as the solution is added.
    - Typically add 10 ml at a time and stir for up to 20 ml. 20 to 33 ml is done more slowly adding less between stirring the closer to 33ml. This should take about 30 to 40 minutes
- Spread out in large dish and let sit out overnight. In the morning bottle up impregnated SiO_2.

  - Drying the Impregnated SiO_2
    - Typically 16 g of impregnated SiO_2 is dried at 50 °C for at least 35 h under a flow of N_2.
    - Figure 3-3 displays the change in ρ over time while drying. At the 35 hour mark the catalyst reaches 0.02 g H_2O/ml Catalyst. At this point the water is 93% removed. As shown in Table 3-1 the predicted ρ for a completely dry silica impregnated with $Ce(NO_3)_3$ before calcinations is 0.54 g/mL. After drying for 35 hours the silica reaches 0.56 g/mL.
  - Calcination of Impregnated CeO_2
    - Under a flow of air the 16g impregnated SiO_2 is calcined at 300 °C for 2h.

- Pt impregnation on CeO_2-SiO_2 catalyst
  - Pt Solution Preparation
    - The mass of Pt Precursor per volume solution is given by:

$$\frac{M_{TAPN}}{V_{so\ln}} = \frac{wt\%_{Pt}}{1-wt\%_{Pt}}\left(\frac{Mw_{TAPN}}{Mw_{Pt}}\right)\left(\frac{1}{PV_{CeO2-SiO2}}\right)$$

    - Although the above formula is more general, for the narrow cases done here a 5 wt% Pt solution is prepared ($M_{Pt}/M_{So\ln}$). This is done to compare to the premixed DADNP solution. In such a case the PV is taken to be 0.9 cc/g for all catalysts. With the preceding requirements and the need to mix ammonia in the solution, the following equations are used to determine the mass needed of each component.

        - $M_{TAPN} = M_{total} \cdot wt\%_{Pt,soln} \cdot \left(\frac{Mw_{TAPN}}{Mw_{Pt}} \right)$
        - $M_{NH3} = \frac{M_{total} \cdot wt\%_{NH3,soln}}{wt\%_{NH3,source}}$
        - $M_{H2O} = M_{total} - M_{NH3} - M_{TAPN}$
    - M_{total} is generally equal to the number of grams of CeO_2-SiO_2 catalyst to be impregnated with Pt and wt% NH3 should be about 5%.
    - The TAPN is to be added first, followed by the water. The solution is lightly heated (hotplate set to 70 °C) and manually stirred for about a minute, more if needed.
        - If a high concentration of Ammonia is desired go ahead and add the ammonia to solution then stir (high $\geq$ 20% Ammonia).
    - The solution is then cooled until it is cool to the touch (Set it on a piece of metal in the lab and wait a minute or two).
    - Some water has been lost from the heating and stirring. Place the beaker back on the scale and add the lost water back (Add ammonia if this has already been added to solution).
    - Add the needed amount of ammonia
    - Seal the solution in a vial and let sit overnight to ensure complete mixing
- Pt Impregnation

        - Measure the needed amount of CeO_2-SiO_2 catalyst prepared earlier.
            - This is typically 2 g.
        - Using a syringe add a little more than half the total liquid needed at a quick pace and stir until smooth.
            - Typically about 1ml is added right away
        - Get the remainder of the liquid needed in the syringe then add slowly. Stir in between each addition. The total time should be 30 min to 45 min. 90% of the time is spent on the last 0.15ml.
            - Typically about .8 ml more is needed
    - Pt Drying
        - Spread out the powder in a watch glass and dry in the oven at 125 °C for 3 h.
    - Pt Calcination
        - The powder is placed in a quarts tube and packed with quartz wool on either side.
            - Typically about 2 g catalyst in a .75 ID tube
        - The catalyst is then calcined in a tube furnace set to 500 °C for 1h under flowing air.
            - Typically the air flows at 250 ml/min (Rotometer setting 40).
        - Take the catalyst out and let cool in the tube while the air still flows.

Table 3-1: Predicted and measured ρ for raw materials and after each step during the Pt- CeO_2 on SiO_2 process.

Step	p Calc / g/mL	p Measured / g/mL
Raw SiO2	N/A	0.37
Dry SiO2	N/A	0.35
Addition of CeO2 Soln	0.86	0.88
Sit Overnight	N/A	0.84
Dry in N2 @ 50 C	0.56	0.54
Calc. in Air at 300 C	0.45	0.48
Pt Addition and 3h dry	0.50	0.53
Calc. in Air at 500 C	0.48	0.50

3.2.9 Entrapment in Microfibrous Media

The microfibrous material is made without any particles trapped inside. Typically sheets are made with 6µm and 12µm copper fibers. The sheets are made extremely "fluffy" but still produced through a wet laid process. The extremely high void fraction allows catalyst particles to fall into the metal mesh were it becomes trapped in the tangled, sintered fibers. Pressure is applied to the top of the fibers and the compression locks the catalyst particles into place. This method is dry and requires no extra processing for the catalyst particles[110]. The preforms, as they are called, are available from Intramicron Inc.

Copper and Nickel performs were ordered from Intramicron Inc. Each preform uses 12 µm fibers. 60g of fibers are mixed with 6g of cellulose, blended and then wet laid to form a 1'by 1' uniform metal sheet. The sheet is allowed to dry; then placed on a belt furnace; where it is heated to 450 °C in air to remove the cellulose. After the cellulose is gone, the metal is sintered at 650 °C for Copper and 950 °C for Nickel. Below the 12 µm fibers, there is a 6 µm fiber screen layer which is prepared similarly. The screen layer is sintered to the catalyst layer, and prevents any catalyst from falling through the bottom while entrapping the catalyst particles.

Figure 3-4: Frequency of 5/8" Cu MFM discs which fall into 0.023g bins. These discs contain no catalyst. The Cu discs have an average of 0.85 g/cm^2 Cu fibers.

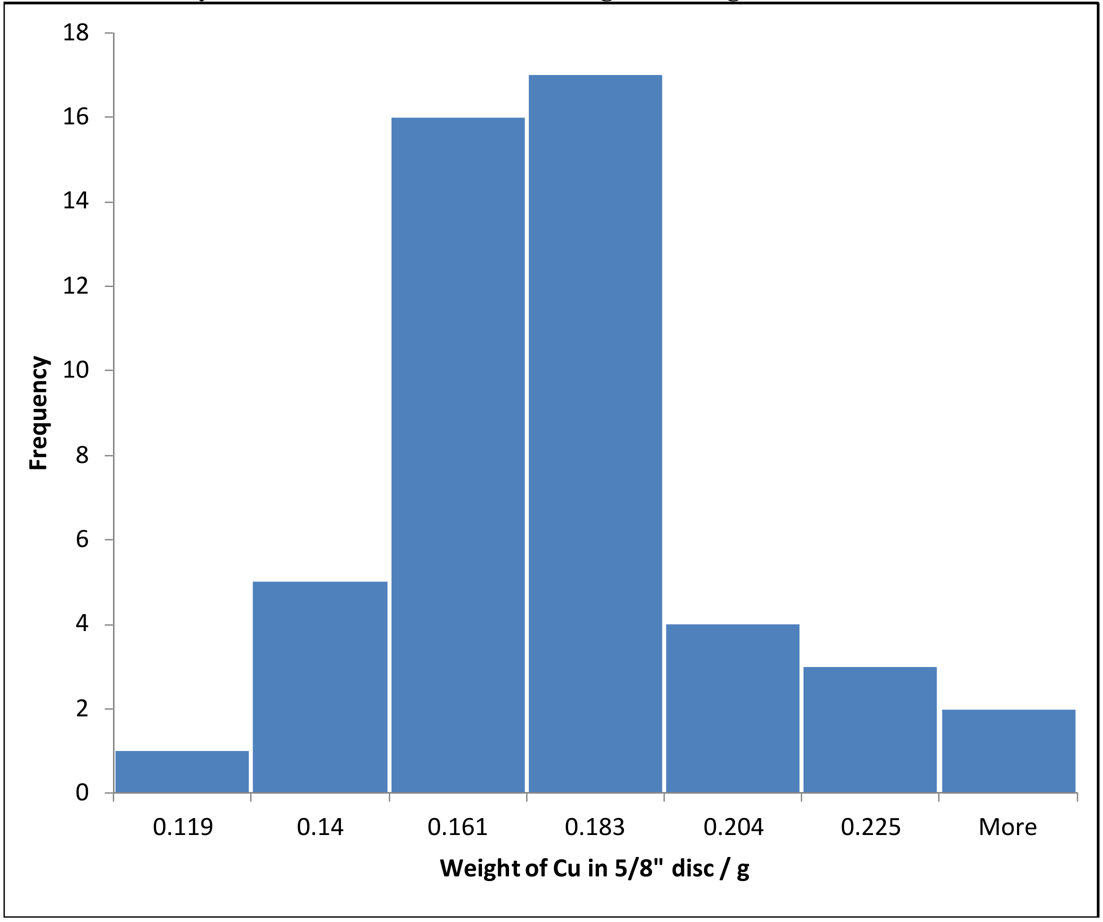

To check the spatial consistency of the microfibrous media, 5/8" disks were punched out and weighed. Figure 3-4 displays the histogram of the various weights measured. The mean weight was 0.1683g per disc with a standard deviation of 0.0268g. The distribution is not a clean normal distribution; it contains a skew of 0.86. This is compared to an acceptable skew of 0.70 for a sample of this size. It can be seen from this histogram that 91% of the discs fall between 0.14g and 0.204g. The sintered Cu sheets typically weighed 0.086g/cm^2 to 0.090g/cm^2 sheet.

Once the metal sheets are prepared, catalyst is loaded into the preforms. Catalyst loading is based on a technique from Sheng et al.'s work[110]. The catalyst particles, 70 to 100 mesh, are sprinkled on the top of the preform. The preform is shaken, and the catalyst particles are allowed to fall through the holes in the mesh. The sheets are then compressed, trapping the catalyst in the sheets.

Figure 3-5 displays two histograms for two different MFM sheets trapped with catalyst done as described above. The 5/8” Cu catalyst entrapped discs show, at first glance, two very different distributions of weights. One would expect a normal distribution from a random process. However, Figure 3-5 a shows a continually increasing frequency as more catalyst is entrapped, while Figure 3-5 b) shows a broader distribution centered around 0.263 g. Both have the majority of their discs between 0.26 g and 0.32 g. They also have 80% of the discs between 0.20 g and 0.32 g.

Figure 3-5: Histograms for two sets of Cu entrapped catalyst. a) and b) are two cut out sheets entrapped in the same manner. Both with 70-100 mesh PCS catalyst.

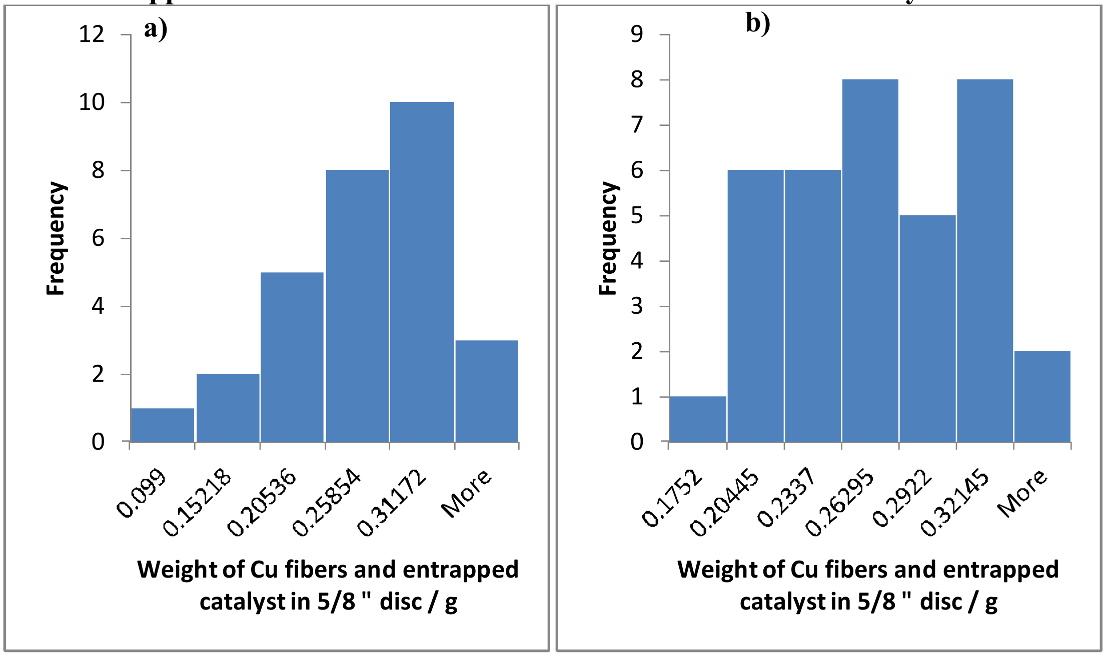

Efficient use of catalyst is paramount when working with Pt based catalyst. Figure 3-6 displays the leftover Cu after punching out 36 5/8” discs. The catalyst in the sheet needs to be recoverable to minimize waste. Table 3-2 details the weights and area of MFM used in 3 different entrapment processes. The loose catalyst is that which falls out of the sheet during the shaking phase to get the catalyst within the MFM and the catalyst that is lost while punching out the Cu discs. The loose catalyst is usually 1/5th to 1/3rd the entire catalyst used. It is very important to not waste this catalyst and collect it during the procedure.

The recovered catalyst from the media is that which resides in webbing after the discs have been punched. The left over webbing is shown in Figure 3-6a. The catalyst in the webbing comprises 10% to 20% of the total catalyst. The vast majority of this catalyst is recoverable. Once all the catalyst is recovered, there are only about 3.5% to 6.5% losses as seen in the last column of Table 3-2. This is very important considering only 40% to 50% of the catalyst used for entrapment actually makes its way into a usable disc. Other geometry would allow for higher utilization, but in this case the losses are acceptable.

Figure 3-6: a) The left over portion of a punched Cu sheet with entrapped catalyst. The Cu sheet is 152 cm^2, 13.287 g without catalyst and has, b), 36 5/8" discs cut from it.

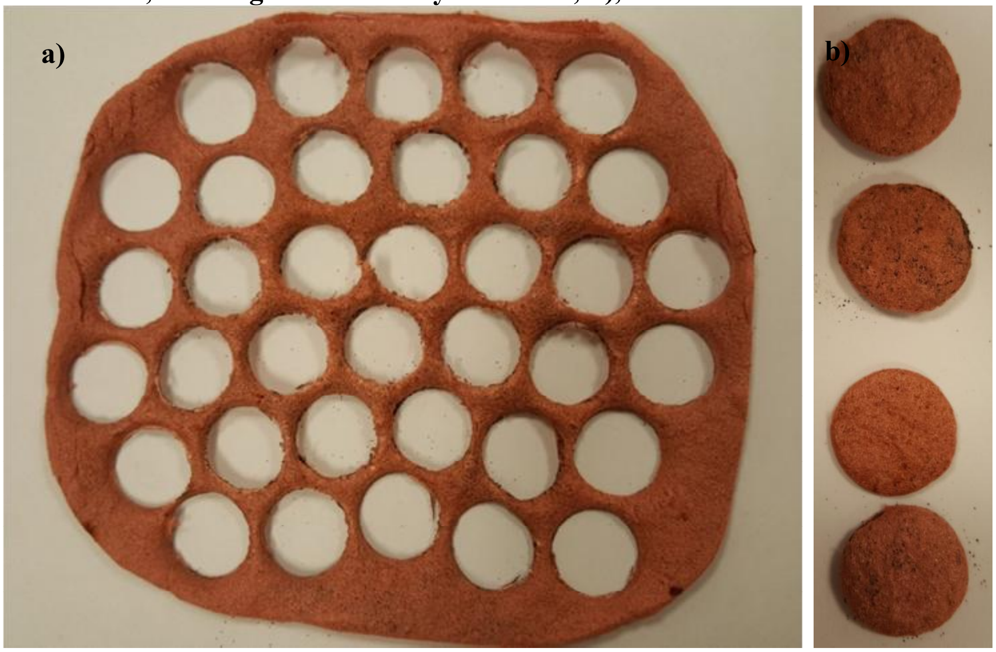

Table 3-2: Various statistics tracking catalyst use and media properties of 3 different Cu MFM sheets during the entrapment process. The total weight and area of the 4% Pt-22% CeO$_2$ on SiO$_2$ catalyst and media are below. The weight of the loose catalyst after punching out the MFEC discs, remaining catalyst in the MFM and that in the discs is also found. The catalyst recovered allows for the fraction of the catalyst loss in the process to be determined.

#	Total MFM /g	Total cat. Entrapped / g	# of Discs	MFM Area / cm^2	Avg. MFM per Area / g/cm^2	Avg. cat. per MFM Area / g/cm^2	Cat. Remaining MFM /g	Loose Cat. After / g	Cat. Entrapped in discs/ g	Recovered Cat. From Media /g	%Loss
1	11.61	4.77	29	134.3	0.0862	0.0354	1.071	1.461	2.07	0.98	5.5%
2	13.28	5.47	36	152.4	0.0872	0.0359	1.245	1.063	2.95	1.1	6.5%
3	14.14	6.82	36	156.7	0.0904	0.0436	0.745	2.292	3.69	0.6	3.5%

Once the MFM entrapped catalyst is punched it is ready to be loaded into the reactor. No further processing is done.

Chapter 4 : Catalyst Recipe: Precursor and pH

4.1 Introduction

The recipe for the catalyst production has already been gone over in detail. The objective of this section is to elucidate the change in activity between the two Pt precursors and the effect of pH of the impregnating solution.

There is three reasons to change from Diammineplatinum(II) nitrite $[(NH_3)_2Pt(NO_2)_2$, DADNP, to Tetraammineplatinum(II) nitrate – $Pt(NH_3)_4(NO_3)_2$, TAPN. First DADNP can only be procured premixed in a 5wt% solution in ammonium hydroxide with pH 11. TAPN, however, comes as a solid powder which dissolves easily in water. This allows TAPN to be mixed to any pH with ammonia and almost any concentration. Second DADNP is light sensitive. It must be stored in the dark and precautions must be taken while using it. And finally, the price of DADNP is almost twice that for TAPN. At the time of this writing DADNP is \$392/g Pt vs. \$203/g Pt of TAPN. This is for small quantities of each, but Pt is extremely expensive and this represents the most expensive component to the research. Any savings are welcome.

4.2 Effect of pH

4.2.1 Theory

Since the 1930's it has been known that the charge on metal hydroxides, or just oxides, is a function of its ionic environment[111]. Regalbutto et al. has published a number of papers on the effect of an oxide support on the solution it is in, and the adsorption process of ions in solution[112][113][114]. Regalbuto derived his inspiration from the use of the Gouy-Chapman electric double layer along with a chargeable hydroxyl groups which adsorb or desorb form the oxide surface, based on pH of solution and nature of the oxide itself[115]. The charging of the surface allows predictions to be made on the adsorption of charged complexes in solution such as a Pt precursor.

The oxide surface is made up of O atoms which can bond with a H$^+$ atom or even two, changing the charge of the surface from negative to neutral to positive.

Figure 4-1: Surface oxide buffering mechanism. ⬬ is a natively charge *surface* site consisting of *a* MO- bond; ● *is* a proton in solution or on the surface; ● is a neutral surface site, and ● *a positive* surface site.

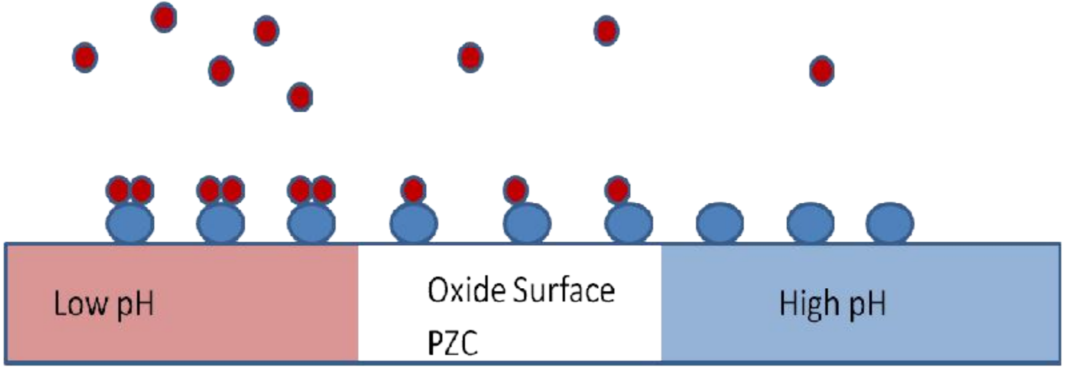

shows the effect of increasing the H$^+$ concentration as the pH is changed in solution. The rate of hydrogen adsorption on the surface is governed by Equation 4-1 and Equation 4-2

Equation 4-1:

$$K_1 = \frac{[MOH][H_s^+]}{[MOH_2^+]}$$

Equation 4-2:

$$K_2 = \frac{[MO^-][H_s^+]}{[MOH]}$$

K_1 and K_2 are the acid equilibrium constants, $[MOH]$, $[MO^-]$ and $[MOH_2^+]$ are the concentration of neutral, negative and positively charged surface groups, and $[H_S^+]$ is the surface proton concentration. $[H_S^+]$ is related to the bulk proton concentration, $[H^+]$:

Equation 4-3:

$$\left[H_S^+\right]=\left[H^+\right]e^{e^- \psi_0 / kT}$$

Equation 4-3 is the Boltzmann distribution with the charge on an electron, e^-, surface potential, ψ_0 , Boltzmann constant, k, and temperature, T. The total surface charge on the surface is the positively charged sites, $[MOH_2^+]$, minus the negatively charged sites, $[MO^-]$. This is divided by the total number of sites to give the average charge per site shown in Equation 4-4

Equation 4-4:

$$\frac{\sigma_o}{F\Gamma}=\frac{\left[MOH_2^+\right]+\left[MO^-\right]}{\left[MOH_2^+\right]+\left[MOH\right]+\left[MO^-\right]}$$

Here σ_0 is the surface charge; F is Faraday's Constant, and Γ is the charged site density. When Equation 4-4 is set to 0, that is the surface charge is neutral, and Equation 4-1, Equation 4-2 and Equation 4-3 are substituted in:

Equation 4-5:

$$pH_{PZC}=\frac{pK_1-pK_2}{2}$$

Equation 4-5 shows the pH and the point of zero charge, PZC, is dependent upon the acid equilibrium constants K_1 and K_2. In a solution with a higher pH than the PZC, the support

Figure 4-2: Uptake vs. solution pH is shown for platinum tetra amine cation on carbon supports of different PZC. PZC of 2.6 is ▲; 4.8 is ■ and 7.9 is ♦[116][117].

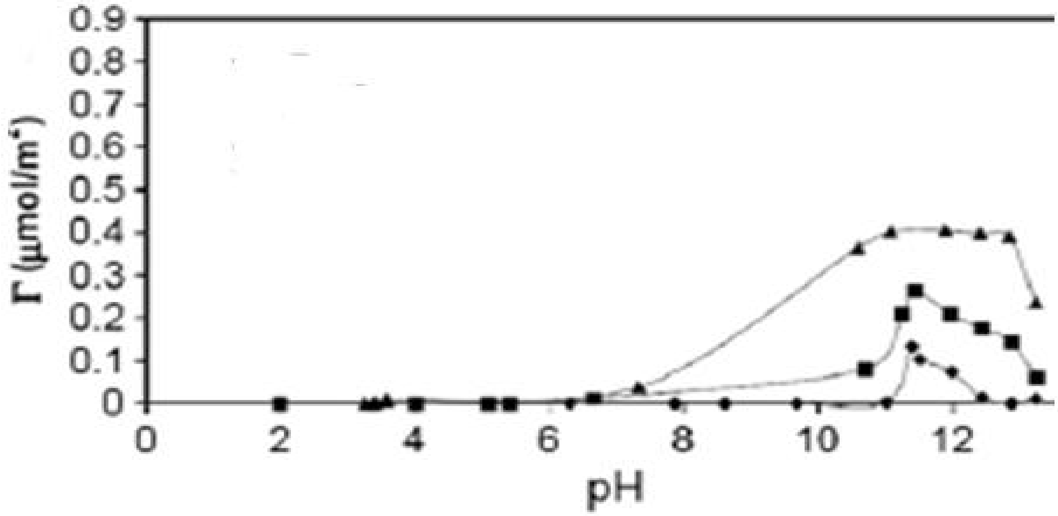

will be negatively charged and thus preferentially adsorb positively charged species on the surface and repulse negatively charged species. Below the PZC the opposite is true.

The adsorption as a function of pH is shown in Figure 4-2. The cation in this case is platinum tetraammine which gives a 2+ charge in solution. As the pH is increased the uptake goes through a maximum. The lower the PZC the more uptake occurs on the support. The adsorption eventually decreases due to high ionic strength of solution[114].

Different oxide supports have different K_1 and K_2 values and thus different PZC's. Some supports like, SiO_2, have a very acidic PZC around pH = 2. Other supports like γ-Al_2O_3 are on the basic side with PZC in the range of 8.5 to 10[118]. Activated Carbon is typically between 4.5 and 7.5, and CeO_2 is very close to 7[116].

Equation 4-1 and Equation 4-2 form a buffering mechanism with the solution the oxide support is mixed in. Figure 4-3 shows this buffering mechanism at work for a support with a PZC of 8. As the solid area to solution mass grows, the oxide support is able to buffer a larger range of solution pH.

4.2.2 Hypothesis

TAPN precursor forms a 2+ cation in solution. A higher solution pH should lead to more Pt adsorbed onto CeO_2 as it becomes negatively charged.

Figure 4-4 shows the change in surface charge for SiO_2 which becomes negatively charged around a pH of 2. Between pH = 2 and a pH equal to the PZC of CeO_2, 6.9, the SiO_2 will attract the cationic Pt ammine precursor while the CeO_2 will repulse it. As the pH is increased passed the PZC of CeO_2, the CeO_2 surface becomes negatively charged and

Figure 4-3: Buffering potential of submerged oxide support. The initial solution pH and the final pH are plotted for different surface area support to solution ratios.

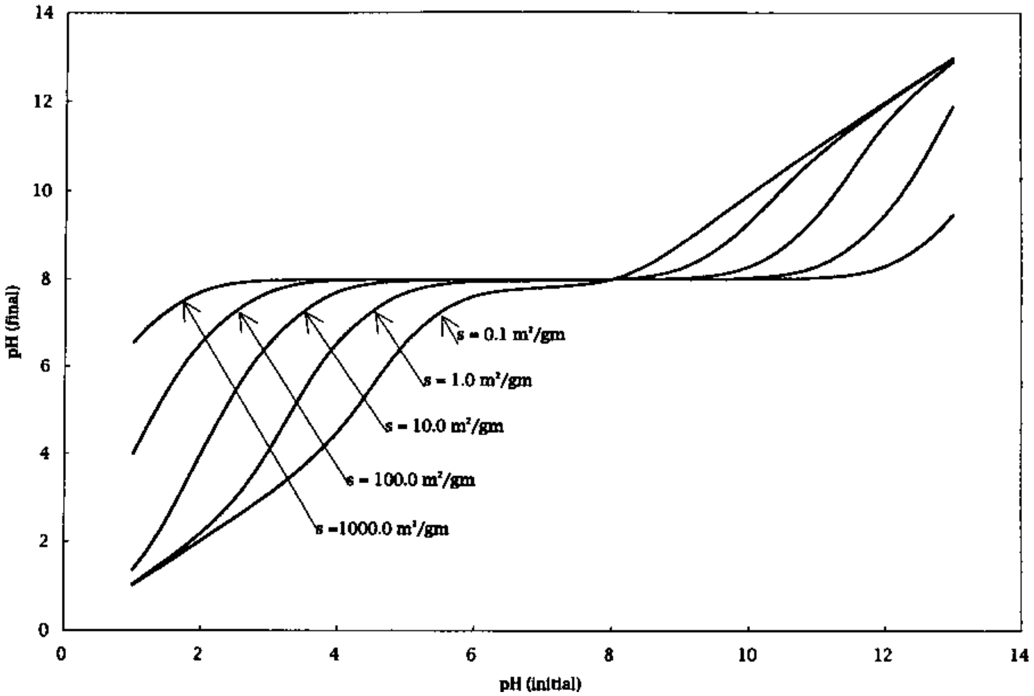

actively attracts cationic Pt adsorption. The SiO_2 also attracts $Pt(NH_3)_4^{2+}$, but it is relatively less favorable compared to CeO_2 at high pH vs. a low pH. The bottom line is increasing the pH of the TAPN solution should increase catalytic activity by adsorbing more Pt onto the CeO_2 surface.

Figure 4-4: Charge on SiO_2 and CeO_2 surface as the pH in the solution changes.

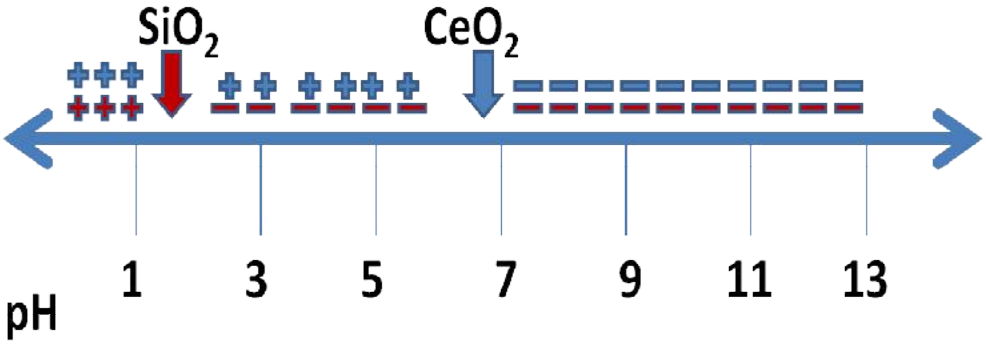

4.2.3 Results and Discussion

Different Pt-CeO_2 on SiO_2 catalysts were prepared with the TAPN precursor, and the pH was increased. The solution started at pH = 5.8 with no ammonia added. The pH was increased slowly by adding ammonia by weight. The pH of the solution was then measured, and the Pt solution was impregnated on the CeO_2-SiO_2 support. The different catalysts were tested for activity and dispersion measured through H_2 chemisorption. The results are in Figure 4-5.

The catalytic activity doubled from the minimum pH of 5.8 where 1.2 μmol/(g·s) was measured to the sample with pH = 10.7 where 2.4 μmol/(g·s) was achieved. This was done at the same time the *%D* decreased from 51% to 35%. Further increases in the pH beyond 10.7 led to a small drop in activity which was within the 95% error bars.

Figure 4-5: Effect of solution pH on performance. Reaction rate after 10 H on stream for catalyst prepared with different ammonia concentration. Testing Conditions: 0.2g Cat + 0.8g Inert; Conc: 300 ppm; FV: 15 cm/s; Temp: 25 C; ID: 0.75 in; RH :50%

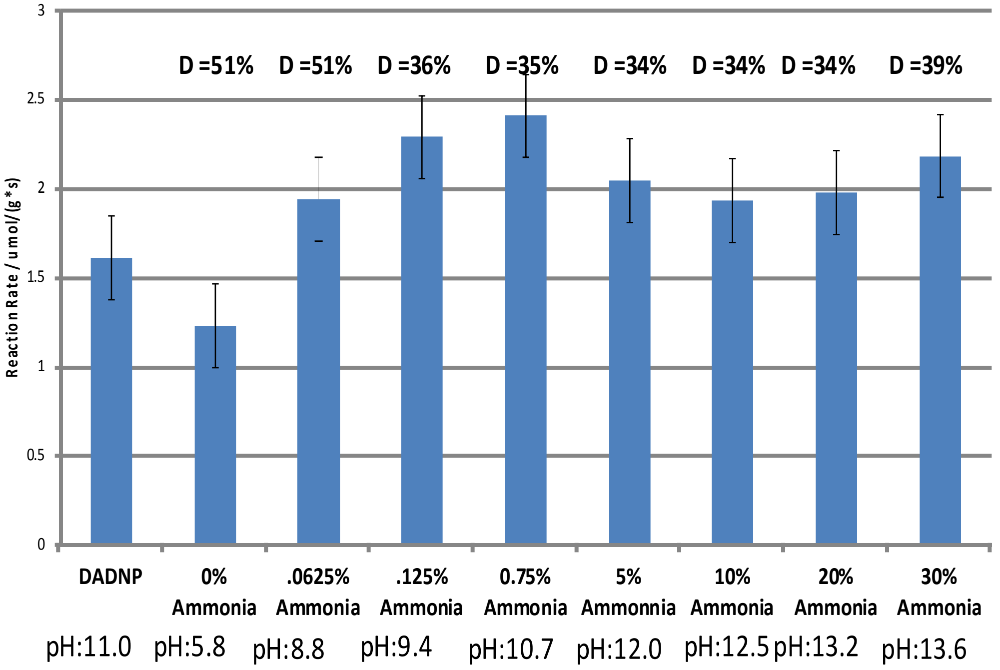

These results indicate that increasing the pH of solution does increase catalytic activity, even though the *%D* of the catalyst decreases. To study the effect of pH further TPR profiles were captured for catalyst prepared with pH 5.8, 10.7, 12, 12.5 and 13.6. Figure 4-6 shows the TPR profiles and the label of the peaks found.

The second and third peaks are the least interesting. They are assigned to surface CeO_2 and bulk CeO_2 respectively. Their values are largely constant as pH is varied. No effect of the solution pH can be found here. The first peak is assigned to dispersed Pt. The higher the dispersion the lower this peak is shifted. This can be seen here with the most dispersed catalyst, pH= 5.8 which has a *%D* = 51%, shifted to 122 °C vs. 140 °C from the other catalyst which are all between 34% and 35% dispersion[119].

The most interesting feature is the change in peak size between the poorly performing, pH = 5.8, Pt-CeO_2 catalyst and the others which all performed much better. Table 4-1 has the catalyst pH, *%D*, H_2 consumption for the first peak and corresponding CO

Table 4-1: H_2 consumption between 54 C and 251°C and catalytic activity. Activity measurements taken at: *v* : 15 cm/s; Inlet CO: 300 ppm; T: 25 C; ID:0.625" after 11 h

pH	%D	H_2 Cons./ mmol	*r* / µmol/(g·s)
5.8	51	0.30	1.22
10.7	34	0.11	2.27
12	35	0.10	2.20
12.5	33	0.13	2.12
13.6	39	0.11	2.17

oxidation reaction rate. The H_2 consumption is 3 times higher for the pH = 5.8 catalyst which also showed half the activity of the pH = 10.7 catalyst. The rest of the catalysts all fall into line. This indicates the Pt on the pH = 5.8 catalyst is more Oxygen rich than the others. The sticking of Oxygen on the Pt surface could be to blame for the decreased activity.

This throws some doubt on the original hypothesis. Could the difference in activity of the high and low platinum solution pH's be due to the oxidation state of Pt at the end of the

Figure 4-6: Effect of pH in Pt Precursor on TPR profile. mmol H_2 consumed vs. Temperature.
4% Pt-22% CeO2 on SiO2 Pt Precursor solution pH: 5.8 _ _ _; 10.7 ___ . . ; 12 ___ ___ ; 12.5 ___ . , and 13.6 _____

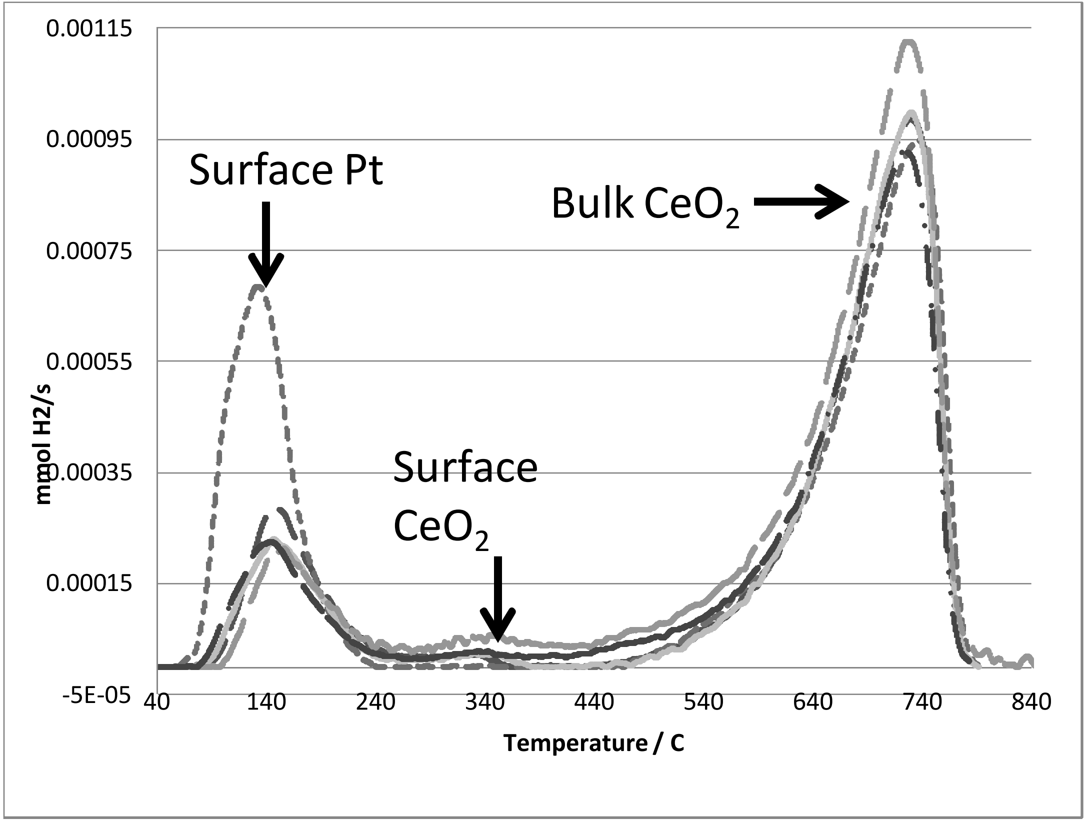

calcinations process? The pH = 5.8 and 10.7 samples were reduced at 140 °C for 30 minutes to remove any Oxygen on the Pt. They were then tested again to see if the pH= 5.8 catalyst would perform better than the catalyst made with pH = 10.7. If it did do better, then the oxidation state of the catalyst would be a possible explanation. If it did the same or worse, then the oxidation state of the catalyst cannot fully explain the difference in activity, and the standing hypothesis of electrostatic adsorption is the best explanation.

Figure 4-7 depicts the results. The pH = 5.8 and the 10.7 catalyst lay right on top of each other after reduction. This is despite the large Pt dispersion difference between the two. This indicates the oxidation state of Pt is to blame for a large part of the inactivity of the catalyst. However, it cannot explain how a catalyst with a 20% lower dispersion performs

Figure 4-7: Outlet CO Concentration vs. Time for two catalysts reduced at 140 C for 30 minutes and the corresponding non-reduced catalysts. 4% Pt-22%CeO2 on SiO2 60%RH ; FV 15 cm/s; Inlet CO: 300 ppm; T:25 C; Tube ID: 0.625"; RH: 60%

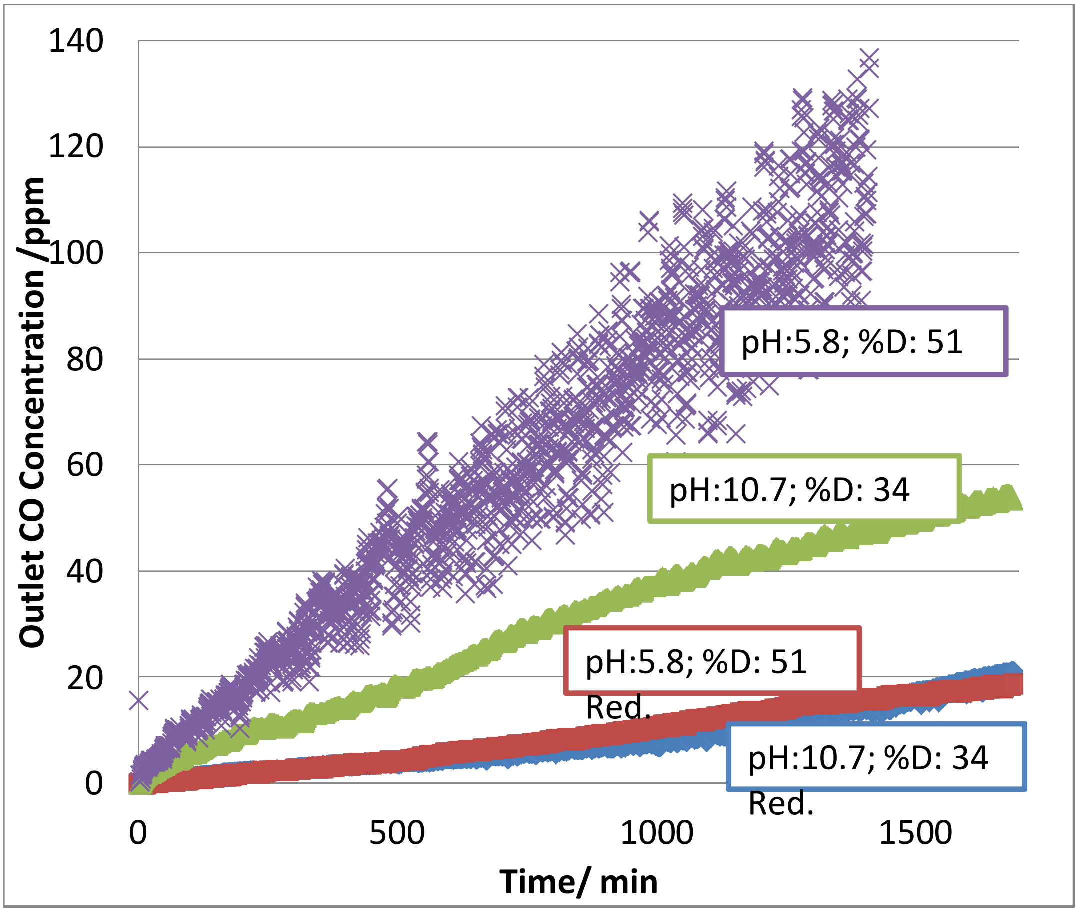

just as well as a catalyst with 51% dispersion. The explanation favored here is the increase of Pt crystallites on the CeO_2 surface due to the increase in pH of the Pt precursor solution.

4.3 Conclusion

The pH of the Pt solution during impregnation is responsible for doubling the reaction rate as pH is increased. The increase in reactivity is explained by higher Pt adsorption on the CeO_2 surface as opposed to the SiO_2 surface. TPR spectra are checked to monitor the surface Pt peak. It is found that this peak is much larger on the poorer performing catalyst. After reduction, the front peaks are equalized and the catalyst reactivity falls right on top of each other. This does not explain how a catalyst with 51% dispersion performs only as well as a catalyst with 34% dispersion. It appears there are two causes for the difference in poor performance. The first is an increase in the oxidation state of the lower pH Pt, and the second is the increase in Pt on the CeO_2 as opposed to SiO_2. Although, the second points still needs work to be proved.

Chapter 5 : Kinetic Testing and Model Building

5.1 Introduction

Differential reactor studies were conducted and a rate law was fitted. With this rate law some predictions on the temperature profile in a reactor can be made. A simple equilibrium reactor model was not able to capture the full range of phenomena, so a model which does not assume equilibrium between gaseous CO and surface coverage concentrations was used. This model proved able to model the catalyst in the activated and extinguished state. The model does not contain any parameters for catalyst deactivation, and is only in 1 dimension.

A wide variety of conditions are desired to account for. The surface coverage based model is able to account for face velocity, humidity, CO concentration, O_2 concentration, Temperature and is suited for transient analysis. The affect of face velocity not only needs to be expressed by changes in eternal mass transfer, but also axial thermal conductivity.

The model also takes the humidity of the gas stream into account. It is found the catalyst works best in wet conditions and deactivates in dry conditions. The catalyst uses SiO_2 as a support which readily adsorbs water. The affect of humidity on catalytic performance is found to be very important. Not only does it affect the catalytic activity directly, it also heats and cools the bed. The heating and cooling is found to be very important for transient activity measurements and cannot be ignored. This is typically the domain of SiO_2/H_2O adsorption chillers[120].

The model adds mathematical quantitative interpretation which, up until this point, has mainly existed as qualitative arguments.

5.2 Experimental

The catalyst used consists of 4% Pt-22% CeO_2 on SiO_2. A complete procedure for catalyst creation can be found in section 3.2.8 Catalyst Recipe Briefly incipient wetness was used to impregnate SiO_2 Gel(Davisil Gel 645) with Cerium(III) Nitrate Hexahydrate aqueous solution. The solution was left to dry overnight then dried in flowing N_2 at 50 °C. After which, it was calcined at 300 °C in flowing air. The CeO_2 on SiO_2 was impregnated again with an aqueous solution of the Pt precursor Tetraammineplatinum(II) nitrate(STEM Chemicals) adjusted with 5% aqueous ammonia. After impregnation the catalyst is dried at 125 °C for 3 hours; then it is calcined in flowing air at 500 °C for 1 h.

An overview of the CO oxidation apparatus can be found in section 3.2.1 Activity measurement Apparatus. Specifically reference Figure 3-1. The tests were generally carried out for an hour unless otherwise noted. The catalyst amount was set such that the conversion was less than 10%. This would be anywhere from 2 mg to 0.15 g. The catalyst was always diluted to 1 cm depth with SiO_2 in a 15.875 mm ID reactor. The catalyst and inert were allowed to adjust to the temperature and humidity of the challenge gas without the CO present in the stream for 30 minutes prior to testing. This ensured no heat rise due to water adsorption on the Silica Gel. The concentrations tested ranged between 25 ppm to500 ppm CO in the challenge gas. Any higher begins to damage the electrochemical Q-Rae sensor. The Q-Rae plus is employed for data logging the CO concentration over time. The data is logged every 30 s. A simple borosilicate glass reactor with 15.875 mm ID was used for all tests.

The catalyst surface area was tested via a 5 point N_2 adsorption isotherm. The BET method was used in conjunction with a Quantachrome AS1 analyzer. The data was plotted and extrapolated with Quantachrome AS1Windows software. CO chemisorption was also carried out at 30 °C on the same Quantachrome AS1to determine the Pt crystallite size. The

CO/Pt adsorption ratio was assumed to be 1 and the particles were assumed to be hemispherical. O_2 chemisorption was performed on the same instrument. The catalyst was further tested via XRD to determine CeO_2 crystallite size. It was tested on a Rigaku Miniflex with Cu source at 30 KV/15mA. Crystallite size analysis was performed using the Sherrer equation, and instrumental line broadening was accounted for by a pure SiO_2 crystal and an annealed CeO_2 on SiO_2 sample.

5.3 CO Oxidation Model

To qualitatively study the reaction mechanism and the effect of thermal conductivity, a reaction model is made to more clearly elucidate the effect of effective thermal conductivity. Two models are made. An equilibrium model which allows the effects of thermal conductivity to be seen and a model which tracks CO surface coverage to more fully capture the on/off behavior of CO oxidation. At this time they both accomplish different tasks, and it is educational to analyze the strengths and weaknesses of each.

For the equilibrium model diffusion limitations are ignored. The model consists of an energy and mass balance. The energy balance is of mixed phase. That is, the solid catalyst and fluid are modeled together. The two balances are:

Equation 5-1:

$$\frac{\partial C_{CO,G}}{\partial t} = D_{ax}\frac{\partial^2 C_{CO,G}}{\partial z^2} - v_z\frac{\partial C_{CO,G}}{\partial z} - r_{Rx}(C,T)$$

Equation 5-2:

$$\rho C_p\frac{\partial T}{\partial t} = k_{eff}\frac{\partial^2 T}{\partial z^2} - \rho_f C_{pf} v_z\frac{\partial T}{\partial z} + \Delta H_{Rx} r_{Rx}(C,T)$$

Equation 5-1 is the mass balance of the fluid phase. Equation 5-2 is the energy balance[121]. The variables are: CO concentration in the gas phase, $C_{CO,G}$, time, t, axial length, z, and temperature, T. The parameters are axial dispersion, D_{AX}, fluid velocity, v_Z, density of both the solid and fluid phase, ρ, mixed Heat capacity, C_P, effective thermal conductivity, k_{eff}, density of gas phase, ρ_f, heat capacity of gas phase, C_{Pf} and heat of reaction, ΔH_{RX}. r_{CO} is the reaction rate which is a function of $CO_{CO,G}$ and T. One of which is an equilibrium reaction in Equation 5-3. Otherwise the gas phase reaction is simply the mass transfer from bulk to pellet surface in Equation 5-18.

The reaction rate is derived from the Langmuir-Henshelwood mechanism between chemisorbed CO and O on the Pt surface. A derivation can be found elsewhere; the result is Equation 5-3[122].

Equation 5-3:

$$r = \frac{kC_{CO,G}}{(1+KC_{CO,G})^2}$$

K is the adsorption equilibrium; k is governed by the Arrhenius equitation to give it the proper temperature dependence:

Equation 5-4:

$$k = A_{CO,R}e^{-E_A/RT}$$

$A_{CO,R}$ is the frequency factor for CO oxidation reaction, E_A is the activation energy and R is the gas constant. To find the parameters needed to model the reaction rate, differential reactor studies are carried out.

Equation 5-3 assumes the surface reaction is the rate limiting step. This is not always the case. External mass transfer limitations, as well as, temperature and concentration based hysteresis complicate the observed behavior. A surface coverage model will alleviate this problem, but at the cost of added complexity and computational solving time.

To get a more accurate model, the rate of CO and O adsorption is not considered to be at equilibrium, so the surface concentration must be tracked. A second reaction is also hypothesized to take place. That is the exchange between O donated from the CeO_2 on the periphery to react with the CO adsorbed onto the Pt surface. Equation 2-5, Equation 2-6, Equation 2-8 and Equation 2-10 lead to adsorption of CO, adsorption/desorption of O_2, reaction between O and CO on the surface and reaction of CO adsorbed on Pt with O adsorbed on CeO_2 respectively. In addition, Equation 2-10 is found to be dependent on the water concentration in the gas stream. For the Pt-CeO_2 catalyst this is of paramount importance. The water dependence is discussed in section 2.3.2: Mechanisms for supported Pt on Metal Oxide and the Role of Water and is also evident during the kinetic studies of this work. Therefore, the oxygen available to react with the Pt, as seen in Equation 2-10 is hypothesized to depend on the water available:

Equation 5-5:

$$\mathrm{O - Ce_{(B)} + Ce_{(Pt)} \xrightarrow{H_sO} O - Ce_{(Pt)} + Ce_{(B)}}$$

Equation 5-5 details the use of water which acts a bridge between the oxygen adsorbed on the bulk cerium oxide and the oxygen which is ready to react with Pt. As mentioned earlier in 2.3.2: Mechanisms for supported Pt on Metal Oxide and the Role of Water this probably proceed through an carbonyl intermediate on the Pt- Ce interface.

The adsorption rate for CO and O on Pt is given by:

Equation 5-6 :

$$r_{ads} = F_i S_i$$

where F_i is the collision rate of the gas onto the surface and S_i the sticking coefficient. F_i is the given by:

Equation 5-7: $$F_i = \sqrt{\frac{R*T}{2\pi M_{W,i}}} * Pt_{area} C_{i,G}$$

Pt_{area} is the area of Pt per mass of catalyst and $C_{i,G}$ is the concentration of component i in the gas phase. The sticking coefficient follows the Kisluik expression for cursor mediate behavior for CO as seen in Figure 2-2 is below. Pt_{area} was found to be 2.9 m^2/g via H_2 chemisorption [67].

Equation 5-8: $$S_{CO} = S_{0,CO}\left(1 + \frac{\theta/\theta_s}{1-\theta/\theta_s} K\right)^{-1}$$

where K is the mobility precursor and θ_S is the saturation coverage. The oxygen sticking coefficient depends on the square of the surface coverage as detailed in section 2.3.1 Self Poisoning and listed below:

Equation 5-9: $$S_{O_2} = S_{0,O_2}(\theta)^2$$

The desorption rate of CO is considered to be 0 at low temperatures but O_2's desorption rate needs to be modeled as talked about in 2.3.1 Self Poisoning. The desorption rate is temperature dependent and depends on the square of the O_2 surface coverage as follows:

Equation 5-10: $$r_D = A_D e^{-Ea_{D,O}/RT} \theta_O{}^2$$

This leads to four surface reactions that must be accounted for: The adsorption of CO,r_1, found in Equation 5-11; the adsorption and desorption of O_2, r_2, found in Equation 5-12; the surface reaction between adsorbed CO and O on the Pt surface, r_3, found in Equation 5-13 and the reaction between adsorbed CO on Pt and O on CeO_2, r_4, found in Equation 5-14.

Equation 5-11:

$$r_1 = F_{CO} S_{CO}$$

Equation 5-12:

$$r_2 = F_{O_2} S_{O_2} - \dot{\rho}_{Pt} A_D e^{-Ea_{D,O}/RT} \theta_O^2$$

Equation 5-13:

$$r_3 = A_3 e^{-Ea_3/RT} \theta_O \theta_{CO}$$

Equation 5-14:

$$r_4 = A_4 e^{-Ea_4/RT} \theta_{CO} \theta_{O,Ce}$$

Equation 5-15:

$$r_5 = A_5 e^{-Ea_5/RT} \theta_W^n (1 - \theta_{O,Ce})$$

Figure 5-1 displays 4 regions of the catalyst surface. The first is the lone Pt crystallite. This Pt surface does not share any borders with CeO_2; thus, only r_1, r_2 and r_3 reactions are possible here. Without r_4 the reaction rate will completely deactivate on this crystallite at moderate CO concentrations at low temperature. The second region is the lone CeO_2 crystallite. These have no CO adsorption on their own and do not contribute to the overall reaction rate. The fourth is the Pt completely on top of the CeO_2 crystallite. This zone allows for all reaction, r_1 through r_5 to occur. On the border between the two, r_4 takes place with the help of r_5. The last zone is the Pt crystallite partially on the CeO_2 crystallite. Here the important border zone is much smaller, so it is expected that the reaction will drop off at lower concentrations than that of the Pt crystallite completely on the CeO_2. Although it would be helpful to know, there was not an attempt to measure the size of the Pt-CeO_2 interface. The maximum amount of O available to react with the CO adsorbed onto the Pt must fit with experimental reaction rate data. This maximum amount of oxygen is termed $C_{\mathrm{O,CE,Max}}$. In Equation 5-15 $\theta_{\mathrm{O,Ce}}$ is the ratio of $C_{\mathrm{O,CE}}$ and $C_{\mathrm{O,CE,Max}}$. As $\theta_{\mathrm{O,Ce}}$ approaches 1, $C_{\mathrm{O,CE}}$ fill all the spots possible and reaction r_5 slows to 0.

Figure 5-1: A model for the Pt-CeO_2 on SiO_2 catalyst is pictured. ● is the Pt crystallites which cover 2.9 m^2/g of the catalyst. 🟡 is the CeO_2 which covers 22.2 m^2/g of the catalyst.

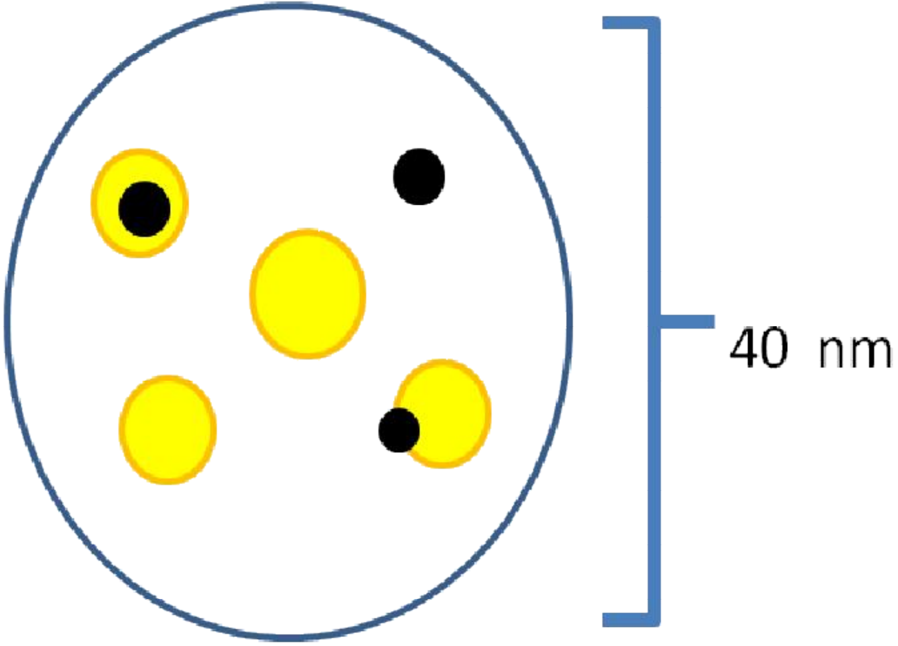

r_5, derived from Equation 5-5, is where the dependence of water is found. The water is not consumed, and the concentration available for reaction is postulated to be driven by the water adsorbed in the silica gel, which will be the local environment to the Pt-CeO_2 sites. To determine the amount of Water adsorption on silica gel, the work of Pedram and Hines will be used[123]. Hines fit water adsorption data on silica gel using Dubinin-Polanyi theory in conjunction with adsorption into a volume considered by Bering et al.[124][125].

The adsorption potential, in this case, is a potential field which varies inversely as the adsorbate's distance increases from the surface. This attractive force creates a potential field given by:

Equation 5-16:

$$\varepsilon = RT\ln\left(\frac{P_{vap}}{P}\right)$$

Here ε is the adsorption potential and P_{vap} over P is one over the relative humidity. P_{vap} is calculated from the Antoine constants. ε from Equation 5-16 is then used in Equation 5-17 to calculate the water adsorbed in the silica gel pores.

Equation 5-17:

$$C_{W,S} = C_{W,S0}\exp\left[-\left(\frac{\varepsilon}{B\cdot E}\right)\right]^{m}$$

Figure 5-2: The natural log of water adsorbed, W, vs. the adsorption potential. Three different adsorption isotherms are fit to a single line by fitting m to 1.2[123].

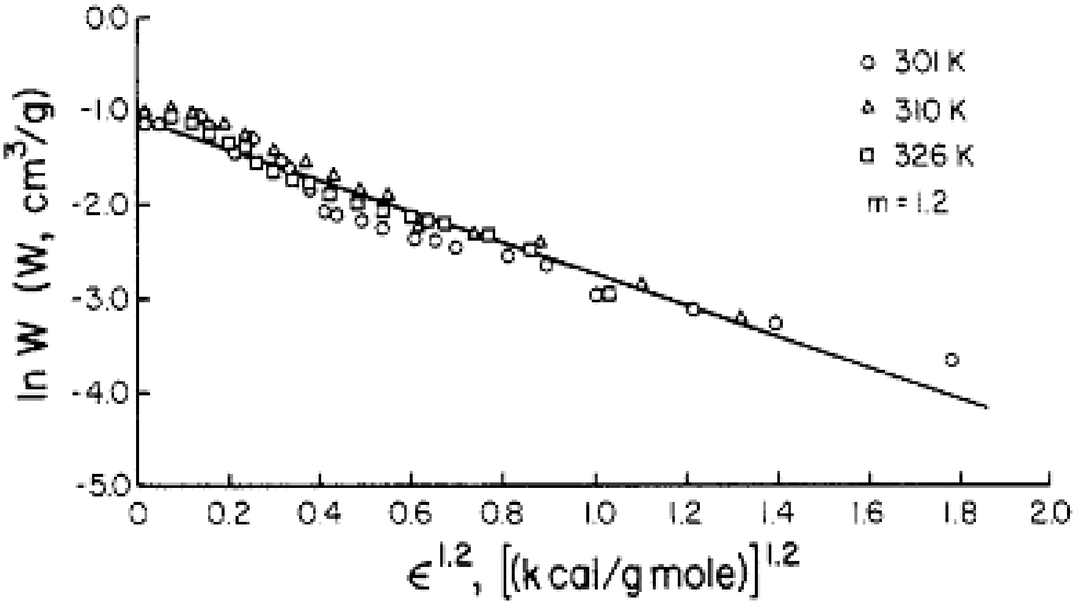

$C_{W,S}$ is the water adsorbed in the pores, $C_{W,S0}$ is the maximum amount which can be adsorbed, m is a constant in the isotherm equation, and B·E is an affinity factor multiplied by the constant characteristic energy. Pedram and Hines fit the data they gathered at 3 different temperatures using Mobil Sorbead R Silica Gel. The results of their work are shown in Figure 5-2. The slope of Figure 5-2 is $-\left(\frac{1}{B \cdot E}\right)^m$ which is found to be -7.0 kJ/mol. The line gives and good fit to the data with an $R^2 = 0.94$. This is appropriated for the silica gel used in this work to predict the water adsorption at different temperatures. The rate of water adsorption and desorption is given by the simple time constant relation:

Equation 5-18:

$$r_6 = \tau\left(C_{W,S,EQ} - C_{W,S}\right)$$

In Equation 5-18 τ is a time constant with the value 4.0e-3 1/s and $C_{W,S,EQ}$ is the amount of water adsorbed in the catalyst if the solid and gas phase water concentration are at equilibrium.

External mass transfer resistance is bound to control the reaction at some point as the gas phase reactant concentration approaches 0. In this case, as will be seen, this takes place around 150 ppm CO. The external mass balance has the simple and familiar form:

Equation 5-19:

$$r_{ext} = k_{ext}\left(C_{CO,B} - C_{CO,P}\right)$$

The external mass transfer coefficient, k_{ext}, will have affect illustrated in Figure 5-3. The linear portion is mass transfer limited. As mass transfer resistance increases the slope of the r_{rx} vs. concentration curve decreases[87]. k_{ext} is broken down into two parts. Equation 5-20

Equation 5-20: $$k_{ext} = a_P \cdot k_c$$

Figure 5-3: Equation 5-3 paired with mass transfer limitations, Equation 5-17, yield the reaction rate curves below. The three curves are none, medium and high mass transfer resistance. This corresponds to lowering the velocity [87].

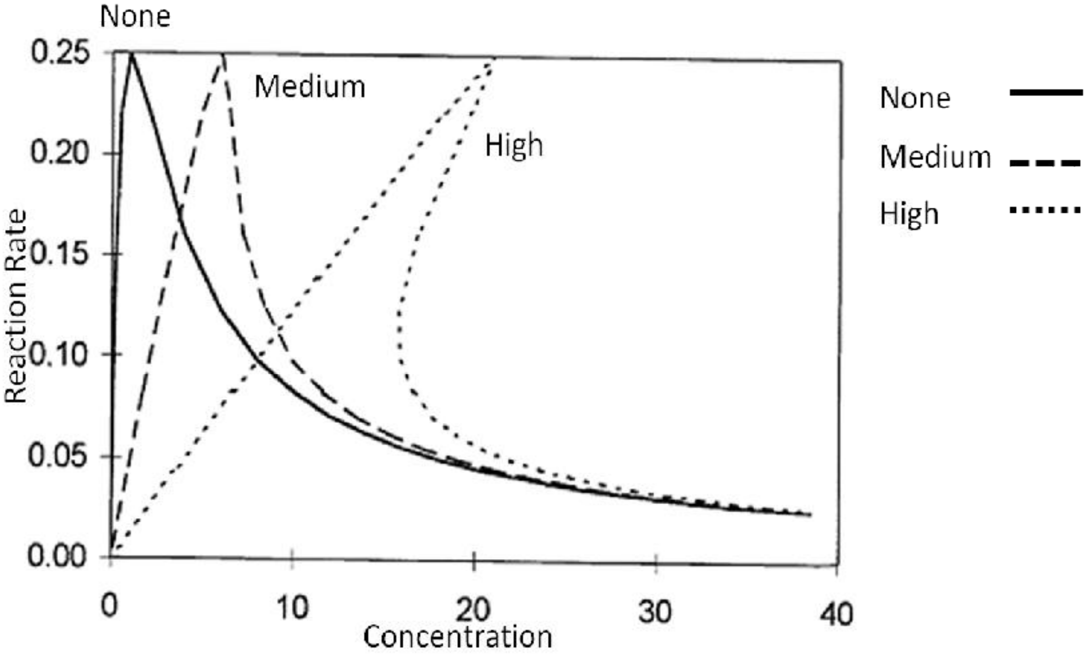

Shows k_{ext} as the product of the a_P which is the external surface area of catalyst per volume of catalytic bed given by:

Equation 5-21: $$a_P = {}^{6(1-\phi)}\!/_{d_P}$$

And k_c, which is:

Equation 5-22: $$k_c = \frac{D_{AB}}{\delta}$$

In Equation 5-22 the diffusivity, D_{AB}, divided by the film thickness, δ, gives the external mass transfer coefficient per area of external catalyst pellet surface. k_c can be derived from literature with the Thoenes-Kramers correlation[126]:

Equation 5-23:

$$\mathrm{Sh}' = \mathrm{Re}'^{1/2}\,\mathrm{Sc}^{1/3}$$

Expanded the Sherwood, Reynolds and Schmidt numbers are:

Equation 5-24:

$$\left[\frac{k_c d_p}{D_{AB}}\left(\frac{\phi}{1-\phi}\right)\frac{1}{\gamma}\right] = \left[\frac{u d_p \rho_f}{\mu(1-\phi)}\right]^{1/2}\left(\frac{\mu}{\rho_f D_{AB}}\right)^{1/3}$$

Simplifying Equation 5-24 it is possible to see k_c is proportional to $u^{1/2}$. k_c can be found experimentally from the slope of the reaction rate vs. concentration line when the reaction is mass transfer limited. When different velocities are tested and k_c is plotted against the square root of the velocity, the resulting correlation should be linear if Equation 5-24 holds. It is also desirable to know how k_C will change with temperature. Equation 5-24 can also be rearranged to show k_c is proportional to $D_{AB}^{2/3} \Big/ \left(\mu/\rho\right)^{1.6}$ which equals $T^{11/12}$.

There are 7 mass balances to consider. The first is Equation 5-1 with Equation 5-19 as the reaction rate between the bulk and catalyst surface. Two others track the CO and O coverage on Pt:

Equation 5-25:

$$\frac{\partial C_{O,S}}{\partial t} = 2 \cdot r_2 - r_3$$

Equation 5-26:

$$\frac{\partial C_{CO,S}}{\partial t} = r_1 - r_3 - r_4$$

where $C_{\mathrm{O,S}}$ and $C_{\mathrm{CO,S}}$ are O and CO adsorbed onto the Pt surface, as seen in chapter 2, represented as O-Pt$_{(S)}$ and CO-Pt$_{(S)}$ respectively. The oxygen available to react with Pt on the periphery of the crystallite must also be taken into account.

Equation 5-27:

$$\frac{\partial C_{OCE,S}}{\partial t} = r_5 - r_4$$

The concentration of CO on the external pellet surface must be balanced as well to yield:

Equation 5-28:

$$\frac{\partial C_{CO\,P}}{\partial t} = r_{ext} - r_1$$

Water in both the gas and solid phase must also be balanced for the final two mass balances:

Equation 5-29:

$$\frac{\partial C_{W,G}}{\partial t} = D_{ax}\frac{\partial^2 C_{W,G}}{\partial z^2} - v_z\frac{\partial C_{W,G}}{\partial z} - r_6$$

Equation 5-30:

$$\frac{\partial C_{W,S}}{\partial t} = r_6$$

The final equation needed is the energy balance which takes the form of Equation 5-2. $\Delta H_{\mathrm{Rx}} \cdot r_{\mathrm{Rx}}$ is the sum of the two CO oxidation reaction,(r_3 + r_4), multiplied by the heat of reaction, in this case 283 kJ/mol from heat of formation data. The adsorption and desorption of water must also be accounted for with a heat of adsorption of water, $\Delta H_{W,\mathrm{ADS}}$, of 42.9 kJ/mol multiplied by the adsorption rate, r_6. The substitution is:

Equation 5-31:

$$\Delta H_{Rx} = \Delta H_{CO}\left(r_3 + r_4\right) + \Delta H_{W,ADS}\left(r_6\right)$$

The mass balances, energy balance and reaction rates are the heart of the surface coverage model. The remaining parameters needed are the physical constants of the system and adjustments that are made when the bed is diluted. Bed dilution affects the bed mass, thermal mass, water adsorbed and reaction rate of the system per unit volume. A few quantities need to be defined. r_3, r_4 and r_5 have the units of mol reacted/ (mol surface Pt ·s), or more simply 1/s. To transform these to a volume bases, they must be multiplied by the density of Pt sites in catalyst, $\overset{\bullet}{\rho}_{Pt}$:

Equation 5-32:

$$\overset{\bullet}{\rho}_{Pt} = Wt\%_{Pt} \cdot \%D \cdot \rho_{s,Cat} \Big/ M_{W,Pt}$$

In Equation 5-32 $Wt\%_{\mathrm{Pt}}$ is the platinum loading weight percent in the catalyst; %D is the dispersion as defined in section 2.2 Comparison of Different Catalyst Recipes; $\rho_{\mathrm{S,Cat}}$ is the density of catalyst in the reactor, and $M_{\mathrm{W,Pt}}$ is the molecular weight of Pt. These quantities are defined in Table 5-1.

The bed is diluted in all experiments, so this must be accounted for. This is done simply by multiplying the quantities based on volume by the ratio of catalyst particle density in the actual reactor over catalyst particles tapping density, $\rho_{\mathrm{S,Cat}}$. The maximum water adsorption in the bed is a weighted average of the water adsorbed by the inert, $C_{\mathrm{W,0,In}}$, and that adsorbed by the catalyst itself, $C_{W,0,Cat}$.. Only the water adsorbed in the catalyst affects the reaction rate however.

Equation 5-33:

$$C_{W,0,Cat,In} = \frac{\rho_{Cat,act} C_{W,0,Cat} + \rho_{In,act} C_{W,0,In}}{\rho_{Cat,act} + \rho_{In,act}}$$

The thermal mass of the bed is computed for each phase. The gas phase is simply the sum of the contributions from the air and from the water vapor.

Equation 5-34:

$$\rho_f C_{pf} = \varepsilon\left(\rho_{air} \cdot C_{P,Air} + C_{W,G} \cdot C_{P,H2O}\right)$$

The reaction is dilute, so no changes in composition of air are taken into account. The change in $C_{W,Air}$ is of course tracked via Equation 5-29. The thermal mass of the solid phase is made up of the inert, catalyst and water adsorbed in the particles. This is done by calculating the thermal mass of the dry portion and adding it to the contribution from the water:

Equation 5-35:

$$\rho_S C_{P,S} = \rho_{Cat,act} C_{P,Cat} + \rho_{In,act} C_{P,In} + C_{W,S} C_{P,W}$$

And then to get the total thermal mass of the system Equation 5-34 and Equation 5-35 are added together to give the coefficient of the first term in Equation 5-2.

Table 5-1: Various physical quantities for the catalyst, inert, gas and water in the reactor.

	Catalyst	Inert	Water	Gas
ρ/ kg/m^3	670	329		1.18
C_p kJ/(kg·K)	0.752	0.876	4.181	1.006
$C_{W,S,0}$ g H_2O /g	0.8	1.1		

To find the other parameters literature resources were tapped. Dispersion is the mixing that occurs not only from the typical diffusion of gases, but also from the eddies in turbulent flow which arise when a fluid passes through a porous medium. As a result the dispersion depends on the molecular diffusion, flow rate, particle size and porosity. It is also anisotropic. D_{AX} can be seen in more detail elsewhere [128].

Equation 5-36:

$$D_{ax} = \tau_{ax} D_m + \frac{v_z d_p}{Pe_\infty \varepsilon \left(1 + \frac{\beta_{ax} \tau_{ax} D_m \varepsilon_b}{u d_p}\right)}$$

In Equation 5-36 τ_{AX} the axial tortuosity factor, D_m is the molecular diffusion coefficient, d_p the particle size diameter, Pe_∞ the limiting value of the Peclet number, ε the porosity and the radial dispersion factor β_{AX}. τ_{AX} is given by:

Equation 5-37:

$$\tau_{ax} = 0.45 + .55\varepsilon$$

β_{AX} can be shown to be 8 and Pe_∞ is:

Equation 5-38:

$$Pe_\infty = 670 d_p$$

D_M can be estimated from data at the critical point as shown by Brokaw[128]. Equation 5-39, Equation 5-40 and Equation 5-41 make up the system need to estimate D_m.

Equation 5-39:

$$D_m = \frac{0.001858 T^{3/2} M_{AB}^{1/2}}{P \sigma_{AB}^2 \Omega_D}$$

Equation 5-40: $$\Omega_D = (44.54T^{*-4.909} + 1.911T^{*-1575})^{0.1}$$

Equation 5-41: $$T^* = \frac{kT}{\varepsilon_{AB}}$$

The diffusion collision integral, Ω_D, is defined in Equation 5-40 with the help of Equation 5-41. M_{AB} is the mean of the molecular weight of the gases in question. P, the pressure, σ^2_{AB} the mean of the characteristic length and ε_{AB} is the characteristic Lennard-Jones energy. σ_i and ε_i are given by critical point data in Equation 5-42 and Equation 5-43:

Equation 5-42: $$\sigma_i = 0.841 V_c^{1/3} \, or \, 2.44\left(T_C / P_C\right)^{1/3}$$

Equation 5-43: $$\frac{\varepsilon_i}{k} = 0.75T_c$$

The critical point data to complete the computation is given in Table 5-2

At 300 K and 1 bar the diffusion rate of CO in N_2 is $1.13 \cdot 10^{-6}$ m^2/s. Equation 5-36 yields $7.55 \cdot 10^{-7}$ m^2/s with d_p=150 um and $\varepsilon = 0.4$ at 300 K and 1 bar.

The effective thermal conductivity, k_{eff}, for a packed bed can also be estimated from literature. The basis is shown in section 2.3.3 Effect of Temperature. Briefly, k_{eff} is the sum

Table 5-2: Critical point and molecular weight data for CO and N_2

Gas	T_C / K	V_C / m^3/kmol	P_C / Pa	M_W/ kg/kmol
N_2	126.1	.0901	3.3944e6	28.014
CO	132.92	.0930	3.4988e6	28.010

of the stagnant and moving contributions. Yagi then proposes the relation[89]:

Equation 5-44:

$$\frac{k_K}{k_g} = \frac{Pe}{K}$$

Here, k_K is the moving contribution to k_{eff} , k_g is the thermal conductivity of the gas phase, Pe is the Peclet number and K is taken as 2 for the axial case[90]. With k_g as 0.0257 W/(m·K), and conductivity of the silica gel 1.38 W/(m·K) the k_{eff} varies from 0.179 W/(m·K) at v_z of 5 cm/s and 0.196 at 30 cm/s. In this work k_{eff} will be taken to be a constant 0.18 W/(m·K).

The boundary conditions needed for such a simulation are the Dankwertz boundary at the entrance and the zero flux boundary at the exit for the gas phase mass balance and energy balance. The Dankwertz boundary captures the discontinuity between the catalyst and air barrier. The Dankwertz boundary is shown below with Q as the quantity in question, either $C_{CO,G}$, $C_{W,G}$ or T; c is the effective diffusion rate, D_{AX} or k_{eff} and flux is v_Z or $v_Z{\cdot}\rho_f{\cdot}C_{p,f}$.

Equation 5-45:

$$c\frac{\partial Q}{\partial z} = flux(Q_{in} - Q)$$

Mass balances of adsorbed species all require the zero flux boundary condition on all sides.

5.4 Parameter Solving Strategies Using Kinetic Data

The system of PDEs that the mass and energy balance create can be solved with Comsol 4.3a. Comsol discretizes the PDE's using the method of finite elements. The solution is arrived at through an implicit solver based on the method of lines. Fitting the model to data is performed using Matlab's built in function fmincon. fmincon is a non-linear constrained minimization solver. It can minimize a wide range of non-linear functions; in this case, the sum squared errors between the experimental and calculated values. It uses a quasi-Newton approximation of the Jacobian and Hessian to determine a path to the minimum [129] [130]. The complete program used can be found in appendix A1.

There are 10 parameters solved for by the model. Solving for all 10 parameters at once would be far too computationally intensive, so the job is broken up into four steps. The first step solves for k_c. This is done at low concentration at a single temperature and humidity. The second solves for k_3, k_4 and $S_{\mathrm{CO},0}$. These are done at a single temperature and humidity. They, however, take into account all of the different $C_{\mathrm{CO,G}}$ inlet concentrations. The third step solves for k_5, $C_{\mathrm{O,CE,Max}}$ and the order of r_5 with respect to H_2O. In this step the water is allowed to vary while the $C_{\mathrm{CO,G}}$ inlet and T are kept constant. Finally, T is allowed to vary with $C_{\mathrm{W,B}}$ in the final step. Ea_3, Ea_4 and Ea_5 are solved for while only $C_{CO,B}$ at the inlet is kept constant.

The first step, solving for k_{ext}, is done without the PDE solver. k_{ext} is easily solved for by plotting the r_{ext} vs. the exit $C_{\mathrm{CO,G}}$ for the linear portion of the curve, as seen in Figure 5-3. It is simple to see form Equation 5-19 the slope of this graph will be k_{ext} or $a_{\mathrm{P}} \cdot k_c$. Once k_{c} has been determined for multiple v_z, k_{c} vs $v_z^{1/2}$ will be plotted to form a straight line as predicted in Equation 5-24.

The second step begins to use Comsol to solve the coupled PDE's. The humidity is kept at 60% and the temperature is 26 °C. S_{CO} was allowed to vary because the unique Pt-CeO_2 interactions did not fit a sticking coefficient equal to 0.8 or higher as seen in the literature from Table 2-7. The only boundary set was to keep k_3 and k_4 above 0.

The third and forth step are done similarly. k_5, $C_{\mathrm{O,Ce,Max}}$ of r_5 are all solved for using data with $C_{\mathrm{CO,G}}$ constant at 300 ppm. n is allowed to vary only as integers and the simulation is rerun for numbers 1 to 6. The fourth step has no boundaries on any activation energies.

5.5 Results and Discussion

5.5.1 Catalyst Characterization

Figure 5-4: XRD pattern for 22% CeO_2 on SiO_2. Cu source: 30 kV/15mA; Scanning speed: 2°/min(2θ) from 5° to 85 °.

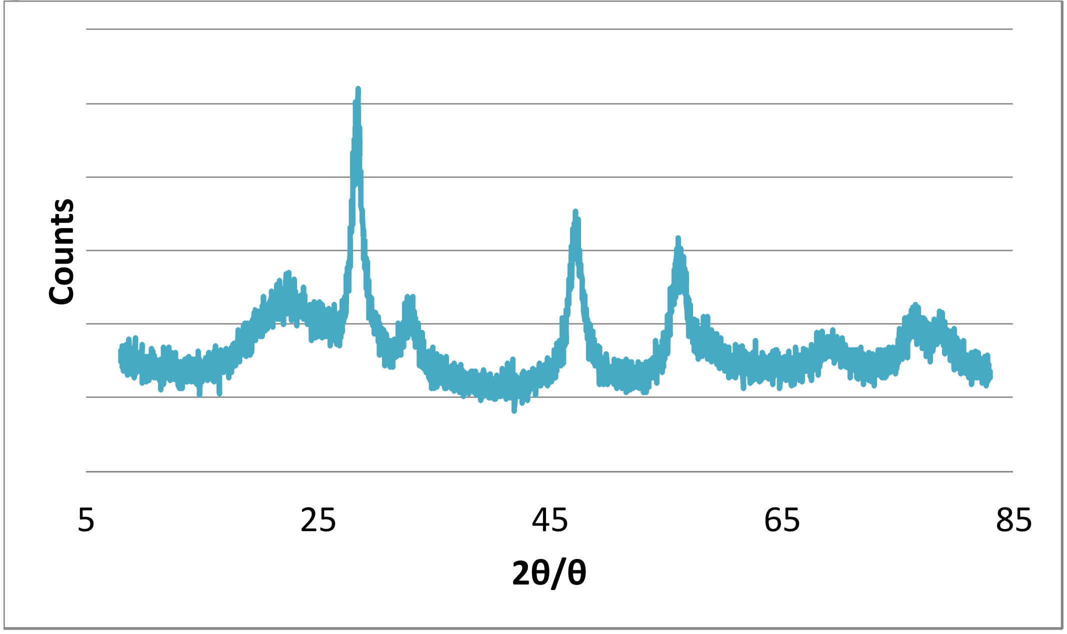

The BET surface area and other catalyst characterization data can be found in Table 5-3. The Pt crystallite size accounts for a 30 %*D* with a crystallite size of 3.5 nm. The BET surface area of 176 m^2/g is what is left after addition of both CeO_2 and Pt and the respective calcinations at 300 °C and 500 °C. Figure 5-4 shows the CeO_2 spectrum. The crystallite size was determined from the Sherrer equation using the peak located at 47.2 ° 2θ and a full width

Table 5-3: Surface areas and crystallite sizes for the 4% Pt-20% CeO2 on SiO2 catalyst. The total surface area was determined by N_2 adsorption and BET analysis; Pt crystallite size and surface area from CO chemisorption; CeO_2 crystallite size form XRD and surface area from O_2 chemisorption.

BET Surface Area / m^2/g	Pt Crystallite *d* / nm	Pt Surface Area/ m^2/g	CeO_2 Crystallite *d* / nm	CeO_2 Surface Area/ m^2/g
176	3.5	2.9	7.5	22.2

at half max of 1.354 to yield 7.5 nm. This was the largest result and rests in the (2 2 0) plane. The CeO_2 surface area was found to be 22.2 m^2/g via O_2 chemisorption and this also led to a crystallite size of 6.9 nm. This is in good agreement with the XRD results and validates the assumption of no amorphous phase.

5.5.2 Kinetic Tests and Model Fitting

The first step is testing and fitting the external mass transfer for concentrations below 100 ppm CO. Figure 5-5 shows the results of fitting the reaction data with a straight line below 100 ppm. The good linear fit indicates mass transfer resistance. The slope of each line is k_{ext} for that v_z. The reaction is severely mass transfer limited at low concentration even while using 150 μm to 210 μm particles.

Figure 5-5: External mass transfer resistance up to 100 ppm $C_{CO,G}$ at 5 cm/s, 10 cm/s, 15 cm/s and 30 cm/s. T: 26°C; RH: 60%; wt: 0.02 – 0.05 g; Conversion < 10%. The good fit to a straight line indicates the reaction rate is mass transfer limitations.

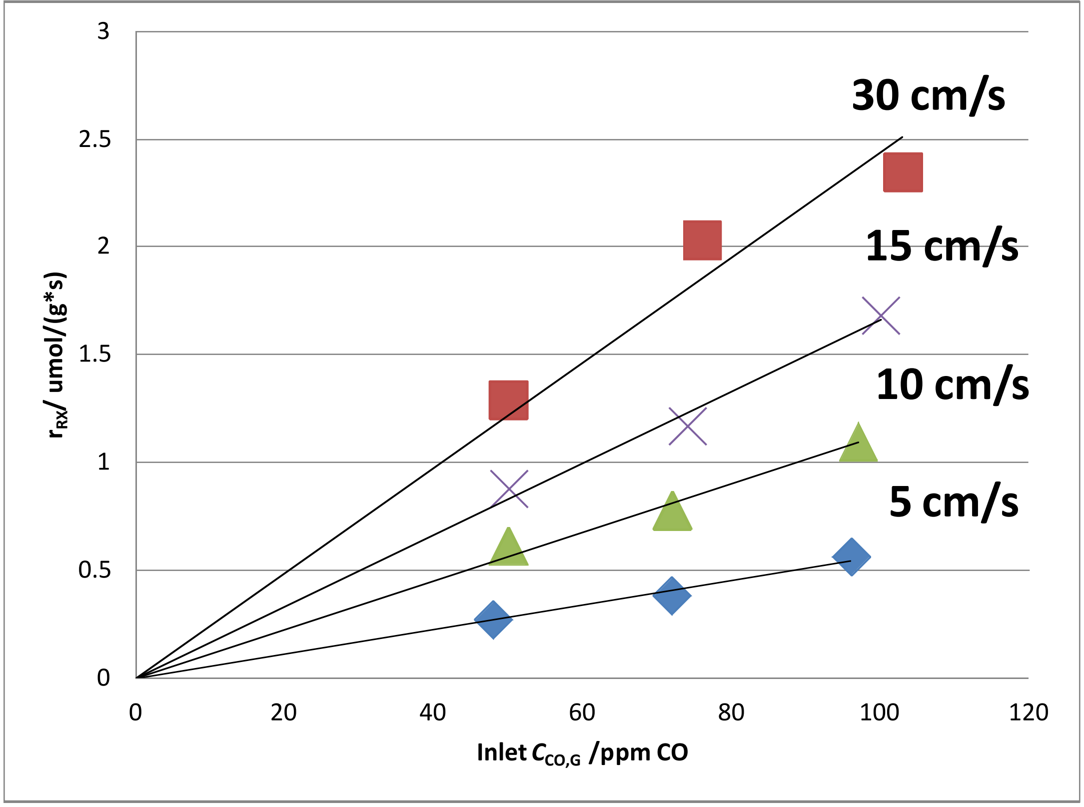

To solve for k_c Figure 5-6 was constructed. It is found k_c vs. $u^{1/2}$ does indeed give a straight line with an excellent coefficient of determination of 0.99. The data also agrees reasonably well with the predicted values from the Thones-Kramer correlation at higher face velocities. As the face decreases, however, the agreement fails jumping from a 13% error at 10 cm/s to a 59% error at 5 cm/s. The Thoens-Kramer correlation does not support Re numbers this low, so some divergence is expected. The equation :

Equation 5-46:

$$k_c = 0.0381(m/s)^{1/2}u^{1/2} - 0.0077(m/s)$$

offers reliable mass transfer prediction based on the superficial velocity of the system.

Figure 5-6: k_c vs. $u^{1/2}$. The excellent fit to a straight line validates the applicability of the Thoenes-Kramer correlation.

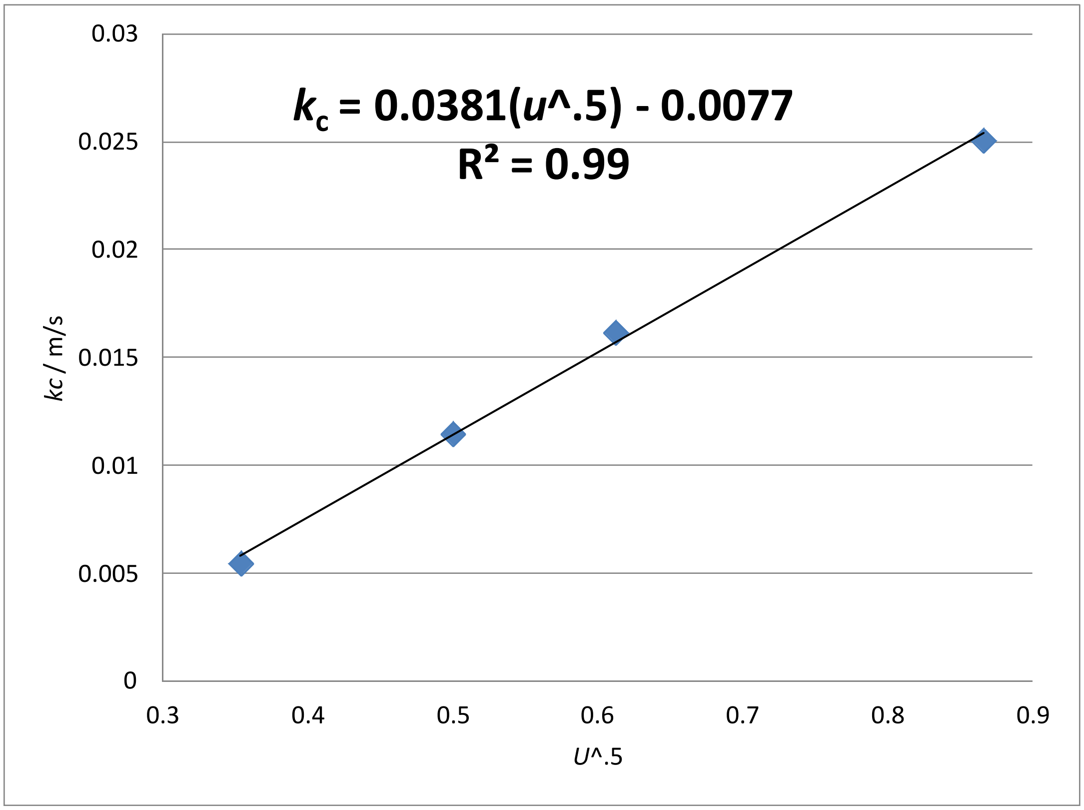

Table 5-4: Experimentally determined and calculated k_C are compared. k_c calculated is determined from the Thoenes-Kramer correlation.

u / cm/s	k_c Exp. / m/s	k_c Calc. / m/s	Error
5	0.0055	0.00873	-59%
10	0.0115	0.013	-13%
15	0.0162	0.0168	-4%
30	0.0251	0.0253	-1%

The results of the second step are found in Figure 5-7. The sum squared error for all of the points is 1.64. There is some scatter, but simulated data does capture the drop off above 150 ppm to 200 ppm and the settling of r_{RX} around one which is dominated by r_4 as the concentration increases. The values fitted are $S_{CO,0}$ of 0.00208. This is much lower than the literature values for CO adsorption on SiO_2. This could be due to unique structural difference in the Pt on CeO_2. k_3 is 3990 $cm^3/(mol \cdot s)$ for the undiluted catalyst. k_4 was found to be a

Figure 5-7: All of the data 25 ppm and higher $C_{CO,G}$ at 10 cm/s, 15 cm/s and 30 cm/s. ◆ are experimental points and 🟥 simulated. T: 26°C; RH: 60%; wt: 0.02 – 0.05 g; Conversion < 10%. The shape is well represented with a sum squared error of 1.64 for all points.

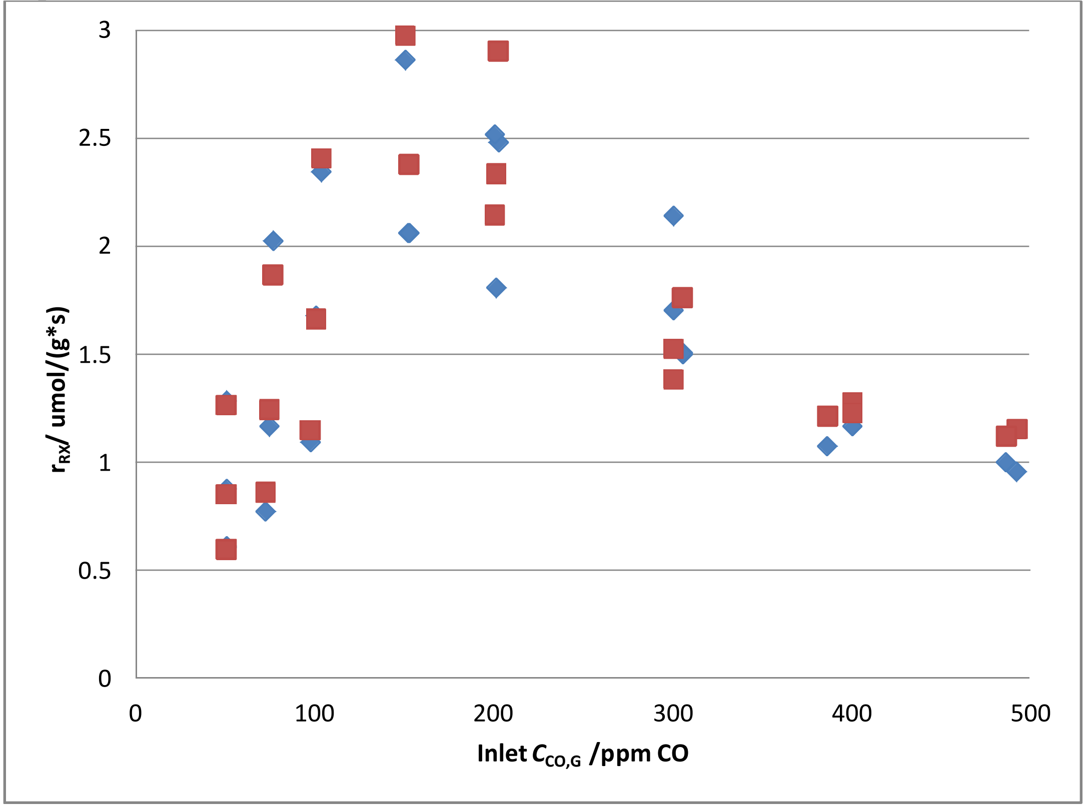

similar 3404 $cm^3/(mol\cdot s)$. The shape of the drop off around 200 ppm is much slower than expected from Figure 5-3. It does however, begin to level off as expected around 400 and 500 ppm while still gently sloping downward as $C_{CO,G}$ increases. The r_{RX} rate will never completely go to zero because r_4 can function with a Pt surface entirely covered by CO.

The results of step 3 can be seen in Figure 5-8. The simulated results produce a sigmodal rise in r_{RX} as the RH increases. It fails to capture the eccentricities of the data, but still capture the shape very closely. The simulated points drop to 0 at low RH, below 15%. The actual data is much more gradual. The simulation overestimates data at the high range of RH. This could be due to water beginning to clog the pores of the catalyst. There is no mechanism in the model to capture this. The Pt-CeO_2 on SiO_2 catalyst is extremely water sensitive. Estimating the local active site environment, by assuming the SiO_2 will drive the water adsorption provides a good fit to the experimental data.

Figure 5-8: r_{RX} vs. RH for $C_{CO,G}$ =300 ppm. ◆ are experimental points and ■ simulated. T: 26°C; RH: 60%; wt: 0.02 – 0.05 g; Conversion < 10%.

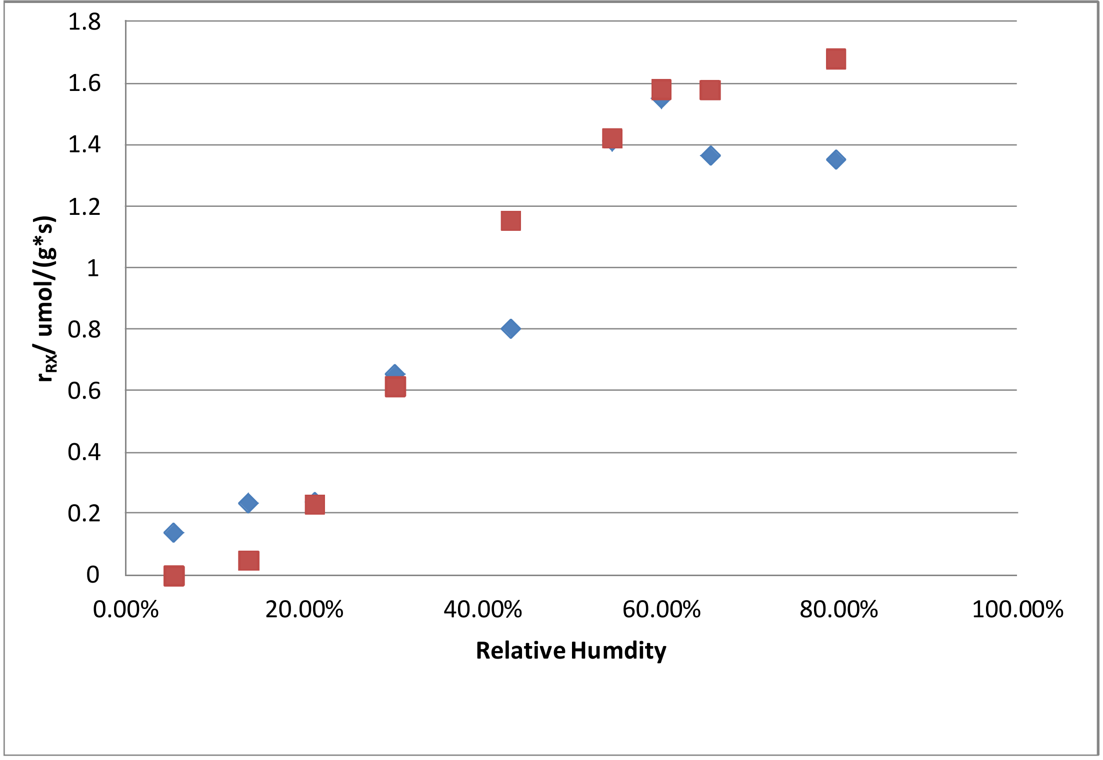

k_5 is found to be 8200 cm^3/(mol·s) and n is 3. $C_{O,CE,Max}$ is 5e-6 mol/cm^3. This result can be compared with the total surface Pt concentration of 4.12e-5 mol/cm^3 of the undiluted bed. The ratio of O$_{CE}$ sites that can donate to total surface Pt is 12%. This is a very reasonable number. If the O available to react

The final step is to solve for all of the activation energies: Ea_3, Ea_4, Ea_5. Figure 5-9 shows the fit for all points at 30 °C, 40 °C and 50 °C. The 30 °C points rise very slowly until they reach their peak at 2 μmol/(g·s). The hotter the *T*, the more abrupt the change from low reactivity to high. At low RH all of the points cluster together. At 33% RH 40 °C sharply rises in reactivity to depart from the 30 °C line. The 50 °C line departs at only 22% RH. This is a very low water content. The transfer of oxygen from must not be as important as the

Figure 5-9 r_{RX} vs. RH for $C_{CO,G}$ =300 ppm at 3 different *T*'s. ■, ▲ and ● are experimental points at 30 °C, 40 °C and 50 °C respectively. ■, ▲ and ● are simulated points at 30 °C, 40 °C and 50 °C respectively. wt: 0.02 – 0.05 g; Conversion < 10%.

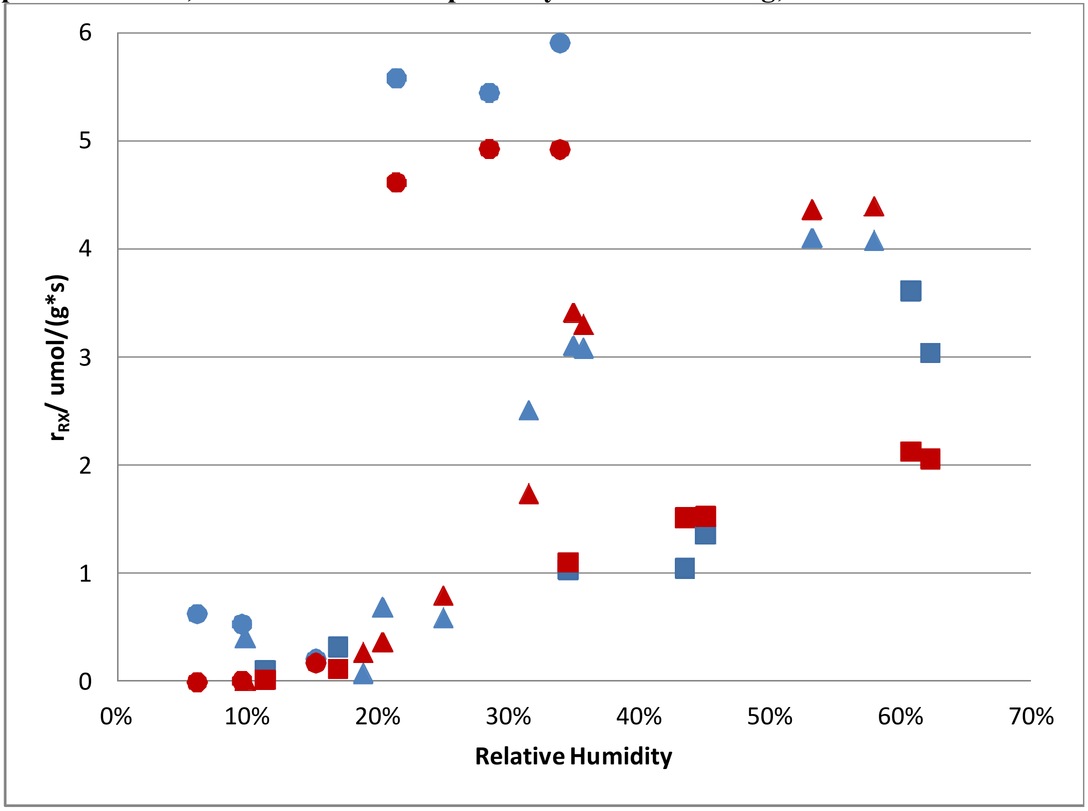

temperature rises, or the increased temperatures speed of r_5 more than the loss of water slows it down.

The activation energy for the reaction between O and CO adsorbed on Pt is 19.7 kJ/mol. Ea_4 was found to be 89.4 kJ/mol while Ea_5 is only 1.1 kJ/mol. The side reaction between CO adsorbed on Pt and the O donated by the CeO_2 is extremely temperature sensitive. This reaction, r_4, is what allows r_3 to have any O to react at all on the surface. Thus, r_4 increasing so rapidly with temperature has a pronounced temperature affect on r_3. This is contrasted with the low value of Ea_5. r_5 is driven by water content in the solid phase which has its own temperature dependence built in via the adsorption potential in Equation 5-16. The extremely low value of 1.1 kJ/mol could mean the adsorption potential is too temperature sensitive and, when it is combined in r_5, the activation energy is left to compensates, so it reaches a much smaller value than its true value. At 40°C and 50 °C below 10% RH the r_{RX} experimental data actually begins to rise. This is not captured at all in the model. It is not understood why this happens. The water may suppress a reaction pathway which is only

Figure 5-10: The Objective function, ◆ , is plotted with Ea_3, Ea_4 and Ea_5 represented by ■ , ▲, ● respectively.

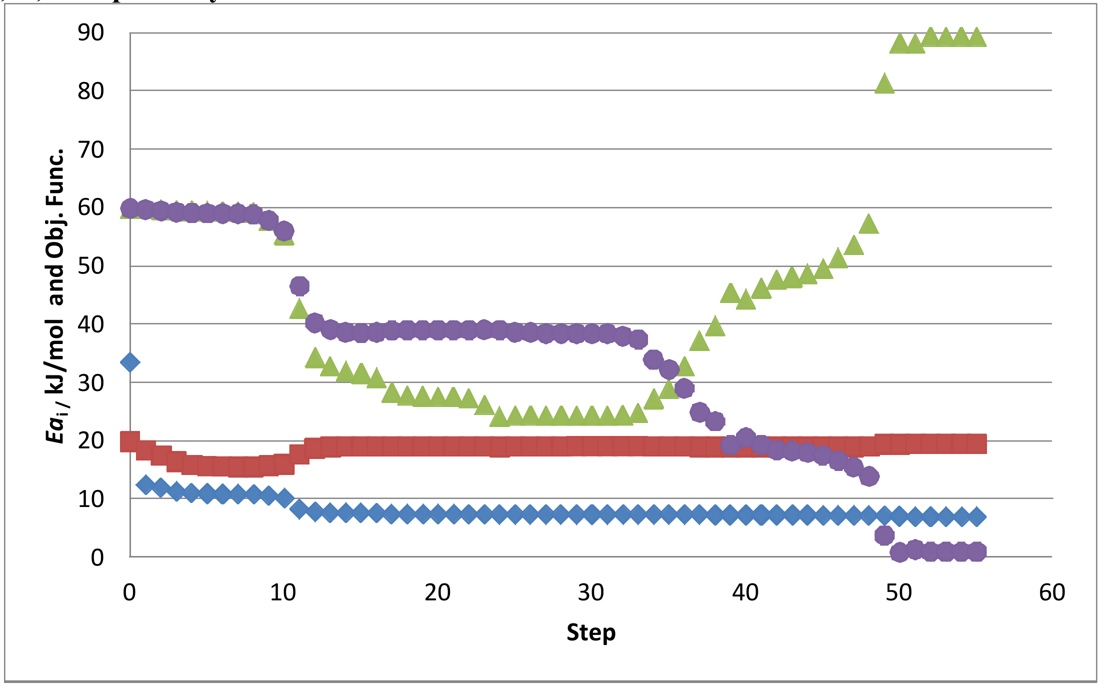

available at high temperature.

Figure 5-10 charts the progress of the solver as it minimizes the sum squared error between the experimental and simulated data. The activation energies Ea_4 and Ea_5 start at very different values than where they end up. Ea_5 begins all the way at 60 kJ/mol along with Ea_4. The two track each other's changes while Ea_3 grows. Around step 36, however, Ea_5 begins a steep drop that happens simultaneously as Ea_4 begins to rise. There is not much change in the objective function at this point, despite large changes in Ea_4 and Ea_5. The objective function is made up of a number of points that are not changing during this time mostly concentrated in the low RH range. These points add to the value of the objective

Figure 5-11: Predicted r_{RX} vs. Actual r_{RX}. The center black line is represents a perfect match. There are 56 data points which are used to predict 10 parameters.

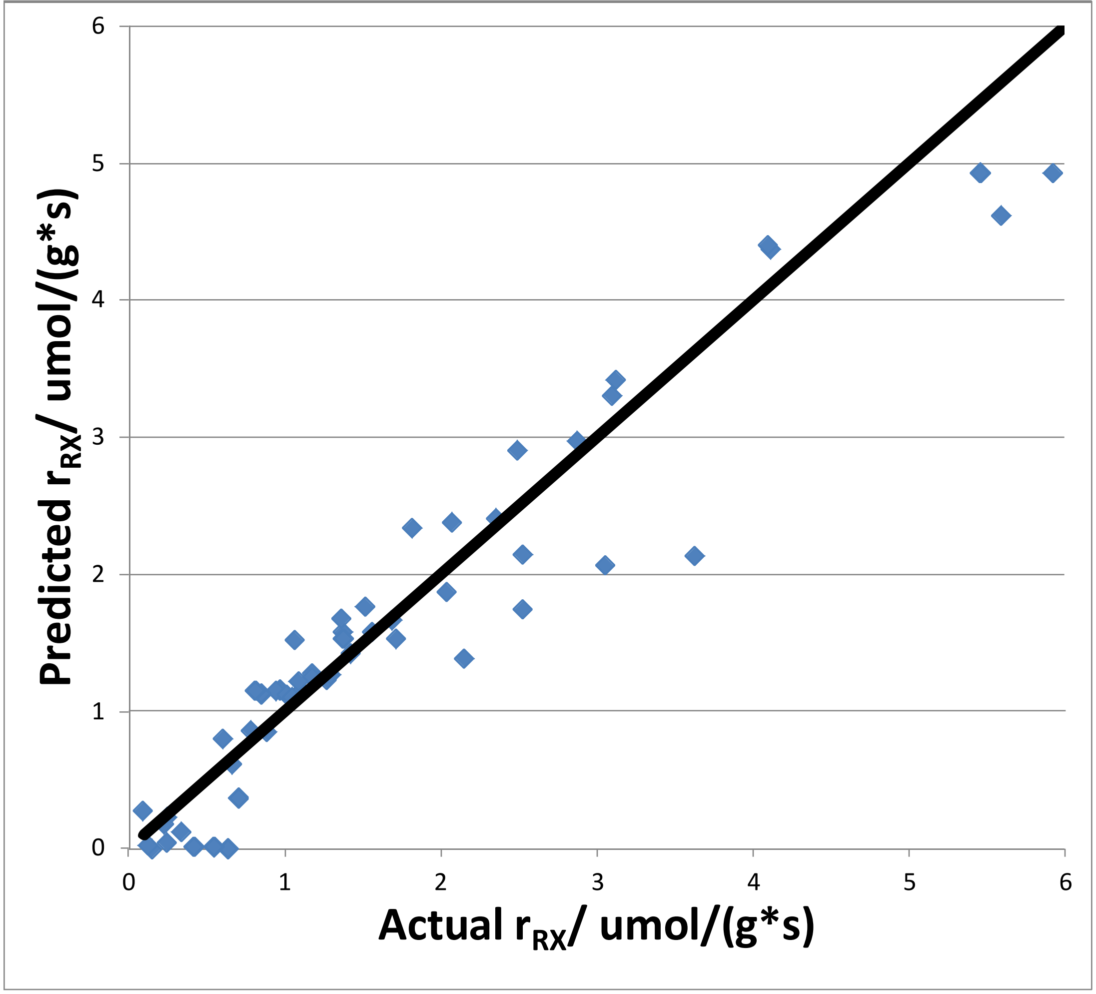

function making the change, from points more sensitive to changes in Ea_4 and Ea_5, appear small.

Figure 5-11 displays the predicted vs. actual r_{RX} for all data points. The 56 data points taken result in a coefficient of determination of 0.91. The fit seems to under predict at the high and low end. The very low r_{RX}'s are primarily taken at very low RH. There is the rise in reactivity at 40 °C and 50 °C to blame. However, the model predicts a much steeper drop in activity than is observed experimentally as seen at the low end of Figure 5-8. This could be because n, the order of reaction for water in r_5 is too high. n is constrained to only whole numbers in the solver. The value might lie between 2 and 3; different water based complexes could be responsible for forming the bridge between CeO_2 and Pt. The under prediction at the high end could be due to reliance on Equation 5-24 and the correlation that k_c scales with

Table 5-5: All values for fitted parameters along with the coefficient of determination. The volume bases of k_i and $C_{O,CE,Max}$ are all of an undiluted packed bed. The parameters were derived from a four step optimization process.

Parameter	Value
k_c / m/s	0.0381(u^.5) - 0.0077
k_3 / cm^3/(mol·s)	3990
k_4 / cm^3/(mol·s)	3404
$S_{CO,0}$	.00208
k_5 cm^3/(mol·s)	8500
$C_{O,CE,Max}$/ mol/cm^3	5e-6
n	3
Ea_3 / kJ/mol	19.7
Ea_4/ kJ/mol	89.4
Ea_5/ kJ/mol	1.16
R^2	0.91

$T^{11/12}$. All the fitted parameters and coefficient of determination are found in Table 5-5.

5.6 Conclusions

A detailed multi-step surface reaction model was developed to aid in the understanding of CO oxidation in a packed bed. The differential reactor mode all the tests were performed in freed the analysis of non-isothermal operation. This greatly simplified a complex task. The surface coverage based model was able to capture the changes in reactivity driven by face velocity, concentration, humidity and temperature. All variables are interlocked and non-linearly related, which necessitated the use of a robust non-linear solver.

The reaction data is not as sharp as expected which led to $S_{\mathrm{CO},0}$ as a free fitted parameter. This value is much lower than expected. $C_{\mathrm{O,CE,Max}}$ was found to be a reasonable 12% of total surface Pt in the catalyst. It is believed that a better catalyst would increase the shared border between the Pt and CeO_2.

It is the intention this model be used to understand how the various surface reactions on the catalyst surface influence the overall kinetics and interplay between heat transfer and reaction kinetics in a packed bed under the influence of a negative order reaction. The ladder is the subject of Chapter 6, where this model is used to test different thermal conductivities and compare them with real world tests.

5.7 Catalyst Poisoning and Regeneration

5.7.1 Introduction

With a negative order reaction kinetics the reactant also functions as a poison. Great care must be taken so as not to confuse this poisoning with an environmental poison such as sulfur or a hydrocarbon mixture. Both can look extremely similar when viewing kinetic data. A deactivation could be slow or fast for each.

The Pt-CeO_2 on SiO_2 catalyst is tested in three different air streams. Two with contaminants and one clean air stream. The two with contaminants are divided into a filtered stream, with an off the shelf oil filter, and with no filter at all. The rates of deactivation are compared and ability to regenerate tested. It is important that the catalyst be proven regenerable even when exposed to suboptimal conditions. These sorts of conditions will be encountered in the real world, and with a Pt based catalyst, one use is not enough. The poisoning on the catalyst is shown to be reversible by flowing N_2 over the catalyst at 200 °C.

5.7.2 Experimental

Activity measurements were performed with the CO oxidation apparatus described in section 3.2.1 Activity measurement Apparatus. The catalyst used in all tests was the 4% Pt-22%CeO_2 on SiO_2. An in depth procedure can be found in section 3.2.8 Catalyst Recipe.

The clean air stream is attained from compressed air, breathing quality purchased from Airgas. The uncharacterized dirty air stream is left unfiltered in some tests and filter with a Motorguard M30 air filter in others. To test the regenerative capabilities of the catalyst, after each run the catalyst is removed from the test apparatus and heated to 200 °C in flowing N_2 in a tube furnace.

5.7.1 Results and Discussion

After the catalyst was aged for 22 h in the same flowing air as the catalyst exposed to CO, it picked up right where the fresh catalyst left off as seen in Figure 5-12. The CO concentrations were essentially identical, and the curves fell one on top of the other. This means the catalyst is undergoing a separate poisoning issue than just CO poisoning. This sort of problem is not evident unless long 12+ hour tests are conducted. The poisoning could be due to too much water adsorption on the SiO_2 surface possibly causing poor blockage, or possible PtO formation on the Pt surface shutting down active sites. There have also been studies that show carbonate formation on the catalyst blocking active sites [131]. However, a simple test between clean air, dirty yet filtered air and dirty unfiltered air will tell the difference.

Figure 5-12: The effect of a dirty air stream with a filter. The fresh catalyst slowly deactivates in the dirty stream and is then compared to catalyst which was exposed to the air and no CO. This line is then shifted and is found to lay directly over that of the fresh catalyst. Catalysts: 4% Pt- 22% CeO_2 on SiO_2. Wt: 0.2 g +0.8g Inert; $C_{CO,I}$ = 300 ppm; v_z = 15 cm/s; T = 26 °C; RH = 60%; Tube ID = .625”

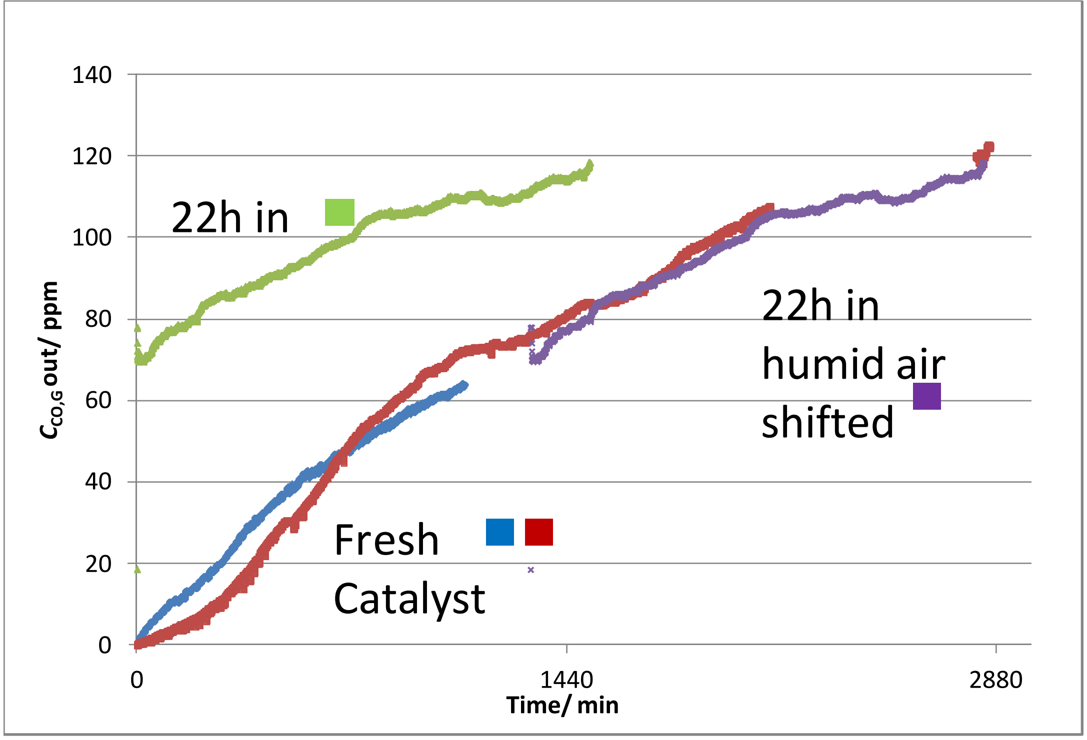

The results of testing the catalyst in three different environments are seen in Figure 5-13. The filter greatly slows the catalyst poisoning rate. The activity when tested without any filter immediately deactivates. The filter manages to keep the conversion of CO above 50% for over 6 days. This is very respectable, and if need be, the conversion can be kept above 90% for 1 day. The catalyst in the clean air stream shows no signs of deactivation even after over 6 days on stream. To further illustrate the detriment of oil based poisons to the catalyst, the clean and filtered air are compared at high conversion. However unlike Figure 5-13, the clean air catalyst is adjusted to be less than complete conversion. This will allow for an actual look into how much of a detriment the poisons are. The results are in Figure 5-14. With half the catalyst the conversion actually increases from 90% to 99%. The catalyst is very susceptible to hydrocarbon poisoning.

Figure 5-13: The catalyst is tested in three different environments. Two of which contain dirty uncharacterized air with and without a filter. The last is clean air with no contamination. Catalysts: 4% Pt- 22% CeO_2 on SiO_2. Wt: 0.2 g +0.8g Inert; $C_{CO,I}$ = 300 ppm; v_z = 15 cm/s; T = 26 °C; RH = 60%; Tube ID = .625

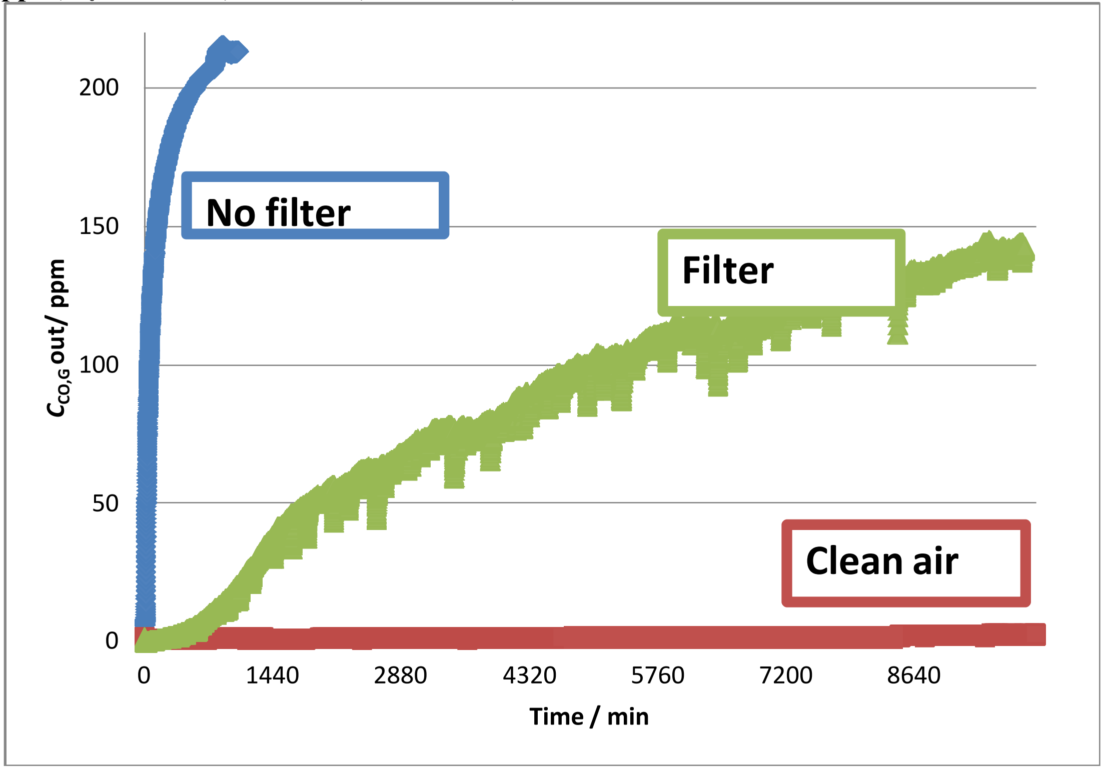

Figure 5-14: The activity of 0.2 g catalyst with dirty air compared to 0.1g catalyst in clean air. Catalysts: 4% Pt- 22% CeO_2 on SiO_2. Wt: 0.2 g or 0.1g +0.8g Inert; $C_{CO,I}$ = 300 ppm; v_z = 15 cm/s; T = 26 °C; RH = 60%; Tube ID = .625

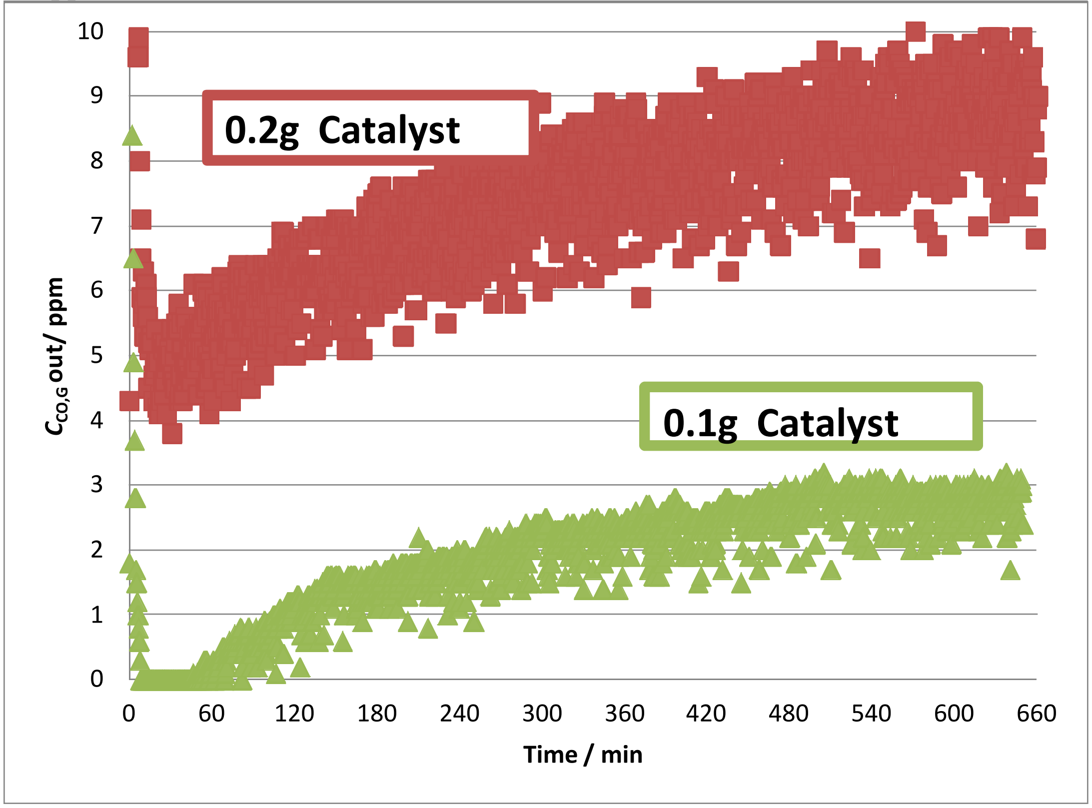

To further illustrate the point, the catalyst is tested at 1000 ppm with no filter and with clean air. The result is found in Figure 5-15. The unfiltered air loses its activity in the first hour. By 1.5 h in the conversion is at 90%.; 3h it is 80% and by 8h it is 50%. The experiment is stopped at 600 ppm to avoid damage to the CO chemical sensor. The clean air, by contrast never exceeds 1ppm. Better than 99% conversion is maintained over 3.5 days.

Figure 5-15: Activity loss from unfiltered air contrasted against clean air. Catalysts: 4% Pt- 22% CeO_2 on SiO_2. Wt: 0.75 g; $C_{CO,I}$ = 1000 ppm; v_z = 15 cm/s; T = 26 °C; RH = 60%; Tube ID = .625

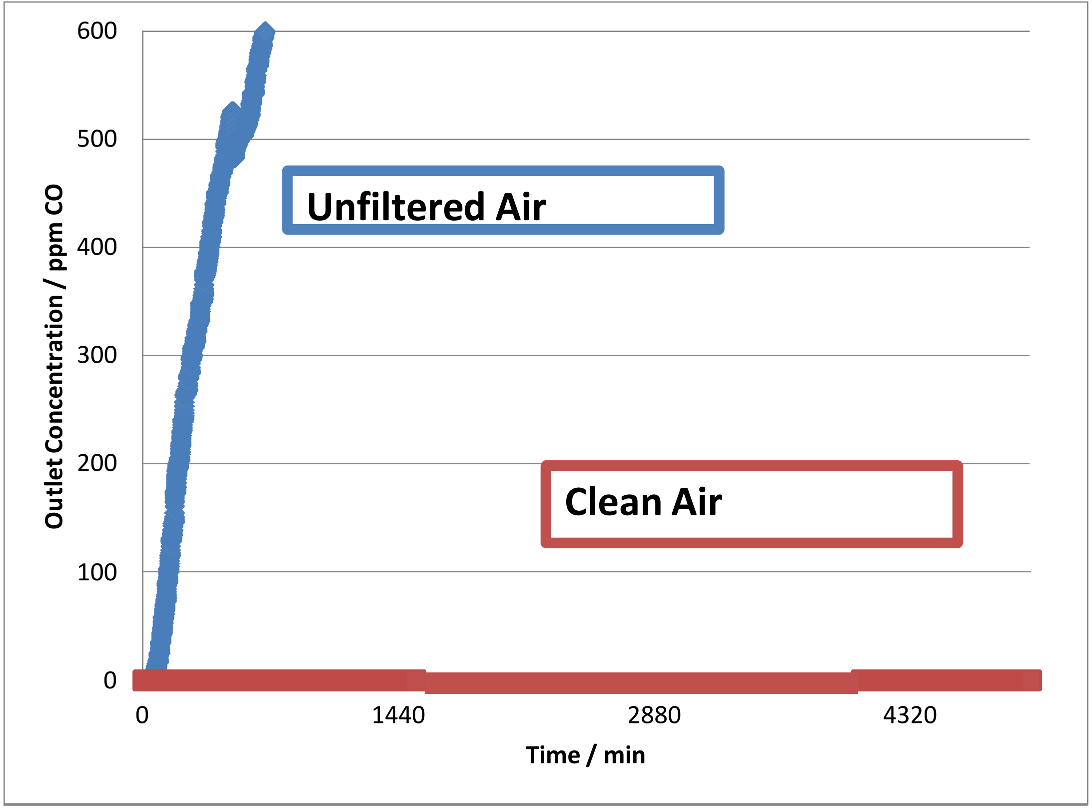

The poisoning of the catalyst by containments in the air requires the catalyst to be regenerable. Pt is a very expensive metal and a onetime use catalyst would not be economical for most applications. Figure 5-16 shows the results of heating the catalyst to 200 °C in flowing N_2 for 1 hour in between runs with the filtered by dirty air. The catalyst appears to be able to fully regenerate. After 6 cycles the outlet concentration hovers around 100 ppm with the best being cycle 3 at 90 ppm and the worst being cycle 5 at 140 ppm.

Figure 5-16: $C_{CO,G}$ vs. t for same catalyst run 6 times after regeneration in N_2 at 200 °C for 1 h. Catalysts: 4% Pt- 22% CeO_2 on SiO_2. Wt: 0.2 g +0.8g Inert; $C_{CO,I}$ = 400 ppm; v_z = 15 cm/s; T_I = 25 °C; RH = 60%; Tube ID = .625”

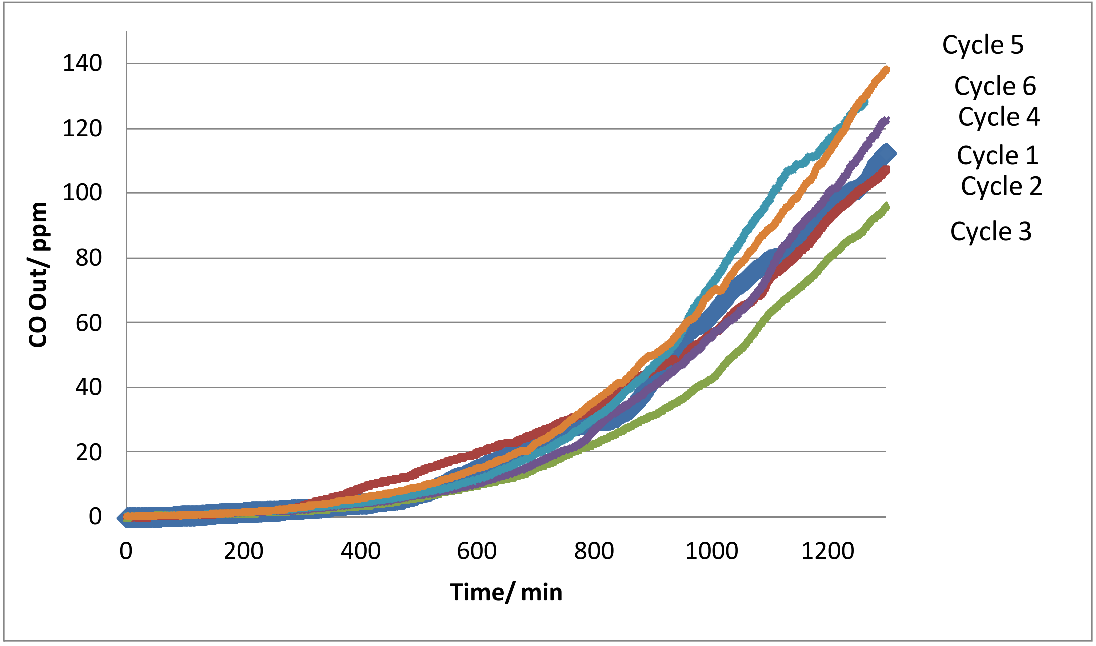

5.7.2 Conclusion

The catalyst is poisoned in humid air with uncharacterized hydrocarbon contamination, both filtered and unfiltered, which is them compared to a clean air stream. This environmental poisoning must be separated from the effect of CO poisoning. The introduction of a filter does significantly increase the longevity of the catalyst. However, the clean air catalysts show no signs of deactivation.

The environmental poisoning was tested in two ways. The first was without any CO in the incoming gas stream for the first 22 hours. This was compared with the catalyst which had been exposed the entire time. They both show the exact same loss in activity. This indicates all of the activity loss is from the contaminates in the gas stream and not the CO. The second was to test the activity with a filter in a dirty air stream, without a filter and with clean air. There was no activity loss when the catalyst was exposed to clean air. The filter did help, but significant deactivation still took place.

In the previous tests the clean air catalyst remained above 99% conversion the entire time. To test the extent of the poisoning, the amount of catalyst was cut in half in the clean air stream. The catalyst still managed 99% conversion. This was contrasted with double the catalyst in the dirty air stream which showed 90% conversion. Once more, the catalyst was tested, but this time with 1000 ppm CO in the challenge gas. The deactivation took place incredibly fast with still no deactivation from the clean air stream. These tests were needed to ensure that there is no confusion as to what activity loss is due to CO covering the Pt surface and what loss is due to air contaminants.

The catalyst is, however, able to regenerate in flowing N_2, indicating the effects of the poisoning are reversible. The catalyst was cycled 6 times with a similar rate of activity loss each time. This is good news for real world use of the catalyst. The air encountered in the real world, be it on a race track or aircraft carrier, is often dirty with unexpected additives. The catalyst, being Pt based, can be very expensive and needs to be able to be reused after being in a punishing environment.

Chapter 6 : Effect of Temperature and Altering Effective Thermal Conductivity

6.1 Introduction

It is desired to understand the catalytic oxidation of CO in qualitative, as well as quantitative ways. Both strategies are pursued in this chapter. The negative reaction order of CO and exothermic nature make a very complex reaction system. This is complicated further by the presence of water in the feed gas. The Pt-CeO_2 on SiO_2 catalyst thrives in water, but the adsorption and desorption of water on the catalyst must be taken into account. The transfer of heat from the back of the catalytic packed bed to the front will be studied. It is the hypothesis of the author that the back diffusion of heat, along with negative reaction kinetics, is responsible for increasing catalytic activity of the entire packed bed.

To test the hypothesis, first the affect of bed depth on the reaction rate is examined. If there is no communication against the flow of gas, then a short bed should deactivate at the same time as a longer bed at the depth of the shorter bed. In order to “look” into a longer bed and see what it is doing in the middle, a reactor is constructed with 8 thermocouples positioned axially down the reactor. A closer look at the reactor can be found in section3.2.7 Axial Temperature Profile Measurement Apparatus and Heater. The exothermic nature of the reaction can be exploited to provide a look at catalyst activity by measuring temperature at different bed depths. The higher the temperature, the higher the activity in that slice of the reactor.

In another experiment a heater is placed at the back of the bed. The object of the heater is to heat the rear of a deactivated packed bed. A small amount of heat should be enough to increase the activity of the bed and send a wave of heat against the flow of fluid in the reactor.

To quantitatively examine the affect of k_{eff} on catalytic activity, k_{eff} must be measured directly and compared with literature correlations. k_{eff} is measured for both a packed bed and microfibrous media by placing a heater at the end of the reactor. The heater creates a temperature difference that is measured, and k_{eff} is fit with a simple heat transfer model

Finally, k_{eff} is altered by changing the carrier gas of the system. Up until this point, N_2 has been the only carrier gas used. He, Ar and Kr are all used to vary k_{eff}. The experiments are carried out at high humidity, and the axial temperature profile is measured in each case. The activity measurements done with the carrier gases with better thermal conductivity should perform better. Microfibrous media is also compared to a packed bed. The model developed in Chapter 5 is put to use to understand the sometimes bizarre behavior of CO oxidation in humid environments.

6.2 Qualitative Understanding of Heat Transfer by Altering Bed Depth and Heating the Back of the Packed Bed

6.2.1 Experimental

Activity measurements were performed with the CO oxidation apparatus described in section 3.2.1 Activity measurement Apparatus. The catalyst used in all tests was the 4% Pt-22%CeO_2 on SiO_2. An in depth procedure can be found in section 3.2.8 Catalyst Recipe

To log axial temperature data, the reactor outlined in Figure 3-2 was used. The reactor has 8, k-type thermocouples spaced 2.8 mm apart down the tube. The actual reactor is pictured in Figure 6-1. If no temperature profile was needed the simple 15.875 mm ID borosilicate glass reactor was used. The temperature reading from each thermocouple is data logged ever second by an Omega DAQ-5300 data logger. The heater in the rear of the bed is a nichrome wire wrapped torus. It is buried in the silica gel to keep it in place. Two wires run out of the reactor(the black wires seen in Figure 6-1 and to a power supply where a DC current is administered.

Figure 6-1: 15.875" ID reactor with 8 thermocouples positioned axially 2.8 mm apart. The thermocouples enter through a 1mm drilled hole above which sits a septum to seal the reactor.

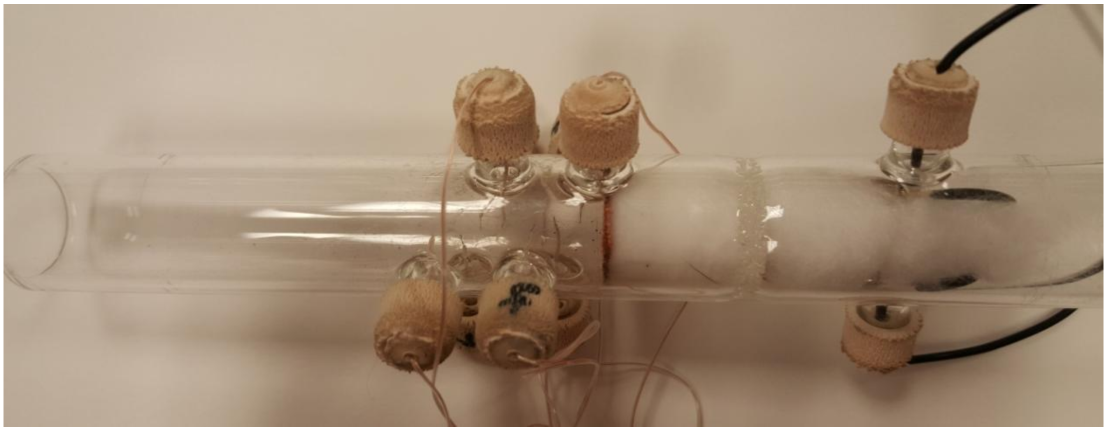

6.2.2 Theory

The high heat of reaction is responsible for igniting the bed at higher CO concentrations. The negative reaction order concentrates heat in the back of the bed. The heat, which is normally assumed to simply be convectively washed out of the back of the bed, is important to keep the catalyst layer ahead of it active. The axial thermal conductivity in the bed is responsible for moving the heat against the flow thus keeping the catalyst active. This is explored in more depth in section 2.3 Mechanistic Studies for CO oxidation. It is making the assumption that k_{eff} can be dropped from Equation 5-2. This would give:

Equation 6-1:

$$\rho C_p \frac{\partial T}{\partial t} = -\rho_f C_{pf} v_z \frac{\partial T}{\partial z} + \Delta H_{Rx} r_{Rx}(C,T)$$

The second part is the need to understand the contribution of D_{AX} as seen in Equation 5-1. When the equation is non-dimensionalized the reactor length becomes the characteristic length of the Peclet number. This is referred to as the Bodenstein number and is given by:

Equation 6-2:

$$\mathrm{Bo} = \frac{v_z L}{D_{ax}}$$

The Bodenstein number, Bo, can be neglected if it is greater than 100. For this system it is found to be 2000 for the shortest, 4.3 mm, bed used.

To test this hypothesis the axial temperature was measured down the reactor. If the front of the bed depends on heat from the back then the layers of catalyst should cool at different rates depending on how much catalyst is behind it. This is saying the first few mm of a long bed will stay active longer than the first few mm of a short bed. However, if no heat is transfer forward in the bed, the beginning of the long bed and the short bed should cool at the same rate.

Another way to get a qualitative idea is put a heater in the back of a poisoned bed and see if a small amount of heat can ignite the forward portions of the catalyst. If the reaction ignites with a small amount of heat from the back of the bed then the up-flow of heat is indeed important. Figure 6-2 depicts the catalyst bed heating up from the rear of reactor and that heat spreading to the front after a small amount of energy is run through the nicrome wire buried just after the catalytic bed. The bed is first poisoned with 3000 ppm CO. After which, the CO is lowered 1100 ppm and watched for 15 minutes to see if the bed will reignite on its

Figure 6-2: Depiction of the reactor proceeding from an extinguished initial state to an active state with the application of a small amount of heat to the back of the catalyst bed.

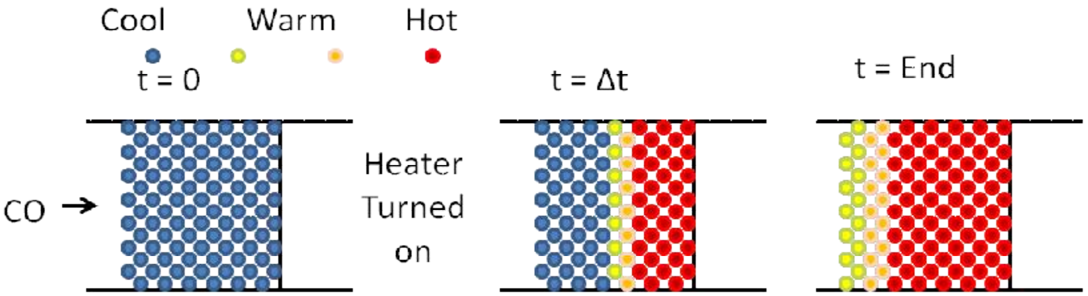

own. The heat in the back of the bed is then turned on such that a 3 °C rise is felt at the end of the catalyst bed

6.2.3 Results and Discussion

The temperature profile is presented for a bed 24.1 mm long. The first 15.5 mm is measured by 6 thermocouples. The thermocouples measure the bed temperature at 4.3mm,

Figure 6-3: Change in ΔT with time along the first 15.5 mm of reactor Bed. 4% Pt-22%CeO2 on SiO2 60%RH ; FV 15 cm/s; Inlet CO: 1090 ppm; T:25 C; Tube ID: 0.625"; RH: 60%; 0.74g Cat. to 2g w/ inert

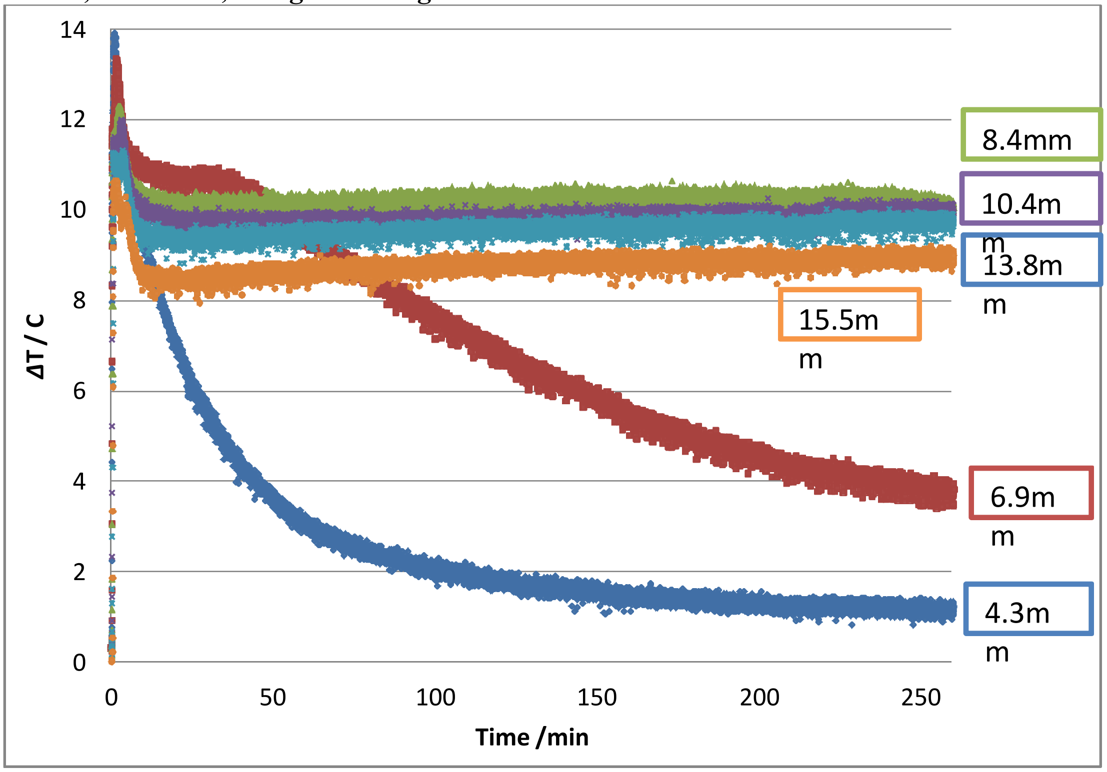

6.9mm 8.4mm, 10.4mm, 13.8mm and 15.5mm. The inlet concentration is 1090 ppm flowing at 15 cm/s. The 1090 ppm leads to a 10.5 °C adiabatic heat rise. Figure 6-3 shows the temperature profile with time.

Initially all points in the reactor jump above the adiabatic temperature rise. This is due to adsorption of water in the SiO_2. The adsorption of water on SiO_2 is explored in more detail in section 5.3 CO Oxidation Model. The first layer poisons almost immediately. The second layer at 6.9mm holds out for about 45 minutes until it starts to decline. The following layers from 8.4mm to 15.5mm show no signs of decline. The other feature to view from Figure 6-3 is the decline in centerline temperature from 6.9mm 8.4mm to 15.5mm. This indicates the reactor is not perfectly adiabatic. After the catalyst activity stabilizes the drop in temperature from 8.4mm to 15.5 mm is about 2 °C. This also indicates a narrow reaction zone between 6.9mm and 8.4mm. In fact, about 4.5 h in the run there is a 6 °C rise in the bed. This indicates 60% of the conversion takes place in this 2.8mm section of the bed. The outlet concentration is 0 for the duration of the test.

Figure 6-4 illustrates the difference in temperature and concentration for each cut vs. the full 24.1mm packed bed. The left is always the difference between the measured inlet temperature, T_{in} and T at the thermocouple, so:

Equation 6-3:

$$\Delta T = T - T_{in}$$

The right side has the CO concentration at the outlet for the shorter bed measured by the electrochemical sensor. It also displays the Outlet concentration arrived at through the energy balance using the heat of reaction and assuming an adiabatic reactor. The adiabatic temperature rise is

Equation 6-4:

$$\Delta T_{Adb} = \frac{C_{CO,I} \cdot X \cdot \Delta H_{RX}}{\rho C_P}$$

where $C_{CO,I}$ is the CO concentration at the inlet, X is the conversion, ΔH_{RX} the heat of reaction, ρ the density and C_P the constant pressure heat capacity. If the reactor is considered adiabatic then $\Delta T = \Delta T_{Adb}$ and after rearranging Equation 6-4 X can be solved for. The outlet concentration of CO arrived at via Equation 6-4, is

Equation 6-5:

$$C_{CO,C} = C_{CO,I} \cdot X$$

where $C_{CO,C}$ is the calculated value of the concentration from ΔT .

In Figure 6-4 the 4.3 mm bed poisons very quickly. The temperature for the short bed drops almost immediately falling to only ΔT = 4 °C with in the first 20 minutes. The first 4.3mm of the 24.1mm bed also deactivates quickly but not quite as fast. It reaches the same 4°C ΔT in 40 minutes. The rate of catalyst deactivation is double in the shorter bed. This is the first indication that heat from the layers behind the first 4.3 mm is important. Although, the rate of poisoning is slower on the longer bed; they both begin to decline at about the same time. $C_{CO,C}$ for the 4.3mm bed tracks very closely with that measured from the electrochemical sensor, $C_{CO,E}$. This lends some confidence to the method. $C_{CO,C}$ for the longer bed lags behind slightly, as one would expect.

Figure 6-4: On the left is measured ΔT vs. t for the shortened bed, ▬ ▬, compared to the 24.1 mm bed, ▬▬. On the right, CO detected at the outlet of the shortened bed, ▪▪▪▪▪▪▪▪, $CO_{CO,C}$ for the short bed, ▬ ▬, and $CO_{CO,C}$ for the 24.1mm beds, ▬▬. The bed length increases down the figure. 4% Pt-22%CeO_2 on SiO_2; 60%RH ; *FV:* 15 cm/s; Inlet CO: 1090 ppm; T:25 C; Tube ID: 0.625"; RH: 60%

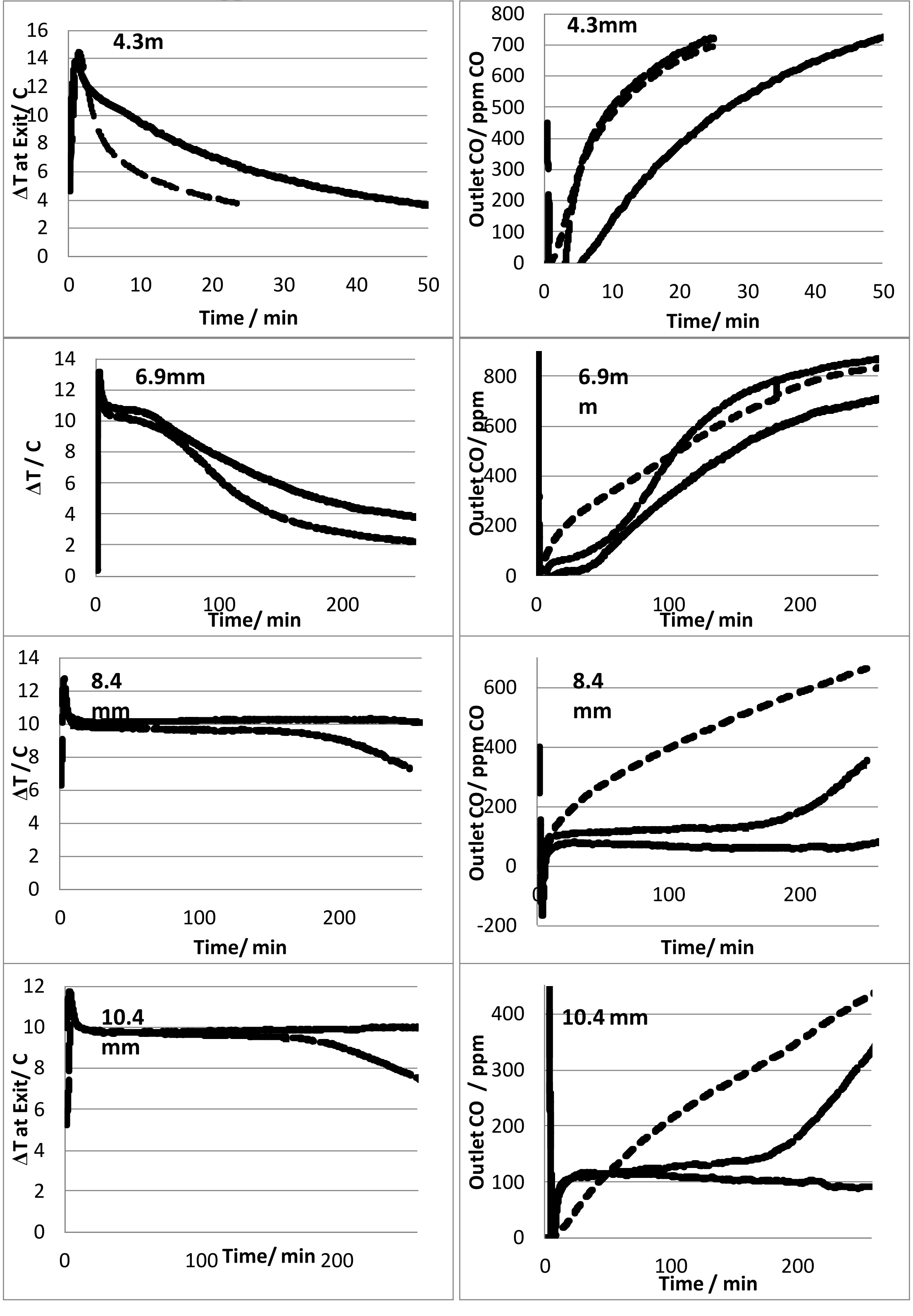

Behind the 4.3mm slice the next cut is made at 6.9mm. The same trend is seen here. The short bed poisons slightly faster than the longer bed. $C_{CO,C}$ lags behind $C_{CO,E}$ for the short bed. This could be due to water adsorption being the cause for some of the heat gained in the beginning.

The 8.4mm bed and the 10.4mm bed both show similar trends. The difference between the long and short bed are more dramatic here. The longer bed shows no signs of deactivation while each short bed begins to show a striking temperature drop around 175 minutes. The importance of the following layers is very important. It is the difference between a completely active bed and a bed which is poisoning at an accelerated rate. The only different between the two is the catalyst at the back, and the only way they communicate is though heat.

The Outlet Concentration of CO displays some interesting results. While the temperature $C_{CO,C}$ is very similar for each graph, $C_{CO,E}$ shows a large difference. The 8.4 mm bed reaches 500 ppm at 150 minutes; while the 10.4mm bed shows 275 ppm. The 10.4mm bed does perform better than the 8.4 mm bed; however, they appear the same when only $C_{CO,C}$ is viewed. In Figure 6-4 the 8.4 mm and 10.4 mm $C_{CO,C}$ jumps to 100 ppm to 150ppm respectively immediately. Figure 6-3 shows the loss of heat out of the sides of the reactor to explain the discrepancy. What we see in the 8.4 mm and 10.4 mm bed is the failure of the adiabatic assumption.

The next question is if a small amount of artificial heat at the back of the bed can bring a poisoned bed back to life.. Figure 6-5 shows the results of a 3 °C temperature rise at the end of the bed, 10.6 mm. At 15 minutes the heater is turned on. At 19 minutes into the experiment the knee is visible where the heater reached a 3°C change on the 10.6 mm line 16 minutes into the experiment. From that point, the rest of the heating done by the reaction itself and heat transfer itself. This heat is propagated backwards to the 8.45 mm thermocouple which registers a heat change of 3 °C. Further up the bed smaller deflections are detected.

This shows how important a small amount of heat can be and how sensitive CO oxidation is to temperature. There are two reasons for the sensitivity. In a first order reaction the decrease in reactants cause the reaction rate to slow. The reactants decrease at the same time the temperature increases. For a negative order reaction, the decrease in reactants and increases in temperature both cause and increase in reaction rate. This is what causes the bed to be so sensitive to a small amount of heat conducted from the back of the bed. The phenomenon is discussed in more detail in section 2.3.3 Effect of Temperature.

Figure 6-5: ΔT from inlet for various bed depths and $C_{CO,E}$ for entire bed. 4% Pt - 22%CeO$_2$ on SiO$_2$; 60%RH ; FV: 15 cm/s; Inlet CO: 1100 ppm; T:25° C; Tube ID: 0.625"; RH: 60%; 0.2g with .8g inert.

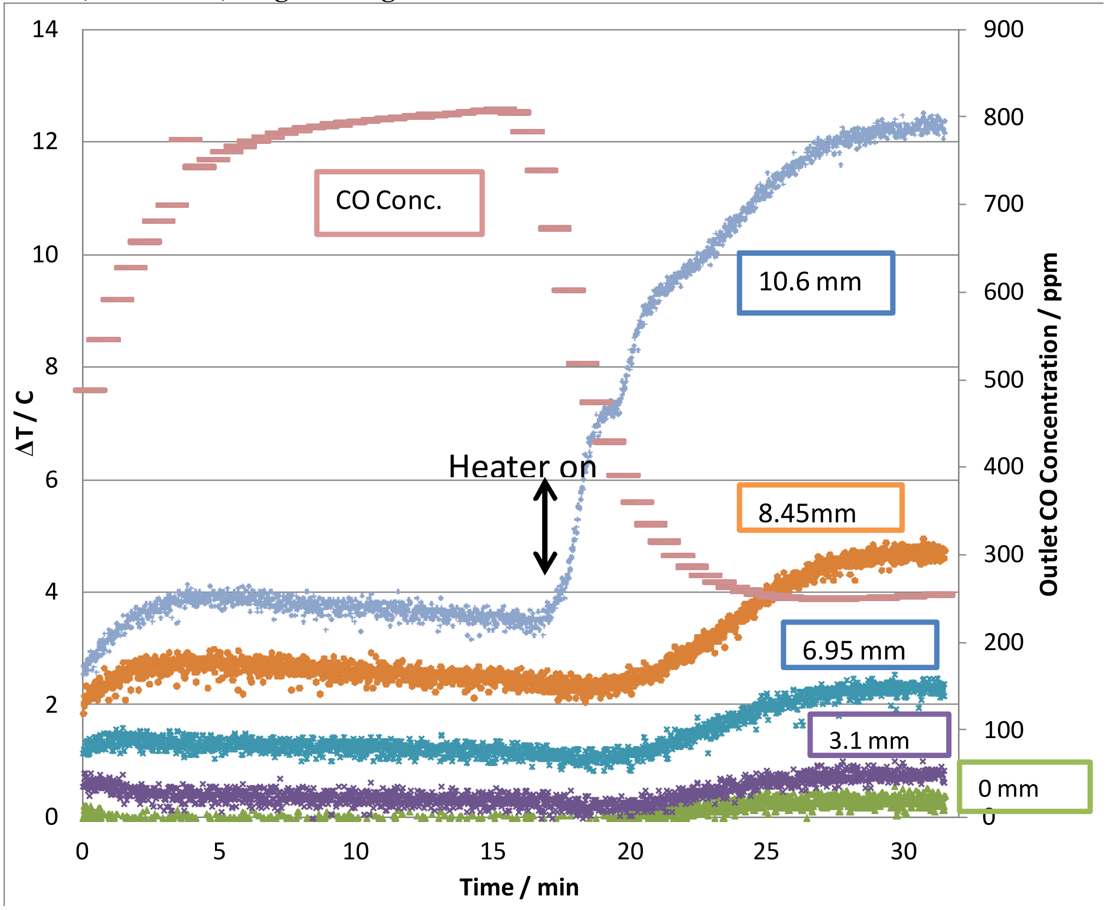

6.2.4 Conclusions

The qualitative understanding of a process is the first step to understanding it well enough to quantitatively model the process. It was hypothesized the heat from the back of the reactor is transported to the front via k_{eff}. This was tested in two ways.

The first was to compare the activity between a long 24 mm packed bed and progressively shorter beds all the way down to 4.3 mm. To measure the activity of the inside of the bed thermocouples were inserted to measure the heat rise and thus reaction rate inside the bed. It was found the shorter beds deactivate much faster than the same depth in the longer beds. Another way to say this is the first slices of a bed deactivate faster if there is no catalyst behind them In fact, when the bed depth reaches 8.4 mm the 24 mm bed showed no signs of deactivation. The 8.4 and 10.4 mm beds, however, did begin to deactivate. This indicates the heat from the back of the bed is important to the activity of the catalyst up stream. It is so important that it kept the catalyst active for the duration of the test.

The sensitivity of the reaction is seen when only a 3 °C rise in the very back of a deactivated bed is enough to ignite the catalyst. The overall conversion rises from 0% all the way to 77%. The CO oxidation reaction is very sensitive in specific regions. The reaction can change drastically to variations of CO concentration, face velocity, and in this work, bed depth and heating. The combination of negative order reaction kinetics, axial heat transfer, and heat generation allow the packed bed to communicate from back to front.

6.3 Experimentally Determined Axial Thermal Conductivity

6.3.1 Experimental

Activity measurements were performed with the CO oxidation apparatus described in section3.2.1 Activity measurement Apparatus. The catalyst used in all tests was the 4% Pt-22%CeO_2 on SiO_2. An in depth procedure can be found in section 3.2.8 Catalyst Recipe. The microfibrous media, MFM, was cut into 15.875 mm discs. The discs were then stacked one on the other until the desired bed depth was reached.

To log axial temperature data the reactor outlined in Figure 3-2 was used. The reactor has 8, k-type thermocouples spaced 2.8 mm apart down the tube. The actual reactor is pictured in Figure 6-1. If no temperature profile was needed the simple 15.875 mm ID borosilicate glass reactor was used. The temperature reading from each thermocouple is data logged ever second by an Omega DAQ-5300 data logger. The heater in the rear of the bed is a nichrome wire wrapped torus. It is buried in the silica gel to keep it in place. Two wires run out of the reactor(the black wires seen in Figure 6-1) and to a power supply where a DC current is administered.

6.3.2 Theory

After it was determined that k_{eff} was important in section 6.2 Qualitative Understanding of Heat Transfer by Altering Bed Depth and Heating the Back of the Packed Bed an independent measure of it was needed to get more accurate results. The energy balance in Equation 5-1: was expanded to two dimensions:

Equation 6-6:

$$\rho C_P \frac{\partial T}{\partial t} = k_{eff} \frac{\partial^2 T}{\partial z^2} + k_{reff} \frac{1}{r} \frac{\partial}{\partial r} r \frac{\partial T}{\partial r} - \rho_f C_{Pf} v_z \frac{\partial T}{\partial z}$$

Figure 6-6: Diagram of the reaction zone and reactor wall. The inside of the reactor is the zone circled by Boundary 1,2 and 3. It is then mirrored at the reactor centerline at *r*=0

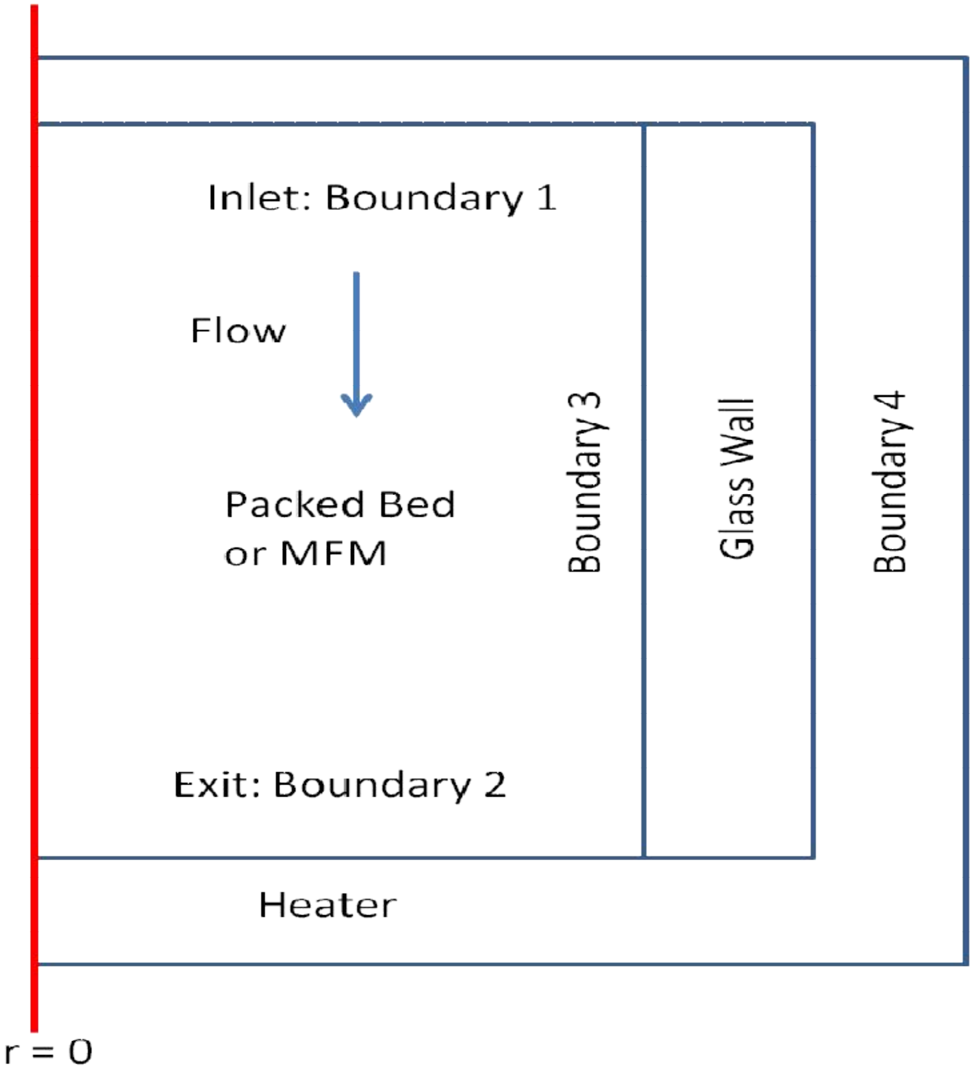

The only change is the second term of the right side. k_{reff} is the radial effective thermal conductivity.

The temperature of the incoming gas stream was measured with the reactor detailed in section 3.2.7 Axial Temperature Profile Measurement Apparatus and Heater and Figure 3-2. The first thermocouple measures the incoming air stream and the last measures temperature at the back of the bed. These two temperatures become the boundary conditions at the front and back of the bed. When the heater is turned on at the back of the bed, an axial temperature gradient is created, and from this gradient k_{eff} is measured.

The first boundary, at $z = 0$ requires utilizes the Dankwertz boundary condition as outlined in Equation 5-45. This is shown in Equation 6-7 where T_{in} is T measured by the first thermocouple.

Equation 6-7:

$$k_{eff} \frac{\partial T}{\partial z} = v \cdot \rho_f C_{Pf} (T_{in} - T)$$

The exit is set to the temperature measured by the last thermocouple, so a Dirichlet boundary condition is used for boundary 2. The result is simply:

Equation 6-8:

$$T = T_8$$

where T_8 is the value of the last thermocouple near the heater. The boundary 3, the boundary between the reactor and reactor wall, is governed by:

Equation 6-9:

$$\rho_w C_{Pw} \frac{\partial T_w}{\partial t} = k_{effw} \frac{\partial^2 T_w}{\partial r^2}$$

where ρ_w, C_{Pw} and k_{effw} are the density, heat capacity and thermal conductivity of the borosilicate wall. The final boundary needed between the wall and the ambient air is:

Equation 6-10:

$$k_{effr} \frac{\partial T}{\partial r} = h(T_w - T_{amb})$$

where h is the heat transfer coefficient between the wall and the ambient air. T_{amb} is the ambient temperature inside the oven, as seen in Figure 3-1. $T_{amb} = T_{in}$.

The effective thermal conductivity, k_{eff}, for a packed bed can also be estimated from literature. The basics are derived in section 5.3 CO Oxidation Model. Briefly, k_{eff} is the sum of the stagnant and moving contributions. Yagi then proposes the relation[89]:

Equation 6-11:

$$\frac{k_K}{k_g} = \frac{Pe}{K}$$

Here, k_K is the moving contribution to k_{eff} , k_g is the thermal conductivity of the gas phase, Pe is the Peclet number and K is taken as 2 for the axial case[90]. With k_g as 0.0257 W/(m·K), and conductivity of the silica gel 1.38 W/(m·K) the k_{eff} varies from 0.179 W/(m·K) at v_z of 5 cm/s to 0.196 at 30 cm/s.

The PDE can be solved easily with Comsol 4.3a [129]. Fitting the model to data is performed using Matlab's built in function nlinfit. nlfit uses the Gauss-Newton method to converge. nlinfit can be paired with nlparci to determine confidence intervals of the fit. h and k_{effr} don't need to be estimated directly. They can be left to float and any uncertainties will find their way into the confidence intervals determined for k_{eff}. The code for both Matlab and Comsol can be found in appendix A2.

6.3.2 Results and Discussion

The flow was adjusted between 5 cm/s to 30 cm/s for the packed bed. A graph of the results is found in Figure 6-7. The packed bed increases from .075 W/(m·K) at 5 cm/s to .40 W/(m·K) at 30 cm/s. The microfibrous media grows from .43 W/(m·K) at 15 cm/s to .8 at W/(m·K). The microfibrous media is typically 2 to 3 times more thermally conductive than a packed bed. The fibers of microfibrous media are oriented in the radial direction, not the axial direction. This greatly decreases the possible thermal conductivity because it relies heavily on the contact between each copper layer. Doubling or tripling k_{eff} could be the reason for the increased stability of the bed as shown in section 6.4 Alteration of Carrier Gas and use of MFM to change k_{eff} and Catalyst Activity.

Figure 6-7: k_{eff} vs. face velocity for a packed bed and microfibrous entrapped copper media. The confidence intervals are 95%. Packed bed is 70-100 mesh SiO_2. The MFM is .8 void 12 µm Cu media. RH: 60%; Tube ID: 15.875mm.

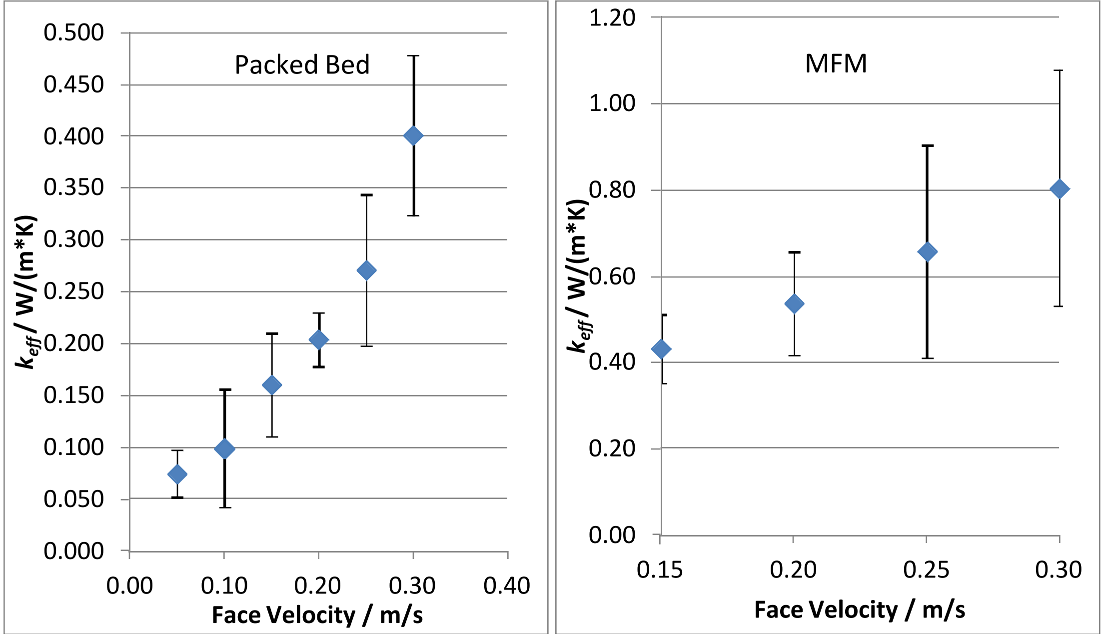

As an example the 5 cm/s and 10 cm/s temperature profiles for the packed bed runs are pictured in Figure 6-8. The simulated results sit directly on top of the experimental data, indicating an excellent fit. The same power was run through the heater in each run. It is no surprise the ΔT at the end of the bed doubles between the two runs. Approaching the front of the bed diminishes the differences between the two runs. The thermocouples at 1.7 mm, 5.15 mm and 8.95 mm sit directly on top of each other and only measure about 0.3 °C, 1 °C and 2 °C rise. At the back of the packed bed, however, there is a 13 °C difference between 16.8 mm and 14.5mm for the 5 cm/s case. The 10 cm/s case has a much smaller 5 °C difference for the same interval.

Figure 6-8: k_{eff} vs. bed depth for 5 cm/s and 10 cm/s in a packed bed. X indicates the fit of the simulation while ◆ and ▲ represent 5 cm/s and 10 cm/s face velocity respectively. Packed bed is 70-100 mesh SiO_2.

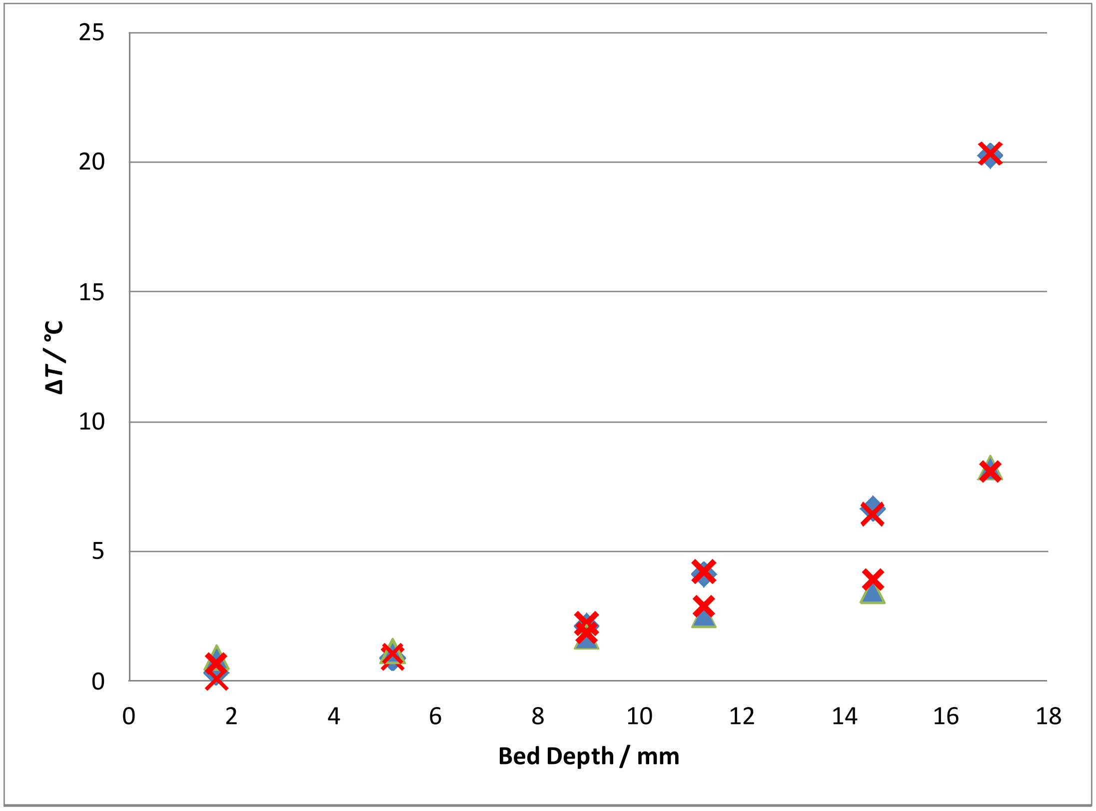

Literature values derived from Equation 6-11 over report the k_{eff} at the high end and under report at the low end as seen in Figure 6-9: k_{eff} vs. face velocity computed from literature sources[89]. The entire range is from 0.179 to 0.196 W/(m·K). Although the relation agrees with experiment at 15 and 20 cm/s, it is not sensitive enough to the fluid velocity to track the large changes observed experimentally.

Figure 6-9: k_{eff} vs. face velocity computed from literature sources[89].

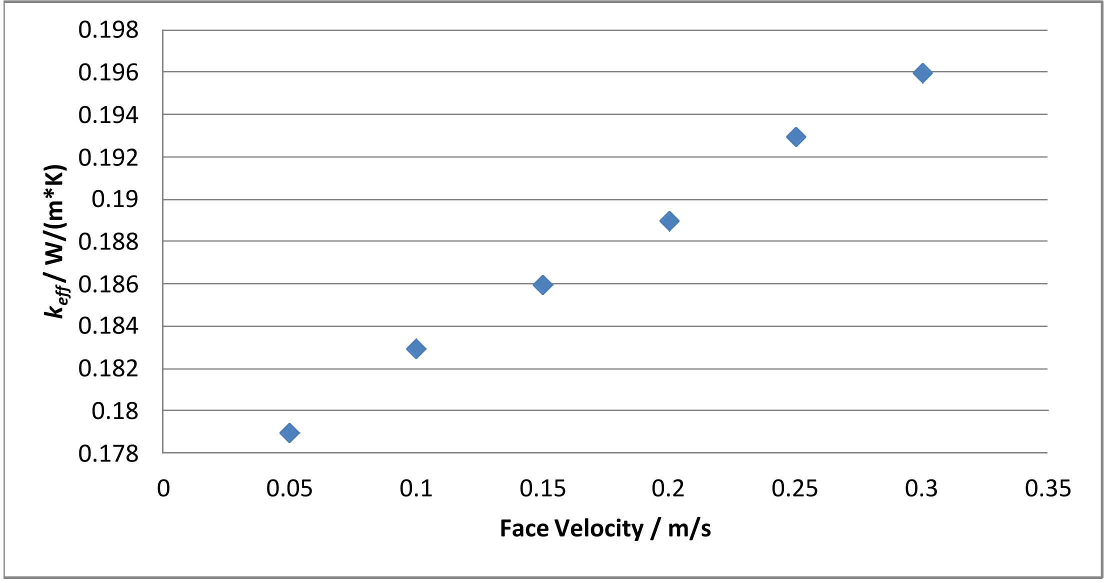

6.3.3 Conclusions

To accurately gauge the value of k_{eff} it was measured experimentally in a custom made reactor with 8 thermocouple inputs spaced 2.8 mm apart. The measurements for the packed bed were close to literature values for velocities at 15 and 20 cm/s. However, the literature correlations used did not accurately track the change in k_{eff} as the velocities varied around this point. The literature correlations may work with other gasses at the 15 cm/s and 20 cm/s velocities, however.

The MFM media displayed more than double the axial k_{eff} as the packed bed. This is very important for k_{eff} sensitive reactions such as CO oxidation. k_{eff} is anisotropic in MFM, much more so than in a packed bed. The fibers in the packed MFM are preferentially oriented in the radial direction as discussed in section 2.4 Microfibrous Media. A different stacking pattern would further improve the axial k_{eff} of the bed and is worth exploring.

6.4 Alteration of Carrier Gas and use of MFM to change k_{eff} and Catalyst Activity.

6.4.1 Theory

The negative reaction order of catalytic CO oxidation, and heat of reaction make for a sensitive combination. The affect of axial thermal conductivity, k_{eff}, on the stability of the reactor is not well known. Figure 6-10 follows a reactor in two different scenarios. They both start out with a thermally cold reactor. After the CO enters the reactor the temperature of the bed rises. First it happens at the front of the bed as the first few layers of catalyst remove all of the CO from the air. These first layers deactivate quickly, and the heat is convectively washed to the back of the reactor. From this point, the reactor can precede one of two ways. If k_{eff} is low then the reactor will eventually deactivate. A deactivation wave will sweep from the front to the back of the reactor. If k_{eff} is high enough, the reactor can find equilibrium and stay active for an extended period of time.

k_{eff} transfers the heat from reaction zone forward into the bed. In section 6.2.3 Results and Discussion it was shown the reaction takes place in a small slice of the reactor.

Figure 6-10: A catalytic bed is pictured from the beginning when CO enters the reactor to the end. The catalyst either deactivates or remains active based on k_{eff},

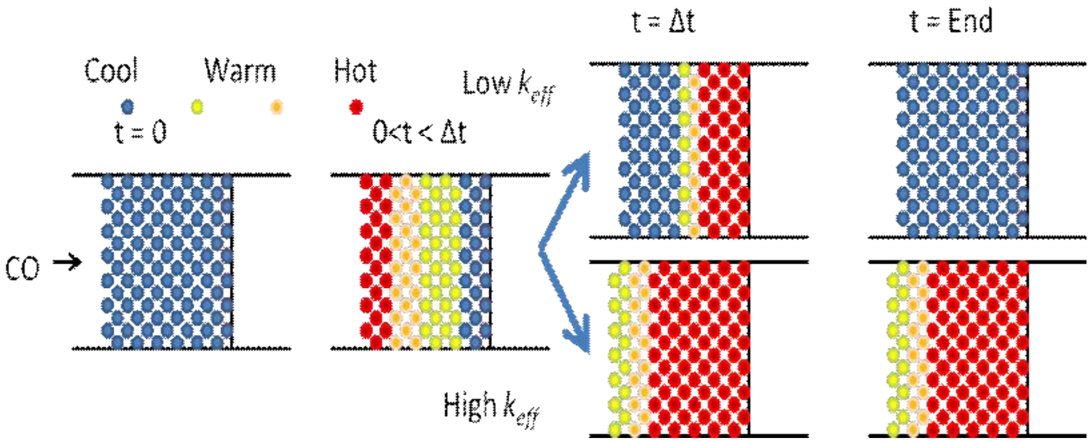

This is due to the negative order kinetics with respect to CO as outlined generally by Duprat et al. This is explored in more detail in section 2.3.3. Figure 2-3 shows the difference between a first and negative order reaction. In light off curves, as the temperature is increased, the first order reaction shows a sigmoidal shape. It tapers off as conversion approaches 1. As the reactants are depleted the reaction rate naturally slows down, even as the reactor heats up. The negative order reaction only speeds up as the conversion approaches 1. The reaction rate is increased as the bed gets hotter, and CO is used. This leads to a hysteresis dependent on temperature and CO concentration. Puszynski was even able to show traveling hot spots during CO oxidation [97]

To alter the k_{eff} of the reactor, 4 gases will be used of differing thermal conductivity, k_{eff} : Kr, Ar, N_2 and He. To calculate the thermal conductivities at a face velocity, v_z, of 15 cm/s(that used here) the method outlined in section 5.3 will be used. The results of the calculation are found in Table 6-1. The k_{eff}'s tested spans a 5 fold range.

Table 6-1: Different k and k_{eff} for each gas used in the reactor.

Gas	k for Gas/ W/(m·K)	k_{eff} for reactor / W/(m·K)
He	0.142	0.51
N_2	.024	0.18
Ar	.016	0.14
Kr	.0088	0.09
Cu MFM		0.43

In addition to using different gases to alter k_{eff}, MFM is also used. The k_{eff} is 0.43 as measured in section 6.3.2 . The MFM is compared to the packed bed. The temperature profile and outlet CO concentration are contrasted.

The model developed in chapter 5 will also be used to simulate experimental conditions. The model will simulate a range of k_{eff} and axial temperature profiles. The surface coverage based model should give insights into what is happening inside the catalyst bed. When working with surface concentrations it is useful to plot temperature, T, Gaseous CO concentration, $C_{\text{CO,G}}$, water adsorbed on the SiO_2 inert and catalyst, $C_{\text{W,S}}$, as well fraction of O available to react with Pt on the Pt-CeO_2 border, $C_{\text{O,CE,S}}$ as dimensionless values with the numerator as the maximum value. In chapter 5 $C_{\text{W,S}}$ and $C_{\text{O,CE,S}}$ are defined fractionally as

$\theta_{W,S}$ and $\theta_{O,CE}$. $C_{CO,G}$ will be represented as a fraction of $C_{CO,G}$ in the inlet and given the symbol ψ. T will be represented $\zeta = \dfrac{T - T_{in}}{T_{Adb} - T_{in}}$.

6.4.2 Experimental

Activity measurements were performed with the CO oxidation apparatus described in section 3.2.1 Activity measurement Apparatus with some alterations. The inlet of the carrier gas is split for two inlets. One for the O_2(99.9% Purity Airgas) which is always mixed to 23 vol% and is controlled by a 0 to 21 L/min Alicat mass flow controller. The other is for the carrier gas, N_2(99.9% Purity Airgas), Ar(UHP 99.99% Purity Airgas), Kr(99.9% Purity Airgas), and He(UHP 99.9% Purity Airgas), which makes up the balance. The gas is fed through an Alicat 0 to 20 L/min mass flow controller. The gas streams are mixed then split once again, where some fraction is diverted through the bubbler to achieve the desired humidity, and finally the 5% CO in N_2 stream is mixed to prepare the challenge gas.

The catalyst used in all tests was the 4% Pt-22%CeO_2 on SiO_2. An in depth procedure can be found in section 3.2.8 Catalyst Recipe. The entrapment of the catalyst in the microfibrous media, MFM is gone over in detail in section 3.2.9 Entrapment in Microfibrous Media.0.75g of the catalyst will be diluted to 2 g with inert and run at 95% RH and 2500

Figure 6-11: A schematic of the reactor as used here. The thermocouples are all placed 2.8 mm apart. The first one sits at 2mm in the bed.

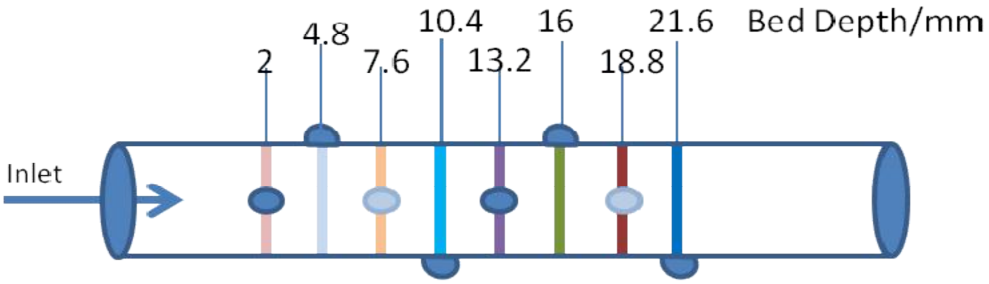

ppm. The catalyst is soaked in the humid challenge gas stream for 6 h prior to introduction of the CO.

To log axial temperature data, the reactor outlined in Figure 6-11. The reactor has 8, k-type thermocouples spaced 2.8 mm apart down the tube. The actual reactor is pictured in Figure 6-1. The temperature reading from each thermocouple is data logged every second by an Omega DAQ-5300 data logger. For a more information on the reactor consult section 3.2.7 Axial Temperature Profile Measurement Apparatus and Heater.

6.4.3 Results and Discussion

6.4.3.1 Kinetic Testing of Packed Bed and Microfibrous Material

The outlet $C_{CO,G}$ is plotted against time in Figure 6-12 for each gas. The longevity of

Figure 6-12: $C_{CO,G}$ for each gas potted over t. The gases are Kr, Ar, N_2 and He. The higher k_{eff} the longer the catalyst bed stayed active. 4% Pt- 22% CeO_2 on SiO_2. Wt: 0.75 g +1.25g Inert; $C_{CO,G}$ = 2500 ppm; v_z = 15 cm/s; T = 26 °C; RH = 95%; Tube ID = .625

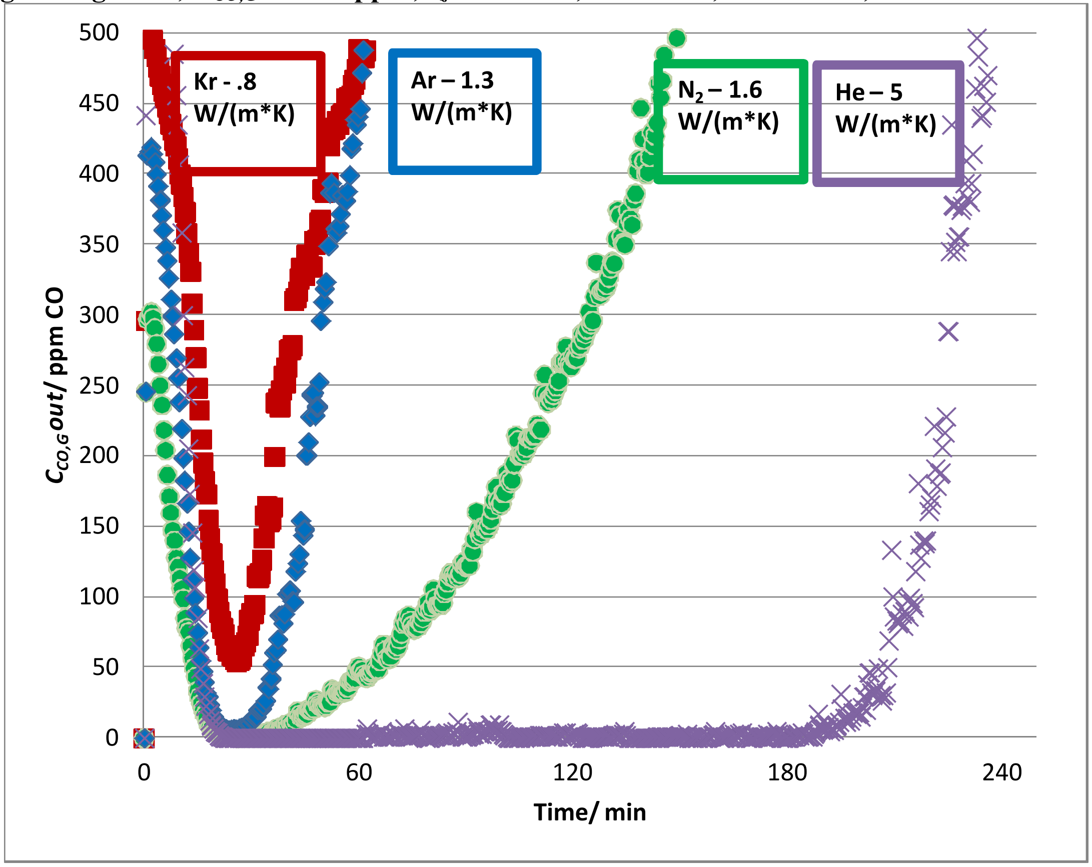

the bed is positively correlated with k_{eff}. The He carrier lasted over 3 h under reaction conditions. This contrasted with N_2, the next closest which began to deactivate before the first hour. The Ar carrier gas only stayed active for 45 minutes. The Kr carrier ,the gas lowest k_{eff}, never made it to 100% conversion at all. The initial activity of the bed in the first 30 minutes was low for all carrier gases. This occurs while catalytic bed is heating up. It takes this long for the heat evolved from the oxidation of CO to desorb the water in the SiO_2 inert and Pt-CeO_2 SiO_2 catalyst. The difference in activity between the He carrier and all the others is extremely large.

Figure 6-13:*T* plotted against time for multiple bed depths. 4% Pt- 22% CeO_2 on SiO_2. Wt: 0.75 g +1.25g Inert; $C_{CO,G}$ = 2500 ppm; v_z = 15 cm/s; *T* = 26 °C; RH = 95%; Tube ID = .625 Carrier Gas: Kr

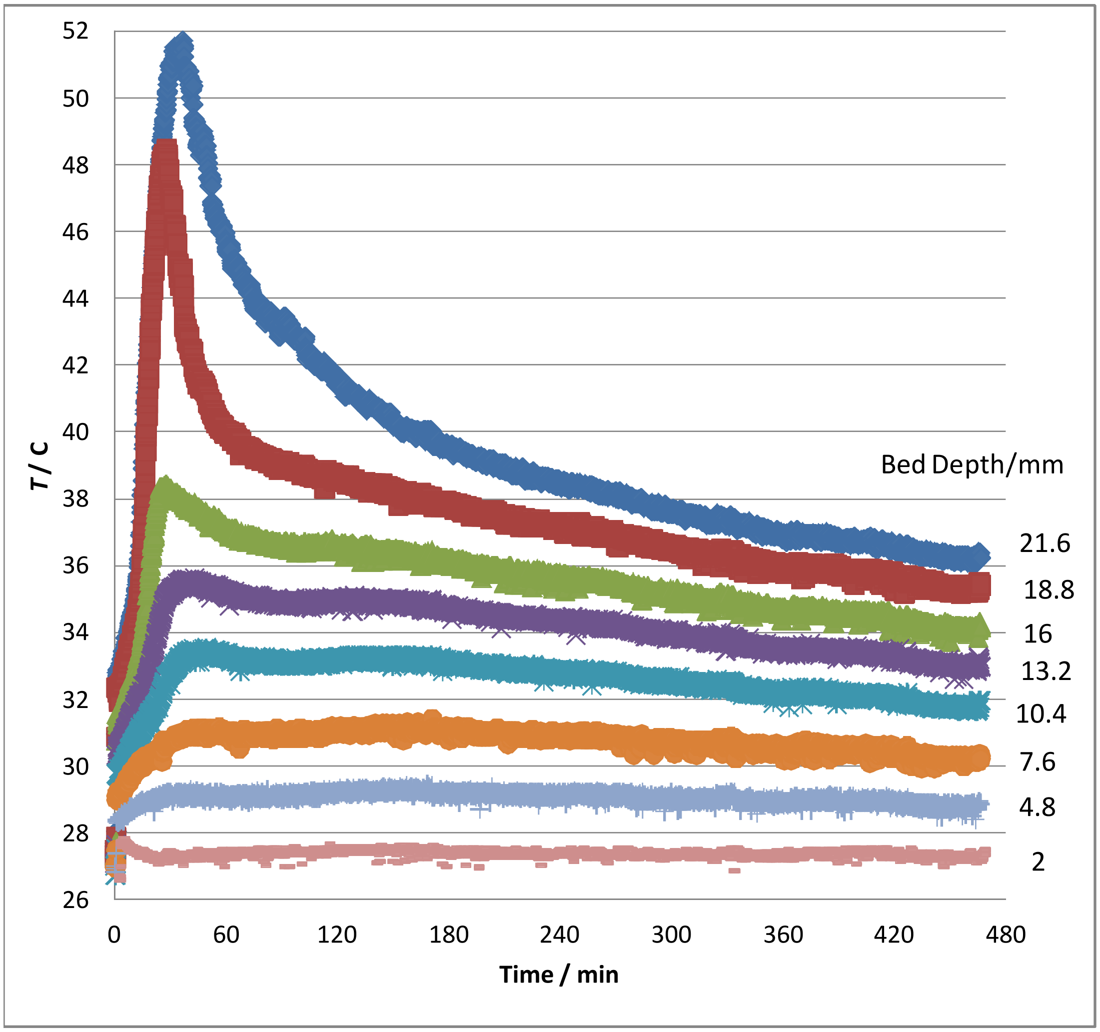

Figure 6-13 displays the axial temperature profile for the Kr carrier gas. The last temperature probe at 21.6 mm does reach all the way to 52 °C. This corresponds to 90% conversion which comes close to maximum recorded conversion of 98% in the outlet stream. The temperature rise starts in the back of the bed between the 18.8 mm and 21.6 mm bed depth. It also begins to fall first in this region as well. The entire bed's temperature rises together as the thermal mass of the reactor is overcome by the energy released by the reaction. At 16mm and shallower the temperature rise is not very dramatic, nor does the explosive rise at 18.8mm and back seem to transfer forward.

The Kr carrier gas is contrasted most heavily with He carrier. The He demonstrates extremely high temperature rises for the entire reactor. In the begging all thermocouples jump

Figure 6-14: *T* plotted against time for multiple bed depths. 4% Pt- 22% CeO_2 on SiO_2. Wt: 0.75 g +1.25g Inert; $C_{CO,G}$ = 2500 ppm; v_z = 15 cm/s; *T* = 26 °C; RH = 95%; Tube ID = .625 Carrier Gas: He

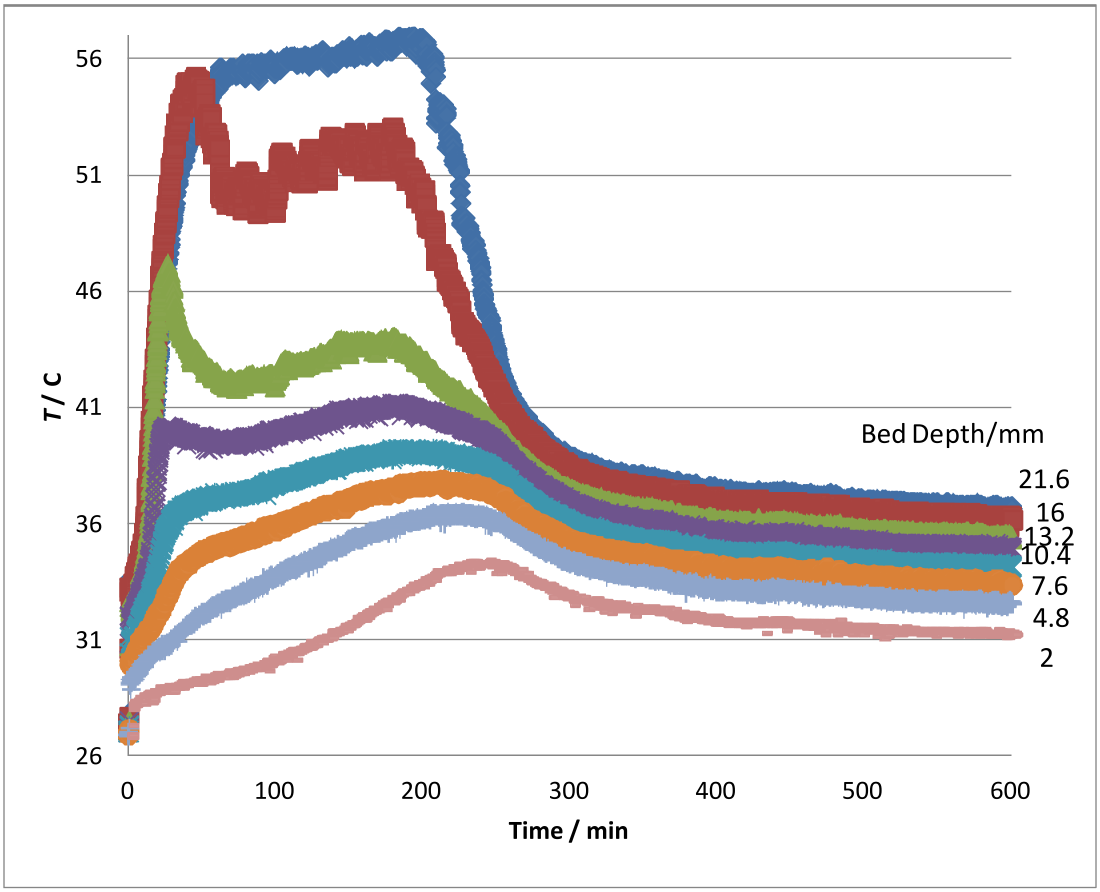

together similar to the Kr stream. However, when the Kr stream simply deactivated around 40 minutes; the He carrier keeps rising. The largest difference in temperature is still between the 16 mm and 18.8 mm bed depth. However, all thermocouples shallower in the bed show a very large bump in temperature. At 2 mm the temperature rises 34 °C. At 4.8 mm down the packed bed the temperature rises to 36 °C. This is contrasted with the Kr thermocouple which never makes it past 29 °C. This trend continues all the way to the back of the bed, where the last layer is kept at the adiabatic limit for almost 4 hours. The temperature 16mm into the reactor seems to oscillate. This has been observed in many CO oxidation studies.

The Ar reacts very similarly as the Kr. Carrier gas stream. The N_2 carrier gas

Figure 6-15 *T* plotted against time for multiple bed depths. 4% Pt- 22% CeO_2 on SiO_2. Wt: 0.75 g +1.25g Inert; $C_{CO,G}$ = 2500 ppm; v_z = 15 cm/s; *T* = 26 °C; RH = 95%; Tube ID = .625 Carrier Gas: N_2

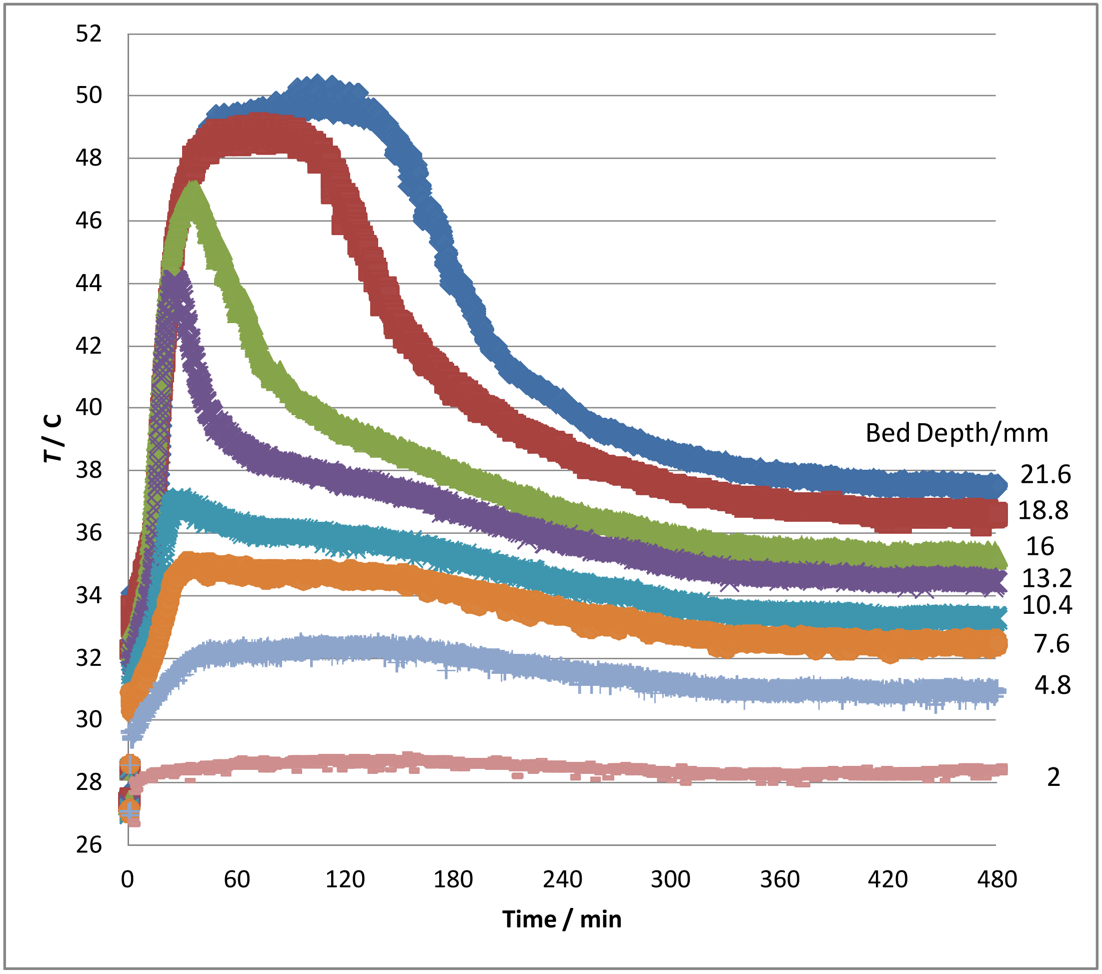

temperature profile resembles the He stream, although it deactivates quicker. Figure 6-15 shows the change in the axial temperature profile over time for N_2 as the carrier. N_2 is at a disadvantage compared to the other gases due to its higher C_P. The adiabatic limit is 51 °C for N_2. Still, the N_2 carrier manages to keep the bed active for an hour. This is longer than the Kr or Ar carrier gases. The majority of the reaction is still carried about between 16 mm and 18.8 mm of bed similar to all the other gases. While the N_2carrier does keep the bed active for much longer it does not have the increase in temperature after the initial heating. He is the only gas to display such behavior.

In Figure 6-16 the temperature of the rear of the beds for each carrier gas are plotted.

Figure 6-16: *T* for each gas potted over *t* at 21 mm depth. The gases are Kr, Ar, N_2 and He. The higher k_{eff} the longer the catalyst bed stayed active. 4% Pt- 22% CeO_2 on SiO_2. Wt: 0.75 g +1.25g Inert; $C_{CO,G}$ = 2500 ppm; v_z = 15 cm/s; *T* = 26 °C; RH = 95%; Tube ID = .625

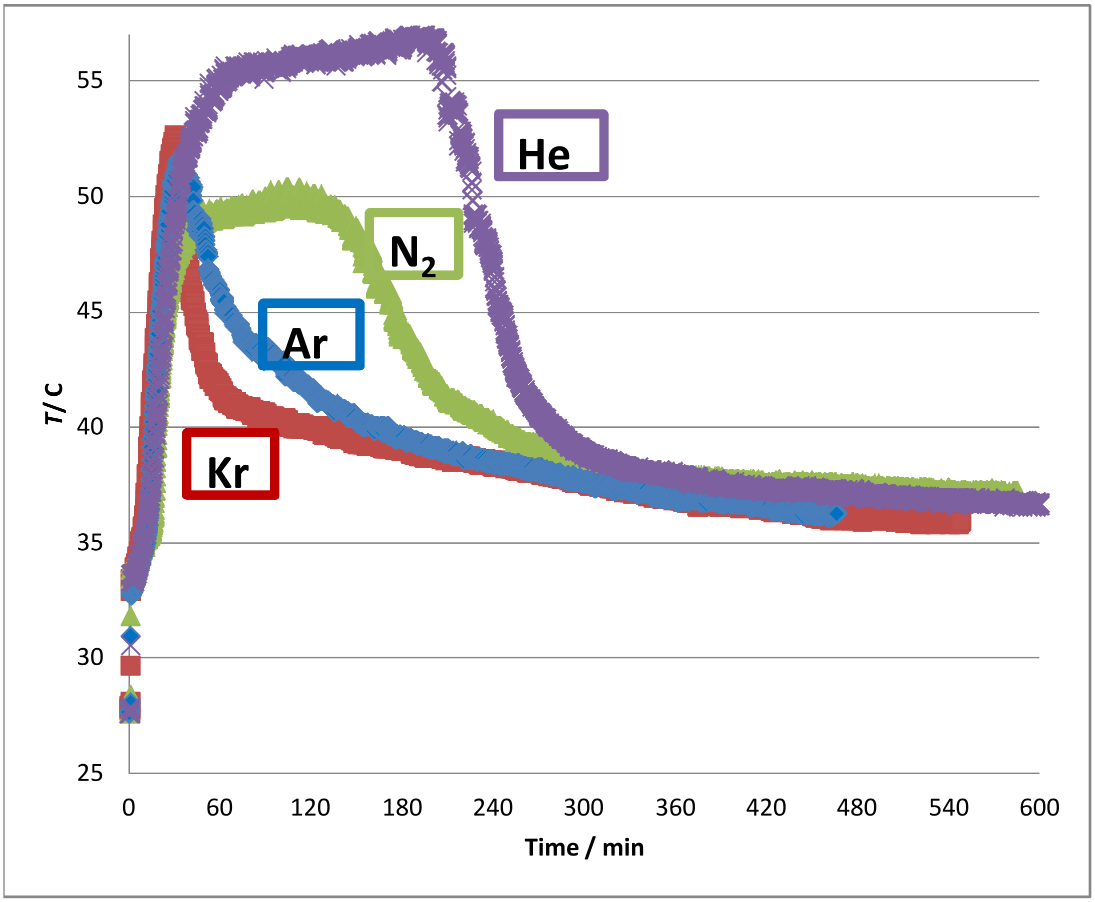

The Kr and Ar streams immediately deactivate. The N_2 and He streams manage to hit their adiabatic limit for 2 h and 3.5 h respectively. When the middle cut, seen in Figure 6-17 10 mm is viewed the same way, the characteristic temperature rise, as only seen in the He carrier, is clearly observed. At 45 minutes into the experiment all the catalysts begin to deactivate except the He carrier. The temperature continues to rise 2 °C more to reach a max of 39 °C. 2 °C translates into 200 ppm more CO reacted. The heat from the reaction, in conjunction with the negative order reaction kinetic is activating the entire catalyst bed.

Figure 6-17: *T* for each gas potted over *t* at 10.4 mm depth. The gases are Kr, Ar, N_2 and He. The higher k_{eff} the longer the catalyst bed stayed active. 4% Pt- 22% CeO_2 on SiO_2. Wt: 0.75 g +1.25g Inert; $C_{CO,G}$ = 2500 ppm; v_z = 15 cm/s; *T* = 26 °C; RH = 95%; Tube ID = .625

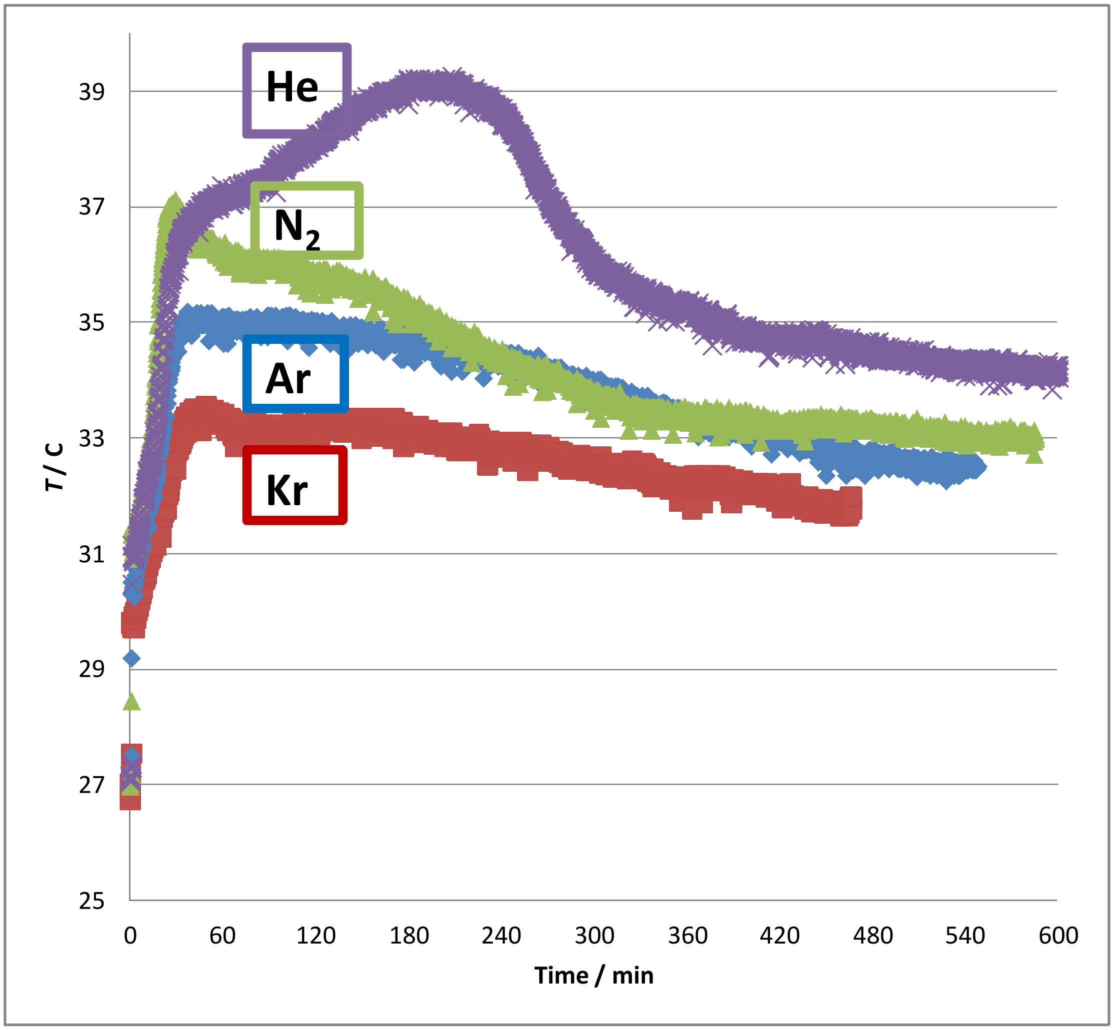

Finally the largest difference can be seen at the front of the bed, 2 mm in. In Figure 6-18 there is essentially no change in the temperature for the N_2, Ar and Kr carrier gases. They do, however, increase in temperature as k_{eff} is increased. This difference is only about 1 °C though. The He carrier, on the other hand increases drastically. It continues to increase all the way to 34.5 °C. That is a 6 °C difference over the next closest carrier gas N_2. The heat from the back of the bed is able to spread further forward through a combination of negative reaction kinetics and k_{eff} ; in the case of He there are large temperature differences all the way at the front of the bed. Where the N_2, Ar and Kr are able to remove 150 ppm to 200 ppm in

Figure 6-18: *T* for each gas potted over *t* at 2 mm depth. The gases are Kr, Ar, N_2 and He. The higher k_{eff} the longer the catalyst bed stayed active. 4% Pt- 22% CeO_2 on SiO_2. Wt: 0.75 g +1.25g Inert; $C_{CO,G}$ = 2500 ppm; v_z = 15 cm/s; *T* = 26 °C; RH = 95%; Tube ID = .625

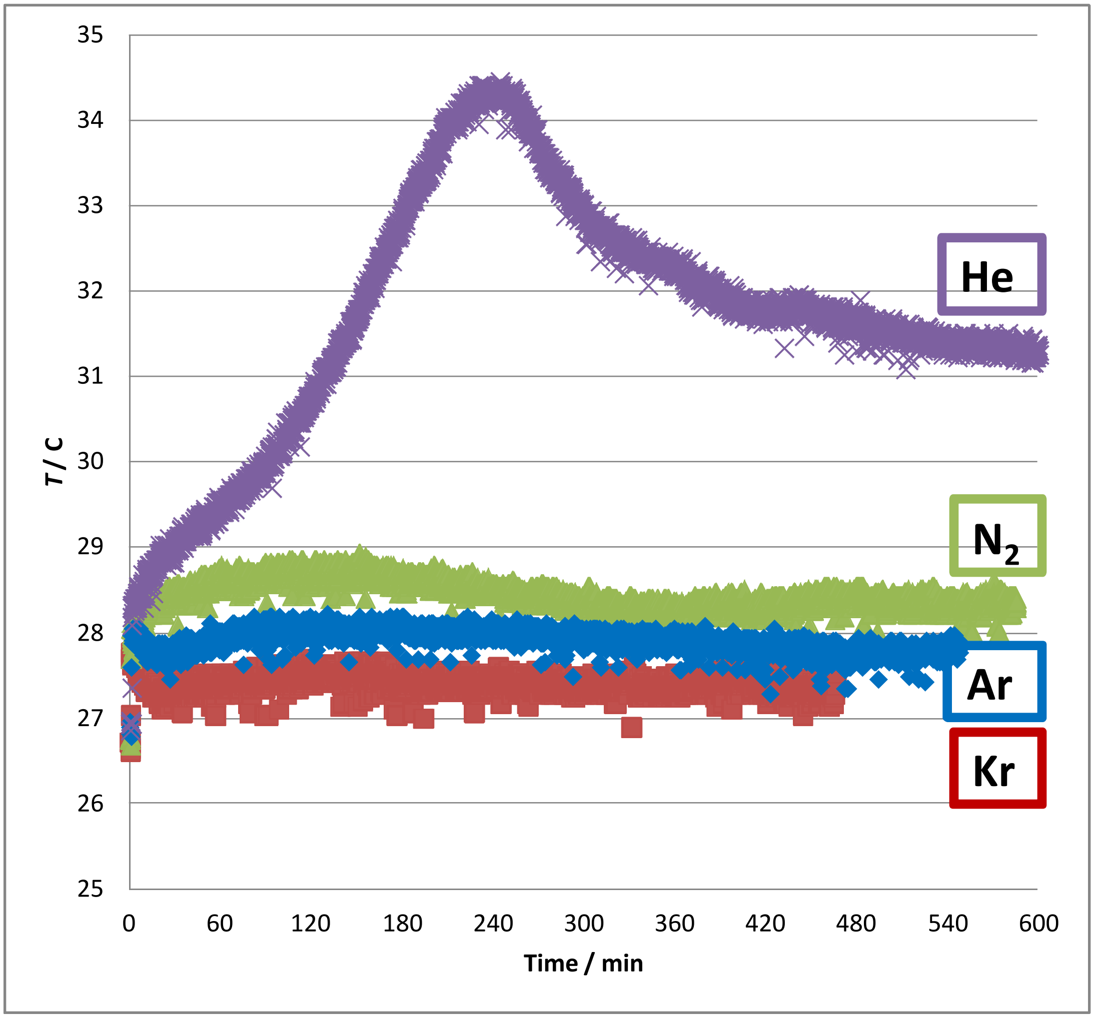

the first 2mm, the He carrier stream is able to remove 800 ppm. This is the key that keeps the

Figure 6-19: $C_{CO,G}$ MFM and N_2 carrier gas over t. The higher k_{eff} the longer the catalyst bed stayed active. 4% Pt- 22% CeO_2 on SiO_2. Wt: 1.2 g; $C_{CO,G}$ = 1500 ppm; v_z = 10 cm/s; T = 26 °C; RH = 50%; Tube ID = .625 MFM void : 0.8

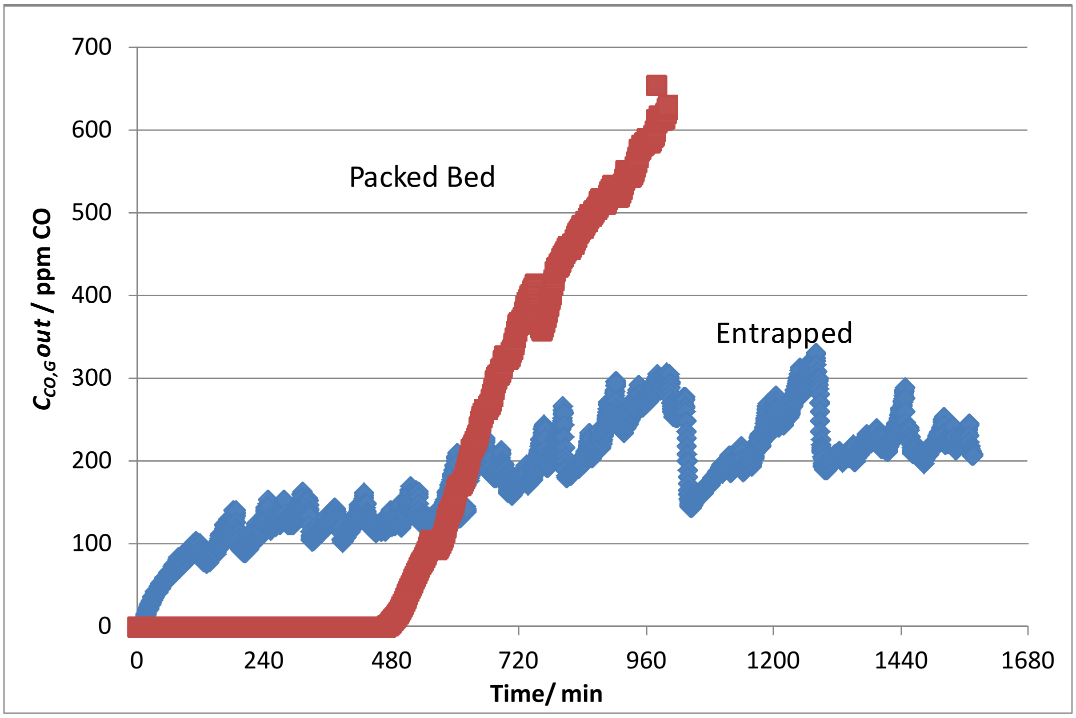

bed active for so long.

To further test the implications of k_{eff} MFM is tested and compared to N_2 as the carrier gas in the same conditions. The Entrapped catalyst immediately begins to show signs of deactivation proceeding very quickly to 100 ppm CO out. The packed bed during this same time remains at 100 % conversion. This is probably due to the lower gas to solid mass transfer rate of the entrapped catalyst. The void in the MFM is 0.8. This is compared with 0.4 for the packed bed.

After 8 hours the packed bed begins to deactivate. This is contrasted with entrapped catalyst which bounces in between 100 and 300 ppm for the entire 26 h run. To get a better understanding, the temperature profiles of the two reactors are compared in Figure 6-21. In Figure 6-20 a) the packed bed and Figure 6-20 b) the MFM entrapped catalyst both start out

Figure 6-20: T profile for a packed bed a) and MFM entrapped catalyst b). 4% Pt- 22% CeO_2 on SiO_2. Wt: 1.2 g; $C_{CO,G}$ = 1500 ppm; v_z = 10 cm/s; T = 26 °C; RH = 50%; Tube ID = .625 MFM void : 0.8

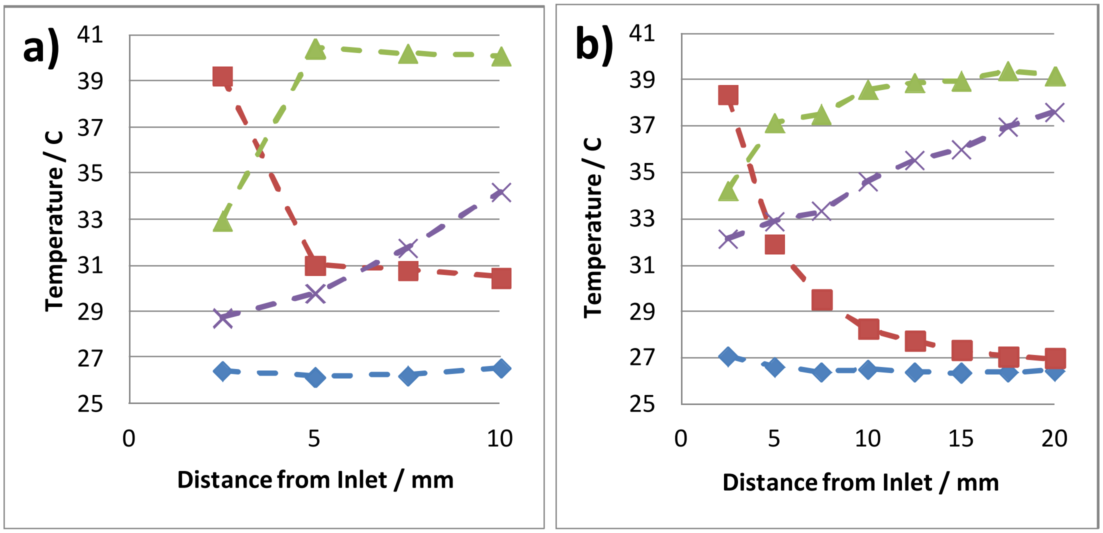

the same. Once the catalyst has been active for only 4 minutes, it is possible to see changes. The entrance of the entrapped catalyst is 2 °C higher than the packed bed. This is still at 100 % conversion for each. When the catalyst has been on stream for 1000 minutes the entrapped catalyst has a much more even temperature profile. The catalyst has stabilized at about 32 °C; the packed bed has dropped to 29 °C at this point and is only at 56% conversion while the MFM entrapped catalyst is at 87%.

6.4.3.2 Simulation of Packed Bed at Different k_{eff}

To gain a better understanding a two phase reactor model is employed. The results for the effect of k_{eff} on catalyst activity can be seen in Figure 6-21. The k_{eff} needed to change the outlet concentration over time is high. For comparison, the highest carrier gas only had 0.5 W/(m·K). The sensitivity to k_{eff} is not captured fully here. However, the trend is the same that is seen during the experimental tests. The catalyst bed is predicted to start at essentially 0% conversion. During the first 20 minutes the conversion of the catalyst bed increases to its maximum. At 0.16 W/(m·K) this is only 58% conversion. This gradually increases until at 3 W/(m·K) the conversion reaches 100%. The conversion stays above 90% for increasingly long periods of time as k_{eff} increases.

Figure 6-21:Outlet $C_{CO,G}$ vs. time for the simulated effect of k_{eff} on Catalyst Activity. The higher k_{eff} the longer the catalyst bed stayed active. 4% Pt- 22% CeO_2 on SiO_2. Wt: 0.75 g +1.25g Inert; $C_{CO,G}$ = 2500 ppm; v_z = 15 cm/s; T = 26 °C; RH = 95%; Tube ID = .625

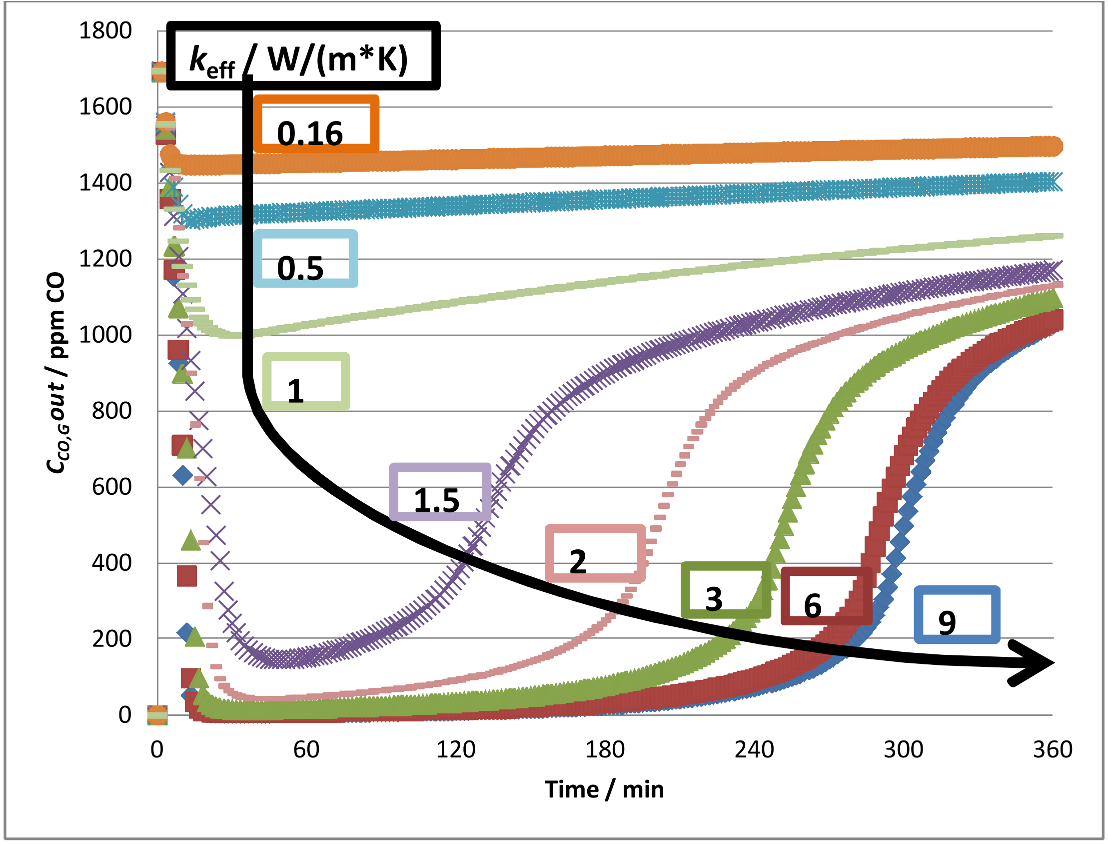

Figure 6-22: *T* vs. time for first 2mm of catalyst bed to show the simulated effect of k_{eff} on Bed *T*. The higher k_{eff} the longer the catalyst bed stayed active. 4% Pt- 22% CeO_2 on SiO_2. Wt: 0.75 g +1.25g Inert; $C_{CO,G}$ = 2500 ppm; v_z = 15 cm/s; *T* = 26 °C; RH = 95%; Tube ID = .625

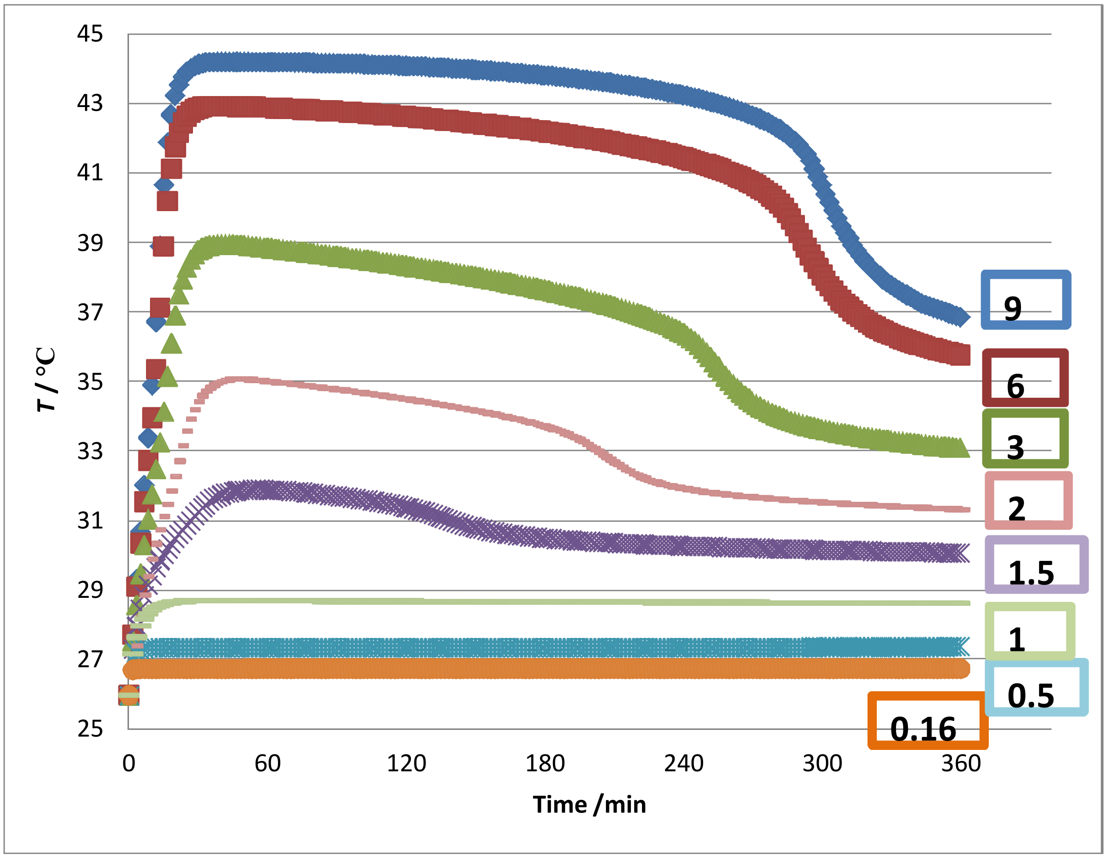

The Temperature for each k_{eff} is plotted in Figure 6-22. There is moderate but flat temperature increases until 1.5 W/(m·K). The temperature increases along with the conversion for the first 20 minutes at 1.5 W/(m·K) and above. This mirrors very closely the same phenomenon in the experimental results. As k_{eff} is increased, the amount of heat that makes it to the first 2mm of the bed also increases. The front of the bed stays hotter longer as well. Over time the temperature and conversion drop for all k_{eff} above 1 W/(m·K).

To get an understanding of what is happening while the catalyst is heating and deactivating, the species adsorbed on the SiO_2 are tracked. ψ, ζ, $\theta_{\text{O,CE}}$ and θ_{H2O} are tracked shown after the first two minutes of the reaction in Figure 6-23. ψ is at goes from 1 to 0.67 from beginning to end of the reactor. The surface reaction between O and CO is still too small to make a difference while the temperature, ζ, has yet to heat up. At exit of the reactor ζ is only 0.1. $\theta_{O,CE}$ and θ_{H2O} both start near maximum. The $\theta_{O,CE}$ will start full in any reaction and θ_{H2O} simply reflects the RH of 95%.

Figure 6-23: Simulated ψ, ζ, $\theta_{O,CE}$ and θ_{H2O} represented by▬ ▬ ▬ , ▬▬▬ ,▬ ▬ , ▬ ▪ ▬ respectively and are plotted against bed depth. The axial profile is taken at 2 min with k_{eff} = 3 W/(m·K). 4% Pt- 22% CeO_2 on SiO_2. Wt: 0.75 g +1.25g Inert; $C_{CO,G}$ = 2500 ppm; v_z = 15 cm/s; T = 26 °C; RH = 95%; Tube ID = .625

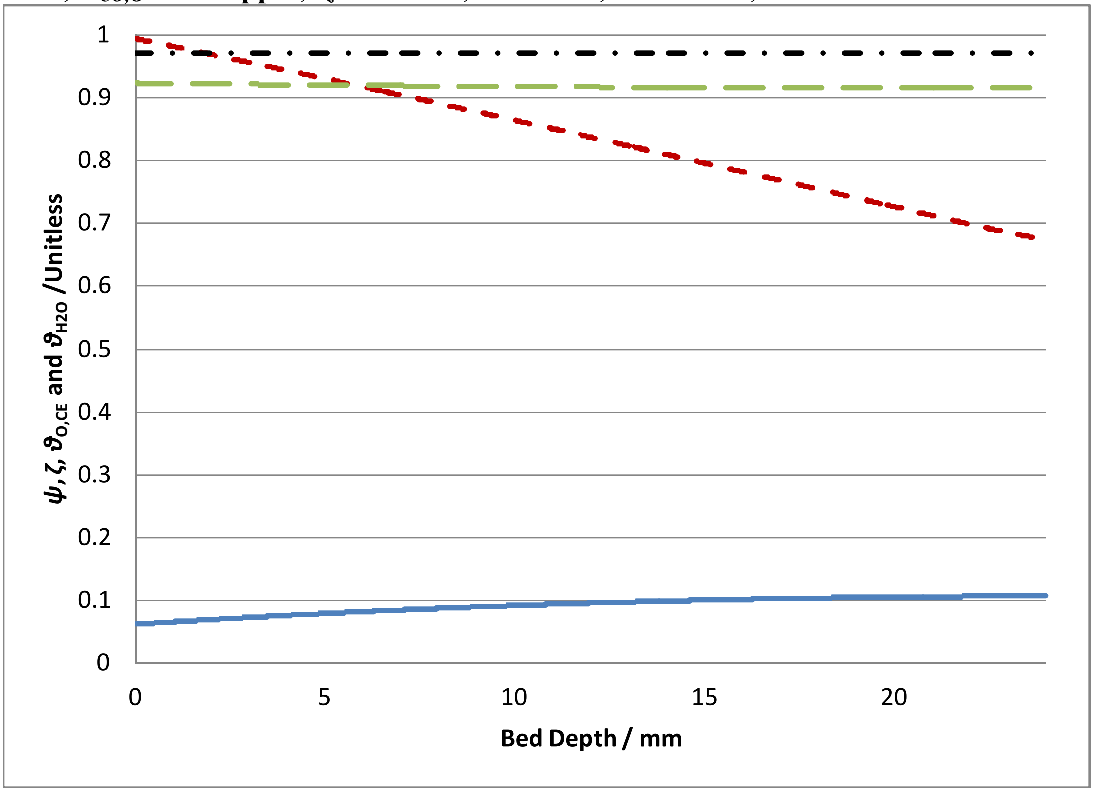

As the time approaches 12 minutes Figure 6-24 a)shows ψ has decreased to 0.3 to give 70% conversion. ζ continues to rise to a little over half the adiabatic limit at the exit. The front of the bed is at half that value. $\theta_{O,CE}$ has fallen dramatically from 0.92 at 2 minutes to 0.80 at 12. The water content adsorbed on the SiO_2 still remains high. The rise in temperature and conversion go hand in hand.

Figure 6-24: Simulated ψ, ζ, $\theta_{O,CE}$ and θ_{H2O} represented by – – –, ——, – – –, – · – respectively and are plotted against bed depth. The axial profile is taken at a) 12 min and b) 30 min with k_{eff} = 3 W/(m·K). 4% Pt- 22% CeO_2 on SiO_2. Wt: 0.75 g +1.25g Inert; $C_{CO,G}$ = 2500 ppm; v_z = 15 cm/s; T = 26 °C; RH = 95%; Tube ID = .625

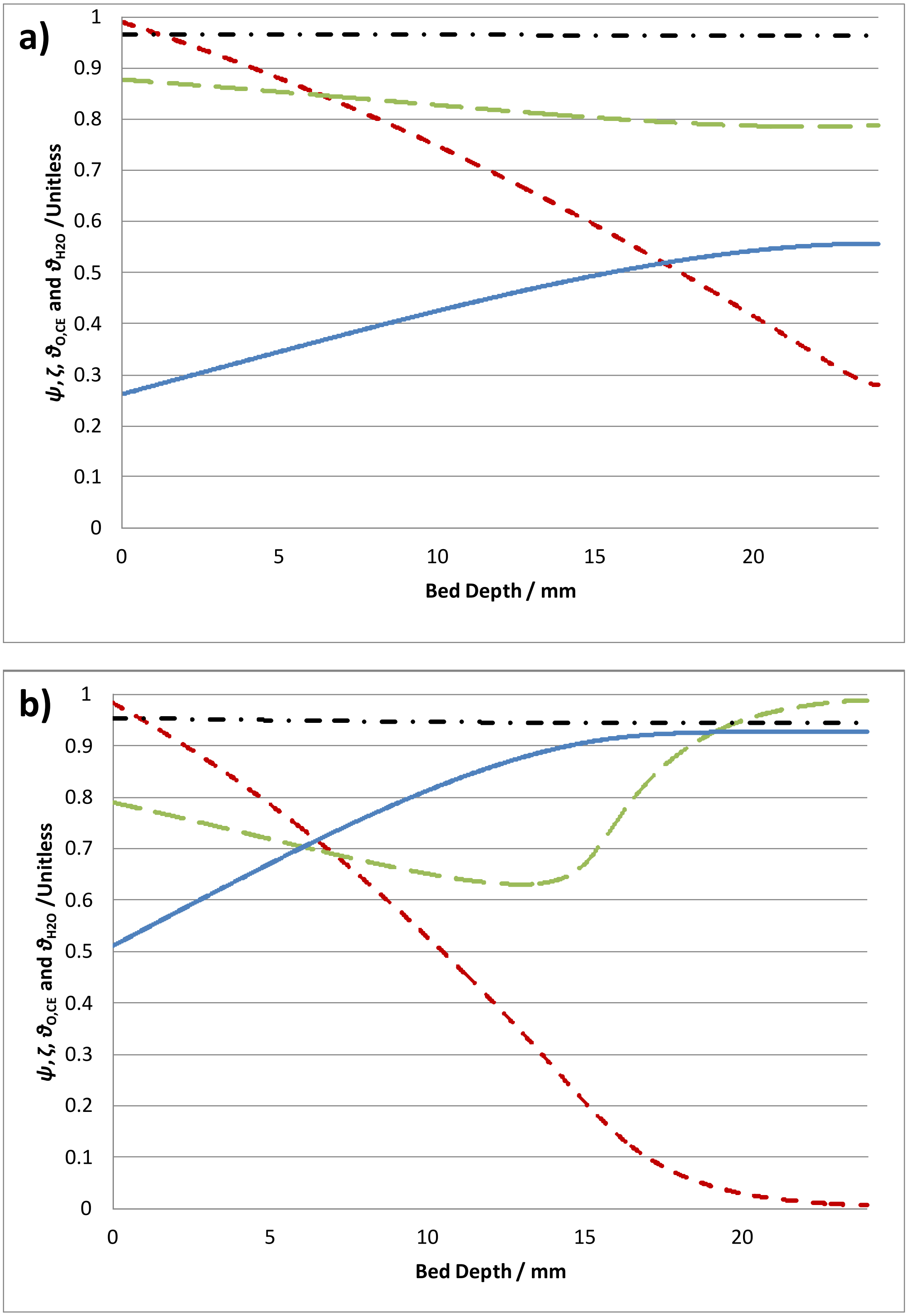

After 30 minutes in Figure 6-24 b), ζ reaches the adiabatic limit for the latter third of the bed, and half the limit at the reactor entrance. ψ shows 100% conversion at the back of the bed. The last 5mm of the bed are not reacting at all. This allows $\theta_{O,CE}$ to rebound to almost 100% in the back of the packed bed. $\theta_{O,CE}$ falls rapidly in the front and middle of the packed bed. This is the region that is reacting fastest with the highest CO coverage. θ_{H2O} begins to fall slightly between 12 and 30 minutes. This is due to the temperature reaching the adiabatic limit and holding it for some time.

After 3 h the conversion finally begins to drop at the back of the reactor. Figure 6-25 ζ starts to fall as the reaction slows down. The reaction slows down due to the severe shortage of oxygen available to react on the Pt-CeO$_2$ border. $\theta_{O,CE}$ has fallen to almost 0.4 18 mm into the packed bed. The big story here, however is the desorption of water. θ_{H2O} has fallen to

Figure 6-25 : Simulated ψ, ζ, $\theta_{O,CE}$ and θ_{H2O} represented by — — — , ——— , — — — , — · — respectively and are plotted against bed depth. The axial profile is taken at 3 h with k_{eff} = 3 W/(m·K). 4% Pt- 22% CeO$_2$ on SiO$_2$. Wt: 0.75 g +1.25g Inert; $C_{CO,G}$ = 2500 ppm; v_z = 15 cm/s; T = 26 °C; RH = 95%; Tube ID = .625

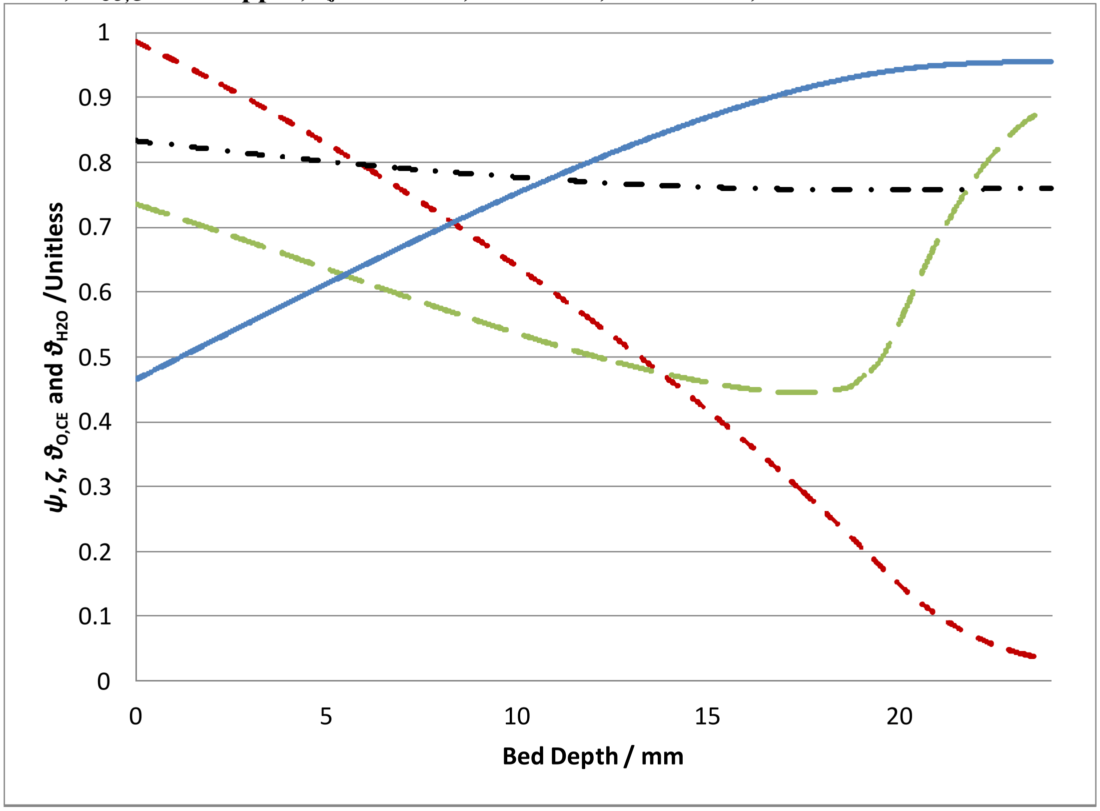

below 0.8 for the majority of the reactor. The increased temperature has desorbed the water over time. The low value of θ_{H2O} slows down the replenishment of O to the Pt-CeO$_2$ border as seen in Equation 5-15. This reaction is very water sensitive.

As the water find equilibrium with the plummeting RH of air, the entire reaction slows down. Figure 6-26 shows the bed 4.5 h in. The conversion has dropped considerably to an equilibrium value of 66%. The low θ_{H2O} between 0.8 and 0.7 slows down the replenishment of O on the periphery of the crystallite further. The temperature begins to drop to reach a maximum of only 70% the adiabatic limit. The initial low conversion is due to the catalyst bed starting cold and pre-adsorbed with water. Once the bed heats up $C_{CO,G}$ drops, but

Figure 6-26: Simulated ψ, ζ, $\theta_{O,CE}$ and θ_{H2O} represented by – – – , —— , – – – , – · – respectively and are plotted against bed depth. The axial profile is taken at 4.5 h with k_{eff} = 3 W/(m·K). 4% Pt- 22% CeO$_2$ on SiO$_2$. Wt: 0.75 g +1.25g Inert; $C_{CO,G}$ = 2500 ppm; v_z = 15 cm/s; T = 26 °C; RH = 95%; Tube ID = .625

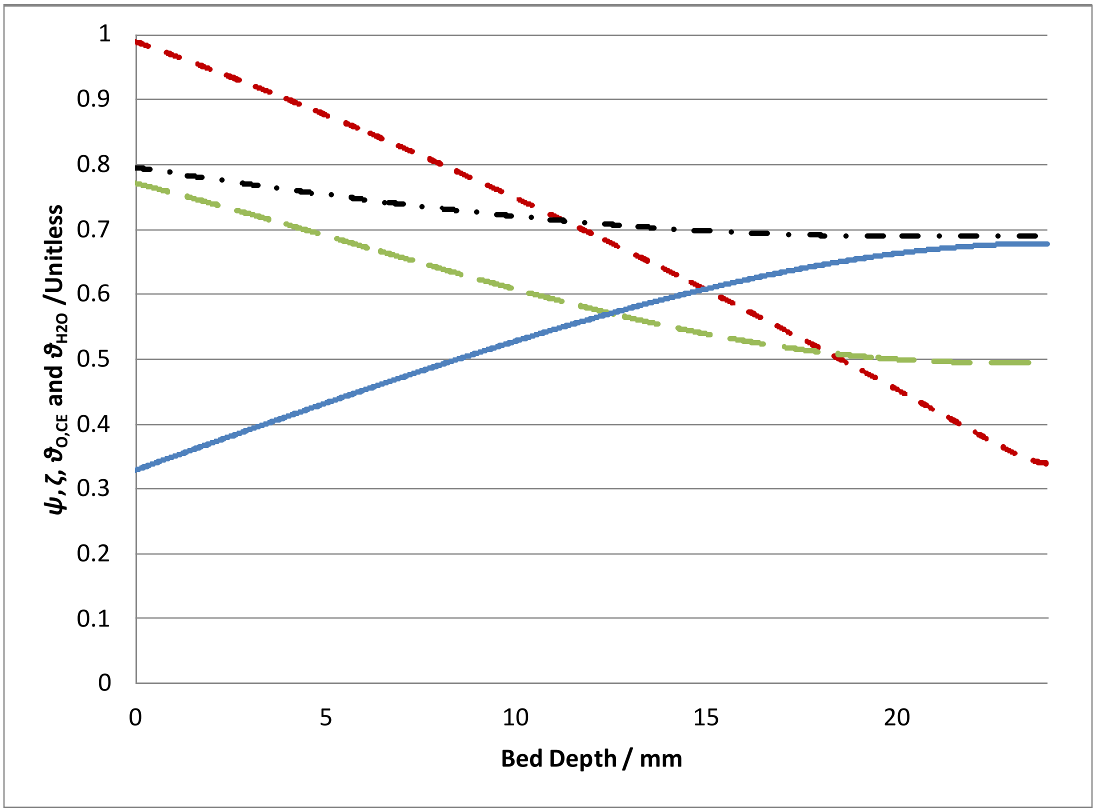

over time so does the adsorbed water. When the water get to low, the water sensitive catalyst loses activity and $C_{CO,G}$ begins to rise again to settle at an equilibrium value.

6.4.4 Conclusions

The object was to test the impact of k_{eff} on the catalytic oxidation of CO in a humid environment. The catalyst activity increased when exposed to a higher k_{eff} carrier gas. The order for the activity improvement followed exactly the order of k_{eff}: He>N_2>Ar>Kr. This is postulated to primarily be due to the back diffusion of heat against the convective flow. This back flow of heat would not be possible without the sensitivity of negative reaction kinetics.

The temperature profile of each gas was examined. The N_2 and He showed much larger portion of the bed active than the Ar or Kr carrier gasses. The He carrier gas did by far the best. A temperature wave was recorder that extended all the way to the front of the packed bed. The rise at the front of the bed was recorded at 8 °C. This is contrasted with the next best gas N_2 which only showed a 3 °C increase.

The novel reactor structure microfibrous media was used to entrap the catalyst and improve k_{eff} over a packed bed. The MFM was compared with the N_2 carrier gas. The microfibrous catalyst managed to stay above 80% conversion for 26 hours. The packed bed only managed this for 9 hours on stream time. Examining the axial temperature profile revealed a much more even distribution in the MFM. The front of the MFM was 6 °C above the inlet temp. The packed bed was only 2 °C. The microfibrous media improved the catalyst stability.

A simulation of the packed bed was performed and compared with experimental results. The results match the trend well. Although, a k_{eff} of 3 W/(m·K) was needed to come close to the activity recorded with the He carrier gas which has a k_{eff} of 0.5 W/(m·K). Even thought k_{eff} was inflated, the qualitative aspects of the temperature profile and exit concentration of carbon monoxide were mirrored by the model quite well.

The model revealed the catalyst went through 4 main stages. At first the bed heats up and the conversion increases with the bed temperature. This is followed by the conversion improving and the amount of active bed decreasing as a concentration of 0 CO is moved further in the packed bed. As the catalytic bed heated up further, the water pre-adsorbed on the SiO_2 inert and catalyst support decreased, which slows the reaction between O adsorbed on the CeO_2 and the CO adsorbed on the Pt. Once a critical amount of water is lost, the bed slowly deactivates and reaches a much less active equilibrium.

Chapter 7 : Conclusion and Recommendations for Future Work

7.1 Conclusions

The catalytic oxidation of CO was carried out in humid conditions at room temperature. This is an under researched area. Most kinetic experiments typically run at 1% CO in the feed with no in depth look into the effect of humidity. This work stuck to low CO concentrations, below 2500 ppm.

The selection of catalysts that operate in this opportunity space are sparse. Many formulations were tested as seen in Table 2-5. An in house catalyst was used which consisted of Pt-CeO_2 on SiO_2. This work built on the work of previous catalyst optimization by decreasing the cost of Pt precursor and removing a vacuum drying step. It was shown that the pH of the Pt precursor solution plays a large role in the activity of the catalyst. A pH of 10.7 was found to optimal when using Tetraammineplatinum(II) nitrate precursor as the Pt source. It was also found drying in N_2 at 50 °C led to a superior catalyst than vacuum drying.

Kinetic studies were carried out on the Pt-CeO_2 on SiO_2 catalyst developed earlier which ranged from 25 ppm to 500 ppm CO, 5 cm/s to 30 cm/s face velocity, 5% relative humidity all the way to 95%, and the temperature was altered between 25 °C and 50 °C. The tests showed heterogeneous mass transfer is the limiting step below 150 ppm. The kinetic results also showed a profound effect of water on catalyst activity. The model used to fit the water adsorption is that of water adsorbed on SiO_2 and not Pt. The hypothesis is the water adsorbed on the Pt is controlled by its local environment. In this case, it is catalyst support SiO_2.

A heterogeneous kinetic model based on adsorption and CO and O_2 on the Pt surface and adsorption of H_2O on the SiO_2 gave a very good fit. The reaction mechanism is postulated to be the product of 3 main reactions. These are explored in detail in Chapter 5. The reactions are the Langmur-Henshelwood reaction between CO and O on Pt; the reaction between CO adsorbed on Pt and O donated from the CeO_2 that reacts at the Pt-CeO_2 interface, and the availability of O from the bulk CeO_2 to a position on the Pt-CeO_2 interface that is available to react with CO. The last reaction is water dependent. The activation energies of the three reactions were regressed to be 19.7 kJ/mol, 89.4 kJ/mol and 1.16 kJ/mol respectively. The ratio of total Pt-CeO_2 interfacial sites to total surface Pt was also regressed to be 12%. In the end, the model proved reliable in the prediction of catalytic CO oxidation for a wide range of humidity(5% to 90%), temperature(25 °C to 50 °C) and CO concentrations(0 ppm to 2500 ppm).

To better understand the role of heat transfer during CO oxidation, experiments were carried out that added heat to the back of bed through a heater, or changed the thermal conductivity of the bed completely. The former was done using a small nichrome wrapped ceramic heater placed at the back of the packed bed. Once the heater was turned on, the previously poisoned catalytic bed ignited from the back and past the heat to the front. The axial temperature profile was monitored and showed a 3 °C rise led to an increase of 12 °C in the back of the bed and 6°C further up.

The thermal conductivity of the bed was changed by using different carrier gases. Typically N_2 is used. Here He, N_2, Ar and Kr changed effective thermal conductivity of the bed from .51 W/(m*K) to .091 W/(m*K). The results showed an increase in activity as thermal conductivity increased. The temperature profile of each run showed much more heat at the front of the bed for the higher thermal conductivity gases. This is direct evidence that the combination of negative order reaction kinetics and enhanced thermal conductivity lead to the transfer of heat from the rear active zone of the bed to the deactivated zone in the front. The He carrier showed a temperature rise not seen in the other carrier gases. This was also tested with microfibrous entrapped catalyst. The enhanced microfibrous catalyst showed much longer activity than the packed bed counterpart.

The reactor model created in Chapter 5 was employed to explain the evolution in activity seen in the carrier gas experiments. It was found the packed bed goes through 4 main stages. At first the bed heats up and the conversion increases with the bed temperature. This is followed by the conversion improving and the amount of active bed increasing as a concentration of 0 CO is moved further in the packed bed. As the catalytic bed heated up further, the water pre-adsorbed on the SiO_2 inert and catalyst support decreased, which slows the reaction between O adsorbed on the CeO_2 and the CO adsorbed on the Pt. Once a critical amount of water is lost, the bed slowly deactivates and reaches a much less active equilibrium.

This work accomplished 3 main goals. A more active, cheaper, easier to produce catalyst was made. A kinetic model was produced which can predict the behavior of a packed bed a wide range of conditions, including wet environments. Finally, the back diffusion of heat was tested qualitatively and quantitatively; it was shown to be important to catalyst activity by varying the effective thermal conductivity and inducing a poisoned bed to activate from the back to the front.

7.2 Future Work

To explore the affect of axial conductivity directly, microfibrous material will need to be employed. This can now be made into performs discussed earlier and dry packed with catalyst. The preforms allow an apples to apples comparison between different microfiber types and a packed bed. Currently nickel and copper can be produced. Stainless steel is also possible but more difficult. This gives three different axial conductivities to test in microfibrous form. These can be further tweaked by increasing sintering time[110]. The dry entrapment procedure allows the catalyst particles to skip the wet lay process and all of the sintering, so the particles being compared in different meshes are the same. This will help isolate the effects of the mesh itself.

To accomplish the goal of altering the effective axial thermal conductivity, collecting the axial temperature profile independent of the oxidation reaction is key. The heater described in 3.2.7 Axial Temperature Profile Measurement Apparatus and Heater along with the analysis in Figure 6-7 needs to be repeated for the other micofibrous materials. The stainless steel and nickel should follow an analogous procedure as the copper. Measuring this quantity instead of relying on literature correlations is needed because the system is unique and depends on an accurate thermal conductivity parameter. The air is humid and the materials used are unique.

In addition to the axial thermal conductivity, the radial thermal conductivity also needs to be studied. The radial orientation of the microfibrous fibers means the radial thermal conductivity is much higher than axial[110]. This could have large implications on the adiabatic reactor assumption used earlier.

Another reactor design needed to determine k_{effr}. Thermocouple ports at the same bed depth, followed by more at a higher bed depth can measure the radial temperature profile at two axially distinct locations at the same time. With two radial profiles at different positions down the bed, k_{effr}, the heat transfer coefficient between the bed and reactor wall, as well as, the reactor wall and the ambient air can be determined. A strong understanding of the heat flows in the packed bed and the energy balance can be modeled confidently leaving the CO oxidation reaction as a separate issue.

It is mentioned that in section 5.5.2 Kinetic Tests and Model Fitting that the 12% of the surface Pt has access to O from the CeO_2. This can be checked with EXAFS. The nearest

Pt neighbor can be determined. An increase in CeO_2 character should be able to be detected. The procedure to do so has already been explored by Nagai et al. [132].

There are also two reactor design criteria which could be explored. It was shown in Chapter 5 that the reaction is mass transfer limited below about 150 ppm. A reactor structure could be designed to taper toward the rear of the bed. The lower cross section would lead to an increase in velocity and thus an increase in mass transfer between the catalyst particles and the bulk. Another reactor could make use of a composite bed. In Chapter 2 the Au on TiO_2 catalyst is shown to be active in dry conditions but not wet. This is the opposite behavior of the Pt-CeO_2 on SiO_2 catalyst. A composite bed could combine the strengths of the two catalyst to produce a filter that can work from 0 to 95% RH and very low(-20 °C) to very high temperatures.

Works Cited

[1] F. Rodkey, J. Oneal, H. Collision and D. Uddin, "Relative Affinity ofo Hemoglobin-S and Hemoglobin-A for Carbon-Monoxide and Oxygen," *CLINICAL CHEMISTRY,* vol. 20, no. 1, pp. 83-84, 1974.

[2] A. Ernst and J. Zibrak, "Carbon Monoxide Poisoning," *The New England Journal of Medicine,* vol. 339, pp. 1603-1608, 26 November 1998.

[3] J. M. Moore, P. L. Adcock, J. B. Lakeman and G. O. Mepsted, "The effects of battlefield contaminants on PEMFC performance," *Journal of Power Sources,* no. 85, pp. 254-260, June 1999.

[4] W. C. B. o. B. Columbia, "Carbon Monoxide in Industry," 2009.

[5] I. Langmuir, "The mechanism of the catalytic action of platinum in the reactions 2Co + O2= 2Co2 and 2H2+ O2= 2H2O," *Transactions of the Faraday Society,* vol. 17, pp. 621 - 654, 1922.

[6] A. B. Lamb, W. C. Bray and J. C. Frazer, "The Removal of Carbon Monoxie From Air," *The Journal of Industrial and Engineering Chemistry,* vol. 12, no. 3, pp. 213-221, January 1920.

[7] J. A. Almquist and C. W. Bray, "The Catalytic Oxidation of Carbon Monoxide. I. Efficiency of the Catalysts, Manganese Dioxide, Cupric Oxide and Mixtures of These Oxides," *Journal of the American Chemical Society,* vol. 45, no. 10, pp. 2305-2322, October 1923.

[8] M. Haruta, N. Yamada, T. Kobayahi and S. Iijima, "Gold catalysts prepared by coprecipitation for low-temperature oxidation of hydrogen and of carbon monoxide," *Journal of Catalysis,* vol. 115, no. 2, pp. 301-309, February 1989.

[9] E. D. Park and J. S. Lee, "Effects of Pretreatment Conditions on CO Oxidation over Supported Au Catalysts," *Journal of Catalysis,* vol. 186, pp. 1-11, April 1999.

[10] H. Imai, M. Date and S. Tsubota, "Preferential Oxidation of CO in H2-Rich Gas at Low Temperatures over Au Nanoparticles Supported on Metal Oxides," *CATALYSIS LETTERS,* vol. 124, no. 1-2, pp. 68-73, 2008.

[11] S. Li, G. Liu, H. Lian, M. Jia, G. Zhao, D. Jiang and W. Zhang, "Low-temperature CO oxidation over supported Pt catalysts prepared," *Catalysis Communications,* vol. 9, pp. 1045-1049, 8 October 2008.

[12] H. Zhu, Z. Qin, W. Shan, W. Shen and J. Wang, "Low-temperature oxidation of CO over Pd/CeO2–TiO2 catalysts," *Journal of Catalysis,* vol. 233, pp. 41-50, 23 May 2005.

[13] Y. Huang, A. Wang, X. Wang and T. Zhang, "Preferential oxidation ofCOunder excessH2 conditions," *International Journal of Hydrogen Energy,* vol. 32, pp. 3880-3886, May 2007.

[14] M. M. Yung, E. M. Holmgreen and U. S. Ozkan, "Low-temperature Oxidation of Carbon Monoxide on Co/ZrO2," *Catalysis Letters,* vol. 118, pp. 180-186, July 2007.

[15] Z. Zhao, M. Yung and U. Ozkan, "Effect of support on the preferential oxidation of CO over cobalt catalysts," *Catalysis Communications,* vol. 9, no. 6, pp. 1465-1471, March 2008.

[16] J. D. Cox, D. D. Wagman and V. A. Medvedev, CODATA Key Values for Thermodynamics, New York, New York: Hemisphere Publishing Corp, 1989.

[17] F. Liang, H. Zhu, Z. Qin, H. Wang, G. Wang and J. Wang, "Positive Effect of Water Vapor on CO Oxidation at Low," *Catalyst Letters,* vol. 126, pp. 353-360, August 2008.

[18] M. A. Centeno, C. Portales, I. Carrizosa and J. Ordiozola, "Gold supported

CeO2/Al2O3 catalysts for CO oxidation: influence of the ceria phase," *CATALYSIS LETTERS,* vol. 102, no. 3-4, pp. 289-297, 2005.

[19] Y.-M. Kang and B.-Z. Wan, "Pretreatment effect of gold/iron/zeolite-y on carbon monoxide oxidation," *Catalysis Today,* vol. 26, no. 1, pp. 59-69, 30 August 1995.

[20] M. A. Bollinger and M. A. Vannice, "A kinetic and DRIFTS study of low-temperature carbon monoxide oxidation over Au—TiO2 catalysts," *Applied Catalysis B: Environmental,* vol. 8, no. 4, pp. 417-443, July 1996.

[21] M. Date and M. Maruta, "Moisture Effect on CO Oxidation over Au/TiO2 Catalyst," *Journal of Catalysis,* vol. 201, no. 2, pp. 221-224, July 2001.

[22] M. Data, M. Okumura, S. Tsubota and M. Haruta, "Vital Role of Moisture in the Catalytic Activity of Supported Gold Nanoparticles," *Angewandte Chemie International Edition,* vol. 43, no. 16, pp. 2129-2132, April 2004.

[23] L. E. Briand, W. E. Farneth and I. E. Wachs, "Quantitative determination of the number ofactive surface sites and the turnover frequencies for methanol oxidation over metal oxide catalysts I. Fundamentals of the methanol chemisorption technique and application to monolayer supported molybdenum oxide," *Catalysis Today,* vol. 62, pp. 219-229, 2000.

[24] J. F. Scholten, A. P. Pijpers and A. M. L. Hustings, "Surface Characterization of Supported and Nonsupported Hydrogenation Catalyst," *Catalysis Reviews: Science and Engineering,* vol. 27, no. 1, pp. 151-206, 1985.

[25] A. Borodzinski and M. Bonarowka, "Relation between Crystallite Size and Dispersion on Supported Metal Catalysts," *Langmuir,* vol. 13, no. 21, 1997.

[26] C.-B. Wang, C.-W. Tang, H.-C. Tsai, M.-C. Kuo and S.-H. Chien, "In situ FT-IR Spectroscopic Studies on the Mechanism of the Catalytic Oxidation of Carbon

Monoxide over Supported Cobalt Catalysts," *Catalysis Letters,* vol. 107, no. 1-2, pp. 31-37, 25 November 2006.

[27] M. Okumura, S. Nakamura, S. Tsubota, T. Nakamura, M. Azuma and M. Haruta, "Chemical vapor deposition of gold on Al2O3, SiO2, and TiO2 for the oxidation of CO and of H2," *Catalysis Letters,* vol. 51, no. 1-2, pp. 53-58, 9 January 1998.

[28] M. Haruta, S. Tsubota, T. Kobayashi, H. Kageyama, M. J. Genet and B. Delmon, "Low-Temperature Oxidation of CO over Gold Supported on TiO2, a-Fe2O3, and Co3O4," *Jounral of Catalysis,* vol. 144, pp. 175-192, 14 June 1993.

[29] M. Data, Y. Ichihashi, T. Yamashita, A. Chiorino, F. Boccuzzi and M. Haruta, "Performance of Au/TiO2 catalyst under ambient conditions," *Catalysis Today,* vol. 72, no. 1-2, pp. 89-94, 15 Februrary 2002.

[30] F. Boccuzzi, A. Chiorio, M. Manzoli, P. Lu, T. Akita, S. Ichikawa and M. Haruta, "Au/TiO2 Nanosized Samples: A Catalytic, TEM, and FTIR Study," *Journal of Catalysis,* vol. 202, pp. 256-267, 21 May 2001.

[31] J.-Y. Luo, M. Meng, X. Li, X.-G. Li, Y.-Q. Zha, T.-D. Hu, Y.-N. Xie and J. Zhang, "Mesoporous Co3O4–CeO2 and Pd/Co3O4–CeO2 catalysts:," *Journal of Catalysis,* vol. 254, pp. 310-324, 4 January 2008.

[32] L. F. Liotta, G. Dicarlo, A. Longo, G. Pantaleo and A. M. Venezia, "Support effect on the catalytic performance of Au/Co3O4–CeO2 catalysts for CO and CH4 oxidation," *Catalysis Today,* vol. 139, no. 3, pp. 174-179, 30 December 2008.

[33] F. J. Gracia, L. Bollmann, E. E. Wolf, J. T. Miller and A. J. Kropf, "In situ FTIR, EXAFS, and activity studies of the effect of crystallite size on silica-supported Pt oxidation catalysts," *Journal of Catalysis,* vol. 220, no. 2, pp. 382-391, 10 Devember 2003.

[34] S. Wang, J. Huang, L. Geng, B. Zhu, X. Wang, S. Wu, S. Zhang and W. Huang, "Tin Dioxide Supported Nanometric Gold: Synthesis, Characterization, and Lowtemperature Catalytic Oxidation of CO," *CATALYSIS LETTERS,* vol. 108, no. 1-2, pp. 97-102, 2006.

[35] G. P. Osorio, S. F. Moyado, V. Petranovskii and A. Simakov, "PdO/Al2O3–(Ce1-XZrX)O2 catalysts: effect of the sol-gel support composition," *CATALYSIS LETTERS,* vol. 110, no. 1-2, pp. 53-60, August 2006.

[36] G. Dong, J. Wang, Y. Gao and S. Chen, "A novel catalyst for CO oxidation at low temperature," *Catalysis Letters,* vol. 58, no. 1, pp. 37-41, 12 January 1999.

[37] O. S. Alexeev, S. Y. Chin, M. H. Engelhard, L. Ortiz-Soto and M. D. Amiridis, "Effects of Reduction Temperature and Metal−Support Interactions on the Catalytic Activity of Pt/γ-Al2O3 and Pt/TiO2 for the Oxidation of CO in the Presence and Absence of H2," *The Journal of Physical Chemistry B,* vol. 109, no. 49, pp. 23430-23443, 22 November 2005.

[38] O. Pozdnyakova, D. Teschner, A. Wootsch, J. Krohnert, B. Steinhauer, H. Sauer, L. Toth, F. C. Jentoft, A. Knop-Gericke, Z. Paal and R. Schlogl, "Preferential CO oxidation in hydrogen (PROX) on ceria-supported catalysts, part I: Oxidation state and surface species on Pt/CeO2 under reaction conditions," *Journal of Catalysis,* vol. 237, no. 1, pp. 1-16, 1 January 2006.

[39] D. Li, X. Liu, Q. Zhang, Y. Wang and H. Wan, "Cobalt and Copper Composite Oxides as Efficient Catalysts for Preferential Oxidation of CO in H2-Rich Stream," *Catalysis Letters,* vol. 127, no. 3-4, pp. 377-385, 11 November 2009.

[40] S. Guerrero, J. T. Miller and E. E. Wolf, "Activity and selectivity control by niobium for the preferential oxidation of co on pt supported catalysts," *Applied Catalysis A:*

General, vol. 328, no. 1, pp. 27-34, 31 August 2007.

[41] J. Yang, V. Tschamber, D. Habermacher, F. Garin and P. Gilot, "Effect of sintering on the catalytic activity of a Pt based catalyst for CO oxidation: Experiments and modeling," *Applied Catalysis B: Environmental,* vol. 83, no. 3-4, pp. 229-239, 23 September 2008.

[42] J. T. Calla and R. J. Davis, "X-ray absorption spectroscopy and CO oxidation activity of Au/Al2O3 treated with NaCN," *Catalysis Letters,* vol. 99, no. 1-2, pp. 21-26, 2004.

[43] J. L. Ayastuy, M. P. Gonzalez-Marcos, A. Gil-Rodriguez, J. R. Gonzalez-Velasco and M. A. Gutierrez-Ortiz, "Selective CO oxidation over CeXZr1-XO2-supported Pt catalysts," *Catalysis Today,* vol. 116, pp. 391-399, 2006.

[44] N. Maeda, T. Matsushima, H. Uchida, H. Yamashita and M. Watanabe, "Performance of Pt-Fe/mordenite monolithic catalysts for preferential oxidation of carbon monoxide in a reformate gas for PEFCs," *Applied Catalysis A: General,* vol. 341, pp. 93-97, 2008.

[45] M. Watanabe, H. Uchida, K. Ohkubo and H. Igarashi, "Hydrogen purification for fuel cells: selective oxidation of carbon monoxide on Pt–Fe/zeolite catalysts," *Applied Catalysis B: Enviromental,* vol. 46, pp. 595-600, 2003.

[46] G. Uysal, A. N. Akin, Z. I. Onsan and R. Yildrim, "Preferential CO oxidation over Pt–SnO2/Al2O3 containing CO2and H2O in hydrogen rich streams containing CO2and H2O (CO removal from H2," *Catalysis Letters,* vol. 111, no. 3-4, pp. 173-176, 2006.

[47] T. Komatsu and A. Tamura, "Pt3Co and PtCu intermetallic compounds: Promising catalysts for preferential oxidation of CO in excess hydrogen," *Journal of Catalysis,* vol. 258, pp. 3066-314, 2008.

[48] A. Luengnaruemitchai, M. Nimsuk, P. Naknam, S. Wonkasemjit and S. Osuwan, "A

comparative study of synthesized and commercial A-type zeolite-supported Pt catalysts for selective CO oxidation in H2-rich stream," *International Journal of Hydrogen Energy,* vol. 33, pp. 206-213, 2008.

[49] Y. Bi, L. Chen and G. Lu, "Constructing surface active centres using Pd–Fe–O on zeolite for CO oxidation," *Journal of Molecular Catalysis A: Chemical,* vol. 266, pp. 173-179, 2007.

[50] F. Liang, H. Zhu, Z. Qin, H. Wang, G. Wang and J. Wang, "Positive Effect of Water Vapor on CO Oxidation at Low Temperature over Pd/CeO2–TiO2," *Catalysis Letters,* vol. 126, pp. 353-360, 2008.

[51] S. S. Punde and B. J. Tatarchuk, "Microfibrous Entrapped Catalysts for Low Temperature CO Oxidation," in *AIChE Annual Meeting Conference Proceedings*, Salt Lake City, UT, 2010.

[52] S. S. Punde and J. B. Tatarchuk, "Metal microfibers entrapped catalysts as effective ambient temperature CO oxidation catalysts," *Applied Catalysis A: General,* Vols. 441-442, no. 54-64, October 2012.

[53] T. Engel and G. Ertl, "lementary Steps in the Catalytic Oxidation of Carbon Monoxide on Platinum Metals," *Advances in Catalysis,* vol. 28, pp. 1-78, 1979.

[54] S. Royer and D. Duprez, "Catalytic Oxidation of Carbon Monoxide over Transition Metal Oxides," *ChemCatChem,* vol. 3, pp. 24-65, 2011.

[55] G. Ertl, P. R. Norton and J. Rustig, "Kinetic Oscillations in the Platinum-Catalyzed Oxidation of CO," *Physical Review Letters,* vol. 49, no. 2, pp. 177-180, 1982.

[56] N. V. Peskov, M. M. Slinko and N. I. Jaeger, "Stochastic model of reaction rate oscillations during CO oxidation over zeolite-supported catalysts," *Chemical Engineering Science,* vol. 58, pp. 4797-4803, 2003.

[57] A. Bournane, O. Dulaurent and D. Bianchi, "Heats of Adsorption of Linear and Multibound Adsorbed CO Species on a Pt/Al2 under Adsorption Equilibrium," *Journal of Catalysis,* vol. 198, no. 1, pp. 115-125, 2000.

[58] Y. Y. Yeo, L. Vattuone and D. A. King, "Calorimitric heats for CO and oxygen adsorption and for the catalytic CO oxidation reaction on Pt{111}," *Journal of Chemical Physics,* vol. 106, no. 1, pp. 392-401, 1997.

[59] G. Borden, G. Pirug and H. P. Bonzel, *Surface Science,* vol. 72, p. 45, 1978.

[60] R. W. McCabe and L. D. Schmidt, *Surface Science,* vol. 66, p. 101, 1977.

[61] R. W. McCabe and L. D. Schmidt, *Surface Science,* vol. 60, p. 85, 1976.

[62] C. M. Comrie and R. M. Lambert, *Journal of the Chemical Society, Faraday Transactions 1: Physical Chemistry in Condensed Phase,* vol. 72, p. 1659, 1976.

[63] J. M. Martinez and J. B. Hudson, *Journal of Vacuum Science and Technology A,* vol. 10, p. 35, 1973.

[64] G. Ertl, H. Neumann and K. M. Steit, *Surface Science,* vol. 64, p. 393, 1977.

[65] C. T. Cambell, G. Ertl, H. Kuppers and J. Segner, *Surface Science,* vol. 107, p. 207, 1981.

[66] R. G. Compton, C. H. Bamford and F. H. Tippert, Eds., Simple Processes at the Gas-Solid Interface, vol. 19, Elsevier Science Publishing Company Inc., 1984.

[67] D. A. King, "The influence of weakly bound intermediate states on thermal desorption kinetics," *Surface Science,* vol. 64, no. 1, pp. 43-51, 1977.

[68] H. P. Bonzel and R. Ku, *Surface Science,* vol. 40, p. 85, 1973.

[69] L. R. Clavenna and L. D. Schmidt, *Surface Science,* vol. 33, p. 11, 1972.

[70] G. Ertl, K. Krischer and R. M. Eiswirth, "Nonlinear Dynamics in the CO-Oxidation on

Pt Single Crystal Surfaces," *Applied Physics A,* vol. 51, pp. 79-90, 1990.

[71] M. Alnot, A. Cassuto, J. Fusy and A. Pentenero, *Japanese Journal of Applied Physics Part 2,* vol. 2, p. 79, 1974.

[72] M. Wilf and P. T. Dawson, *Surface Science,* vol. 65, p. 399, 1977.

[73] C. T. Campbell, G. Ertl, M. Kuipper and J. Senger, *Surface Science,* vol. 107, p. 220, 1981.

[74] G. Kim, "Ceria-Promoted Three-Way Catalyst for Auto Exhaust Emission Control," *Industrial & Engineering Chemistry Product Research and Development,* vol. 21, no. 2, pp. 267-274, 1982.

[75] S. K. Jain, E. M. Crab, L. E. Smart, D. Thompsett and A. M. Steele, "Controlled modification of Pt/Al2O3 for the preferential oxidation of CO in hydrogen: A comparative study of modifying element," *Applied Catalysis B: Enviromental,* vol. 89, pp. 349-355, 2009.

[76] L. Xu, Y. Ma, Y. Zhang, Z. Jiang and W. Huang, "Direct Evidence for the Interfacial Oxidation of CO with Hydroxyls Catalyzed by Pt/Oxide Nanocatalysts," *Journal of the American Chemical Society,* vol. 131, no. 45, pp. 16366-16367, 2009.

[77] U. Oran and D. Uner, "Mechanisms of CO oxidation reaction and effect of chlorine ions on the CO oxidation reaction over Pt/CeO2 and Pt/CeO2," *Applied Catalysis B: Enviroemntal,* vol. 54, pp. 183-191, 2004.

[78] R. H. Nibbelke, M. J. Campman, J. J. Hoebink and G. B. Marin, "Kinetic Study of the CO Oxidation over Pt/°-Al2 and Pt/Rh/CeO2/°-Al2O3 in the Presence of H2," *Journal of Catalysis,* vol. 171, no. 2, pp. 358-373, 1997.

[79] S. H. Cho, J. S. Park, S. H. Choi, S. K. Lee and S. H. Kim, "Effect of water vapor on carbon monoxide oxidation over promoted platinum catalysts," *Catalysis Letters ,* vol.

103, no. 3-4, pp. 257-261, October 2005.

[80] J. Bergeld, B. Kasemo and D. V. chakarov, "CO oxidation on Pt(111) promoted by coadsorbed H2O," *Surface Science,* vol. 495, no. 3, pp. L815-L820, 2001.

[81] X.-Q. Gong, P. Hu and R. Raval, "The catalytic role of water in CO oxidation," *The Journal of Chemical Physics,* vol. 119, no. 12, pp. 6324-6334, 2003.

[82] A. B. Mhadashwar and D. G. Vlachos, "Microkinetic Modeling for Water-Promoted CO Oxidation, Water-Gas Shift, and Preferential Oxidation of CO on Pt," *Journal of Physical Chemistry B,* vol. 108, pp. 15246-15258, 2004.

[83] M. Date, M. Okumura, S. Tsuboata and M. Haruta, "Vital Role of Moisture in the Catalytic Activity of Supported Gold Nanoparticles," *Angewandte Chemie Internal Edition,* vol. 43, no. 16, pp. 2129-2132, March 2004.

[84] K.-i. Tanaka, M. Shou, H. He, X. Shi and X. Zhang, "Dynamic Characterization of the Intermediates for Low-Temperature PROX Reaction of CO in H2sOxidation of CO with OH via HCOO Intermediate," *Journal of Physical Chemistry C,* vol. 113, pp. 12427-12433, 2009.

[85] G. N. Ozyonum, A. N. Akin and R. Yildrim, "Kinetic Study of Selective CO Oxidation over Pt-Co-Ce/Al2O3 Catalyst in Hydrogen-Rich Streams.," *Turkish Journal of Chemistry,* vol. 31, no. 5, pp. 445-453, 2007.

[86] S. Ren and X. Hong, "CO selective oxidation in hydrogen-rich gas over platinum catalysts," *Fuel Processing Technology,* vol. 88, no. 4, 2007.

[87] Y. J. Mergler, A. v. Aalst, J. v. Delft and B. E. Nieuwenhuys, "CO oxidation over promoted Pt Catalyst," *Applied Catalysis B: Enviromental ,* vol. 10, pp. 245-261, 1996.

[88] F. Duprat, "Light-o curve of catalytic reaction and kinetics," *Chemical Engineering Science,* vol. 57, pp. 901-911, 2002.

[89] E. Achenbach, "Heat and Flow Characteristics of Packed Beds," *Experimental Thermal and Fluid Science,* vol. 10, pp. 17-21, 1995.

[90] S. Yagi, D. Kunii and K. Endo, "Heat Tranfer in Packed Beds Through Which Water Is Flowing," *International Journal of Heat and Mass Transfe,* vol. 7, pp. 333-339, 1964.

[91] D. Vortmeyer, "Packed Bed Thermal Dispersion Models and Consistent Sets of Coefficients," *Chemical Engineering and Processing: Process Intensification,* vol. 26, pp. 263-268, 1989.

[92] E. U. Schlunder, "Warme-und Stoffunbertragung zwischen durch-stromten Schuttengen und darin eingenbetteten Einzelkorpern," *Chemie Ingenieur Technik,* vol. 38, pp. 767-979, 1966.

[93] C. S. Sharma and R. Hughes, "The thermal conductivity of porous catalyst compacts," *The Canadian Journal of Chemical Engineering,* vol. 1976, pp. 358-363, 1976.

[94] E. W. Schumann and V. Voss, "Heat flow through granulated material," *Fuel in Science and practice,* vol. 13, pp. 249-256, 1934.

[95] V. Yakhnin and M. Menzinger, "Stationary and traveling hot spots in the catalytic combustion of hydrogen in monoliths," *Chemical Engineering Science,* vol. 57, pp. 4559-4567, 2002.

[96] M. Sun, E. B. Croiset, R. R. Hudgins, P. L. Silveston and M. Menzinger, "Steady-State Multiplicity and Superadiabatic Extinction Waves in the Oxidation of CO/H2 Mixtures over a Pt/Al2O3-Coated Monolith," *Industrial & Engineering Chemistry Research,* vol. 42, pp. 37-45, 2003.

[97] J. Puszynski and V. Hlavacek, "Experimental study of traveling waves in nonadiabatic fixed bed reactors for the oxidation of carbon monoxide," *Chemical Engineering Science,* vol. 35, no. 8, pp. 1769-1774, 1980.

[98] J. Puszynksi, D. Snita, V. Hlavacek and H. Hofmann, "A Revision of Mulitplicy and Parametric Sensitivity Concents in Nonisothermal Nonadiabatic Packed Bed Chemical Reactors," *Chemical Engineering Science,* vol. 36, no. 10, pp. 1605-1609, 1981.

[99] O. Bilous and N. R. Amundson, "Chemical reactor stability and sensitivity: II. Effect of parameters on sensitivity of empty tubular reactors," *AIChE Journal,* vol. 2, no. 1, pp. 117-126, 1956.

[100] D. Harris, D. Cahela and B. Tatarchuk, "Wet layup and sintering of metal-containing microfibrous composites for chemical processing opportunities," *Composites Part A: Applied Science and Manufacturing,* vol. 32, no. 8, pp. 1117-1126, 2001.

[101] R. R. Kalluri, "Microfibrous Entrapped Catalyst And Sorbents: Microsturcted Heterogeneous Contancting Systems With Enhanced Efficiency," Auburn, AL, 2008.

[102] C. J. Marrion, D. R. Cahela, S. Ahn and B. J. Tatarchuk, "Composite fiber structures for catalysts and electrodes," *Journal of Power Sources,* vol. 47, pp. 294-302, 1994.

[103] D. Kennedy, "Fuel cell cathode air filters: methodologies for design and optimization.," Auburn, AL, 2007.

[104] R. Kalluri, "Microfibrous entrapped catalyst and sorbents: microstructure heterogeneous contacting systems with enhanced efficiency.," Auburn AL, 2008.

[105] M. R. Karanjikar, "Low Temperature Oxidation Of Carbon Monoxide Using Microfibrous Entrapped Catalysts For Fire Escape Mask Appication," Auburn, AL, 2005.

[106] B.-K. Chang, "Fuel Processing For Fuel Cells: Preferential Oxidation (PROX) Of Carbon Monoxide From Practical Reformates For PEM H2-O2 Fuel Cells Using Hight Contacting Efficiency Microfibrous Entrapped Catalysts," Auburn, AL, 2004.

[107] Q. Gu, R. T. Henderson and J. B. Tatarchuk, "Comparision of packed beds, wash-

coated monoliths and microfibrous entrapped catalysts for ozone decomposition at high columetric flow rates in pressurized systems," *Applied Catalysis B: Enviromental,* To Be Published.

[108] R. R. Kalluri, D. R. Cahela and B. J. Tatarchuk, "Comparative heterogeneous contacting efficiency in fixed bed reactors:Opportunities for new microstructured systems," *Applied Catalysis B: Enviromental,* vol. 90, pp. 507-515, 2009.

[109] A. Kolodziej and J. Lojewska, "Short-channel structured reactor for catalytic combustion:Design and evaluation," *Chemical Engineering and Processing,* vol. 48, no. 2, pp. 637-648, 2007.

[110] B.-K. Chang and B. J. Tatarchuk, "Microfibrous Entrapment of Small Catalyst Particulates for High Contacting Efficiency Removal of Trace CO From Practical Reformates for PEM H2-O," *Journal of Materials Engineering and Performance,* vol. 15, no. 4, pp. 453-456, August 2006.

[111] M. Sheng, "Enhanced Heat Transfer Catalyst Structures for Fischer-Tropsch Synthesis," Auburn, AL, 2011.

[112] S. Mattson and J. Pugh, "The Laws Of Soul Colloidal Behavior: XIV. The Electrokinetics Of Hydrous Oxides And Their Ionic Exchange," *Soil Science,* vol. 38, no. 4, pp. 299-314, 1934.

[113] J. Park and J. R. Regalbuto, "A Simple, Accurate Determination of Oxide PZC and the Strong Buffereing Effect of Oxide Surfaces at Incipient Wetness," *Journal of Colloid And Interface Science,* vol. 175, pp. 239-252, 1995.

[114] S. Marc, T. E. Feltes, M. T. Schaal and J. R. Regalbuto, "The determination of oxide surface charging parameters for a predictive metal adsorption model," *Journal of Colloid and Interface Science,* vol. 348, pp. 571-578, 2010.

[115] M. Schreier and J. R. Regalbuto, "A fundamental study of Pt tetraammine impregnation of silica 1. The electrostatic nature of platinum adsorption," vol. 225, pp. 190-202, 2004.

[116] T. W. Healy and L. R. White, "Ionizable surface group models of aqueous interfaces," *Advances in Colloid and Interface Science,* vol. 9, no. 4, pp. 303-345, June 1978.

[117] X. Hao, S. Barnes and J. R. Regalbuto, "A fundamental study of Pt impregnation of carbon: Adsorption equilibrium and particle synthesis," *Journal of Catalysis,* vol. 279, pp. 48-65, 2011.

[118] X. Hao, L. Quach, J. Korah, W. A. Spieker and J. R. Regalbuto, "The control of platinum impregnation by PZC alteration of oxides and carbon," *Journal of Molecular Catalysis A: Chemical,* vol. 219, no. 1, pp. 97-107, 2004.

[119] G. A. Parks, "The Isoelectric Points of Solid Oxides, Solid Hydroxides, and Aqueous Hydroxo Complex Systems," *Chemical Reviews,* vol. 65, no. 2, pp. 177-198, 1 April 1965.

[120] B. Harrison, A. F. Diwell and C. Hallet, "Promoting Platinum Metals by Ceria Metal-Support Interactions in Autocatalysts," *Platinum Metals Review,* vol. 32, no. 2, pp. 73-83, 1988.

[121] E. C. Boelman, B. B. Saha and T. Kashiwagi, "Experimental investigation of the silica gel-water adsorption refrigeration cycle - The influence of operating conditions on cooling output and COP," 1995.

[122] R. B. Bird, W. E. Stewart and E. N. Lightfoot, Transport Phenomena Second Editions, Danvers, MA: John Wiley & Sons Inc, 2002.

[123] S. E. Voltz, C. R. Morgan, D. Liederman and S. M. Jacob, "Kinetic study of carbon monoxide and propylene oxidation on platinum catalysts.," *Industrial & Engineering*

Chemistry and Product Research and Development, vol. 12, no. 4, pp. 294-301, 1973.

[124] E. O. Pedram and A. L. Hines, "Pure Vapor Adsorption of Water on Mobil Sorbead R Silica Gel," *Journal of Chemical and Engineering Data,* vol. 28, pp. 11-14, 1983.

[125] M. M. Dubinin, "The Potential Theory of Adsorption of Gases and Vapors for Adsorbents with Energetically Nonuniform Surfaces," *Chemical Reviews,* vol. 60, no. 2, pp. 235-241, 1960.

[126] B. P. Bering, M. M. Dubinin and V. V. Serpinsky, "Theory of volume filling for vapor adsorption," *Journal of Colloid and Interface Science,* vol. 21, no. 4, pp. 378-393, 1966.

[127] D. Thoenes and H. Kramers, "Mass transfer from spheres in various regular packings to a flowing fliud," *Chemical Engineering Science,* vol. 8, no. 3, pp. 271-283, 1958.

[128] G. Langer, A. Roethe, K. P. Roethe and D. Gelbin, "Heat and Mass Transfer in Packed Beds - III. Axial Mass Dispersoin," *International Journal of Heat Mass Tranfer,* no. 21, pp. 751-759, 1978.

[129] R. S. Brokaw, "Predicting Transport Properties of Dilute Gases," *Industrial & Enineering Chemistry Process Design and Devlopement,* vol. 8, no. 2, pp. 240-253, 1969.

[130] Comsol Inc., "Comsol Multiphysics 4.3a," Comsol Inc., Burlington, MA, 2014.

[131] The Mathworks Inc., "MATLAB R 2014A," Mathworks Inc., Natick, MA, 2014.

[132] S. Nousir, S. Keav, J. Barbier, M. Bensitel, R. Brahmi and D. Duprez, "Deactivation phenomena during catalytic wet air oxidation (CWAO) of phenol over platinum catalysts supported on ceria and ceria–zirconia mixed oxides," *Applied Catalysis B: Environmental,* vol. 84, pp. 723-731, 2008.

[133] T. Nagai, T. Hirabayashi, K. Dohmae, N. Takagi, T. Manami, H. Shinjoh and S.

Matsumoto, "Sintering inhibition mechanism of platinum supported on ceria-based oxide and Pt-oxide-support interactions," *Journal of Catalysis,* vol. 242, pp. 103-109, 2006.

[134] C. Song, "Fuel processing for low-temperature and high-temperature fuel cells: Challenges, and opportunities for sustainable development in the 21st centur," *Catalysis Today,* vol. 77, no. 1-2, pp. 17-49, December 2002.

[135] C. Li, Y. Chen, W. Li and Q. Xin, "Spillover of atomic oxygen and reverse spillover of dioxygen species on Pt/CeO2 catalyst," *Studies in Surface Science and Catalysis,* vol. 77, pp. 217-222, 1993.

[136] Y. Nagai, T. Hirabayashi, K. Dohmae, N. Takagi, T. Minami, H. Shinjoh and S. Matsumoto, "Sintering inhibition mechanism of platinum supported on ceria-based oxide and Pt-oxide–support interaction," *Journal of Catalysis,* vol. 242, pp. 103-109, 2006.

[137] G. Langer, A. Roethe, K. P. Roethe and D. Gelbin, "Heat and Mass Transfer in Packed Beds - III," *International Journal of Heat and Mass Transfer,* vol. 21, no. 6, pp. 751-759, 1978.

[138] S. Salasc, V. Perrichon, M. Primet, M. Chevrier and N. Mouaddib-Moran, "Oxygen Titration of Spill-Over Hydrogen in Ceria and Ceria-Alumina Supported Platinum-Rhdium Catalysts: Application to theDtermination of the Ceria Surface in Contact with Metal," *Journal of Catalysis,* vol. 189, no. 2, pp. 401-109, 2000.

[139] R. Henderson and B. J. Tatarchuk, "Sensitivity of Room Temperature CO Oxidation: Sensitivity in a Negative Order Reaction," Salt Lake City, UT, 2010.

[140] S. S. Punde and B. J. Tatarchuk, "Microfibrous Entrapped Catalysts for Low Temperature CO oxidation," Salt Lake City, UT, 2010.

Appendix A Matlab and Comsol Code

A.1 Matlab Code for Fitting Kinetic Model Parameters

```
%This calls functions
% Step2k3k4COn
% Step2k3k4COnconc
% r4rate
% Step3k5Capcep
% Step3k5Capcepconc
% Step4Ea345p
% Step4Ea345pconc



k0 = [St(1);St(2);St(3)];


A0 = [];
b0 = [];
Aeq = [];
Beq = [];
ub = [10;.0121;.005];
lb = [.00001;.00001;.00001];
%ub = [10;1];
%lb = [0.00001;.00001];
nonlcon = [];
%options = optimset('Algorithm','interior-
point','MaxFunEvals',1200);
options = optimset('MaxFunEvals',1,'Algorithm','interior-
point','PlotFcns',@optimplotfval,'TolCon', 1e-6);
%A0=[-1,0,0;0,-1,0;0,0,-1;1,0,0;0,1,0;0,0,1];
%b0=[0;0;5e-6;700000;700;5e-3];
[soln2,fval]=fmincon(@Step2k3k4COn,k0,A0,b0,Aeq,Beq,lb,ub,nonlcon,op
tions);

sheet = 1;
Headings11 = {'SO'};
xlswrite('steps.xls',Headings11,sheet,'A1')
xlswrite('steps.xls',.23,sheet,'A2')

sheet = 2;
Headings21 = {'k3p/3e7','k4p','Con','fval','r4300'};
xlswrite('steps.xls',Headings21,sheet,'A1')
solnf = [soln2',fval];
xlswrite('steps.xls',solnf,sheet,'A2')
Headings22 = {'Step','Sum Error Squared'};
h = findobj(gca,'Type','line');
x=get(h,'Xdata');
```

```
y=get(h,'Ydata');
A = [x',y'];
%close h;
xlswrite('steps.xls',Headings22,sheet,'G1')
xlswrite('steps.xls',A,sheet,'G2')

Headings23 = {'Sum Error Squared','k3p/1e7','k4p','Con'};
M = csvread('step2.txt');
xlswrite('steps.xls',Headings23,sheet,'J1')
xlswrite('steps.xls',M,sheet,'J2')

Headings34 = {'ppmCO','Exp rr','Calc rr'};
N = Step2k3k4COnconc(soln2)
xlswrite('steps.xls',Headings34,sheet,'O1')
xlswrite('steps.xls',N,sheet,'O2')
rvar = r4rate(soln2);
xlswrite('steps.xls',rvar,sheet,'E2')

%Step 3

% k0 =[.6487
%     .5186];
% k0 = [6.044189422081E-01
% 4.209857363117E-01];

k0 = [St(4);St(5)];

%A0 = [-.5,1;0,0];
%b0=[0;0];
A0 = [];
b0 = [];
Aeq = [];
Beq = [];
%ub = [10;5;1];
%lb = [.00001;.00001;.00001];
ub = [100;100];
lb = [.001;.001];
nonlcon = [];
%options = optimset('Algorithm','interior-
point','MaxFunEvals',1200);
options = optimset('MaxFunEvals',400,'Algorithm','interior-
point','PlotFcns',@optimplotfval,'TolCon', 1e-6);
%A0=[-1,0,0;0,-1,0;0,0,-1;1,0,0;0,1,0;0,0,1];
%b0=[0;0;5e-6;700000;700;5e-3];
%params are k3p/1e7,k4p,Con,r4300
param = [soln2(1);soln2(2);soln2(3);rvar];
[soln3,fval3]=fmincon(@(kst)Step3k5Capcep(kst,param),k0,A0,b0,Aeq,Be
q,lb,ub,nonlcon,options)

sheet = 3;
Headings31 = {'k5o/1e18','Oce300/1e-7','fval'};
xlswrite('steps.xls',Headings31,sheet,'A1')
solnf3 = [soln3',fval3];
xlswrite('steps.xls',solnf3,sheet,'A2')
Headings32 = {'Step','Sum Error Squared'};
```

```
h = findobj(gca,'Type','line');
x=get(h,'Xdata');
y=get(h,'Ydata');
A3 = [x',y'];
%close h;
xlswrite('steps.xls',Headings32,sheet,'E1')
xlswrite('steps.xls',A3,sheet,'E2')

Headings33 = {'Sum Error Squared','k5o/1e18','Oce300/1e-7'};
M3 = csvread('step3.txt');
xlswrite('steps.xls',Headings33,sheet,'H1')
xlswrite('steps.xls',M3,sheet,'H2')

Headings34 = {'ppmCO','Exp rr','Calc rr'};
N3 = Step3k5Capcepconc(soln3,param);
xlswrite('steps.xls',Headings34,sheet,'L1')
xlswrite('steps.xls',N3,sheet,'L2')

%Step 4


k0 = [St(6);St(7);St(8)];

%k0 = [5;1e-2]
%A0 = [-.5,1;0,0];
%b0=[0;0];
A0 = [];
b0 = [];
Aeq = [];
Beq = [];
ub = [600;300;300];
lb = [1;1;1];
%ub = [100;200];
%lb = [.1;.1];
nonlcon = [];
%options = optimset('Algorithm','interior-
point','MaxFunEvals',1200);
options = optimset('MaxFunEvals',400,'Algorithm','interior-
point','PlotFcns',@optimplotfval,'TolCon', 1e-6);
%A0=[-1,0,0;0,-1,0;0,0,-1;1,0,0;0,1,0;0,0,1];
%b0=[0;0;5e-6;700000;700;5e-3];
%params are k3p/1e7,k4p,Con,r4300,k5o/1e18,Oce300/1e07
params = [soln2(1);soln2(2);soln2(3);rvar;soln3(1);soln3(2)];

[soln4,fval4]=fmincon(@(kst)Step4Ea345p(kst,params),k0,A0,b0,Aeq,Beq
,lb,ub,nonlcon,options)

sheet = 4;
Headings41 = {'Ea3','Ea4','Ea5','fval'};
xlswrite('steps.xls',Headings41,sheet,'A1')
solnf4 = [soln4',fval4];
xlswrite('steps.xls',solnf4,sheet,'A2')
Headings42 = {'Step','Sum Error Squared'};
h = findobj(gca,'Type','line');
x=get(h,'Xdata');
```

```
y=get(h,'Ydata');
A4 = [x',y'];
%close h;
xlswrite('steps.xls',Headings42,sheet,'F1')
xlswrite('steps.xls',A4,sheet,'F2')

Headings43 = {'Sum Error Squared','Ea3','Ea4','Ea5'};
M4 = csvread('step4.txt');
xlswrite('steps.xls',Headings43,sheet,'I1')
xlswrite('steps.xls',M4,sheet,'I2')

Headings44 = {'ppmCO','Exp rr','Calc rr'};
N4 = Step4Ea345pconc(soln4,params);
xlswrite('steps.xls',Headings44,sheet,'N1')
xlswrite('steps.xls',N4,sheet,'N2')
```

Step2k3k4kCOn

```
function out = noTemp(kst);
%
% 812noTemp.m
%
% Model exported on Aug 20 2014, 12:17 by COMSOL 4.2.0.150.




Datafit;
dim = size(Datafit,1);
poop3 = zeros(dim,3);
ks = kst;
errorh = [.04,1e-2
            .01,1e-4
            .008,1e-6
            .004,1e-8
            .001,1e-8];
for ii = 1:dim;
  erc = 1;
  erc1 = 0;
  while erc > erc1
      erc1 = 1+erc1;
    try
   strict = errorh(erc,:);
    datai = Datafit(ii,:);


import com.comsol.model.*
import com.comsol.model.util.*

model = ModelUtil.create('Model');
```

```
model.modelPath('C:\School\Recent\sdfkj');

model.name('812 no Temp diff reactor.mph');

model.hist.enable

model.param.set('ppmCOin', datai(1), 'Inlet CO concentration');
model.param.set('gcat', datai(3), 'Grams Catalyst');
model.param.set('ginert', '1-gcat', 'g Inert');
model.param.set('vel', datai(4), 'cm/s Superficial Velocity');
model.param.set('pcat', '670', 'kg/m^3 density of cat');
model.param.set('pinert', '329', 'kg/m^3 density of inert');
model.param.set('Atube', '1.98', 'cm^2 Area of Reactor');
model.param.set('L',
'gcat*100/(Atube*(pcat/100^2))/1000+ginert*100/(Atube*(pinert/100^2)
)/1000', 'cm Length Occupied by Catalyst and Inert');
model.param.set('V', 'L*Atube', 'cm^3 Volume Occupied by Catalyst
and Inert');
model.param.set('Rg', '8.314e-3', 'kJ/(mol*K) Gas Constant');
model.param.set('Tst', '299.15', 'K Starting Temp');
model.param.set('Mco', '28.01', 'g/mol Molecular Weight of CO');
model.param.set('Pst', 'gcat*(100^3/1000)/(V)', 'kg/m^3 Density of
Catalyst in Reactor');
model.param.set('Ptg', '2.9', 'm^2/g Surface Area Pt in Reactor');
model.param.set('Ptar', 'Ptg*Pst*1000/100', 'cm^2/cm^3 Surface Area
Pt per volume bed');
model.param.set('Fcoc',
'((Rg*1000*1000*Tst/(2*pi*Mco))^0.5)*Ptar*100', '1/s Bombardment
Rate of CO on Pt for 1 mol CO per Bed Volume in a second');
model.param.set('wtPt', '.04', 'Fraction Pt by weight');
model.param.set('mwPt', '195', 'g/mol Molecular weight Pt');
model.param.set('dsp', '.3', 'Pt Dispersion');
model.param.set('void', '.4', 'Void Fraction');
model.param.set('dp', '2.1e-4', 'm Particle Diameter');
model.param.set('ac', '6*(1-void)*(Pst/pcat)/dp', 'm^2 external
surface/m^3 Bed External surface area over Bed Volume');
model.param.set('Pts', 'wtPt*dsp*Pst*1000/(mwPt*100^3)', 'mol Pt/
cm^3 bed Moles of Pt at the surface per Volume Bed');
model.param.set('Fo2',
'((Rg*1000*1000*Tst/(2*pi*Mo2))^0.5)*Ptar*100', '1/s Bombardment
Rate of O2 on Pt for 1 mol O2 per Bed Volume in a second');
model.param.set('Mo2', '32', 'g/mol Molecular weight O2');
model.param.set('SO', '.23', 'Sticking Coeffecient of Oxygen');
model.param.set('O2', 'P/(Rg*1000*299.15)*Of*(1/100^3)', 'mol/cm^3
Concentration of Oxygen in the Reactor');
model.param.set('P', '101325', 'Pa Pressure in Reactor');
model.param.set('Of', '.21', 'Fraction Oxygen in Reactor');
model.param.set('Tin', '299.15', 'K Inlet Temp');
model.param.set('Coin',
'P/(Rg*1000*299.15)*(ppmCOin/1000000)*(1/100^3)', 'mol/cm^3 Inlet CO
Concnetration');
model.param.set('vels', 'vel/void', 'cm/s Velocity');
model.param.set('Dco', '.755', 'cm^2/s Diffusion Coeffecient for CO
in Air');
model.param.set('ke', 'keblork');
```

```
model.param.set('keblork', .0381*((datai(4)/(.4*100))^0.5)-
1.510732097154177e-002, 'm/s Fitted Value for transport Rate from
Bulk to Surface of Catalyst Pellet');
model.param.set('keold', '(0.0168*((vels/100)^0.5)-0.003)');
model.param.set('k3p', 30000000*ks(1), 'cm^2 Pt/(mol*s) Surface
Reaction Rate constant of adsorbed CO and O');
model.param.set('k4p', ks(2), 'cm^2 Pt/(mol*s) Surface Reaction Rate
constant of adsorbed CO and Oce');
model.param.set('k3', 'k3p/Ptar', 'cm^3 Bed/(mol*s) Volumetric
Reaction Rate constant of adsorbed CO and Oce');
model.param.set('k4', 'k4p/Ptar', 'cm^3 Bed/(mol*s) Volumetric
Reaction Rate constant of adsorbed CO and Oce');
model.param.set('kn2o', '10^13*exp(63/(Rg*299.15))', '1/s Surface
Desorption rate constnat of O on Pt.');
model.param.set('kn2', 'kn2o/(Pts)', 'cm^3 Bed/(s*mol) desorption
rate constant of O2 per volume bed');
model.param.set('Le', 'ke*ac', '1/s diffusion rate constnat
multiplied by area of CO to surface');
model.param.set('L1', 'Fcoc');
model.param.set('L2', 'Fo2*O2*SO');
model.param.set('Ln2', 'kn2');
model.param.set('L3', 'k3');
model.param.set('L4', 'k4');
model.param.set('Cost', 'Pts/(sqrt(Ln2/(L2))*Pts+1)', 'mol O
adsorbed onto surface per cm^3 bed to start');
model.param.set('theaOst', 'Cost/Pts');
model.param.set('dsdsd', 'P/(Rg*1000*Tin)*(1/1000000)*(1/100^3)');
model.param.set('rwer', 'Coin/dsdsd');
model.param.set('coadsrate', 'Fcoc*Coin');
model.param.set('o2adsrate', 'Fo2*O2*SO');
model.param.set('fg', 'O2/Coin');
model.param.set('gh', '1/.004');
model.param.set('sdf', '19.21*.004/.02933');
model.param.set('fgfg', '1/655');
model.param.set('fsfsfsf', 'Fo2/Fcoc');
model.param.set('Derr', '.00001');
model.param.set('COn', ks(3));
model.param.set('On', 1);
vel1 = datai(4);
Atube1 = 1.98;
Coin1 = 101325/(8.314e-3*1000*299.15)*(datai(1)/1000000)*(1/100^3);
ginert1 = (1-datai(3));
pcat1 = 670;
pinert1 = 329;
L1 =
datai(3)*100/(Atube1*(pcat1/100^2))/1000+ginert1*100/(Atube1*(pinert
1/100^2))/1000;




model.modelNode.create('mod1');

model.func.create('rm1', 'Ramp');
model.func('rm1').model('mod1');
```

```
model.func('rm1').set('location', '.1');
model.func('rm1').set('cutoffactive', true);
model.func('rm1').set('smoothloc', true);
model.func('rm1').set('smoothcutoff', true);

model.geom.create('geom1', 1);
model.geom('geom1').feature.create('i1', 'Interval');
model.geom('geom1').feature('i1').set('p2', 'L');
model.geom('geom1').run;

model.variable.create('var1');
model.variable('var1').model('mod1');
model.variable('var1').set('theta', '(C3+C2)/Pts');
model.variable('var1').set('re', 'Le*(Cg-C1)');
model.variable('var1').set('r1', 'L1*C1*((1-theta)*(COn))');
model.variable('var1').set('r2', 'L2*(1-theta)^2-Ln2*(C3)^2');
model.variable('var1').set('r3', 'L3*C2*C3');
model.variable('var1').set('r4', 'L4*C2*(1*Ptar)');

model.physics.create('c', 'CoefficientFormPDE', 'geom1');
model.physics('c').feature.create('dir1', 'DirichletBoundary', 0);
model.physics('c').feature('dir1').selection.set([1]);
model.physics.create('cdeq', 'ConvectionDiffusionEquation',
'geom1');
model.physics('cdeq').feature.create('flux1', 'FluxBoundary', 0);
model.physics('cdeq').feature('flux1').selection.set([1]);

model.mesh.create('mesh1', 'geom1');
model.mesh('mesh1').feature.create('auto_f1', 'Edge');



model.physics('c').field('dimensionless').component({'C1' 'C2'
'C3'});
model.physics('c').field('dimensionless').field('C');
model.physics('c').feature('cfeq1').set('c', {'Derr'; '0'; '0'; '0';
'Derr'; '0'; '0'; '0'; 'Derr'});
model.physics('c').feature('cfeq1').set('f', {'re-r1'; 'r1-r3-r4';
'2*r2-r3'});
model.physics('c').feature('init1').set('C3', 'Cost');
model.physics('c').feature('dir1').selection.active(false);
model.physics('c').feature('dir1').set('r', {'C1'; 'C2'; 'C3'});
model.physics('c').feature('dir1').active(false);
model.physics('cdeq').field('dimensionless').component({'Cg'});
model.physics('cdeq').feature('cdeq1').set('f', '-re/void');
model.physics('cdeq').feature('cdeq1').set('c', 'Dco/void');
model.physics('cdeq').feature('cdeq1').set('be', 'vel/void');
model.physics('cdeq').feature('flux1').set('g',
'vels*Coin*rm1(t*1[1/s])');
model.physics('cdeq').feature('flux1').set('q', 'vels');

model.mesh('mesh1').feature('size').set('table', 'plasma');
model.mesh('mesh1').feature('size').set('hmax', strict(1));
model.mesh('mesh1').feature('size').set('hmin', '7.59E-4');
model.mesh('mesh1').feature('size').set('hcurve', '0.2');
```

```
model.mesh('mesh1').feature('size').set('hgrad', '1.1');
model.mesh('mesh1').feature('size').set('hauto', '1');
model.mesh('mesh1').feature('size').set('hmax', strict(1));
model.mesh('mesh1').feature('size').set('hmin', '7.59E-4');
model.mesh('mesh1').run;


model.study.create('std1');
model.study('std1').feature.create('time', 'Transient');
model.study('std1').feature.create('stat', 'Stationary');

model.sol.create('sol1');
model.sol('sol1').study('std1');
model.sol('sol1').attach('std1');
model.sol('sol1').feature.create('st1', 'StudyStep');
model.sol('sol1').feature.create('v1', 'Variables');
model.sol('sol1').feature.create('t1', 'Time');
model.sol('sol1').feature('t1').feature.create('fc1',
'FullyCoupled');
model.sol('sol1').feature('t1').feature.remove('fcDef');


model.study('std1').feature('time').set('tlist',
'range(0,7200,7200)');
model.study('std1').feature('time').set('rtol', strict(2));
model.study('std1').feature('time').set('rtolactive', true);
model.study('std1').feature('stat').active(false);

model.sol('sol1').feature('v1').set('control', 'time');
model.sol('sol1').feature('t1').set('control', 'time');
model.sol('sol1').feature('t1').set('tlist', 'range(0,7200,7200)');
model.sol('sol1').feature('t1').set('atolglobal', '1e-5');
model.sol('sol1').feature('t1').set('fieldselection', 'mod1_C3');
model.sol('sol1').feature('t1').set('atolmethod', {'mod1_C1'
'global' 'mod1_C2' 'global' 'mod1_C3' 'global' 'mod1_Cg' 'global'});
model.sol('sol1').feature('t1').set('atol', {'mod1_C1' '1e-3'
'mod1_C2' '1e-3' 'mod1_C3' '1e-3' 'mod1_Cg' '1e-3'});
model.sol('sol1').feature('t1').set('atoludot', {'mod1_C1' '1e-3'
'mod1_C2' '1e-3' 'mod1_C3' '1e-3' 'mod1_Cg' '1e-3'});
model.sol('sol1').feature('t1').set('atoludotactive', {'mod1_C1'
'off' 'mod1_C2' 'off' 'mod1_C3' 'off' 'mod1_Cg' 'off'});
model.sol('sol1').feature('t1').feature('fc1').set('dtech', 'auto');
model.sol('sol1').runAll;
    catch
        erc = erc+1;

    end
  end
poop1 = vel1*Atube1*((Coin1-
mphinterp(model,'Cg','coord',L1,'T',7200))/datai(3))*1000000;
poop3(ii,:) = [datai(1),datai(2),poop1];
poop2(ii) = (poop1-datai(2))^2;
if ii >1
        for n =1:length(msg)
    fprintf('\b')
```

```
        end
end
   msg = sprintf('Inlet \tDew \tTemp \trexp \trcalc \n%0.0f
\t%0.2f\t%0.2f\t%0.3f\t%0.3f
',datai(1),datai(5),datai(6),datai(2),poop1);
     fprintf(msg)
end
for n =1:length(msg)
    fprintf('\b')
end
Objfun = sum(poop2);
ks
Objfun
poop3
towrite = [Objfun,ks(1),ks(2),ks(3)];
dlmwrite('step2.txt',towrite,'-append', 'precision', 16);
out = sum(poop2);
```

r4rate

```



Datafit = [300,1.707260141,0.02096, 15,17.65,299.15]


Datafit;
dim = size(Datafit,1);
poop3 = zeros(dim,3);
ks = kst;
errorh = [.04,1e-2
            .01,1e-4
            .008,1e-6
            .004,1e-8
            .001,1e-8];
for ii = 1:dim;
  erc = 1;
  erc1 = 0;
  while erc > erc1
      erc1 = 1+erc1;
    try
   strict = errorh(erc,:);
    datai = Datafit(ii,:);


import com.comsol.model.*
import com.comsol.model.util.*

model = ModelUtil.create('Model');

model.modelPath('C:\School\Recent\sdfkj');

model.name('812 no Temp diff reactor.mph');

model.hist.enable
```

```
model.param.set('ppmCOin', datai(1), 'Inlet CO concentration');
model.param.set('gcat', datai(3), 'Grams Catalyst');
model.param.set('ginert', '1-gcat', 'g Inert');
model.param.set('vel', datai(4), 'cm/s Superficial Velocity');
model.param.set('pcat', '670', 'kg/m^3 density of cat');
model.param.set('pinert', '329', 'kg/m^3 density of inert');
model.param.set('Atube', '1.98', 'cm^2 Area of Reactor');
model.param.set('L',
'gcat*100/(Atube*(pcat/100^2))/1000+ginert*100/(Atube*(pinert/100^2)
)/1000', 'cm Length Occupied by Catalyst and Inert');
model.param.set('V', 'L*Atube', 'cm^3 Volume Occupied by Catalyst
and Inert');
model.param.set('Rg', '8.314e-3', 'kJ/(mol*K) Gas Constant');
model.param.set('Tst', '299.15', 'K Starting Temp');
model.param.set('Mco', '28.01', 'g/mol Molecular Weight of CO');
model.param.set('Pst', 'gcat*(100^3/1000)/(V)', 'kg/m^3 Density of
Catalyst in Reactor');
model.param.set('Ptg', '2.9', 'm^2/g Surface Area Pt in Reactor');
model.param.set('Ptar', 'Ptg*Pst*1000/100', 'cm^2/cm^3 Surface Area
Pt per volume bed');
model.param.set('Fcoc',
'((Rg*1000*1000*Tst/(2*pi*Mco))^0.5)*Ptar*100', '1/s Bombardment
Rate of CO on Pt for 1 mol CO per Bed Volume in a second');
model.param.set('wtPt', '.04', 'Fraction Pt by weight');
model.param.set('mwPt', '195', 'g/mol Molecular weight Pt');
model.param.set('dsp', '.3', 'Pt Dispersion');
model.param.set('void', '.4', 'Void Fraction');
model.param.set('dp', '2.1e-4', 'm Particle Diameter');
model.param.set('ac', '6*(1-void)*(Pst/pcat)/dp', 'm^2 external
surface/m^3 Bed External surface area over Bed Volume');
model.param.set('Pts', 'wtPt*dsp*Pst*1000/(mwPt*100^3)', 'mol Pt/
cm^3 bed Moles of Pt at the surface per Volume Bed');
model.param.set('Fo2',
'((Rg*1000*1000*Tst/(2*pi*Mo2))^0.5)*Ptar*100', '1/s Bombardment
Rate of O2 on Pt for 1 mol O2 per Bed Volume in a second');
model.param.set('Mo2', '32', 'g/mol Molecular weight O2');
model.param.set('SO', '.23', 'Sticking Coeffecient of Oxygen');
model.param.set('O2', 'P/(Rg*1000*299.15)*Of*(1/100^3)', 'mol/cm^3
Concentration of Oxygen in the Reactor');
model.param.set('P', '101325', 'Pa Pressure in Reactor');
model.param.set('Of', '.21', 'Fraction Oxygen in Reactor');
model.param.set('Tin', '299.15', 'K Inlet Temp');
model.param.set('Coin',
'P/(Rg*1000*299.15)*(ppmCOin/1000000)*(1/100^3)', 'mol/cm^3 Inlet CO
Concnetration');
model.param.set('vels', 'vel/void', 'cm/s Velocity');
model.param.set('Dco', '.755', 'cm^2/s Diffusion Coeffecient for CO
in Air');
model.param.set('ke', 'keblork');
model.param.set('keblork', .0381*((datai(4)/(.4*100))^0.5)-
1.510732097154177e-002, 'm/s Fitted Value for transport Rate from
Bulk to Surface of Catalyst Pellet');
model.param.set('keold', '(0.0168*((vels/100)^0.5)-0.003)');
model.param.set('k3p', 30000000*ks(1), 'cm^2 Pt/(mol*s) Surface
Reaction Rate constant of adsorbed CO and O');
```

```
model.param.set('k4p', ks(2), 'cm^2 Pt/(mol*s) Surface Reaction Rate
constant of adsorbed CO and Oce');
model.param.set('k3', 'k3p/Ptar', 'cm^3 Bed/(mol*s) Volumetric
Reaction Rate constant of adsorbed CO and Oce');
model.param.set('k4', 'k4p/Ptar', 'cm^3 Bed/(mol*s) Volumetric
Reaction Rate constant of adsorbed CO and Oce');
model.param.set('kn2o', '10^13*exp(63/(Rg*299.15))', '1/s Surface
Desorption rate constnat of O on Pt.');
model.param.set('kn2', 'kn2o/(Pts)', 'cm^3 Bed/(s*mol) desorption
rate constant of O2 per volume bed');
model.param.set('Le', 'ke*ac', '1/s diffusion rate constnat
multiplied by area of CO to surface');
model.param.set('L1', 'Fcoc');
model.param.set('L2', 'Fo2*O2*SO');
model.param.set('Ln2', 'kn2');
model.param.set('L3', 'k3');
model.param.set('L4', 'k4');
model.param.set('Cost', 'Pts/(sqrt(Ln2/(L2))*Pts+1)', 'mol O
adsorbed onto surface per cm^3 bed to start');
model.param.set('theaOst', 'Cost/Pts');
model.param.set('dsdsd', 'P/(Rg*1000*Tin)*(1/1000000)*(1/100^3)');
model.param.set('rwer', 'Coin/dsdsd');
model.param.set('coadsrate', 'Fcoc*Coin');
model.param.set('o2adsrate', 'Fo2*O2*SO');
model.param.set('fg', 'O2/Coin');
model.param.set('gh', '1/.004');
model.param.set('sdf', '19.21*.004/.02933');
model.param.set('fgfg', '1/655');
model.param.set('fsfsfsf', 'Fo2/Fcoc');
model.param.set('Derr', '.00001');
model.param.set('COn', ks(3));
model.param.set('On', 1);
vel1 = datai(4);
Atube1 = 1.98;
Coin1 = 101325/(8.314e-3*1000*299.15)*(datai(1)/1000000)*(1/100^3);
ginert1 = (1-datai(3));
pcat1 = 670;
pinert1 = 329;
L1 =
datai(3)*100/(Atube1*(pcat1/100^2))/1000+ginert1*100/(Atube1*(pinert
1/100^2))/1000;




model.modelNode.create('mod1');

model.func.create('rm1', 'Ramp');
model.func('rm1').model('mod1');
model.func('rm1').set('location', '.1');
model.func('rm1').set('cutoffactive', true);
model.func('rm1').set('smoothloc', true);
model.func('rm1').set('smoothcutoff', true);
```

```
model.geom.create('geom1', 1);
model.geom('geom1').feature.create('i1', 'Interval');
model.geom('geom1').feature('i1').set('p2', 'L');
model.geom('geom1').run;

model.variable.create('var1');
model.variable('var1').model('mod1');
model.variable('var1').set('theta', '(C3+C2)/Pts');
model.variable('var1').set('re', 'Le*(Cg-C1)');
model.variable('var1').set('r1', 'L1*C1*((1-theta)*(COn))');
model.variable('var1').set('r2', 'L2*(1-theta)^2-Ln2*(C3)^2');
model.variable('var1').set('r3', 'L3*C2*C3');
model.variable('var1').set('r4', 'L4*C2*(1*Ptar)');

model.physics.create('c', 'CoefficientFormPDE', 'geom1');
model.physics('c').feature.create('dir1', 'DirichletBoundary', 0);
model.physics('c').feature('dir1').selection.set([1]);
model.physics.create('cdeq', 'ConvectionDiffusionEquation',
'geom1');
model.physics('cdeq').feature.create('flux1', 'FluxBoundary', 0);
model.physics('cdeq').feature('flux1').selection.set([1]);

model.mesh.create('mesh1', 'geom1');
model.mesh('mesh1').feature.create('auto_f1', 'Edge');



model.physics('c').field('dimensionless').component({'C1' 'C2'
'C3'});
model.physics('c').field('dimensionless').field('C');
model.physics('c').feature('cfeq1').set('c', {'Derr'; '0'; '0'; '0';
'Derr'; '0'; '0'; '0'; 'Derr'});
model.physics('c').feature('cfeq1').set('f', {'re-r1'; 'r1-r3-r4';
'2*r2-r3'});
model.physics('c').feature('init1').set('C3', 'Cost');
model.physics('c').feature('dir1').selection.active(false);
model.physics('c').feature('dir1').set('r', {'C1'; 'C2'; 'C3'});
model.physics('c').feature('dir1').active(false);
model.physics('cdeq').field('dimensionless').component({'Cg'});
model.physics('cdeq').feature('cdeq1').set('f', '-re/void');
model.physics('cdeq').feature('cdeq1').set('c', 'Dco/void');
model.physics('cdeq').feature('cdeq1').set('be', 'vel/void');
model.physics('cdeq').feature('flux1').set('g',
'vels*Coin*rm1(t*1[1/s])');
model.physics('cdeq').feature('flux1').set('q', 'vels');

model.mesh('mesh1').feature('size').set('table', 'plasma');
model.mesh('mesh1').feature('size').set('hmax', strict(1));
model.mesh('mesh1').feature('size').set('hmin', '7.59E-4');
model.mesh('mesh1').feature('size').set('hcurve', '0.2');
model.mesh('mesh1').feature('size').set('hgrad', '1.1');
model.mesh('mesh1').feature('size').set('hauto', '1');
model.mesh('mesh1').feature('size').set('hmax', strict(1));
model.mesh('mesh1').feature('size').set('hmin', '7.59E-4');
model.mesh('mesh1').run;
```

```
model.study.create('std1');
model.study('std1').feature.create('time', 'Transient');
model.study('std1').feature.create('stat', 'Stationary');

model.sol.create('sol1');
model.sol('sol1').study('std1');
model.sol('sol1').attach('std1');
model.sol('sol1').feature.create('st1', 'StudyStep');
model.sol('sol1').feature.create('v1', 'Variables');
model.sol('sol1').feature.create('t1', 'Time');
model.sol('sol1').feature('t1').feature.create('fc1',
'FullyCoupled');
model.sol('sol1').feature('t1').feature.remove('fcDef');


model.study('std1').feature('time').set('tlist',
'range(0,7200,7200)');
model.study('std1').feature('time').set('rtol', strict(2));
model.study('std1').feature('time').set('rtolactive', true);
model.study('std1').feature('stat').active(false);

model.sol('sol1').feature('v1').set('control', 'time');
model.sol('sol1').feature('t1').set('control', 'time');
model.sol('sol1').feature('t1').set('tlist', 'range(0,7200,7200)');
model.sol('sol1').feature('t1').set('atolglobal', '1e-5');
model.sol('sol1').feature('t1').set('fieldselection', 'mod1_C3');
model.sol('sol1').feature('t1').set('atolmethod', {'mod1_C1'
'global' 'mod1_C2' 'global' 'mod1_C3' 'global' 'mod1_Cg' 'global'});
model.sol('sol1').feature('t1').set('atol', {'mod1_C1' '1e-3'
'mod1_C2' '1e-3' 'mod1_C3' '1e-3' 'mod1_Cg' '1e-3'});
model.sol('sol1').feature('t1').set('atoludot', {'mod1_C1' '1e-3'
'mod1_C2' '1e-3' 'mod1_C3' '1e-3' 'mod1_Cg' '1e-3'});
model.sol('sol1').feature('t1').set('atoludotactive', {'mod1_C1'
'off' 'mod1_C2' 'off' 'mod1_C3' 'off' 'mod1_Cg' 'off'});
model.sol('sol1').feature('t1').feature('fc1').set('dtech', 'auto');
model.sol('sol1').runAll;
    catch
        erc = erc+1;

    end
  end
poop1 = vel1*Atube1*((Coin1-
mphinterp(model,'Cg','coord',L1,'T',7200))/datai(3))*1000000;
poop3(ii,:) = [datai(1),datai(2),poop1];
poop2(ii) = (poop1-datai(2))^2;
if ii >1
        for n =1:length(msg)
    fprintf('\b')
        end
end
   msg = sprintf('Inlet \tDew \tTemp \trexp \trcalc \n%0.0f
\t%0.2f\t%0.2f\t%0.3f\t%0.3f
',datai(1),datai(5),datai(6),datai(2),poop1);
```

```
     fprintf(msg)
end
for n =1:length(msg)
    fprintf('\b')
end
Objfun = sum(poop2);
ks
Objfun
poop3
% towrite = [Objfun,ks(1),ks(2),ks(3)];
% dlmwrite('step2.txt',towrite,'-append');
%towrite = [poop3(:,3),Datafit(:,1),Datafit(:,3),Datafit(:,4)]
%dlmwrite('rrppmweightvel1.txt',towrite);
rout = mphinterp(model,'r4','coord',L1/2,'T',7200)
out = rout;
```

Step3k5Capcep.m

```
function out = noTemp(kst,param);
%
% noTempworkingRH.m
%
% Model exported on Sep 22 2014, 00:34 by COMSOL 4.2.0.150.
param

Datafit = [303, 0.141801711,    0.05064,    15, -15.37,299.15
    303,    0.238302168,    0.0452, 15, -3.68,299.15
    302,    0.240515764,    0.02488,    15, 2.2,299.15
    300,    0.657184745,    0.01639 ,15,    7.24,299.15
    295,    0.805252442,    0.01189,    15, 12.54,299.15
    297,    1.414407613,    0.011,  15, 16.14,299.15
    300,    1.553801903,    0.03158,    15, 17.65,299.15
    295,    1.367778791,    0.0105, 15, 19.06,299.15
    295,    1.354875217,    0.0106, 15, 22.21,299.15];


dim = size(Datafit,1);
poop3 = zeros(dim,3);
ks = kst;
errorh = [.04,1e-2
            .01,1e-4
            .008,1e-6
            .004,1e-8
            .001,1e-8];
for ii = 1:dim;
  erc = 1;
  erc1 = 0;
  while erc > erc1
      erc1 = 1+erc1;
    try
```

```
   strict = errorh(erc,:);
    datai = Datafit(ii,:);

import com.comsol.model.*
import com.comsol.model.util.*

model = ModelUtil.create('Model');

model.modelPath('C:\School\Recent\sdfkj');

model.name('812 no Temp diff reactor w RH1.mph');

model.hist.enable

model.param.set('ppmCOin', datai(1), 'Inlet CO concentration');
model.param.set('gcat', datai(3), 'Grams Catalyst');
model.param.set('ginert', '1-gcat', 'g Inert');
model.param.set('vel', datai(4), 'cm/s Superficial Velocity');
model.param.set('pcat', '670', 'kg/m^3 density of cat');
model.param.set('pinert', '329', 'kg/m^3 density of inert');
model.param.set('Atube', '1.98', 'cm^2 Area of Reactor');
model.param.set('L',
'gcat*100/(Atube*(pcat/100^2))/1000+ginert*100/(Atube*(pinert/100^2)
)/1000', 'cm Length Occupied by Catalyst and Inert');
model.param.set('V', 'L*Atube', 'cm^3 Volume Occupied by Catalyst
and Inert');
model.param.set('Rg', '8.314e-3', 'kJ/(mol*K) Gas Constant');
model.param.set('Tin', '299.15', 'K Inlet Temp');
model.param.set('Tst', '299.15', 'K Starting Temp');
model.param.set('Mco', '28.01', 'g/mol Molecular Weight of CO');
model.param.set('Pst', 'gcat*(100^3/1000)/(V)', 'kg/m^3 Density of
Catalyst in Reactor');
model.param.set('Ptg', '2.9', 'm^2/g Surface Area Pt in Reactor');
model.param.set('Ptar', 'Ptg*Pst*1000/100', 'cm^2/cm^3 Surface Area
Pt per volume bed');
model.param.set('Fcoc',
'((Rg*1000*1000*Tst/(2*pi*Mco))^0.5)*Ptar*100', '1/s Bombardment
Rate of CO on Pt for 1 mol CO per Bed Volume in a second');
model.param.set('wtPt', '.04', 'Fraction Pt by weight');
model.param.set('mwPt', '195', 'g/mol Molecular weight Pt');
model.param.set('dsp', '.3', 'Pt Dispersion');
model.param.set('void', '.4', 'Void Fraction');
model.param.set('dp', '2.1e-4', 'm Particle Diameter');
model.param.set('ac', '6*(1-void)*(Pst/pcat)/dp', 'm^2 external
surface/m^3 Bed External surface area over Bed Volume');
model.param.set('Pts', 'wtPt*dsp*Pst*1000/(mwPt*100^3)', 'mol Pt/
cm^3 bed Moles of Pt at the surface per Volume Bed');
model.param.set('Fo2',
'((Rg*1000*1000*Tst/(2*pi*Mo2))^0.5)*Ptar*100', '1/s Bombardment
Rate of O2 on Pt for 1 mol O2 per Bed Volume in a second');
model.param.set('Mo2', '32', 'g/mol Molecular weight O2');
model.param.set('SO', '.23', 'Sticking Coeffecient of Oxygen');
model.param.set('O2', 'P/(Rg*1000*Tin)*Of*(1/100^3)', 'mol/cm^3
Concentration of Oxygen in the Reactor');
model.param.set('P', '101325', 'Pa Pressure in Reactor');
model.param.set('Of', '.21', 'Fraction Oxygen in Reactor');
```

```
model.param.set('Coin',
'P/(Rg*1000*299.15)*(ppmCOin/1000000)*(1/100^3)', 'mol/cm^3 Inlet CO
Concnetration');
model.param.set('vels', 'vel/void', 'cm/s Velocity');
model.param.set('Dco', '.755', 'cm^2/s Diffusion Coeffecient for CO
in Air');
model.param.set('ke', 'keblork');
model.param.set('keblork', .0381*((datai(4)/(.4*100))^0.5)-
1.510732097154177e-002, 'm/s Fitted Value for transport Rate from
Bulk to Surface of Catalyst Pellet');
model.param.set('keold', '(0.0168*((vels/100)^0.5)-0.003)');
model.param.set('k3p', 30000000*param(1), 'cm^2 Pt/(mol*s) Surface
Reaction Rate constant of adsorbed CO and O');
model.param.set('k4p', param(2), 'cm^2 Pt/(mol*s) Surface Reaction
Rate constant of adsorbed CO and Oce');
model.param.set('COn', param(3));
model.param.set('k3', 'k3p/Ptar', 'cm^3 Bed/(mol*s) Volumetric
Reaction Rate constant of adsorbed CO and Oce');
model.param.set('k4', 'k4p/Ptar', 'cm^3 Bed/(mol*s) Volumetric
Reaction Rate constant of adsorbed CO and Oce');
model.param.set('kn2o', '10^13*exp(63/(Rg*299.15))', '1/s Surface
Desorption rate constnat of O on Pt.');
model.param.set('kn2', 'kn2o/(Pts)', 'cm^3 Bed/(s*mol) desorption
rate constant of O2 per volume bed');
model.param.set('Le', 'ke*ac', '1/s diffusion rate constnat
multiplied by area of CO to surface');
model.param.set('L1', 'Fcoc');
model.param.set('L2', 'Fo2*O2*SO');
model.param.set('Ln2', 'kn2');
model.param.set('L3', 'k3');
model.param.set('L4', 'newk4');
model.param.set('Cost', 'Pts/(sqrt(Ln2/(L2))*Pts+1)', 'mol O
adsorbed onto surface per cm^3 bed to start');
model.param.set('theaOst', 'Cost/Pts');
model.param.set('dsdsd', 'P/(Rg*1000*Tin)*(1/1000000)*(1/100^3)');
model.param.set('rwer', 'Coin/dsdsd');
model.param.set('coadsrate', 'Fcoc*Coin');
model.param.set('o2adsrate', 'Fo2*O2*SO');
model.param.set('fg', 'O2/Coin');
model.param.set('gh', '1/.004');
model.param.set('sdf', '19.21*.004/.02933');
model.param.set('fgfg', '1/655');
model.param.set('fsfsfsf', 'Fo2/Fcoc');
model.param.set('Derr', '.00001');
model.param.set('Capce1', 'Capcep*Ptar');
model.param.set('Capcep', '1e-8');
model.param.set('PH2O', '(RH/100)*100*10^(6.2096-
2354.7/(299.15+7.559))');
model.param.set('Wo', '.8');
model.param.set('m', '1.2');
model.param.set('sl', '-1.68');
model.param.set('Dewpt', datai(5));
model.param.set('RH',
'100*(exp((17.625*Dewpt)/(243.04+Dewpt))/exp((17.625*(Tst-
273.15))/(243.04+(Tst-273.15))))');
model.param.set('Rcal', '1.987e-3');
model.param.set('mwH2O', '18.01');
```

```
model.param.set('CH2O', '(WH2O*Pst/mwH2O/1000)^n');
model.param.set('WH2O', 'Wo*exp(sl*((Tst*Rcal*log(100/RH))^m))');
model.param.set('k5o', 1e18*ks(1));
model.param.set('k5', 'k5o/(Ptar^n)');
model.param.set('L5', 'k5');
model.param.set('newk4', 'k4*Ptar300/Oce300');
model.param.set('r4300', param(4));
model.param.set('Capce300', 'r4300/(k5300*(CH2O300^n))+Oce300');
model.param.set('Oce300', 1e-7*ks(2));
model.param.set('Capce', 'Capce300*(Ptar/Ptar300)');
model.param.set('k5300', 'k5o/(Ptar300^n)');
model.param.set('CH2O300', '2.073e-4');
model.param.set('Ptar300', '202.1356831286061');
model.param.set('dsff', 'Oce300/Capce300');
model.param.set('n', '3');
model.param.set('try', '(k5300*(CH2O300^n))');

vel1 = datai(4);
Atube1 = 1.98;
Coin1 = 101325/(8.314e-3*1000*299.15)*(datai(1)/1000000)*(1/100^3);
ginert1 = (1-datai(3));
pcat1 = 670;
pinert1 = 329;
L1 =
datai(3)*100/(Atube1*(pcat1/100^2))/1000+ginert1*100/(Atube1*(pinert
1/100^2))/1000;

model.modelNode.create('mod1');

model.func.create('rm1', 'Ramp');
model.func('rm1').model('mod1');
model.func('rm1').set('location', '.1');
model.func('rm1').set('cutoffactive', true);
model.func('rm1').set('smoothloc', true);
model.func('rm1').set('smoothcutoff', true);

model.geom.create('geom1', 1);
model.geom('geom1').feature.create('i1', 'Interval');
model.geom('geom1').feature('i1').set('p2', 'L');
model.geom('geom1').run;

model.variable.create('var1');
model.variable('var1').model('mod1');
model.variable('var1').set('theta', '(u3+u2)/Pts');
model.variable('var1').set('re', 'Le*(Cg-u1)');
model.variable('var1').set('r1', 'L1*u1*((1-theta)*(COn))');
model.variable('var1').set('r2', 'L2*(1-theta)^2-Ln2*(u3)^2');
model.variable('var1').set('r3', 'L3*u2*u3');
model.variable('var1').set('r4', 'L4*u2*u4');
model.variable('var1').set('r5', 'L5*CH2O*(Capce-u4)');

model.physics.create('cdeq', 'ConvectionDiffusionEquation',
'geom1');
model.physics('cdeq').feature.create('flux1', 'FluxBoundary', 0);
model.physics('cdeq').feature('flux1').selection.set([1]);
model.physics.create('c2', 'CoefficientFormPDE', 'geom1');
```

```
model.mesh.create('mesh1', 'geom1');
model.mesh('mesh1').feature.create('auto_f1', 'Edge');


model.physics('cdeq').field('dimensionless').component({'Cg'});
model.physics('cdeq').feature('cdeq1').set('f', '-re/void');
model.physics('cdeq').feature('cdeq1').set('c', 'Dco/void');
model.physics('cdeq').feature('cdeq1').set('be', 'vel/void');
model.physics('cdeq').feature('flux1').set('g',
'vels*Coin*rm1(t*1[1/s])');
model.physics('cdeq').feature('flux1').set('q', 'vels');
model.physics('c2').field('dimensionless').component({'u1' 'u2' 'u3'
'u4'});
model.physics('c2').field('dimensionless').field('u');
model.physics('c2').feature('cfeq1').set('c', {'Derr'; '0'; '0';
'0'; '0'; 'Derr'; '0'; '0'; '0'; '0'; 'Derr'; '0'; '0'; '0'; '0';
'Derr'});
model.physics('c2').feature('cfeq1').set('f', {'re-r1'; 'r1-r3-r4';
'2*r2-r3'; 'r5-r4'});
model.physics('c2').feature('init1').set('u3', 'Cost');
model.physics('c2').feature('init1').set('u4', 'Capce');

model.mesh('mesh1').feature('size').set('table', 'plasma');
model.mesh('mesh1').feature('size').set('hmax', strict(1));
model.mesh('mesh1').feature('size').set('hmin', '7.59E-4');
model.mesh('mesh1').feature('size').set('hcurve', '0.2');
model.mesh('mesh1').feature('size').set('hgrad', '1.1');
model.mesh('mesh1').feature('size').set('hauto', '1');
model.mesh('mesh1').feature('size').set('hmax', strict(1));
model.mesh('mesh1').feature('size').set('hmin', '7.59E-4');
model.mesh('mesh1').run;


model.study.create('std1');
model.study('std1').feature.create('time', 'Transient');
model.study('std1').feature.create('stat', 'Stationary');

model.sol.create('sol1');
model.sol('sol1').study('std1');
model.sol('sol1').attach('std1');
model.sol('sol1').feature.create('st1', 'StudyStep');
model.sol('sol1').feature.create('v1', 'Variables');
model.sol('sol1').feature.create('t1', 'Time');
model.sol('sol1').feature('t1').feature.create('fc1',
'FullyCoupled');
model.sol('sol1').feature('t1').feature.remove('fcDef');



model.study('std1').feature('time').set('tlist',
'range(0,7200,7200)');
model.study('std1').feature('time').set('rtol', strict(2));
model.study('std1').feature('time').set('rtolactive', true);
model.study('std1').feature('stat').active(false);
```

```
model.sol('sol1').feature('v1').set('control', 'time');
model.sol('sol1').feature('t1').set('control', 'time');
model.sol('sol1').feature('t1').set('tlist', 'range(0,7200,7200)');
model.sol('sol1').feature('t1').set('atolglobal', '1e-5');
model.sol('sol1').feature('t1').set('fieldselection', 'mod1_Cg');
model.sol('sol1').feature('t1').set('atolmethod', {'mod1_Cg'
'global' 'mod1_u4' 'global' 'mod1_u3' 'global' 'mod1_u2' 'global'
'mod1_u1' 'global'});
model.sol('sol1').feature('t1').set('atol', {'mod1_Cg' '1e-3'
'mod1_u4' '1e-3' 'mod1_u3' '1e-3' 'mod1_u2' '1e-3' 'mod1_u1' '1e-
3'});
model.sol('sol1').feature('t1').set('atoludot', {'mod1_Cg' '1e-3'
'mod1_u4' '1e-3' 'mod1_u3' '1e-3' 'mod1_u2' '1e-3' 'mod1_u1' '1e-
3'});
model.sol('sol1').feature('t1').set('atoludotactive', {'mod1_Cg'
'off' 'mod1_u4' 'off' 'mod1_u3' 'off' 'mod1_u2' 'off' 'mod1_u1'
'off'});
model.sol('sol1').feature('t1').feature('fc1').set('dtech', 'auto');
model.sol('sol1').runAll;

catch
        erc = erc+1

    end
  end
poop1 = vel1*Atube1*((Coin1-
mphinterp(model,'Cg','coord',L1,'T',7200))/datai(3))*1000000;
poop3(ii,:) = [datai(5),datai(2),poop1];
poop2(ii) = (poop1-datai(2))^2;
if ii >1
        for n =1:length(msg)
    fprintf('\b')
        end
end
   msg = sprintf('Inlet \tDew \tTemp \trexp \trcalc \n%0.0f
\t%0.2f\t%0.2f\t%0.3f\t%0.3f
',datai(1),datai(5),datai(6),datai(2),poop1);
      fprintf(msg)
end
for n =1:length(msg)
    fprintf('\b')
        end
Objfun = sum(poop2);
ks
Objfun
poop3
towrite = [Objfun,ks(1),ks(2)];
dlmwrite('Step3.txt',towrite,'-append', 'precision', 16);
%towrite = [poop3(:,3),Datafit(:,1),Datafit(:,3),Datafit(:,4)]
%dlmwrite('rrppmweightvel1.txt',towrite);

out = 100*sum(poop2);
```

Step4Ea345.m

```
function out = noTemp(kst,params);
%
% noTempworkingRH.m
%
% Model exported on Sep 22 2014, 00:34 by COMSOL 4.2.0.150.




dim = size(Datafit,1);
poop3 = zeros(dim,3);
ks = kst;
errorh = [.04,1e-2
            .01,1e-4
            .008,1e-6
            .004,1e-8
            .001,1e-8];
for ii = 1:dim;
  erc = 1;
  erc1 = 0;
  while erc > erc1
      erc1 = 1+erc1;
    try
   strict = errorh(erc,:);
    datai = Datafit(ii,:);

import com.comsol.model.*
import com.comsol.model.util.*

model = ModelUtil.create('Model');

model.modelPath('C:\School\Recent\sdfkj');

model.name('812 no Temp diff reactor w RH1.mph');

model.hist.enable

model.param.set('ppmCOin', datai(1), 'Inlet CO concentration');
model.param.set('gcat', datai(3), 'Grams Catalyst');
model.param.set('vel', datai(4), 'cm/s Superficial Velocity');
model.param.set('Dewpt', datai(5));
model.param.set('ginert', '1-gcat', 'g Inert');
model.param.set('pcat', '670', 'kg/m^3 density of cat');
model.param.set('pinert', '329', 'kg/m^3 density of inert');
model.param.set('Atube', '1.98', 'cm^2 Area of Reactor');
model.param.set('L',
'gcat*100/(Atube*(pcat/100^2))/1000+ginert*100/(Atube*(pinert/100^2)
)/1000', 'cm Length Occupied by Catalyst and Inert');
model.param.set('V', 'L*Atube', 'cm^3 Volume Occupied by Catalyst
and Inert');
model.param.set('Rg', '8.314e-3', 'kJ/(mol*K) Gas Constant');
model.param.set('Tin', datai(6), 'K Inlet Temp');
```

```
model.param.set('Tst', datai(6), 'K Starting Temp');
model.param.set('Mco', '28.01', 'g/mol Molecular Weight of CO');
model.param.set('Pst', 'gcat*(100^3/1000)/(V)', 'kg/m^3 Density of
Catalyst in Reactor');
model.param.set('Ptg', '2.9', 'm^2/g Surface Area Pt in Reactor');
model.param.set('Ptar', 'Ptg*Pst*1000/100', 'cm^2/cm^3 Surface Area
Pt per volume bed');
model.param.set('Fcoc',
'((Rg*1000*1000*Tst/(2*pi*Mco))^0.5)*Ptar*100', '1/s Bombardment
Rate of CO on Pt for 1 mol CO per Bed Volume in a second');
model.param.set('wtPt', '.04', 'Fraction Pt by weight');
model.param.set('mwPt', '195', 'g/mol Molecular weight Pt');
model.param.set('dsp', '.3', 'Pt Dispersion');
model.param.set('void', '.4', 'Void Fraction');
model.param.set('dp', '2.1e-4', 'm Particle Diameter');
model.param.set('ac', '6*(1-void)*(Pst/pcat)/dp', 'm^2 external
surface/m^3 Bed External surface area over Bed Volume');
model.param.set('Pts', 'wtPt*dsp*Pst*1000/(mwPt*100^3)', 'mol Pt/
cm^3 bed Moles of Pt at the surface per Volume Bed');
model.param.set('Fo2',
'((Rg*1000*1000*Tst/(2*pi*Mo2))^0.5)*Ptar*100', '1/s Bombardment
Rate of O2 on Pt for 1 mol O2 per Bed Volume in a second');
model.param.set('Mo2', '32', 'g/mol Molecular weight O2');
model.param.set('SO', '.23', 'Sticking Coeffecient of Oxygen');
model.param.set('O2', 'P/(Rg*1000*299.15)*Of*(1/100^3)', 'mol/cm^3
Concentration of Oxygen in the Reactor');
model.param.set('P', '101325', 'Pa Pressure in Reactor');
model.param.set('Of', '.21', 'Fraction Oxygen in Reactor');
model.param.set('Coin',
'P/(Rg*1000*299.15)*(ppmCOin/1000000)*(1/100^3)', 'mol/cm^3 Inlet CO
Concnetration');
model.param.set('vels', 'vel/void', 'cm/s Velocity');
model.param.set('Dco', '.755', 'cm^2/s Diffusion Coeffecient for CO
in Air');
model.param.set('ke', 'keblork*(1/(299.15^(11/12)))*(Tst^(11/12))');
model.param.set('keblork',  .0381*((datai(4)/(.4*100))^0.5)-
1.510732097154177e-002, 'm/s Fitted Value for transport Rate from
Bulk to Surface of Catalyst Pellet');
model.param.set('keold', '(0.0168*((vels/100)^0.5)-0.003)');
model.param.set('k3p', 'a3p*exp(-Ea3/(Rg*Tst))', 'cm^2 Pt/(mol*s)
Surface Reaction Rate constant of adsorbed CO and O');
model.param.set('k4p', 'a4p*exp(-Ea4/(Rg*Tst))', 'cm^2 Pt/(mol*s)
Surface Reaction Rate constant of adsorbed CO and Oce');
model.param.set('COn', params(3));
model.param.set('k3', 'k3p/Ptar', 'cm^3 Bed/(mol*s) Volumetric
Reaction Rate constant of adsorbed CO and Oce');
model.param.set('k4', 'k4p/Ptar', 'cm^3 Bed/(mol*s) Volumetric
Reaction Rate constant of adsorbed CO and Oce');
model.param.set('kn2o', '10^13*exp(63/(Rg*299.15))', '1/s Surface
Desorption rate constnat of O on Pt.');
model.param.set('kn2', 'kn2o/(Pts)', 'cm^3 Bed/(s*mol) desorption
rate constant of O2 per volume bed');
model.param.set('Le', 'ke*ac', '1/s diffusion rate constnat
multiplied by area of CO to surface');
model.param.set('L1', 'Fcoc');
model.param.set('L2', 'Fo2*O2*SO');
model.param.set('Ln2', 'kn2');
```

```
model.param.set('L3', 'k3');
model.param.set('L4', 'newk4');
model.param.set('Cost', 'Pts/(sqrt(Ln2/(L2))*Pts+1)', 'mol O
adsorbed onto surface per cm^3 bed to start');
model.param.set('theaOst', 'Cost/Pts');
model.param.set('dsdsd', 'P/(Rg*1000*Tin)*(1/1000000)*(1/100^3)');
model.param.set('rwer', 'Coin/dsdsd');
model.param.set('coadsrate', 'Fcoc*Coin');
model.param.set('o2adsrate', 'Fo2*O2*SO');
model.param.set('fg', 'O2/Coin');
model.param.set('gh', '1/.004');
model.param.set('sdf', '19.21*.004/.02933');
model.param.set('fgfg', '1/655');
model.param.set('fsfsfsf', 'Fo2/Fcoc');
model.param.set('Derr', '.00001');
model.param.set('Capcel', 'Capcep*Ptar');
model.param.set('Capcep', '1e-8');
model.param.set('PH2O', '(RH/100)*100*10^(6.2096-
2354.7/(299.15+7.559))');
model.param.set('Wo', '.8');
model.param.set('m', '1.2');
model.param.set('sl', '-1.68');
model.param.set('RH',
'100*(exp((17.625*Dewpt)/(243.04+Dewpt))/exp((17.625*(Tst-
273.15))/(243.04+(Tst-273.15))))');
model.param.set('Rcal', '1.987e-3');
model.param.set('mwH2O', '18.01');
model.param.set('CH2O', '(WH2O*Pst/mwH2O/1000)^n');
model.param.set('WH2O', 'Wo*exp(sl*((Tst*Rcal*log(100/RH))^m))');
model.param.set('k5o', 'a5p*exp(-Ea5/(Rg*Tst))');
model.param.set('k5', 'k5o/(Ptar^n)');
model.param.set('L5', 'k5');
model.param.set('newk4', 'k4*Ptar300/Oce300');
model.param.set('r4300', params(4));
model.param.set('Capce300', 'r4300/(k5300*(CH2O300^n))+Oce300');
model.param.set('Oce300', 1e-7*params(6));
model.param.set('Capce', 'Capce300*(Ptar/Ptar300)');
model.param.set('k5300', 'a5p*exp(-Ea5/(Rg*299.15))/(Ptar300^n)');
model.param.set('CH2O300', '2.073e-4');
model.param.set('Ptar300', '202.1356831286061');
model.param.set('dsff', 'Oce300/Capce300');
model.param.set('n', '3');
model.param.set('try', '(k5300*(CH2O300^n))');
model.param.set('k3p299', 30000000*params(1));
model.param.set('k4p299', params(2));
model.param.set('k5p299', 1e18*params(5));
model.param.set('Ea3', ks(1), 'activation energy Kj/mol');
model.param.set('Ea4', ks(2), 'activation energy Kj/mol');
model.param.set('Ea5', ks(3), 'activation energy Kj/mol');
model.param.set('a3p', 'k3p299*exp(Ea3/(Rg*299.15))', 'pre
exponential factor');
model.param.set('a4p', 'k4p299*exp(Ea4/(Rg*299.15))', 'pre
exponential factor');
model.param.set('a5p', 'k5p299*exp(Ea5/(Rg*299.15))', 'pre
exponential factor');

T = datai(6);
```

```
vel1 = datai(4);
Atube1 = 1.98;
Coin1 = 101325/(8.314e-3*1000*299.15)*(datai(1)/1000000)*(1/100^3);
ginert1 = (1-datai(3));
pcat1 = 670;
pinert1 = 329;
L1 =
datai(3)*100/(Atube1*(pcat1/100^2))/1000+ginert1*100/(Atube1*(pinert
1/100^2))/1000;

model.modelNode.create('mod1');

model.func.create('rm1', 'Ramp');
model.func('rm1').model('mod1');
model.func('rm1').set('location', '.1');
model.func('rm1').set('cutoffactive', true);
model.func('rm1').set('smoothloc', true);
model.func('rm1').set('smoothcutoff', true);

model.geom.create('geom1', 1);
model.geom('geom1').feature.create('i1', 'Interval');
model.geom('geom1').feature('i1').set('p2', 'L');
model.geom('geom1').run;

model.variable.create('var1');
model.variable('var1').model('mod1');
model.variable('var1').set('theta', '(u3+u2)/Pts');
model.variable('var1').set('re', 'Le*(Cg-u1)');
model.variable('var1').set('r1', 'L1*u1*((1-theta)*(COn))');
model.variable('var1').set('r2', 'L2*(1-theta)^2-Ln2*(u3)^2');
model.variable('var1').set('r3', 'L3*u2*u3');
model.variable('var1').set('r4', 'L4*u2*u4');
model.variable('var1').set('r5', 'L5*CH2O*(Capce-u4)');

model.physics.create('cdeq', 'ConvectionDiffusionEquation',
'geom1');
model.physics('cdeq').feature.create('flux1', 'FluxBoundary', 0);
model.physics('cdeq').feature('flux1').selection.set([1]);
model.physics.create('c2', 'CoefficientFormPDE', 'geom1');

model.mesh.create('mesh1', 'geom1');
model.mesh('mesh1').feature.create('auto_f1', 'Edge');


model.physics('cdeq').field('dimensionless').component({'Cg'});
model.physics('cdeq').feature('cdeq1').set('f', '-re/void');
model.physics('cdeq').feature('cdeq1').set('c', 'Dco/void');
model.physics('cdeq').feature('cdeq1').set('be', 'vel/void');
model.physics('cdeq').feature('flux1').set('g',
'vels*Coin*rm1(t*1[1/s])');
model.physics('cdeq').feature('flux1').set('q', 'vels');
model.physics('c2').field('dimensionless').component({'u1' 'u2' 'u3'
'u4'});
model.physics('c2').field('dimensionless').field('u');
```

```
model.physics('c2').feature('cfeq1').set('c', {'Derr'; '0'; '0';
'0'; '0'; 'Derr'; '0'; '0'; '0'; '0'; 'Derr'; '0'; '0'; '0'; '0';
'Derr'});
model.physics('c2').feature('cfeq1').set('f', {'re-r1'; 'r1-r3-r4';
'2*r2-r3'; 'r5-r4'});
model.physics('c2').feature('init1').set('u3', 'Cost');
model.physics('c2').feature('init1').set('u4', 'Capce');

model.mesh('mesh1').feature('size').set('table', 'plasma');
model.mesh('mesh1').feature('size').set('hmax', strict(1));
model.mesh('mesh1').feature('size').set('hmin', '7.59E-4');
model.mesh('mesh1').feature('size').set('hcurve', '0.2');
model.mesh('mesh1').feature('size').set('hgrad', '1.1');
model.mesh('mesh1').feature('size').set('hauto', '1');
model.mesh('mesh1').feature('size').set('hmax', strict(1));
model.mesh('mesh1').feature('size').set('hmin', '7.59E-4');
model.mesh('mesh1').run;


model.study.create('std1');
model.study('std1').feature.create('time', 'Transient');
model.study('std1').feature.create('stat', 'Stationary');

model.sol.create('sol1');
model.sol('sol1').study('std1');
model.sol('sol1').attach('std1');
model.sol('sol1').feature.create('st1', 'StudyStep');
model.sol('sol1').feature.create('v1', 'Variables');
model.sol('sol1').feature.create('t1', 'Time');
model.sol('sol1').feature('t1').feature.create('fc1',
'FullyCoupled');
model.sol('sol1').feature('t1').feature.remove('fcDef');



model.study('std1').feature('time').set('tlist',
'range(0,7200,7200)');
model.study('std1').feature('time').set('rtol', strict(2));
model.study('std1').feature('time').set('rtolactive', true);
model.study('std1').feature('stat').active(false);

model.sol('sol1').feature('v1').set('control', 'time');
model.sol('sol1').feature('t1').set('control', 'time');
model.sol('sol1').feature('t1').set('tlist', 'range(0,7200,7200)');
model.sol('sol1').feature('t1').set('atolglobal', '1e-5');
model.sol('sol1').feature('t1').set('fieldselection', 'mod1_Cg');
model.sol('sol1').feature('t1').set('atolmethod', {'mod1_Cg'
'global' 'mod1_u4' 'global' 'mod1_u3' 'global' 'mod1_u2' 'global'
'mod1_u1' 'global'});
model.sol('sol1').feature('t1').set('atol', {'mod1_Cg' '1e-3'
'mod1_u4' '1e-3' 'mod1_u3' '1e-3' 'mod1_u2' '1e-3' 'mod1_u1' '1e-
3'});
model.sol('sol1').feature('t1').set('atoludot', {'mod1_Cg' '1e-3'
'mod1_u4' '1e-3' 'mod1_u3' '1e-3' 'mod1_u2' '1e-3' 'mod1_u1' '1e-
3'});
```

```
model.sol('sol1').feature('t1').set('atoludotactive', {'mod1_Cg'
'off' 'mod1_u4' 'off' 'mod1_u3' 'off' 'mod1_u2' 'off' 'mod1_u1'
'off'});
model.sol('sol1').feature('t1').feature('fc1').set('dtech', 'auto');
model.sol('sol1').runAll;

catch
        erc = erc+1

    end
  end
poop1 = vel1*Atube1*((Coin1-
mphinterp(model,'Cg','coord',L1,'T',7200))/datai(3))*1000000;
poop3(ii,:) = [datai(5),datai(2),poop1];
poop2(ii) = (poop1-datai(2))^2;
if ii >1
        for n =1:length(msg)
    fprintf('\b')
        end
end
   msg = sprintf('Inlet \tDew \tTemp \trexp \trcalc \n%0.0f
\t%0.2f\t%0.2f\t%0.3f\t%0.3f
',datai(1),datai(5),datai(6),datai(2),poop1);
     fprintf(msg)
end
for n =1:length(msg)
    fprintf('\b')
        end
Objfun = sum(poop2);
ks
Objfun
poop3
towrite = [Objfun,ks(1),ks(2),ks(3)];
dlmwrite('Step4.txt',towrite,'-append', 'precision', 16);


out = sum(poop2);
```

A.2 Matlab Code for Fitting Heat Transfer Equation

```
function out = heatrss(blarg)

beep = blarg;

filename = '.15 vel mfm.xlsx';
sheet = 1;
vel = .15

Data = xlsread(filename, sheet);

Data
```

```
X = Data(:,1)
y = Data(:,2)
Tamb = [Data(1,3),Data(8,3)]
BoundT = [Data(7,3),Data(8,2)]
param = zeros(3,2);
param(1,:) = Tamb;
param(2,:) = BoundT;
param(3,1) = vel;
param
keffax = .219;
keffr = .209;
h = 100;
k0 = zeros(3,1);
k0(1) = keffax;
k0(2) = keffr;
k0(3) = h;
options = optimset('MaxFunEvals',9999);

[beta,R,J,CovB,MSE] =
nlinfit(X,y,@(fitp,X)comheat1(fitp,X,param),k0,options);
ci = nlparci(beta,R,'jacobian',J);
calc1 = comheat1(beta,X,param);
dataend = [beta,ci]
[calc1,y]

out = 13013

function out = comheat1(fitp,X,param)

keffax = fitp(1)
keffr = fitp(2)
h = fitp(3)
%min
%alphw = alphw*(alphw>=0);
keffax = keffax*(keffax>=0);
keffr = keffr*(keffr>=0);
h = h*(h>=0);
%max
max = 1000;
%alphw = alphw*(alphw<=max)+max*(alphw>max)*max/(1+alphw);
keffax = keffax*(keffax<=max)+max*(keffax>max)*max/(1+keffax);
keffr = keffr*(keffr<=max)+max*(keffr>max)*max/(1+keffr);
h = h*(h<=max)+max*(h>max)*max/(1+h);
vel = param(3,1);
Tamb=param(1,:);
BoundT = param(2,:);
y = zeros(14,1);
i = 1;
    param1=[Tamb(1,i);BoundT(1,i);vel;i];
    X1 = X(i*7-6:7*i);
    y(i*7-6:7*i)=(comheat3(fitp,X1,param1));
 i = 2;
    param2=[Tamb(1,i);BoundT(1,i);vel;i];
    X2 = X(i*7-6:7*i);
    y(i*7-6:7*i)=(comheat2(fitp,X2,param2));
```

```
out =y

function out = comheat2(fitp,X,param)
%
% comheatnew.m
%
% Model exported on Jul 1 2013, 01:58 by COMSOL 4.2.0.150.
X=X./1000;
import com.comsol.model.*
import com.comsol.model.util.*

model = ModelUtil.create('Model');

model.modelPath('C:\School\Recent');

keffax=fitp(1);
keffr=fitp(2);
h=fitp(3);
vel = param(3,1);
i = param(4,1);
Tamb = param(1,1)+273
BoundT = param(2,1)+273


model.param.set('lent', '.019985');
model.param.set('vel', vel);
model.param.set('pf', '31.1');
model.param.set('Cpf', '29.45');
model.param.set('keffax', keffax);
model.param.set('keffr', keffr);
model.param.set('Tst', '300');
model.param.set('Tamb', Tamb);
model.param.set('alphw', h);
model.param.set('Tend', BoundT);
model.param.set('Tin', BoundT);
model.modelNode.create('mod1');



model.geom.create('geom1', 2);
model.geom('geom1').axisymmetric(true);
model.geom('geom1').feature.create('r1', 'Rectangle');
model.geom('geom1').feature('r1').set('createselection', true);
model.geom('geom1').feature('r1').set('size', {'.0079' 'lent'});
model.geom('geom1').run;

model.physics.create('c', 'CoefficientFormPDE', 'geom1');
model.physics('c').identifier('T');
model.physics('c').feature.create('flux1', 'FluxBoundary', 1);
model.physics('c').feature('flux1').selection.set([2]);
model.physics('c').feature.create('flux2', 'FluxBoundary', 1);
model.physics('c').feature('flux2').selection.set([4]);

model.mesh.create('mesh1', 'geom1');
model.mesh('mesh1').feature.create('ftri1', 'FreeTri');
```

```
model.view('view1').axis.set('xmin', '-0.002875993959605694');
model.view('view1').axis.set('xmax', '0.010775993578135967');
model.view('view1').axis.set('ymin', '-9.99250914901495E-4');
model.view('view1').axis.set('ymax', '0.02098424918949604');

model.physics('c').field('dimensionless').component({'T'});
model.physics('c').field('dimensionless').field('T');
model.physics('c').feature('cfeq1').set('c', {'keffr' '0' '0'
'keffax'});
model.physics('c').feature('cfeq1').set('da', '0');
model.physics('c').feature('cfeq1').set('be', {'0' 'vel*pf*Cpf'});
model.physics('c').feature('init1').set('T', 'Tst');
model.physics('c').feature('flux1').set('g', 'vel*pf*Cpf*(Tin -
T)');
model.physics('c').feature('flux2').set('g', 'alphw*Tamb');
model.physics('c').feature('flux2').set('q', 'alphw');

model.mesh('mesh1').run;

model.study.create('std1');
model.study('std1').feature.create('stat', 'Stationary');

model.sol.create('sol1');
model.sol('sol1').study('std1');
model.sol('sol1').attach('std1');
model.sol('sol1').feature.create('st1', 'StudyStep');
model.sol('sol1').feature.create('v1', 'Variables');
model.sol('sol1').feature.create('s1', 'Stationary');
model.sol('sol1').feature('s1').feature.create('fc1',
'FullyCoupled');
model.sol('sol1').feature('s1').feature.remove('fcDef');

model.result.dataset.create('rev1', 'Revolve2D');
model.result.create('pg1', 'PlotGroup2D');
model.result('pg1').feature.create('surf1', 'Surface');
model.result.create('pg2', 'PlotGroup3D');
model.result('pg2').feature.create('surf1', 'Surface');

model.sol('sol1').feature('st1').name('Compile Equations:
Stationary');
model.sol('sol1').feature('st1').set('studystep', 'stat');
model.sol('sol1').feature('v1').set('control', 'stat');
model.sol('sol1').feature('s1').set('control', 'stat');
model.sol('sol1').runAll;

model.result.dataset('rev1').set('startangle', '-90');
model.result.dataset('rev1').set('revangle', '225');
model.result('pg1').set('title', 'Surface: Dependent variable T ');
model.result('pg1').set('titleactive', false);
Y = zeros(size(X));
z = zeros(size(X));
X = transpose(X)
z = transpose(z);
Y = transpose(Y);
```

```
a = mphinterp(model,'T','coord',[0;X(2)]);
Y = mphinterp(model,'T','coord',[z;X]);
Y
Y = Y-273.15
out = Y;

function out = comheat3(fitp,X,param)
%
% comheatnew.m
%
% Model exported on Jul 1 2013, 01:58 by COMSOL 4.2.0.150.
X=X./1000;
import com.comsol.model.*
import com.comsol.model.util.*

model = ModelUtil.create('Model');

model.modelPath('C:\School\Recent');

keffax=fitp(1);
keffr=fitp(2);
h=fitp(3);
vel = param(3,1);
i = param(4,1);
Tamb = param(1,1)+273
BoundT = param(2,1)+273


model.param.set('lent', '.019985');
model.param.set('vel', vel);
model.param.set('pf', '31.1');
model.param.set('Cpf', '29.45');
model.param.set('keffax', keffax);
model.param.set('keffr', keffr);
model.param.set('Tst', '300');
model.param.set('Tamb', Tamb);
model.param.set('alphw', h);
model.param.set('Tend', BoundT);
model.param.set('Tin', Tamb);
model.modelNode.create('mod1');




model.geom.create('geom1', 2);
model.geom('geom1').axisymmetric(true);
model.geom('geom1').feature.create('r1', 'Rectangle');
model.geom('geom1').feature('r1').set('createselection', true);
model.geom('geom1').feature('r1').set('size', {'.0079' 'lent'});
model.geom('geom1').run;

model.physics.create('c', 'CoefficientFormPDE', 'geom1');
model.physics('c').identifier('T');
model.physics('c').feature.create('flux1', 'FluxBoundary', 1);
model.physics('c').feature('flux1').selection.set([2]);
model.physics('c').feature.create('flux2', 'FluxBoundary', 1);
```

```
model.physics('c').feature('flux2').selection.set([4]);
model.physics('c').feature.create('dir1', 'DirichletBoundary', 1);
model.physics('c').feature('dir1').selection.set([3]);

model.mesh.create('mesh1', 'geom1');
model.mesh('mesh1').feature.create('ftri1', 'FreeTri');

model.view('view1').axis.set('xmin', '-0.002875993959605694');
model.view('view1').axis.set('xmax', '0.010775993578135967');
model.view('view1').axis.set('ymin', '-9.99250914901495E-4');
model.view('view1').axis.set('ymax', '0.02098424918949604');

model.physics('c').field('dimensionless').component({'T'});
model.physics('c').field('dimensionless').field('T');
model.physics('c').feature('cfeq1').set('c', {'keffr' '0' '0'
'keffax'});
model.physics('c').feature('cfeq1').set('da', '0');
model.physics('c').feature('cfeq1').set('be', {'0' 'vel*pf*Cpf'});
model.physics('c').feature('init1').set('T', 'Tst');
model.physics('c').feature('flux1').set('g', 'vel*pf*Cpf*(Tin -
T)');
model.physics('c').feature('flux2').set('g', 'alphw*Tamb');
model.physics('c').feature('flux2').set('q', 'alphw');
model.physics('c').feature('dir1').set('r', 'Tend');

model.mesh('mesh1').run;

model.study.create('std1');
model.study('std1').feature.create('stat', 'Stationary');

model.sol.create('sol1');
model.sol('sol1').study('std1');
model.sol('sol1').attach('std1');
model.sol('sol1').feature.create('st1', 'StudyStep');
model.sol('sol1').feature.create('v1', 'Variables');
model.sol('sol1').feature.create('s1', 'Stationary');
model.sol('sol1').feature('s1').feature.create('fc1',
'FullyCoupled');
model.sol('sol1').feature('s1').feature.remove('fcDef');

model.result.dataset.create('rev1', 'Revolve2D');
model.result.create('pg1', 'PlotGroup2D');
model.result('pg1').feature.create('surf1', 'Surface');
model.result.create('pg2', 'PlotGroup3D');
model.result('pg2').feature.create('surf1', 'Surface');

model.sol('sol1').feature('st1').name('Compile Equations:
Stationary');
model.sol('sol1').feature('st1').set('studystep', 'stat');
model.sol('sol1').feature('v1').set('control', 'stat');
model.sol('sol1').feature('s1').set('control', 'stat');
model.sol('sol1').runAll;

model.result.dataset('rev1').set('startangle', '-90');
model.result.dataset('rev1').set('revangle', '225');
```

```
model.result('pg1').set('title', 'Surface: Dependent variable T ');
model.result('pg1').set('titleactive', false);
Y = zeros(size(X));
z = zeros(size(X));
X = transpose(X)
z = transpose(z);
Y = transpose(Y);
a = mphinterp(model,'T','coord',[0;X(2)]);
Y = mphinterp(model,'T','coord',[z;X]);
Y
Y = Y-273.15
out = Y;
```